POLITECNICO DI MILANO

Scuola di Ingegneria dei Processi Industriali

Corso di Laurea Specialistica in
Ingegneria Nucleare

High temperature behaviour of nuclear materials investigated by laser heating and fast pyrometry

Relatore: Prof. Lelio LUZZI

Co-relatore: Dr. Konstantinos BOBORIDIS

Dr. Dario MANARA

Tesi di Laurea di:

Luca CAPRIOTTI Matr. 750814

Andrea QUAINI Matr. 745639

Anno Accademico 2010 - 2011

Acknowledgements

The opportunity to have been involved in an international project side by side with people coming from, essentially, all the continents is as good as is a rare occurrence. We are very grateful to the European Commission and Politecnico di Milano to have made this possible.

We would firstly like to express our gratitude to Prof. T. Fanghänel, Director of the Institute for Transuranium Elements (Joint Research Centre, ITU, Karlsruhe, Germany) and Prof. R.J.M. Konings, Head of the Materials Research Unit of the ITU, for giving us the opportunity to complete this eight months traineeship, and supporting our work.

We wish to thank our supervisor at Politecnico di Milano Prof. L. Luzzi, who played a crucial role in the definition of the final work outline and, moreover, has helped us to start this adventure.

We warm thank our supervisors, in ITU, Dr. D. Manara and Dr. K. Boboridis, who have led us through the entire project with their experience in Material Science and Laser Heating Technique. We are thoroughly in debt with them, for the constant support, the fruitful scientific discussions and for the infinite patience in the correction of this manuscript.

We would also like to thank all the ITU staff, in particular:

- R. Böhler and Dr. M. J. Welland, who have helped us during the experimental campaign and the simulations.
- Dr. R. Eloirdi, M. Ernstberger, Dr. A. Janßen and A. Thiele who performed for us the characterisation of numerous samples.
- J.-Y. Colle for the technical support during the entire traineeship.
- The administrative ITU staff, especially Mrs. K. Barczi who firstly welcomed at ITU and has helped us with bureaucratic practices and Mrs. P. Stube who has been of great help regarding whatever administrative issue.

We would finally thank all the special people, some of whom have already been mentioned, who have lived and worked beside us during these eight months:
Marco and Octavian with whom we have played the “Tuesday – football – match” since the beginning of the traineeship;
Sylvain, Valentino, Giovanni, Mattia and Ivana with whom we have shared many nights in Karlsruhe, and Zeynep who has become a perfect Italian student.

Last but not least we are deeply grateful with the “ITU Italian Group”, Elisa, Fidelma, Simona, Valentina and Zap, with whom we shared plenty of lunches and dinners, kilos of pasta and gorgeous time.

Thank you all !

Contents

Acronyms

ADC	Analogic to Digital Converter
ADS	Accelerator Driven System
AHWR	Advanced Heavy Water Reactor
bcc	Body Centred Cubic crystal
BSE	Back – Scattered Electron
DC	Direct Current
DPRK	Democratic People's Republic of Korea
EA	Energy Amplifier
EDS	Energy Dispersive Spectroscopy
fcc	Face Centred Cubic crystal
HT	High Temperature
HTGR	High Temperature Gas Reactor
IAEA	International Atomic Energy Agency
IMF	Inert Matrix Fuel
IMGC	Istituto di Metrologia "G. Colonnetti"
INRIM	Instituto Nazionale di Ricerca Metrologica
ITS 90	International Temperature Scale of 1990
ITU	Institute for Transuranium Elements
LMFBR	Liquid Metal Fast Breeder Reactor
LO	Longitudinal Optical band
LWR	Light Water Reactor
MOX	Mixed Uranium – Plutonium OXides
NEA	Nuclear Energy Agency
NIST	National Institute of Standard and Technology
NPP	Nuclear Power Plant
NPT	Non-Proliferation Treaty of nuclear weapons
NSE	Normal Spectral Emittance
OECD	Organisation for Economic Co-operation and Development
OIML	Organisation Internationale de Métrologie Légale
O/Th	Ratio between O and Th atomic concentration
PM	Photomultiplier

R&D	Research and Development
SE	Secondary Electron
SEM	Scanning Electron Microscopy
SOFC	Solid – Oxide Fuel Cell
SRP	Secondary Reference Point
SSE	Size – of – Source Effect
TA	Transversal Acoustic band
TG	Thermo – Gravimetry
TO	Transversal Optical band
TOX	Mixed Uranium – Thorium OXides
UV	Ultra-Violet
XRD	X – Ray Diffraction
WCED	World Commission of Environment and Development

List of Figures

List of Tables

Abstract

The main goal of this work has been the study of the high temperature behavior of some high-melting oxides of interest for the nuclear industry. In particular, the investigated ThO_2 and $(U,Th)O_2$ mixed oxides can be employed as a "sustainable" nuclear fuel. Other oxides (CaO, CeO_2) have been studied in parallel, as to better understand the optical semitransparency effect, typical of ThO_2, and their oxygen behavior.

Many experimental difficulties have been faced, such as high chemical reactivity, the fast oxidation/reduction processes, volatilization, the interaction of the specimens with the container and the temperature detection itself.

New experimental data have been produced by using an innovative method developed at ITU. It is based on laser heating coupled with fast pyrometry. The current results are in fair agreement with literature, whereby they add new important data points to databases which are still limited and uncertain. In particular, the melting behavior of CaO has been studied here under reducing and oxidizing conditions for the first time. This approach has shown that the large discrepancy found in literature is due to the paramount influence of the environment on its melting behavior. Similar results have been obtained for CeO_2. Furthermore, the high-temperature phase diagram of the UO_2-ThO_2 system has been reassessed. The solidus/liquidus lines, which define the melting behavior of this nuclear fuel and constitute fundamental information for a reactor design, have been observed to present a minimum melting temperature around 3050 K for a composition of 5 mol% ThO_2. For higher thoria contents, the most recent literature data on the melting point of pure ThO_2 (around 3620 K) have been reproduced.

Meanwhile, the current method has been validated through the measurements of the radiance temperature of melting of five refractory metals (secondary references points for the ITS-90). These tests have also served to identify some important error sources.

Finally, a set of experimental data was produced as to validate a theoretical model for the simulation of fast laser experiments and the spatial beam profile of the laser employed was determined.

Keywords: Laser heating technique, (U,Th) mixed oxides, ThO_2, semitrasparent materials.

Estratto

1 Introduzione

Il presente lavoro è stato svolto in collaborazione tra Politecnico di Milano e Istituto degli Elementi Transuranici (ITU), Centro Comune di Ricerca della Commissione Europea sito in Karlsruhe (Germania), durante un periodo di tirocinio della durata di 8 mesi presso lo stesso Istituto degli Elementi Transuranici.

Questo progetto si colloca in una delle tematiche fondamentali del 7° Programma Quadro per la Ricerca della Comunità Europea [1] riguardante la sicurezza dei reattori nucleari, e in particolare il comportamento del combustibile nucleare in condizioni estreme, nonché nella ricerca fondamentale e applicata sulle proprietà ad alte temperature degli attinidi e dei loro composti. Attività di ricerca in questo campo ricevono stimoli sempre maggiori dalla necessità sempre più stringente di produrre energia in maniera sostenibile, particolarmente se da fonte nucleare.

La tecnica sperimentale impiegata in questa ricerca è il riscaldamento laser rapido con misurazione della temperatura attraverso pirometri con risoluzione del microsecondo. Con essa si sono condotte campagne sperimentali atte a investigare le temperature di fusione di vari materiali nucleari e non.

Più nello specifico, si è misurata la temperatura di fusione in varie condizioni (riducenti ed ossidanti) del diossido di torio, un materiale refrattario che può essere usato come componente di combustibile nucleare "sostenibile", sia nella veste di sorgente fertile, sia in quella di matrice inerte [2]. Data la proprietà ottica di semitrasparenza[1] del ThO_2, sono stati studiati altri materiali non nucleari con simili

[1] La semitrasparenza è la proprietà di un materiale, in un certo campo spettrale, di essere trasparente alla radiazione elettromagnetica fino a una certa temperatura critica e opaco al di là di detta temperatura. È inoltre utile specificare che la maggiore difficoltà sperimentale in questi casi consiste nel superare la temperatura critica tramite riscaldamento laser in corpi che sono quasi completamente trasparenti alla radiazione.

proprietà ottiche, come l'ossido di calcio e il diossido di cerio, per una migliore comprensione del comportamento di questi composti sottoposti a irraggiamento laser.
Si sono inoltre svolte simili attività sperimentali sugli ossidi misti di uranio e torio, per una più completa caratterizzazione ad alta temperatura di questo tipo di combustibile nucleare.
In parallelo è stata condotta una campagna sperimentale riguardante la validazione della tecnica usata mediante la misurazione delle temperature di radianza di fusione di cinque metalli puri: vanadio, niobio, molibdeno, tantalio e tungsteno. In questo quadro si è inoltre fornito un set di dati sperimentali sul niobio utili per la validazione di un modello teorico recentemente sviluppato dal Dr. M. J. Welland congiuntamente al Royal Military College di Kingston (Canada) e in ITU per la simulazione "Phase Field", attraverso l'utilizzo del programma COMSOL, del rapido riscaldamento di elementi di combustibile. Tale modello si basa sulle equazioni della Termodinamica Irreversibile. Allo scopo di fornire ulteriori dati indispensabili per la simulazione degli esperimenti, si sono infine effettuate misure originali del profilo spaziale del raggio laser usato per i presenti esperimenti attraverso un profilo-metro laser.

2 Metodi sperimentali e di caratterizzazione dei materiali

Come anticipato nell'introduzione, la tecnica sperimentale consiste nel riscaldamento laser con misurazione della temperatura di radianza attraverso pirometri, e successivo calcolo della temperatura "vera" grazie alla misura dell'emittanza normale spettrale mediante uno spettro-pirometro multicanale, un dispositivo per misurare la radianza spettrale. Molti sono i vantaggi rispetto alle tecniche convenzionali normalmente usate, come la ridotta area di contatto tra il materiale investigato e il contenitore, così da evitare "contaminazioni", e il breve tempo di esposizione del campione ad alte temperature che limita la vaporizzazione dello stesso ed altri effetti indesiderati in gran parte dovuti all'elevata reattività chimica dei materiali congiunta alla cinetica accelerata dalle alte temperature.

Più nello specifico, per il riscaldamento dei campioni si è adoperato un laser a stato solido Nd:YAG con lunghezza d'onda a 1064 nm e potenza massima di 4,5 kW. Per quanto riguarda la misurazione delle temperature di radianza e il calcolo dell'emittanza sono stati calibrati e impiegati un pirometro a due lunghezze d'onda (650 nm e 488 nm) e uno spettro-pirometro con matrice di 256 fotodiodi con uno spettro di lunghezze d'onda da 480 a 1010 nm. E' stata anche effettuata la difficile calibrazione di un pirometro UV con lunghezza d'onda efficace di 219 nm, che sarà usato nel seguito di questa ricerca.

I campioni sono stati posizionati verticalmente in contenitori, normalmente con tre o quattro viti di sostegno, posti all'interno di autoclavi munite di finestre e a tenuta di pressione. Sono state condotte misure in vari regimi di pressione, da pressione ambiente fino a 1500 bar, e con vari gas di riempimento (argon, aria, argon + idrogeno, ossigeno). In Fig. 2.1 è sintetizzato lo schema della tecnica sperimentale appena descritta.

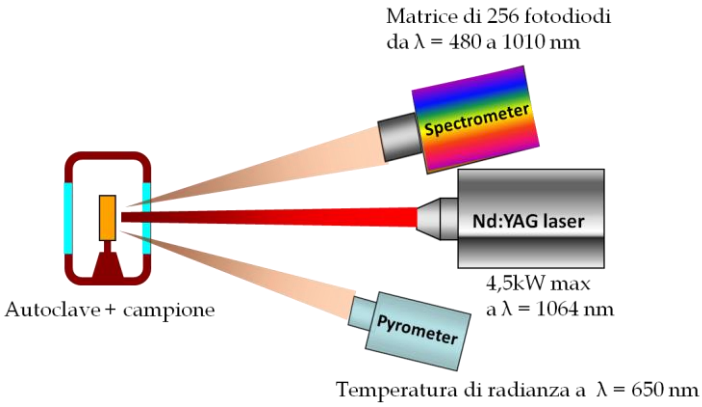

Fig. 2.1. Schema della tecnica sperimentale.

Per quanto riguarda la caratterizzazione dei materiali, i composti studiati sono stati analizzati prima e dopo gli esperimenti laser con varie tecniche, quali: SEM - EDS (microscopio a scansione elettronica – spettroscopia a dispersione di energia), termo-gravimetria, XRD (diffrazione raggi X) e spettroscopia Raman.

3 Risultati

3.1 Validazione della tecnica sperimentale

Nel corso della campagna sperimentale per validare la tecnica usata, si sono misurate le temperature di radianza di fusione di cinque metalli puri: vanadio, niobio, molibdeno, tantalio e tungsteno. Questi materiali hanno temperature di radianza di fusione (T_λ) tra i più alti della tavola periodica e sono stati raccomandati in [3] come possibili punti di riferimento secondari (SRP) della Scala Internazionale delle Temperature del 1990 (ITS-90).

Tabella 3.1. Valori internazionali di riferimento di temperatura di radianza di fusione dei 5 metalli studiati in questo lavoro. La T_λ è riferita a λ = 650 nm.

Metalli	T_λ / K SRP	Rif.
V	1988 ± 7	[4]
Nb	2422 ± 5	[5]
Mo	2530 ± 5	[3]
Ta	2847 ± 6	[3]
W	3207 ± 7	[6]

Gli esperimenti sono stati condotti su campioni metallici di 8 mm di diametro con vari gradi di purezze e di spessore, come riportato in Tabella 3.2.

Tabella 3.2. Caratteristiche dei campioni metallici utilizzati.

Metalli	Spessore / mm	Purezza (mol%)
V	0,075 ; 0,127	99,8
Nb	0,05 ; 0,1 ; 0,125 ; 0,127	99,8 – 99,7
Mo	0,1 ; 0,125 ; 0,127	99,9 ; 99,95
Ta	0,025 ; 0,127	99,9 ; 99,997
W	0,05 ; 0,1	99,95

Si sono svolte prove con diversi profili di potenza nel tempo, come impulsi quadrati con potenze relativamente basse (500 W) ma lunga durata (100 ms) o impulsi più corti (10 – 20 ms) ma massima potenza (4,5 kW).

Un termogramma tipico di questi esperimenti è quello mostrato in Fig. 3.1.

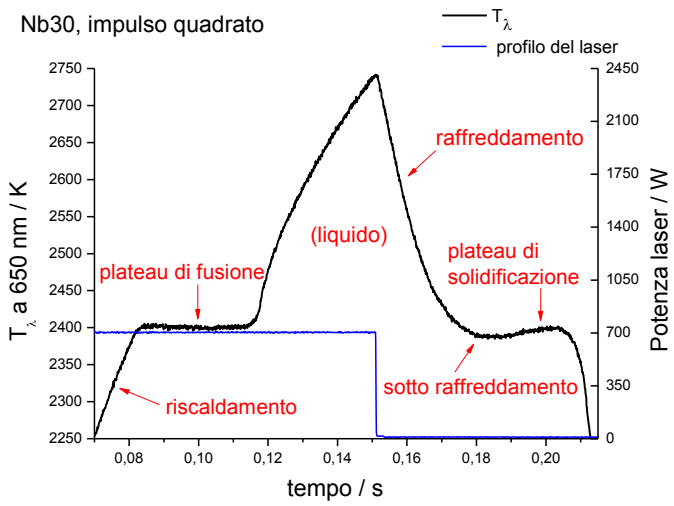

Fig. 3.1. Tipico termogramma ottenuto su un campione di niobio.

Nelle molteplici misure condotte si sono osservati interessanti comportamenti, quali il cambiamento di emittanza all'inizio del plateau di fusione (come riscontrato in letteratura), la non perfetta orizzontalità dei plateau e una leggera discrepanza in temperatura tra plateau di fusione e di solidificazione.

Per quanto riguarda invece le misure delle temperature di radianza di fusione, queste sono riassunte in Tabella 3.3. Il disaccordo tra le presenti temperature di radianza di fusione e quelle riportate in letteratura può essere ascrivibile a più motivi: una non sufficiente purezza dei materiali impiegati, la deviazione dei parametri sperimentali (profilo e potenza del laser) da quelli nominali, che potrebbe influire sui termogrammi, oppure l'effetto "della dimensione della sorgente", dipendente dal comportamento ad alta temperatura dei materiali e del pirometro.

Tabella 3.3. Risultati: temperature di radianza di fusione misurate a λ = 650 nm e valori di letteratura per confronto.

Metalli	Campioni	Esperimenti[i]	T_λ / K [ii] (f) (s)	T_λ / K SRP
V	8	35(29)	1976 ± 28 1975 ± 28	1988 ± 7
Nb	18	111(51)	2400 ± 41 2398 ± 41	2422 ± 5
Mo	5	30(12)	2509 ± 45 2504 ± 45	2530 ± 5
Ta	5	55(15)	2823 ± 53 2825 ± 53	2847 ± 6
W	6	36(13)	3169 ± 71 3156 ± 71	3207 ± 7

[i] I valori tra parentesi rappresentano il numero di esperimenti considerati nella statistica.

[ii] E' riportato un valore di incertezza pari a 2 volte la deviazione standard dei dati sperimentali. (f) sta per temperatura del plateau di fusione e (s) per temperatura del plateau di solidificazione.

Come anticipato nell'introduzione, si è fornito anche un set di dati sperimentali sul niobio per validare il modello teorico; il set si compone di termogrammi con e senza cambiamento di fase e di termogrammi in cui la temperatura è stazionaria, ovvero non dipendente dal tempo. Dai primi risultati ottenuti sulle curve di riscaldamento, si riscontra un buon accordo tra i dati sperimentali e le curve simulate (vedi Capitolo 3). Per quanto riguarda invece la simulazione dei termogrammi con plateau di fusione / solidificazione, il lavoro è tuttora in corso presso l'Istituto degli Elementi Transuranici.

Infine, si sono effettuate misure di profilo spaziale del laser. Da questa indagine si è riscontrata una chiara discrepanza di 5 centimetri tra il punto di messa a fuoco del laser nell'infrarosso (a 1064 nm) e quello del laser pilota visibile (632 nm) usato per le operazioni di messa a punto degli esperimenti. Di conseguenza, anche il profilo spaziale del laser infrarosso sul piano focale è notevolmente diverso da quello ipotizzato (densità di potenza costante e ottica laser nominale di 3 mm in diametro).

3.2 Risultati sperimentali

Ossido di calcio, CaO

Nonostante sia uno tra i materiali refrattari più comunemente usati, il valore della temperatura di transizione solido/liquido dell'ossido di calcio rimane dibattuta. Gli esperimenti ottenuti in passato e riassunti nel lavoro di Yamada et al. [7], forniscono risultati con una dispersione di circa 350 K.

Durante la presente campagna sperimentale, si è risolto il già citato problema della semitrasparenza del CaO impostando un opportuno profilo di potenza del raggio laser in funzione del tempo. Questo ha permesso una migliore comprensione del fenomeno, osservato anche negli esperimenti condotti sul ThO_2. Grazie alla possibilità di controllare il gas in contatto con il campione studiato, si è inoltre osservato che la riproducibilità dei risultati appariva strettamente legata alle condizioni atmosferiche imposte all'interno dell'autoclave durante gli esperimenti di fusione. Quando, durante uno di questi esperimenti, l'autoclave veniva riempita con aria compressa (atmosfera ossidante), l'arresto termico veniva rilevato ad una temperatura prossima ai 3150 K. Di contro, se l'autoclave veniva riempita con argon (simulante di atmosfera riducente), la temperatura di fusione risultava prossima a 2850 K. I risultati acquisiti in atmosfera ossidante sono comparabili a quelli ottenuti in passato con metodi "senza contenitore" e con riscaldamento remoto. Con atmosfera riducente, i risultati sperimentali si allineano a quelli ottenuti con metodi tradizionali di riscaldamento con forno, in cui il campione sotto esame era a diretto contatto con un crogiolo, solitamente in tungsteno. Foex [8] ha mostrato come il diretto contatto con il tungsteno, a temperature prossime alla fusione, porti alla formazione di un ossido ternario del tipo $CaWO_3$, il cui punto di fusione risulta sensibilmente più basso rispetto al puro ossido di calcio. Si può quindi concludere che portare a temperature prossime alla fusione l'ossido di calcio, in presenza di una atmosfera riducente, abbassa sensibilmente la temperatura di transizione liquido/solido rilevata. L'evidente cambio di colorazione dopo un esperimento condotto in atmosfera riducente (la zona fusa diventa nera) porta a credere a modifiche nella struttura cristallina o alla creazione di una nuova fase.

Infatti, mentre dall'analisi Raman post-fusione non si sono evidenziati cambiamenti di tal genere, l'analisi XRD ha mostrato come una seconda fase, probabilmente attribuibile al materiale nero fuso, sia rilevabile. Nonostante questo risultato, ulteriori analisi saranno necessario per meglio definire l'origine di tale fenomeno. Ritenendo quindi gli esperimenti condotti con atmosfera ossidante gli unici utilizzabili per un'analisi statistica sul CaO "puro", la temperatura di fusione dell'ossido di calcio ottenuta in questo lavoro risulta essere (3126 ± 79) K (due deviazioni standard). L'emittanza spettrale dell'ossido di calcio liquido ottenuta al punto di solidificazione è 0,95 ± 0,03.

Diossido di cerio, CeO_2

Il diossido di cerio è, a temperatura ambiente e pressione atmosferica, la fase più stabile del sistema binario Ce-O. Vista la predisposizione alla riduzione del CeO_2 e l'elevato numero di vacanze d'ossigeno presenti nella struttura cristallina, una fusione coerente è attesa solo in condizioni fortemente ossidanti. La conferma di ciò è in letteratura, dove sono riportate temperature di fusione per il diossido di cerio di 2670 K [9], 2753 K [10] e 3000 K [11] rispettivamente per esperimenti condotti in atmosfera riducente, in aria e in atmosfera fortemente ossidante. Con l'attuale lavoro, utilizzando come gas di riempimento sia argon che aria compressa, si sono simulate rispettivamente condizioni atmosferiche riducenti e ossidanti. Anche in questo caso, il profilo temporale dell'impulso laser impiegato per riscaldare i campioni è stato ottimizzato per risolvere il problema della semitrasparenza, ben visibile in Fig. 3.2.

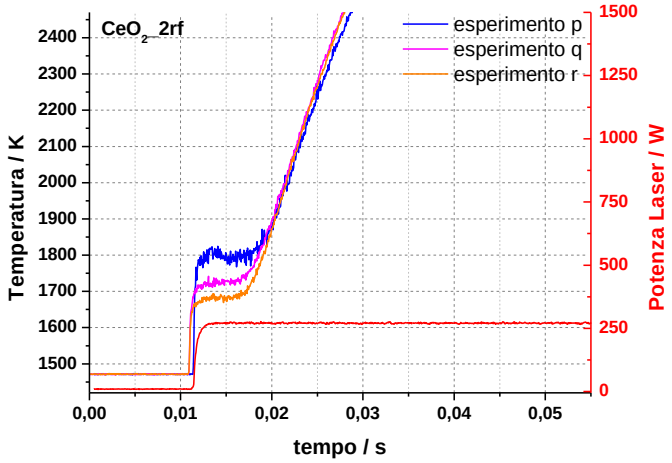

Fig. 3.2. Effetto della semitrasparenza durante tre esperimenti condotti sul campione CeO_2_2rf.

In Fig. 3.3 è mostrata la serie di esperimenti consecutivi condotti sul campione CeO_2_2rf. Il gas utilizzato per riempire l'autoclave in ciascun esperimento è etichettato accanto ad ogni punto sperimentale. Dalla figura è chiara la tendenza della temperatura di fusione rilevata a stabilizzarsi su differenti valori a seconda che il gas di riempimento sia argon o aria compressa.

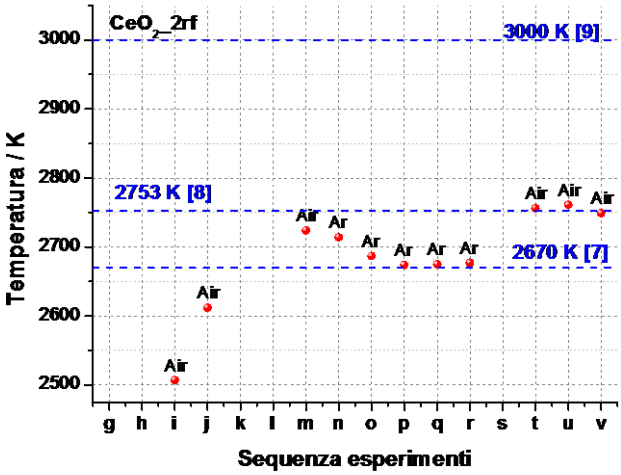

Fig. 3.3. Sequenza di risultati sperimentali ottenuti con il campione denominato CeO_2_2rf. Gli esperimenti condotti in atmosfera riducente sono etichettati con "Ar", mentre gli esperimenti condotti in atmosfera ossidante con "Air".

L'analisi post-fusione tramite spettroscopia Raman sui campioni fusi in atmosfera riducente suggeriscono che potrebbero aver avuto luogo cambiamenti a livello del

reticolo cristallino. Ulteriore conferma è data dal cambiamento di colore dell'area fusa: questa zona, prima della fusione biancastra, appare infatti bluastra e tendente al nero. Questi cambiamenti sono ragionevolmente da imputarsi alla perdita di ossigeno ad alta temperatura e alla susseguente ipostechiometria della regione fusa. In conclusione, una temperatura di fusione per il diossido di cerio è consigliata nel valore (2743 ± 33) K (due deviazioni standard) se la fusione avviene in atmosfera ossidante. Se in atmosfera riducente, il valore suggerito è (2675 ± 47) K. Il valore calcolato per l'emittanza normale spettrale è 0,90.

Diossido di torio, ThO_2

Il diossido di torio è l'ossido binario con il più alto punto di fusione in natura. Il lavoro condotto da Ronchi e Hiernaut [12] suggerisce una temperatura congruente di fusione di (3651 ± 17) K per il diossido di torio stechiometrico. Nel presente lavoro si è studiato il suo comportamento a temperature prossime alla fusione, sia in condizioni riducenti sia in condizioni ossidanti. Un tipico termogramma nelle vicinanze dell'arresto termico è mostrato in Fig. 3.4.

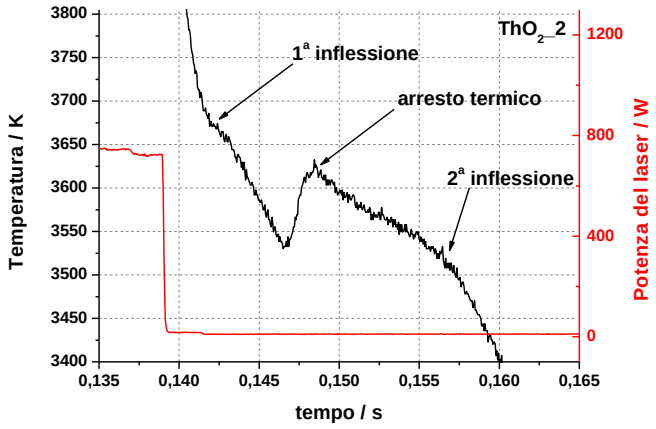

Fig. 3.4. Termogramma misurato su un campione di ThO_2 nelle vicinanze dell'arresto termico corrispondente alla solidificazione (campione ThO_2_2).

Date le estreme condizioni termiche raggiunte durante gli esperimenti, il controllo dello stato di ossidazione dei campioni è risultato difficoltoso. Dall'analisi termogravimetrica deriva infatti che la zona fusa in condizioni riducente risulta ipostechiometrica con un rapporto O/Th~1,5. Una successiva analisi XRD ha

confermato solo in parte tale riduzione del materiale. Finalmente, nonostante i risultati ottenuti in aria e argon per la temperatura dell'arresto termico risultino comparabili, si è scelto di considerare per l'analisi statistica solo gli esperimenti condotti in aria (atmosfera ossidante), ottenendo una temperatura di (3622 ± 65) K (due deviazioni standard). Il grado di incertezza legato alle altre due inflessioni visibili in diversi termogrammi, è fortemente affetto dalla difficoltà nel rilevarle e dalla dispersione dei dati sperimentali. La prima (presumibilmente legata ad una transizione gas/liquido) a (3808 ± 155) K, era già stata riportata in letteratura, ma senza alcun commento. La seconda a più bassa temperatura (riconducibile ad una solidificazione non congruente di diossido di torio non stechiometrico) è stata misurata nel presente lavoro a (3468 ± 77) K. L'emittanza normale spettrale calcolata per il diossido di torio liquido risulta pari a 0,870 ± 0,002 (deviazione computazionale).

Ossidi misti diossido di uranio-diossido di torio, $(U,Th)O_2$

Nonostante gli ossidi misti $(U,Th)O_2$ siano tra i più accreditati a diventare combustibile nucleare "sostenibile", specialmente in certi Paesi ricchi di risorse minerali contenenti torio, il numero di studi ad alta temperatura reperibili in letteratura su tali composti rimane esiguo. Lambertson et al. [13] hanno investigato le temperature di transizione liquido/solido per diverse composizioni intermedie del sistema pseudo - binario UO_2 - ThO_2. Latta, Fryxell e Duderstadt [14] hanno invece focalizzato la loro attenzione sulla regione a basso contenuto di diossido di torio dello stesso sistema. Con il presente lavoro si sono studiate sei differenti composizioni, tali da coprire l'intera estensione del diagramma di fase. Per gli ossidi misti $(U,Th)O_2$ sono apparsi significativi sia i valori di temperatura ottenuti ad alta pressione (fino a 1000 bar di He), sia i risultati sperimentali condotti con un'autoclave limitata a 3 bar. Le temperature, già corrette con l'emittanza normale spettrale, sono riassunti in Tabella 3.4.

Tabella 3.4. Risultati sperimentali condotti sugli ossidi misti $(U,Th)O_2$. La sigla TOX 5 indica una composizione con 5 mol % di ThO_2 e così via per le altre composizioni. Le temperature nella colonna T hp sono state ottenute ad alta pressione.

Composizione	T / K hp	U^{i} / K hp	T / K	U^{i} / K	Emittanza
UO_2	3106	75	3115	30	0,830
TOX 5	/	/	3020	67	0,832
TOX 20	3158	69	3149	19	0,838
TOX 40	3336	39	/	/	0,846
TOX 60	3348	61	/	/	0,854
TOX 80	3573	55	/	/	0,862
TOX 95	/	/	3587	34	0,868
ThO_2	3616	73	3622	65	0,870

[i] Incertezza estesa con intervallo di confidenza del 95%

I risultati riportati in tabella in gran parte confermano e in alcuni casi ridefiniscono i valori della letteratura. Nella regione a basso contenuto di ThO_2 è confermato il brusco cambiamento nella pendenza della linea di transizione liquido/solido, con un minimo attorno a 5 mol % ThO_2, come mostrato nel lavoro di Latta et al. [14]. Nella regione tra 20 e 40 mol % ThO_2, i precedenti risultati vengono essenzialmente confermati. Le temperature di transizione ottenute per i composti ad alto contenuto di ThO_2 (TOX 80 e TOX 95), risultano invece più alti rispetto al lavoro condotto da Lambertson et al., ma in accordo con il recente lavoro di Ronchi e Hiernaut. Una sintesi grafica dei risultati di questo lavoro è riportata in Fig. 3.5.

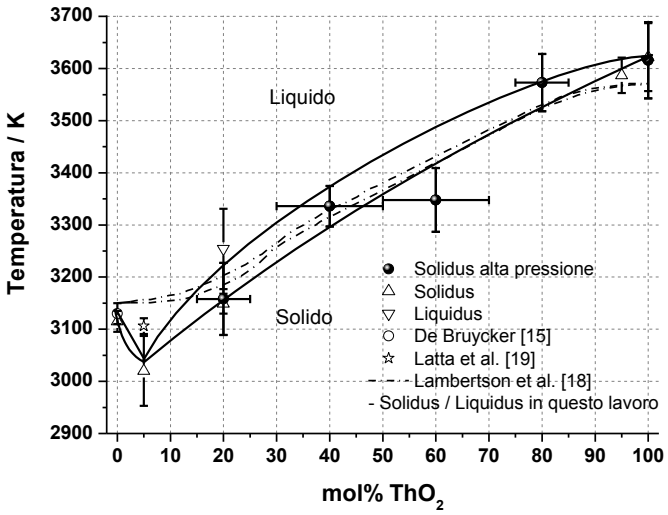

Fig. 3.5. Linee di solidus e liquidus misurate in questo lavoro. Le linee tratteggiate, sono le linee di solidus e liquidus misurate da Lambertson et al. [13]. Le linee piene rappresentano la stima del presente lavoro. Queste, sono da intendersi come linee guida per una migliore comprensione.

Dall'analisi XRD condotta su un campione fuso di TOX 40, sono state rilevate due fasi. Questo fenomeno può essere facilmente relazionato a un processo di segregazione durante la solidificazione. Nonostante dalle altre analisi post-fusione non vi sia traccia dello stesso fenomeno, sono state aggiunte prudentemente delle bande di incertezza orizzontali relative alle composizioni.

4 Conclusioni

Con il presente lavoro si è studiato il comportamento ad alta temperatura di ossidi refrattari, nucleari e non nucleari. Si è inizialmente analizzato lo stato dell'arte e la letteratura al riguardo, revisionando criticamente gli aspetti di maggior interesse per il presente lavoro. Sono state condotte numerose prove sperimentali ottenendo un buon set statistico, sia in condizioni sperimentali già note e investigate (per un confronto con la letteratura esistente), sia in condizioni finora mai trattate. Un sommario della campagna sperimentale condotta sugli ossidi è mostrato in Tabella 4.1. L'elevato potenziale di ossigeno a temperature prossime alla fusione rende lo studio di questi ossidi particolarmente delicato. Grazie all'elevato numero di prove condotte e alla tecnica utilizzata, queste problematiche legate alle estreme condizioni sperimentali sono state affrontate con successo. La riduzione al minimo del contatto tra il campione e il supporto, la rapidità dell'esperimento e il controllo delle condizioni atmosferiche (possibilità di scegliere un ambiente ossidante o riducente) hanno limitato gli effetti legati alla elevata reattività chimica dei composti (esaltata da cinetiche di reazione particolarmente rapide a temperature superiori ai 3000 K) e alla semitrasparenza.

Il metodo, a sua volta, è stato accuratamente validato, attraverso uno studio sulla temperatura di radianza di fusione di vari metalli, raccomandati come riferimenti secondari della ITS-90. Si è fornito inoltre un primo set di dati sperimentali sul niobio per la validazione di un modello teorico simulante gli esperimenti e si è svolta, allo stesso scopo, la misurazione del profilo spaziale del laser.

Comprendere il comportamento ad alta temperatura e in differenti condizioni ambientali di composti contenti attinidi è di fondamentale importanza per la

sicurezza dei reattori nucleari. I risultati più che incoraggianti ottenuti in questo lavoro sul ThO_2 e sugli ossidi misti $(U,Th)O_2$ sono perfettamente in linea con quelli già ottenuti in precedenza con lo stesso approccio sperimentale su UO_{2+x} [16], PuO_2 [15], $(U,Pu)O_2$ [15] e NpO_2 [17], parte dei quali hanno apportato considerevoli correzioni a basi di dati che si credevano ormai stabilite da decenni. Si ritiene perciò che lo studio di altri composti alto-fondenti attraverso questo metodo possa portare a una importante revisione dei diagrammi di fase ad alta temperatura di altrettanti sistemi chimico-fisici di grande interesse per l'industria nucleare e per altre applicazioni. Questa conclusione vale in particolare per i composti di attinidi, il cui comportamento ad alta temperatura costituisce ancora un settore di grande interesse anche dal punto di vista della ricerca fondamentale. La qualità dei risultati ottenuti su CaO e CeO_2 conferma inoltre la validità del metodo sperimentale qui impiegato per lo studio di materiali semitrasparenti con elevato punto di fusione e alto potenziale d'ossigeno.

Tabella 4.1. Sommario dell'attività sperimentale svolta sui composti ossidi

Materiali	Campioni	Numero di esperimenti [i]		Temperatura di fusione / K		Commenti
			hp		hp	
CaO	10	28(10)	42(/)	3126 ± 79	/	
CeO_2	13	41(16)	67(/)	2675 ± 47	/	in Argon
				2743 ± 33	/	in Aria
UO_2	3	5(4)	3(3)	3115 ± 30	3106 ± 75	
TOX 5	1	9(6)	/	3020 ± 67	/	
TOX 20	4	4(4)	15(4)	3149 ± 19	3158 ± 69	
TOX 40	2	/	10(3)	/	3336 ± 39	
TOX 60	1	/	7(7)	/	3348 ± 61	
TOX 80	2	/	5(3)	/	3573 ± 55	
TOX 95	2	6(4)	/	3587 ± 34	/	
ThO_2	6	35(20)	12(8)	3622 ± 65	3616 ± 73	

[i] I valori tra parentesi rappresentano il numero di esperimenti considerati nella statistica.

Riferimenti

[1] http://itu.jrc.ec.europa.eu/

[2] Ch. Hellwig, M. Streit, P. Blair, T. Tverberg, F.C. Klaassen, R.P.C. Schram, F. Vettraino and T. Yamashita, J. Nucl. Mater., 352 (2006), 291.

[3] R.E. Bedford, G. Bonnier, H. Maas and F.Pavese, Metrologia, 33 (1996), 133.

[4] J.L. McClure, A. Cezairliyan, Int. J. Thermophys., 18 (1997), 1.

[5] A. Cezairliyan, A. P. Miiller, Int. J. Thermophys., 13 (1992), 39.

[6] A. P. Miiller, A. Cezairliyan, Int. J. Thermophys., 14 (1993), 511.

[7] T. Yamada, M. Yoshimura, and S. Somiya, J. Am. Ceram. Soc., 69 [10] (1986), C-243.

[8] M. Foex, Solar Energy, 9 [1] (1965), 61.

[9]] O. A. Mordovin, N. I. Timofeeva and L. N. Drozdova, Inorg. Mater. (URSS), 3 (1967), 159.

[10] M. Foex, Rev. Hautes Temp. Refract., 3 (1966), 309.

[11] L. Brewer, Chem. Rev., 52 (1953), 1.

[12] C. Ronchi and J. P. Hiernaut, J. Alloy Compd., 240 (1996), 179.

[13] W. A. Lambertson, M. H. Mueller and F. H. Gunzel, Jr., J. Am. Ceram. Soc., 36 (1953), 397.

[14] R. E. Latta, E. C. Duderstadt and R. E. Fryxell, J. Nucl. Mater., 35 (1970), 347.

[15] F. De Bruycker, “High Temperature Phase Transitions in Nuclear Fuels of the Fourth Generation”, PhD Thesis, Technical Note JRC-ITU-TN-2011/4 (2011).

[16] D. Manara, C. Ronchi, M. Sheindlin, M. Lewis and M. Brykin, J. Nucl. Mater., 342 (2005), 148.

[17] R. Böhler, M. J. Welland, F. De Bruycker, K. Boboridis, A. Janssen, R. Eloirdi, R.J.M. Konings and D. Manara, "Revisiting the melting temperature of NpO_2 and the challenges associated with high temperature actinide compound measurements", submitted to Nature Materials.

Introduction

One of the main current challenges of mankind is the so-called “sustainable development”. This concept can be expressed, using the definition given in 1987 by the Brundtland Commission [1], as the development that meets the needs of the present generation without compromising the needs of future generations. Two fundamental concepts are relied with sustainable development: the mankind needs, and the idea of limitation imposed by the state of technology and social organisation. In a more general manner, sustainable development combines equity between and within countries and generations, and integrates economic growth, environmental protection and social welfare.

Three facets can be identified concerning the energy production sustainability: the economical facet, which deals with costs and resource depletion, the environmental facet, which is related to the preservation of the biosphere, and the social facet mainly related to acceptance by public opinion.

Especially in this historical period of financial crisis, attention should be given to the economic competitiveness of technologies. This constitutes one of the central points of a sustainable development. Beside this, the environmental viewpoint starts to be one crucial benchmark of sustainability, requiring the conservation of plants and animal species, air and water quality, and sustainment of the ecosystem's overall integrity. In the last few years, greenhouse gas-emissions, especially CO_2, have riveted the international community attention, which now considers climate changes and global warming as paramount challenges to sustainable development. In this view, nuclear energy can find its vocation in the required mix of energy sources that is called to mitigate these anthropogenic effects. As a matter of fact, the nuclear option (being essentially carbon-free) may contribute to face these challenges.

In the case of nuclear energy, economic, environmental and social aspects assume even more significance with respect to other energetic options [2]. Economically

speaking, nuclear energy has to compete with a broad range of alternatives (e.g., fossil fuels and renewable energy sources) on the basis of full generation costs, i.e., capital, operation, maintenance, fuel costs and decommissioning. Nowadays, nuclear power plants are competitive thanks to their lower marginal costs of production (the costs not related to fixed costs). Furthermore, since the fuel represents only a small fraction of the cost of nuclear electricity, higher fuel prices could increase available resources without impacting on the competitive position of the nuclear option. On the other hand, the large initial capital cost of nuclear power plants creates financial risks, especially in deregulated markets. In this situation, research and development (R&D) strivings to reduce the capital cost of nuclear power plants play a fundamental role.

Public participation and acceptance of processes and decisions on national energetic programs are the main goals for the social aspects of sustainable development. At the same time, equity and transparency must be central pillars especially when nuclear power is concerned. While the nuclear option is perceived as low – emission of CO_2 alternative, the public opinion feels it as a risky and hardly understandable choice because it is often presented as an "elite" subject. Furthermore, nuclear risks are perceived as imposed and not counterbalanced by worthwhile benefits. The serious nuclear accidents occurred so far (Three Mile Island in 1979, Chernobyl in 1986, Fukushima in 2011) have led to significant improvements in the nuclear safety regulations and measures. However, rightful and understandable doubts still harbour in the public opinion. Moreover, proliferation concerns and long-lived radioactive wastes assume a high relevance.

The most important step made against the production of weapon-grade materials is the Non-Proliferation Treaty of Nuclear Weapons (NPT) of 1970[1] [3]. The compliance with this treaty is monitored by the International Atomic Energy Agency (IAEA) through its safeguard system. In spite of that, concerns remain

[1] In this document, the NPT non-nuclear-weapon States agree never to acquire nuclear weapons and the NPT nuclear-weapon States in exchange agree to share the benefits of peaceful nuclear technology and to pursue nuclear disarmament aimed at the ultimate elimination of their nuclear arsenals.

about illicit trafficking in fissile materials [4], clandestine activities of some countries in violation of their NPT commitment [5] and, most of all, activities of countries that remain outside the NPT.

The handling of radioactive waste, especially long-lived wastes, has become a huge concern for public opinion and scientific community. The geological disposal technique was proposed and is seen by experts as the most promising option, both technically and economically [2]. While significant progress has been made towards the study of this solution, there have also been delays and setbacks due to the failure of the waste management experts and institution to achieve sufficient public and political support [6]. In addition, the associated uncertainties concerning the future impact of this technology projected over thousands of years contributes to chill further the relationship between public opinion and nuclear experts.

In this view, some selected actions must be adopted. The choice of a closed U-Th fuel cycle, for example, which includes the deployment of breeder or iso - breeder reactors, and the development of Pu-burning reactors are plausible sustainable solutions. With closed fuel cycle is intended [7] an indefinitely repeated chain of fuel manufacturing, burning and reprocessing, in which only fertile material needs to be added to the fuel. In this way, the spent fuel does not need to be entirely disposed of, limiting the quantity of long-lived wastes to be managed and the radiotoxicity content is drastically reduced [8]. Considering then the anti-proliferation interest in the reduction of plutonium stockpiles, the promotion of technologies with this aim should be taken into account as well.

The interest of the present work on ThO_2 (thoria) is related with the revival care on thorium-based cycles and their possible employment as anti-proliferation fuel [7]. The use of a uranium-thorium cycle in thermal reactors leads to a greater conversion factor compared to the uranium-plutonium cycle. Furthermore, the use of ^{232}Th instead of ^{238}U as a fertile material could, in some specific cases (e.g., see [9]), lead to advantages in the control of the reactor. The good thermo-physical and

chemical properties of thoria, compared with UO_2, ensure a better in-pile behaviour and a more stable form for the wastes. The features of $(U,Th)O_2$ fuel were studied in depth between the 1950s and 1970s both in High Temperature Gas cooled Reactors (HTGR) and Light Water Reactors (LWR). Furthermore, ThO_2 had been successfully used as blanket material in Liquid Metal Fast Breeder Reactors (LMFBR) (see ref. [10]). Due to the great abundance of thorium on earth, in particular if compared with uranium resources, its applications as fuel take more significance, especially in relation with the sustainable development facet concerning the preservation of mineral resources. Another option is the Inert Matrix Fuel (IMF), allowing to embed plutonium oxide in a U-free matrix fuel, to burn it without production of new plutonium through neutron absorption on ^{238}U. In the IFA-652 experiment (see [11]), carried in OECD Halden Material Test Reactor, matrices both with and without thoria were tested showing a good and stable irradiation behaviour. In addition, future interests related to the possible employment of thoria in Accelerator Driven System (ADS) and Energy Amplifier (EA) should be mentioned [12] [13].

In this scenario, studies on High Temperature (HT) behaviour of thoria, and the mixed uranium-thorium oxides, (TOX), are carried out in this work. In particular, the attention is focused on the melting behaviour of these materials, fundamental feature that must be taken into account during the project of an in-pile fuel assembly and in case of accident. Different atmospheric conditions have been used in order to better define the ThO_2 and ThO_{2-x} liquid-solid transition on the phase diagram of the Th-O system. The same was done with the UO_2 - ThO_2 system. A laser heating method was used to bring the sample surface over the melting temperature. The thermal arrest temperature was detected by a fast two-channel pyrometer, and by a multi-channel spectro-pyrometer a spectral analysis was carried out, allowing emittance determination as well. Due to the semi-transparent nature of ThO_2, other non-radioactive materials with similar optical properties, like CaO (calcium oxide) and CeO_2 (cerium dioxide), were studied in order to better understand the behaviour of this type of compounds under laser irradiation. In addition, CaO is of interest,

from both a scientific and a technological viewpoint, because some discrepancies were found in literature regarding its melting temperature, and a new assessment on it is needed. The Ce-O system presents itself some evident similarities with the Pu-O system [14]. Studying the former may be useful to better understand the latter and to limit more dangerous work associated with the high radio-chemical toxicity of plutonium.

The accuracy of the method was then tested through a measuring campaign on five refractory metals whose radiance temperature of melting are well established and recommended values on ITS-90 as secondary reference points. Furthermore it was provided a set of data for corroborating the theoretical model, simulated by Dr. M. J. Welland (RMC Kingston, Canada, and ITU Karlsruhe) using COMSOL Multiphysics, and finally the spatial beam profile was determined with a laser profile-meter.

The thesis is organized as follows.

Chapter 1 contains a list of the materials investigated during the present work. Their preparation and characterisation, a brief description of the binary phase diagrams and of some characteristic features of the compounds under study are hence shown.

The experimental method (laser heating technique, pyrometry) devised and employed in the current research are described in detail in Chapter 2.

Chapter 3 reports the validation of this method through measurements on the radiance temperature of melting of five reference metals and preliminary results on modelling and profile laser beam.

Chapter 4 summarises the final results on the investigated oxides, critically discussed and compared with the results found in literature.

Finally, a summary of the improvements, obtained through this work, and the perspectives for the future is given in the Conclusions section.

References

[1] WCED, 1987, Our Common Future, http://www.un-documents.net/wced-ocf.htm

[2] OECD "Nuclear Energy in a Sustainable Development Perspective", 2000, Paris.

[3] "Treaty on the non-proliferation of nuclear weapons", IAEA, INFCIRC/140.

[4] IAEA fact sheet, "Illicit and Other Unauthorized Activities involving Nuclear and Radioactive Materials", 2005.

[5] "The DPRK's Violation of its NPT Safeguards Agreement with he IAEA", Excerpt from "History of the International Atomic Energy Agency" by David Fischer (1997, published by the IAEA).

[6] OECD "Progress Towards Geological Disposal of Radioactive Waste: Where Do We Stand?", 1999, Paris.

[7] C. Lombardi, L. Luzzi, E. Padovani and F. Vettraino, Prog. Nucl. Ener., 50 (2008), 944.

[8] C. Fiorina, F. Franceschini, J. Krepel and K. Mikityuk, Proceeding of GLOBAL 2011, Paper No. 500552, Makuhari, Japan, 2011.

[9] C. Lombardi, L. Luzzi, E. Padovani and F. Vettraino, Prog. Nucl. Ener., 38 (2001), 395.

[10] "Thorium fuel cycle – Potential benefits and challenges", IAEA-TECDOC-1450, 2005.

[11] Ch. Hellwig, M. Streit, P. Blair, T. Tverberg, F.C. Klaassen, R.P.C. Schram, F. Vettraino and T. Yamashita, J. Nucl. Mater., 352 (2006), 291.

[12] NEA, "Accelerator- driven System (ADS) and Fast Reactors (FR) in Advanced Nuclear Fuel Cycles", 2002, Paris.

[13] C. Rubbia et al., "Conceptual design of a fast neutron operated high power energy amplifier", 1995, CERN/AT/95-44 (ET).

[14] M. Zinkevich, D. Djurovic and F. Aldinger, Sol. Stat. Ion., 177 (2006), 989.

Chapter 1

Materials

1.1 Metals

Hereafter, are presented the five refractory metals used as reference materials for the validation of the laser heating technique.

These metals were chosen because their radiance temperatures of melting is established well enough to be recommended as secondary reference points for ITS-90 [1], as it will be described in Chapter 3.

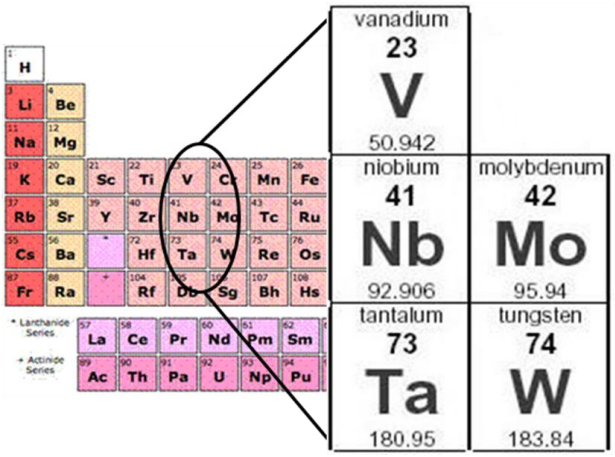

Fig. 1.1. The five refractory metals used as reference for the validation of the present experimental approach [2].

1.1.1 Vanadium

Vanadium is a silvery coloured metal. It is used as an additive in steel to strengthen and protect against corrosion, it is soft and ductile. Vanadium has good structural strength, moderate thermal neutron-capture cross-section, short half-life of the isotopes produced by neutron capture and good resistance to irradiation damage that

makes this metal (vanadium alloys: V-Cr-Ti) a suitable material for the first wall and blanket structure of a fusion reactor [3,4,5].

Several vanadium alloys show superconducting behaviour. Some general properties are shown in Table 1.1.

Table 1.1 Vanadium – general properties [2]

Atomic number	23
Atomic weight	50,9414
Density[i]	6,1 g cm^{-3}
Crystal structure	Cubic body - centered

[i]Density values are reported at room temperature (293 K), for the others metals too

The radiance melting temperature of vanadium (Table 1.2), recommended as secondary reference point for ITS-90, was measured at six wavelengths by a current – pulse transient technique at NIST (National Institute of Standards and Technology, Gaithersbourg, USA) (Appendix A).

Table 1.2. Vanadium – radiance temperature of melting [6]

Wavelength / μm	T / K	Purity (mol%)
0,525	2030 ± 7	99,7 +
0,622	1998 ± 7	99,7 +
0,652	1988 ± 7	99,7 +
0,714	1968 ± 7	99,7 +
0,809	1935 ± 7	99,7 +
0,906	1900 ± 7	99,7 +

1.1.2 Niobium

Niobium is a shiny, grey, soft, and ductile metal, and takes on a bluish cast when exposed to air at room temperature for a long time. It is used mostly in alloys, typically in special steel such as that used in gas pipelines, and in various superconducting materials.

Furthermore, Nb alloys are the most promising for the use in NPP (Nuclear Power Plant) due to beneficial combination of heat resistance, and corrosion properties, nuclear characteristics and processing properties. They can be used for manufacturing fuel element claddings, tubes, pump components and other elements of NPP circuits with liquid metal (Na, K, NaK alloys at 1000–1100 °C) as well as

for super heaters of water cooled NPP. Alloys of zirconium with Nb (1 %, 2,5 %) are used in Russian nuclear technology (fuel element cladding and assembly elements respectively) for high corrosion – resistance and under irradiation environment [7].

Niobium, tantalum, molybdenum, and tungsten alloys have been proposed as potential candidates for high performance materials in fusion reactors for their high operating temperature [3].

Other applications of niobium include its use in welding, electronics, optics, numismatics and jewelry.

Some general properties are shown in Table 1.3.

Table 1.3. Niobium – general properties [2]

Atomic number	41
Atomic weight	92,9064
Density	8,57 g cm^{-3}
Crystal structure	Cubic body - centered

Also the radiance melting temperature of niobium, Table 1.4, of the international reference was measured at six wavelengths by a current – pulse transient technique at NIST (Appendix A).

Table 1.4. Niobium – radiance temperature of melting [8]

Wavelength / μm	T / K	Purity (mol%)
0,522	2497 ± 6	99,9 +
0,617	2445 ± 6	99,9 +
0,653	2422 ± 5	99,9 +
0,708	2393 ± 6	99,9 +
0,809	2337 ± 6	99,9 +
0,906	2282 ± 6	99,9 +

1.1.3 Molybdenum

This metal is silvery white, very hard, but softer and more ductile than tungsten. It has a high elastic modulus. The ability of molybdenum to withstand extreme temperatures without significantly expanding or softening makes it useful in applications that involve intense heat, including the manufacture of armour, aircraft parts, electrical contacts, industrial motors, and filaments. It is also used in steel

alloys for its high corrosion resistance and weld ability, for instance in nuclear fuel element cladding [7]. Some general properties are shown in Table 1.5.

Table 1.5. Molybdenum – general properties [2]

Atomic number	42
Atomic weight	95,94
Density	10,28 g cm^{-3}
Crystal structure	Cubic body - centered

The radiance melting temperature of molybdenum, Table 1.6, was measured at six wavelengths, by a current – pulse transient technique (Appendix A).

Table 1.6. Molybdenum – radiance temperature of melting [1]

Wavelength / μm	T / K	Purity (mol%)
0,521	2612 ± 6	99,9 +
0,617	2555 ± 6	99,9 +
0,653	2530 ± 5	99,9 +
0,708	2498 ± 6	99,9 +
0,808	2437 ± 6	99,9 +
0,906	2377 ± 6	99,9 +

1.1.4 Tantalum

Tantalum is dark (blue-gray), dense, ductile, very hard and it is almost completely immune to chemical attack at temperatures below 150°C.

Tantalum exists in two crystalline phases, alpha and beta, and the beta phase is metastable at ambient conditions. Bulk tantalum is almost entirely alpha phase, and the beta phase usually exists as thin films obtained by magnetron sputtering, chemical vapour deposition or electrochemical deposition from an eutectic molten salt solution [9]. The beta phase was never present in any of the specimens used in this work.

Tantalum is also used to produce a variety of alloys with high strength and melting point, in addition to a good ductility. Alloyed with other metals, it is also used in making carbide tools for metalworking equipment and in the production of super alloys for jet engine components, chemical process equipment, and missile parts [10, 11]. Because of its ductility, tantalum can be drawn into fine wires or filaments, which are used for evaporating metals such as aluminium. The high melting point

and oxidation resistance lead to the use of the metal in the production of vacuum furnace parts. Some general properties are shown hereafter in Table 1.7.

Table 1.7. Tantalum – general properties [2]

Atomic number	73
Atomic weight	180,9479
Density	16,69 g cm^{-3}
Crystal structure (bulk - α Ta)	Cubic body - centered

The radiance melting temperature of tantalum (Table 1.8) used as secondary reference point for ITS-90 was measured at seven wavelengths by a current – pulse transient technique at NIST (Appendix A).

Table 1.8. Tantalum – radiance temperature of melting [1]

Wavelength / μm	T / K	Purity (mol%)
0,520	2943 ± 8	99,99
0,616	2876 ± 8	99,99
0,653	2847 ± 6	99,99
0,708	2812 ± 8	99,99
0,808	2742 ± 8	99,99
0,906	2675 ± 8	99,99
0,995	2619 ± 8	99,99

1.1.5 Tungsten

Pure tungsten is a steel-gray to tin-white metal. Very pure tungsten can be cut with a hacksaw, forged, spun, drawn, and extruded. The impure metal is brittle and can be worked only with difficulty. Tungsten has the highest melting point of all metals, and at temperatures over 1920 K has the highest tensile strength. It displays an excellent corrosion resistance and the lowest coefficient of thermal expansion of any pure metal.

Tungsten and its alloys are used extensively as filaments for electric lamps, electron and television tubes, and for metal evaporation work; for electrical contact points for automobile distributors; X-ray targets; windings and heating elements for electrical furnaces; and for numerous spacecraft and high-temperature applications. Tungsten carbide is of great importance to the metal-working, mining, and petroleum industries. Some general properties are shown hereafter in Table 1.9.

Table 1.9. Tungsten – general properties [2]

Atomic number	74
Atomic weight	183,5
Density	19,25 g cm^{-3}
Crystal structure	Cubic body - centered

The radiance melting temperature of tungsten (Table 1.10) used as a ITS-90 secondary reference point was measured at six wavelengths by a current – pulse transient technique at NIST (Appendix A).

Table 1.10. Tungsten – radiance temperature of melting [12]

Wavelength / μm	T / K	Purity (mol%)
0,519	3319 ± 8	99,95
0,615	3236 ± 8	99,95
0,652	3207 ± 7	99,95
0,707	3157 ± 8	99,95
0,808	3078 ± 8	99,95
0,906	2995 ± 8	99,95

1.2 Oxides

All the pure oxides investigated in the present study (with the exception of UO_2) can be identified as "white oxides", namely they poorly absorb visible light in their pure stoichiometry form. A brief description of their main features is given in this section. Since one of the primary goals of the current work is the study of the high temperature behavior of these oxides, also their phase diagrams are presented and shortly discussed.

1.2.1 Calcium oxide

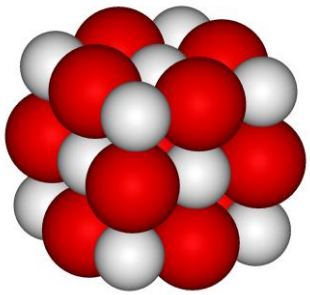

Fig. 1.2. Calcium oxide crystal.

CaO is a common alkaline-earth oxide with a NaCl crystal structure (Fig. 1.2). Known for centuries as a geological material and a disinfectant, calcium oxide is of technological interest because it can withstand temperatures above 1800 K without dissociating or melting, hence it can be considered as a refractory material. It can also be used as a source of heat when it is put in contact with water: an exothermal reaction occurs with a production of calcium hydroxide. Recent studies on Inert Matrix Fuel (IMF) [13] [14] suggest calcia as a stabilising element for this innovative anti-proliferation nuclear fuel.

Optical properties

CaO exhibits a particular behaviour when it is heated beyond 2000 K. Then it emits a dazzling bright white light called limelight or Drummond light [15]. This behaviour has been known since the 1820´s, when Sir Goldsworthy Gurney (not Thomas Drummond who is mistakenly credited with the discovery) discovered that certain metal oxides, including calcium oxide, emit shorter wavelength light when heated than would be expected if the emission were due to incandescence alone. Thermal emission of calcium oxide was used in high-power light sources, film projection and illuminating devices without a physical explanation of the involved phenomena. In 1930´s this phenomenon called cando-luminescence was ascribed to redox mechanisms. At the end of the 1940´s Soviet scientists (see references in [15]) explained the emission of oxides as specific equilibrium thermal emission of a solid whose emittance is strongly dependent both on the wavelength and temperature. Sokolov et al. suggested [16] [17] the existence of cando-luminescence at temperature below 900 K for different materials among which there is calcium oxide. Since in all the Sokolov's experiments the temperature was lower than 1300 K, Kubarev [15] argued that those authors believed calcium oxide did not change in all the temperature range from 1300 K to the melting point, where it would behave as a black body. However, in Kubarev's experiments sharp and evident changes were visible at 2000 K. When this critical temperature value was reached the calcium oxide emittance increased by a factor of about 10 (Fig. 1.3).

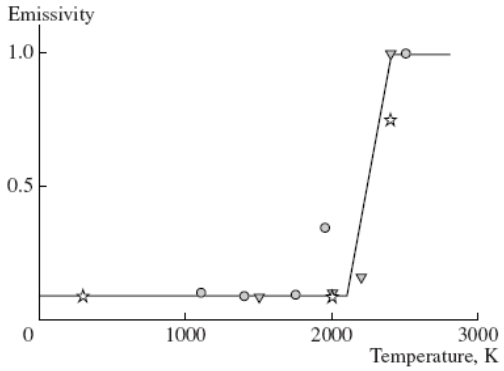

Fig. 1.3. Temperature dependence of the calcium oxide emittance in Kubarev's experiments [15].

Considering an emittance close to one at high temperature, Kubarev obtained a reasonable value of 0,1 at low temperature, which was in agreement with emittance values found in literature [15] for other "white" oxides.

The main result observed by Kubarev was the remarkable change of calcium oxide from a mostly transparent body to an almost ideal black body in a range of temperature from 2000 to 2300 K [17]. Materials with this behaviour can be called "semitransparent". This name is actually related to a "low-absorptance" – "high absorptance" transition. As a matter of fact, the low-emittance (low-absorptance) material is not only "transparent" but also "reflective" at the wavelength of interest.

In the present work, a similar behaviour was observed on calcium oxide. Under different environmental conditions and different types of laser pulse, the presence of plateau at the beginning of the heating process was observed (Fig. 1.4).

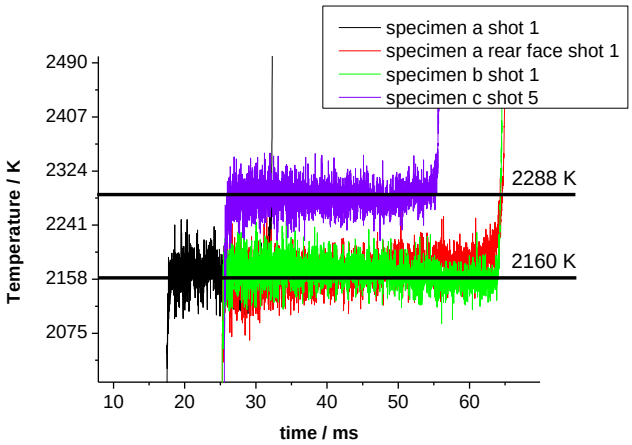

Fig. 1.4. Semi transparency plateau in some shot on different specimens.

The temporal shift between the shot on "specimen a" and the other is artificial. Of more interest is the results obtained on "specimen c". From Fig. 1.4 is remarkable the difference by comparison with the other specimens.

The fact that this "semitransparency plateau" was observed at different temperatures can be due to the different surface morphology in different specimens. However, even more significant can be the fact that before the optical transition some of the heating laser radiation could be reflected by the specimen into the pyrometer detector, resulting in a higher apparent temperature (since the pyrometer was not equipped with any notch filter).

A further confirmation of this effect was obtained using laser pulses with increasing power during the heating of "specimen c" and a constant laser step afterwards (Fig. 1.5 and Fig. 1.6).

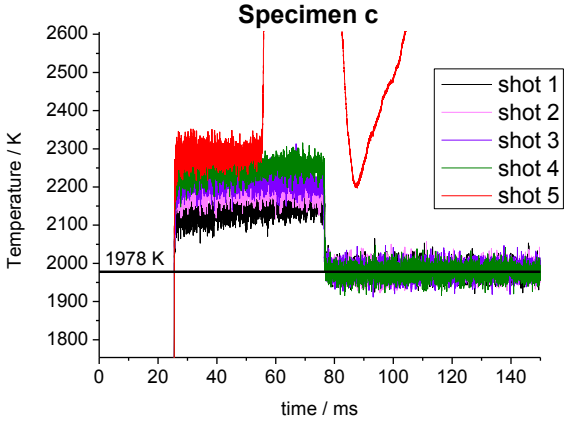

Fig. 1.5. Different shots on CaO "specimen c".

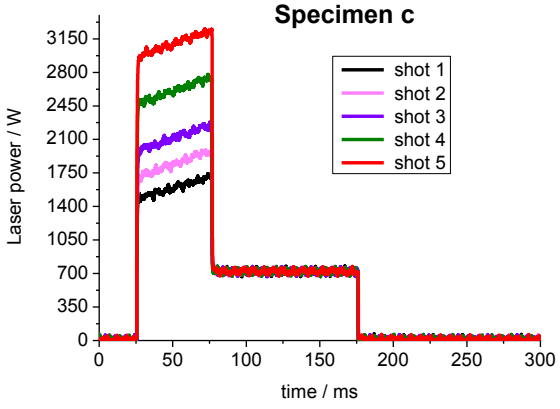

Fig. 1.6. Different laser shapes used for the shots on CaO "specimen c".

As the laser beam delivers its power to the specimen surface, this latter heats up from room temperature to a point where, due to the losses due to the non-opacity of the material (transparency, reflectance) added to the normal conductive, convective and radiative losses, a heat balance is reached, and the observed temperature plateau occurs. Only with an increasingly higher laser power (Fig. 1.6) can these losses be compensated, and the opacity threshold be overcome. During the experiments a bright light was visible at this point. At this stage, as soon as the specimen's absorptance becomes close to unity at the laser wavelength, most of the impinging beam is absorbed, and suddenly a very intense temperature rise occurs. This effect can lead to rapid destruction of the specimen if the experimental parameters are not optimised to avoid that. In particular the laser pulse power vs. time profile had therefore to be optimised by a trial-and-error procedure in the current experiments. It is finally important to notice that the non-opaque / opaque transition is irreversible in these materials. Namely, once the material has been heated to a temperature where it becomes opaque, it remains opaque also after cooling back to room temperature. For this reason, successive laser heating shots on a surface already heated once beyond the transition point were a lot easier to perform. In those cases, a simple rectangular laser power vs. time profile was effective, as the semi-transparency issue was not so incisive any longer.

Phase diagram

Since the only valence state observed for Ca in the condensed oxide is +2, other oxides in addition to calcium oxide should not exist. However, from Fig. 1.7, is possible, in the presence of excess oxygen at room temperature and atmospheric pressure, the coexistence of solid calcium peroxide with solid calcium oxide (between CaO and CaO_2) and solid calcium peroxide and gas (between CaO_2 and O). In the hypostoichiometric region, pure Ca with fcc crystal structure exists in equilibrium with CaO. In the same region, at higher temperature the crystalline structure of pure Ca becomes bcc.

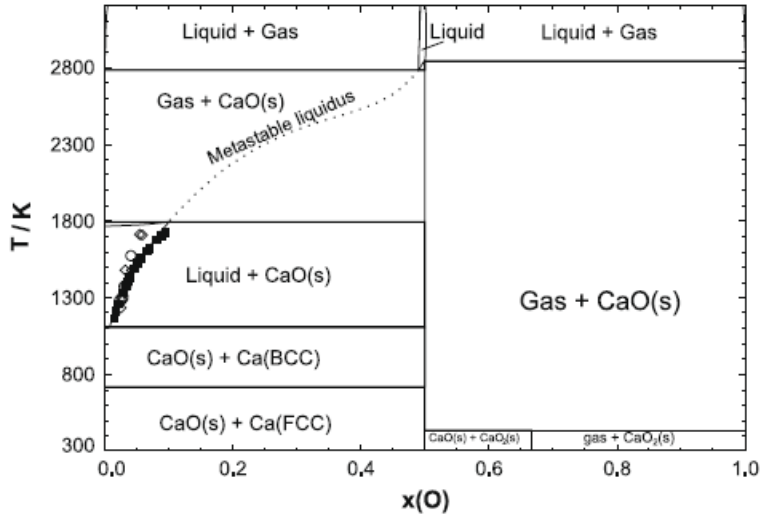

Fig. 1.7. Phase diagram of Ca-O system [18].

Noticeable in Fig. 1.7 is the metastable liquidus line which starts from the eutectic point and arrives to stoichiometric calcium oxide. Lindberg and Chartrand [18] used this line calculated by Zaitsev and Moguntov [19] using chemical analysis (black filled squares in the figure).

Hillert et al. [20] and Huang et al. [21] used a higher CaO melting temperature found in the Thermochemical Tables of NIST-JANAF [22].

In the end, the melting point of calcia is still controversial. Several measurements have been performed in the past giving results with a scattering which exceeds 350 K. The melting points of CaO found in literature are divided in two groups – one around 2880 K and the other close to 3180 K. Schneider [23] has reported four results which vary from 2838 K to 2903 K. These results were obtained using resistance furnaces with both W-strip and graphite tube heating element in a reducing environment. More recent results were reported by Yamada et al. [24] and summarized in Table 1.11.

Table 1.11. Melting temperature of CaO reported by Yamada [24].

Melting temperature / K	References
2863	T. Noguchi et al. (1966) [25]
2890	Z. Panek (1979) [26]
2833	A. V. Shevchenko (1979) [27]
3223	M. Foex (1966) [28]

Panek and Shevchenko's results were obtained using solar furnaces. Foex obtained his result using a solar furnace to melt the centre of a rotating crucible of calcium oxide (Appendix A). Yamada used an arc imaging furnace (Appendix A) with a tailored brightness pyrometer obtaining (3172 ± 3) K as a value for the true melting temperature[1]. Noguchi et al. [25] suggested the second inflection on the cooling curve of their work as the value of the solidification point, but the first inflection on the cooling curve at 3115 K, which the authors considered as a boiling point, is actually very close to the brightness temperature in Yamada's work.

The value given in NIST-JANAF Tables [22] is 3200 K with 50 K as arbitrary uncertainty.

The reasons for the big discrepancy respect to lower temperature results were suggested both by Foex [28] and Yamada [24].

In his work, Foex showed how alkaline–earth oxide in contact with W–supports at high temperature, attack the metallic tungsten yielding tungstates $WO_3 \cdot 3XO$ (X = Ca, Ba, Sr).

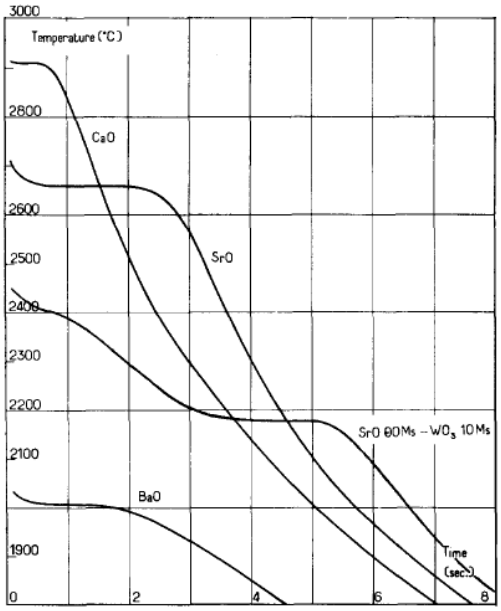

Fig. 1.8. Effect of tungsten contamination on refractory oxide melting temperature [28].

[1] The value for the true temperature was obtained correcting the brightness temperature from the pyrometer with a spectral emittance of 0,98±0,005 [24].

The presence of this mixture causes an important decrease of the melting temperature as shown in Fig. 1.8 in the case of SrO.

Lindberg and Chartrand [18] reported in a recent work, the phase diagram of the Ca-O system (Fig. 1.7) based on Wriedt [29] previous discussion.

They adopted 2845 K as melting point value in accordance with previous work carried out by Pelton and Blander [30] and later Wu et al. [31]. Particularly, in the latter work, the authors considered both the groups of melting points for CaO, but they chose the lower value because in accordance with their work and they did not believe that the specimens used in previous experiments underwent the same amount of contamination. This controversial subject of the melting temperature of CaO and its dependence on the environmental conditions recalls the behaviour observed in some actinide oxides. This topic is addressed in the present work with a laser heating approach.

1.2.2 Cerium dioxide

Cerium dioxide (ceria) is the most stable phase of the Ce-O system at room temperature and under atmospheric conditions. CeO_2 has a fluorite-like crystalline structure, whereby the main defects are oxygen vacancies. These vacancies, which increase the rate of diffusion of the oxygen in the lattice, also increase the catalytic activity making ceria one of the most suitable materials for the implementation of solid-oxide fuel cells (SOFCs) [32]. At room temperature, CeO_2 is transparent for visible light, whereas it absorbs in the ultraviolet range. It can therefore also replace titanium dioxide or zinc dioxide in sunscreens [33] [34]. As far as the present work is concerned, the most interesting feature of CeO_2 is the "semitransparent" behaviour, characteristic similar to that of CaO and ThO_2, and its similarity with the Pu-O system, for which it can be used as a simulant in order to limit a more dangerous work associated with the very high radio-chemical toxicity of plutonium.

Optical properties

At the beginning of a typical thermogram of a melting experiment on cerium dioxide, a plateau is mostly visible, similar to the one reported for CaO. The reason why this happens can once more be ascribed to the semitransparency of this compound.

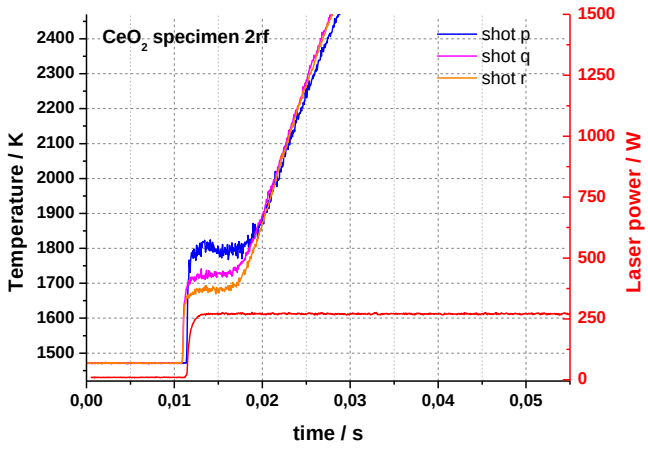

Fig. 1.9. Semitransparency effect on consecutive thermograms on CeO_2.

The phenomena leading to this apparent thermal arrest are similar to those reported for calcium oxide. The sequence of shots in Fig. 1.9 was obtained using the same laser shape in argon. It can be noticed that shot after shot the apparent temperature of the plateau decreases. This is reasonably due to the change in the specimen's surface morphology, resulting in a change in its reflectance and absorptance. In this case, it seems that over consecutive shots, the amount of the energy reflected by the specimen decreases in favour of the absorbed fraction.

Phase diagram

The Ce-O system is characterised at room pressure by a considerable number of phases, especially in the region between a O/Ce ratio of 0,55 and stoichiometric CeO_2, as it can be seen in Fig. 1.10.

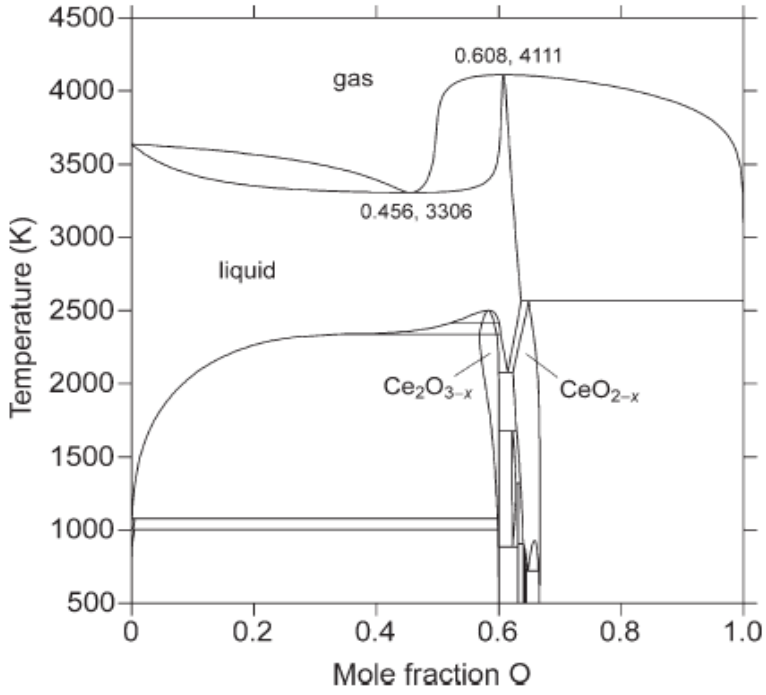

Fig. 1.10. Phase diagram of the Ce-O system under room pressure [35].

Zinkevich et al. [35] performed a thermodynamic modelling of this system. All the phases reported in that region are superstructures of the fluorite-type lattice caused by oxygen deficiencies. If the close-to-stoichiometric CeO_2 region is compared with the PuO_2 one, some likenesses are evident (Fig. 1.11).

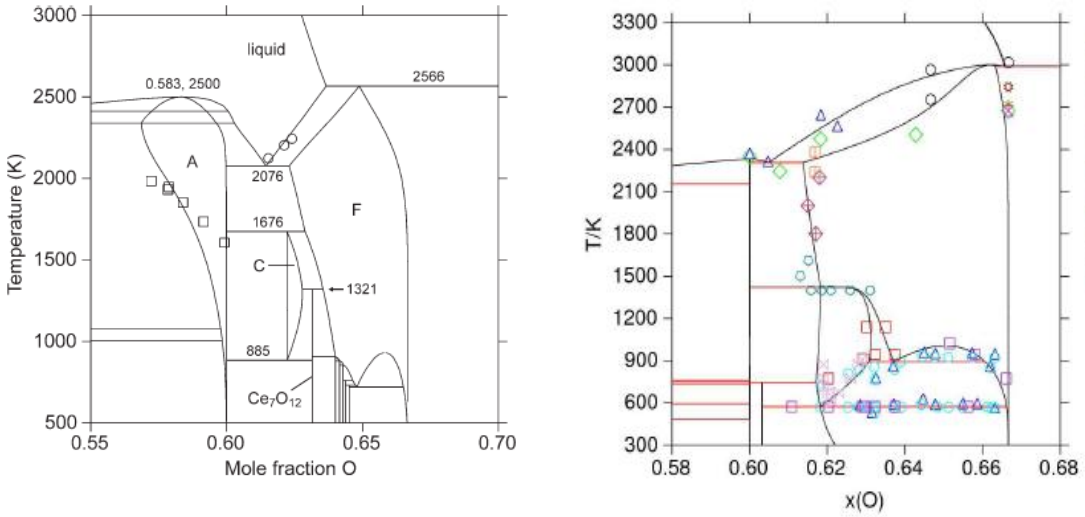

a) b)

Fig. 1.11. a) Magnification of the central part of the diagram in Fig. 1.10 [35]. b) The Pu-O system close to the stoichiometric PuO_2 region [36].

The two systems show a peculiarity of many fluorite-like oxides in the region of interest. They decompose in liquid phase and oxygen gas at a peritectic reaction temperature that for ceria, at 1 atm, is 2566 K. This value is fairly close to the melting temperature of CeO_2 reported in Zinkevich's work. In literature a value of 2670 K [37] for the melting point of ceria under reducing atmosphere was found. Foex [38] obtained a higher value of 2753 K using a solar furnace in air. Due to the common presence of oxygen vacancies and the predisposition to reduction, a congruent melting of ceria can be expected only under a highly oxidising atmosphere. Values of 3073 K and (3000 ± 20) K were attained respectively by Tromble [39] and Brewer [40]. The former performed the experiments under 16 atm of pressure whilst the latter used a pure O_2 atmosphere. The comparison between the Ce-O and the Pu-O systems will not be treated any further in this thesis. However, it is interesting to note some of the similarities here, to highlight once more the interest of a study on cerium dioxide to yield data that can help a better understanding of the behaviour of plutonium dioxide, too.

1.2.3 Thorium dioxide and uranium dioxide

Thorium dioxide (ThO_2) and uranium dioxide (UO_2) crystallise in a fluorite-type structure (Fig. 1.12), as most other actinides dioxides do.

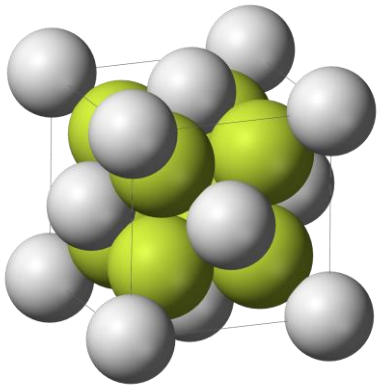

Fig. 1.12. The ThO_2 crystal fluorite-like unit cell.

Because of the radioactivity of thorium and uranium, these compounds must be handled carefully especially when in the powder form.

ThO_2 is known to be a semitransparent material [48], although in a less spectacular way than the already discussed CaO and CeO_2. Therefore, the laser heating parameter optimisation carried out for CaO and CeO_2 was extremely useful to continue the current investigation on thorium dioxide.

In the past, thoria was used in the conventional industry in gas mantles of lanterns and added in glasses in order to increase the refractive index [41]. For applications of this kind, it has been gradually replaced by non-radioactive compounds, as yttrium dioxide or cerium dioxide. It is also used as the main component of heat-resistant ceramics, such as crucibles for laboratories, due to its high melting temperature. In fact, ThO_2 has the highest melting temperature among the binary oxides, and only few elements (e.g., tungsten and carbon) and compounds (e.g., tantalum carbide) display a higher melting point. The present study on thoria takes also place in the renewed interest in thorium-based fuel cycle and the need to develop a sustainable production of energy through anti-proliferation fuel [14]. ThO_2 was used as blanket mantel in LMFBR [42] with good results. It was also tested as a U-free matrix fuel in the IFA-652 experiment [13] with the aim of burning Pu-stockpiles without production of new plutonium, showing a good resistance to irradiation as well.

Urania (UO_2) is the most widely used nuclear fuel. For this reason, is one of the most studied compounds ever. A review of UO_2 properties can be found in [43]. In the present work, UO_2 is mainly studied as a reference material for the pseudo-binary system UO_2–ThO_2. In this perspective, its only property of importance for the current analysis is the melting / freezing temperature of stoichiometric UO_2, assessed at (3130 ± 30) K

The Th –O phase diagram

Fig. 1.13 shows the binary Th-O phase diagram [44]. The maximum valence state of thorium is +4, thus compositions with O/Th>2 do not exist in the condensed phase. These phases are: α-Th, which exists below (1643 ± 30) K at atmospheric pressure, β-Th, liquid-Th, ThO_2 and the hypostoichiometric ThO_{2-x} solid solution,

which is only stable in a narrow composition range at temperatures higher than 1700 K approximately.

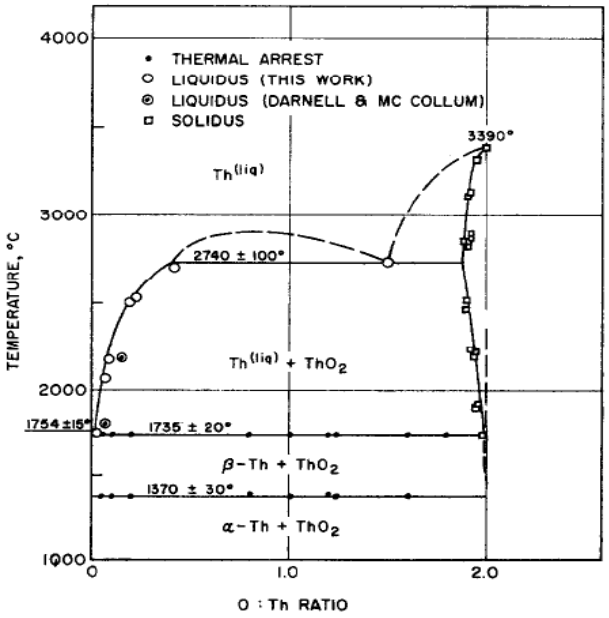

Fig. 1.13. Phase diagram of the Th-O system [44].

A confirmation of the stability of the oxygen-deficient thorium dioxide can be found in [45]. The eutectic occurs at (2008 ± 20) K with a O/Th ratio of 0,016±0,005. A monotectic at (3013 ± 100) K can be detected between $ThO_{0,4}$ to $ThO_{1,5}$. A more recent study led by Kinoshita et al. [46], reports a thermodynamic optimisation of the phase diagram of the Th-O system (Fig. 1.14a).

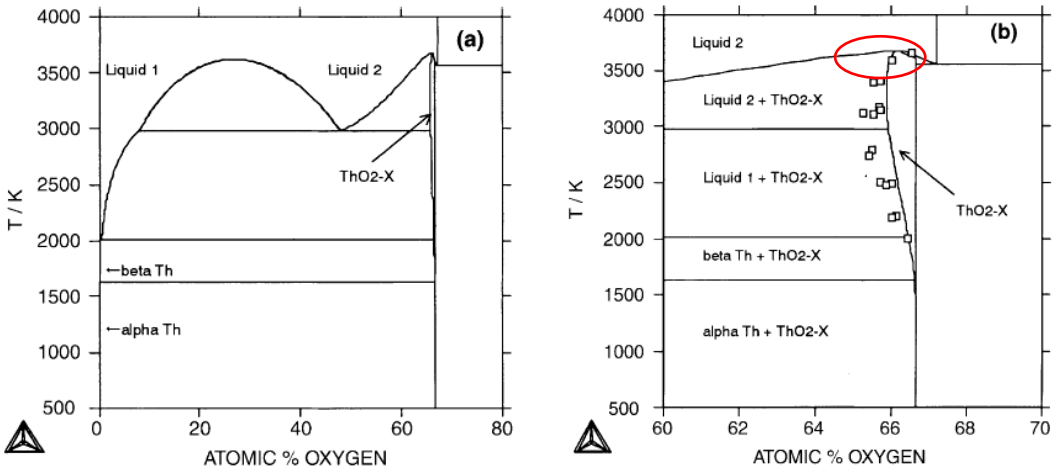

Fig. 1.14. Phase diagram of Th-O system [46]. a) Wider composition range. b) High oxygen content region.

The region in the vicinity of stoichiometric ThO_2 (Fig.1.14b), reproduces experimental results (white squares in Fig. 1.14b) from Benz's work considerably well. In the close-to-stoichiometric region of Kinoshita's model can also be recognised a maximum congruent melting point (region in the red circle in Fig. 1.14b).

A value of (3573 ± 100) K for the melting temperature of stoichiometric thorium dioxide was reported in early literature [47]. This value was also reported in Benz's work. More recently, a higher melting point was observed by Ronchi and Hiernaut [48] by laser heating: (3651 ± 17) K. A melting point of 3663 K was assessed in the Gmelin Handbook of Inorganic Chemistry [49].

1.2.4 The UO_2-ThO_2 system

The use of thorium as fertile material in nuclear fuel has been of interest especially thanks to the abundance of thorium resources on our planet and also for some important neutronic advantages. In fact, thorium-based fuel cycle (Fig. 1.15), when used in LWRs, allows a reduced neutron spectrum hardening, resulting in lower void and temperature coefficients [50]. Lombardi et al. [14] published a scheme of the principal reactions induced by thermal neutrons starting from ^{232}Th and ^{238}U. It is clear, from Fig.1.15, how the thorium-uranium fuel cycle rules out the production of any plutonium isotope in the spent fuel and from this viewpoint leads to a more sustainable process of energy production. In addition, thorium dioxide is a highly stable oxide, not subjected to oxidation beyond the stoichiometric composition, and its thermal conductivity is 10% higher than that of uranium dioxide. These properties together with the very high melting temperature of thoria, constitute obvious advantages in view of the in-pile fuel performance of TOX fuel and also a rather stable form for the waste. Furthermore, the low Pu content and the reduced radiotoxicity [51] in the spent fuel have led to a recent renaissance of interest in this fuel. Some of these features were deeply studied between the 1950s and 1970s especially in LWRs [41]. The feasibility of a possible employment of TOX as fuel for the Indian AHWR is reported in an IAEA report [52].

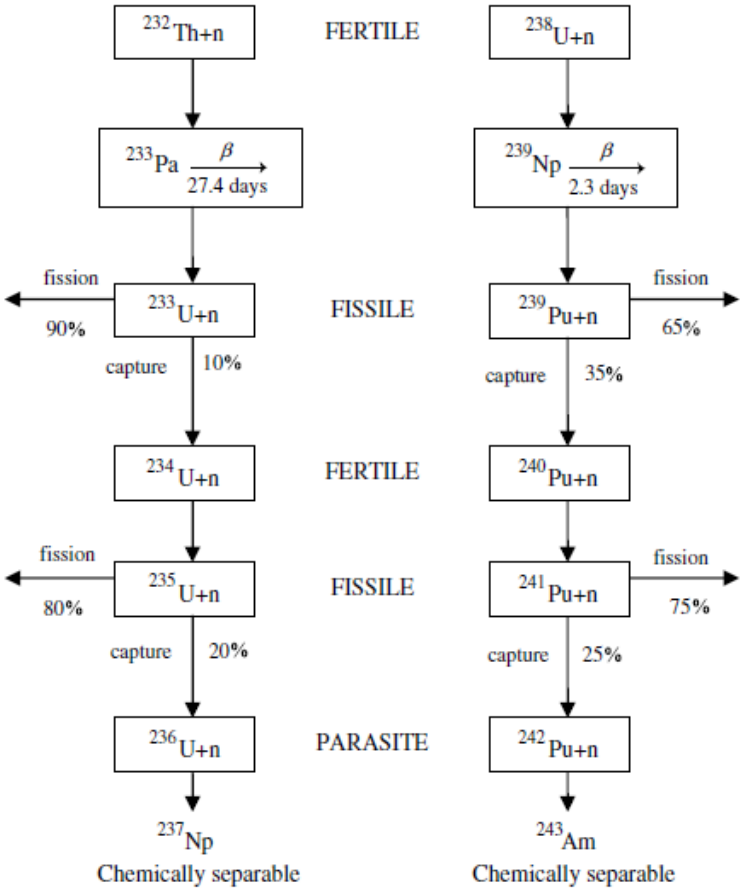

Fig. 1.15. Differences in thorium and uranium fertilisation [14].

Phase diagram

The UO_2-ThO_2 system has an isomorphous binary phase diagram. In this kind of system, only one solid phase form exists at the equilibrium, hence the two end members exhibit a complete solid solubility. Lambertson et al. [47] performed a phase equilibrium study on this system, obtaining the diagram shown in Fig. 1.16.

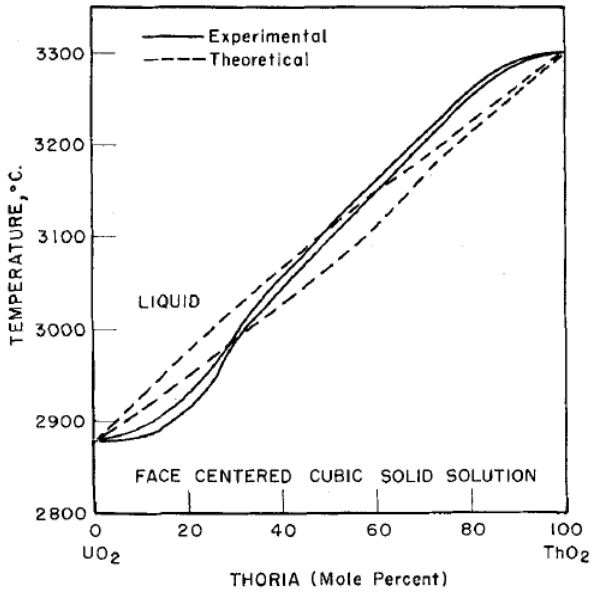

Fig. 1.16. Comparison of theoretical and experimental results led by Lambertson et al. [47].

The theoretical curve was derived by imposing that the melting point of thoria was 3573 K. Although the curves present some evident differences, both of them show a total miscibility of the components in all the proportions. Latta, Duderstadt and Fryxell [53] focused their attention on the region below 20 mol% ThO_2 (Fig. 1.17). They confirmed Cohen and Berman's result [54], in which a shallow minimum in the melting point at 2 mol% ThO_2 was observed.

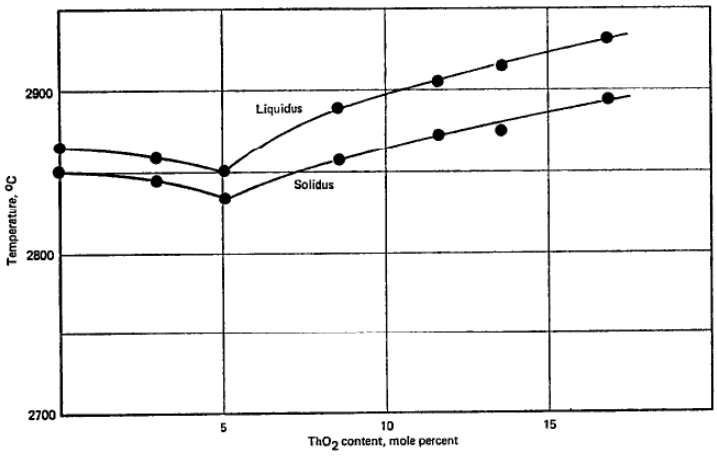

Fig. 1.17. Solidus-liquidus temperature in the low percentage ThO_2 region [53]. The gap between solidus and liquidus at the minimum melting point is due to the data uncertainty.

Cohen and Berman observed an anomaly in the lattice parameter, and a deviation in the Vegard's law [55] above 90 mol% UO_2. In this region three phases, the cubic,

U_3O_8 and U_4O_9 are in equilibrium. They argued these anomalies are related to the formation of another ordered phase in the vicinity of U_4O_9. Latta, Duderstadt and Fryxell observed this deviation at about 5 mol % ThO_2 as shown in Fig. 1.17. All these observations suggest that the pseudo-binary UO_2–ThO_2 phase diagram can be fully understood only in the light of the ternary U–Th–O system. As a first step in this direction, one of the main goals of the present work is a reassessment of the UO_2–ThO_2 pseudo-binary plane, whereby the melting behaviour of these mixed oxides are studied by laser heating and fast pyrometry under controlled atmosphere.

1.3 References

[1] R.E. Bedford, G. Bonnier, H. Maas and F.Pavese, Metrologia, 33 (1996), 133.

[2] Los Alamos National Laboratories, chemistry division, http://periodic.lanl.gov.

[3] M. Ubeyli and S. Yalcin, J. Fusion Energ., 25 (2006), 3.

[4] ATI Wah Chang technical data sheet.

[5] H. Matsui, K. Fukumoto, D. L. Smith, Hee M. Chung, W. van Witzenburg and S. N. Votinov, J. Nuc. Mater., 233-237 (1996), 92.

[6] J.L. McClure and A. Cezairliyan, Int. J. Thermophys., 18 (1997), 1.

[7] IAEA publication, "Thermophysical proprieties of materials for nuclear engineering" (2008).

[8] A. Cezairliyan and A. P. Miiller, Int. J. Thermophys., 13 (1992), 39.

[9] S. L. Lee, M. Doxbeck, J. Mueller, M. Cipollo and P. Cote , Surf. Coat. Tech. , 177 – 178 (2004), 44.

[10] S. M. Cardonne, P. Kumar, C. A. Michaluk and H. D. Schwartz, Int. J. Refract. Met. H., 13 (1995), 187.

[11] R. W. Buckman, Jr, "New applications of tantalum and tantalum alloys", JOM, 2000 March.

[12] P. Miiller and A. Cezairliyan, Int. J. Thermophys., 14 (1993), 511.

[13] Ch. Hellwig, M. Streit, P. Blair, T. Tverberg, F.C. Klaasen, R.P.C. Schram, F. Vettraino and T. Yamashita, J. Nucl. Mater., 352 (2006), 291.

[14] C. Lombardi, L. Luzzi, E. Padovani and F. Vettraino, Prog. In Nucl. Energy, 50 (2008), 944.

[15] V. V. Kubarev, Optics and Spectroscopy, 106 [2] (2009), 242.

[16] V. A. Sokolov, Usp. Fiz. Nauk., 47 [4] (1952), 538.

[17] V. A. Sokolov, I. S. Grozina, and A. N. Gorban´, Opt. Spektrosk., 3 (1957), 92.

[18] D. Lindberg and P. Chartrand, J. Chem. Therm., 41 (2009), 1111.

[19] I. Zaitsev and B. M. Moguntov, Metall. Mater. Trans. B, 26B (2001), 305.

[20] M. Hillert, B. Sundman and X. Wang, Metal. Trans. B, 21B (1990), 303.

[21] W. Huang, M. Hillert and X. Wang, Metal. and Mater. Trans. A, 26A (1996), 2293.

[22] NIST-JANAF, Thermochemical Tables, Fourth Edition, Part I, Journal of Physical and Chemical Reference Data.

[23] S. J. Schneider, Compilation of the Melting Points of the Metal Oxides, NBS Monograph, 68 (1963).

[24] T. Yamada, M. Yoshimura, and S. Somiya, J. Am. Ceram. Soc., 69 [10] (1986), C-243.

[25] T. Noguchi, M. Mizuno, and W. M. Conn, Solar Energy, 11 [3,4] (1967), 145.

[26] Z. Panek, Silikary (Prague), 23 [2] (1979), 97.

[27] V. Shevchenko, L. M. Lopato, A. I. Stegny, G. I. Gerasimyuk, V. S. Dvernyakov, and V. V. Pasichnys, Dokl. Akad. Nauk. SSSR Ser A., 8 (1979), 682.

[28] M. Foex, Solar Energy, 9 [1] (1965), 61.

[29] H.A. Wriedt, Bull. Alloy Phase Diagr., 6 (1985), 337.

[30] A.D. Pelton and M. Blander, Metall. Mater. Trans. B, 17B (1986), 805.

[31] P. Wu, G. Eriksson and A.D. Pelton, J. Am. Ceram. Soc., 76 (1993), 2065.

[32] H. Yokokawa, N. Sakai, T. Horita, K. Yamaji and Yu-ping Xiong, Fuel Chem. Division Preprints, 47[2] (2002), 501.

[33] S. Yabe, M. Yamashita, S. Momose, K. Tahira, S. Yoshida, R. Li, S. Yin and T. Sato, Int. J. Inorg. Mater., 3[7] (2001), 1003.

[34] W. Wu, S. Li, S. Liao, F. Xiang and X. Wu, Rar. Met., 29[2] (2010), 149.

[35] M. Zinkevich, D. Djurovic and F. Aldinger, Sol. Stat. Ion., 177 (2006), 989.

[36] C. Guéneau, N. Dupin, B. Sundman, C. Martial, J.-C. Dumas, S. Gossè, S. Chatain, F. De Bruycker, D. Manara and R. J. M. Konings, J. Nucl. Mater., 419 [1-3] (2011), 145.

[37] O. A. Mordovin, N. I. Timofeeva and L. N. Drozdova, Inorg. Mater. (URSS), 3 (1967), 159.

[38] M. Foex, Rev. Hautes Temp. Refract., 3 (1966), 309.

[39] F. Tromble, Bull. Soc. Fr. Ceram., 3 (1969), 18.

[40] L. Brewer, Chem. Rev., 52 (1953), 1.

[41] "Transport of Consumer Goods containing Small Quantities of Radioactive Materials", Final Report, EC Contract Number: 4.1020/D/99-006 (DG TREN), May 2001.

[42] "Thorium fuel cycle – Potential benefits and challenges", IAEA-TECDOC-1450, 2005.

[43] J.K. Fink, J. Nucl. Mater., 279 (2000), 1.

[44] R. Benz, J. Nucl. Mater., 29 (1969), 43.

[45] R. J. Ackermann, E. G. Rauh, R. J. Thorn and M. C. Cannon, J. Phys. Chem., 67 (1963), 762.

[46] H. Kinoshita, D. Setoyama, Y. Saito, M. Hirota, K. Kurosaki, M. Uno and S. Yamanaka, J. Chem. Therm., 35 (2003), 719.

[47] W. A. Lambertson, M. H. Mueller and F. H. Gunzel, Jr., J. Am. Ceram. Soc., 36 (1953), 397.

[48] C. Ronchi and J. P. Hiernaut, J. Alloy Compd., 240 (1996), 179.

[49] Gmelin Handbuch der Anorganischen Chemie, Springer-Verlag, 1991.

[50] C. Lombardi, L. Luzzi, E. Padovani and F. Vettraino, Progr. Nucl. Ener., 38 (2001), 395.

[51] C. Fiorina, F. Franceschini, J. Krepel and K. Mikityuk, Proceedings of GLOBAL 2011, Paper No. 500552, Makuhari, Japan, 2011.

[52] IAEA, Status report 67 – Advanced Heavy Water Reactor (AHWR), 2010.

[53] R. E. Latta, E. C. Duderstadt and R. E. Fryxell, J. Nucl. Mater., 35 (1970), 347.

[54] I. Cohen and R. M. Berman, J. Nucl. Mater., 18 [2] (1966), 77.

[55] R. Denton and N. W. Ashcroft, Phys. Rev. A, 43[6] (1991), 3161.

Chapter 2

Experimental methods and material characterisation

2.1 Laser heating

In conventional techniques for measuring thermophysical properties at high temperatures, a specimen, normally contained in a crucible, is heated in an oven. Using these devices, usually, experimental data are influenced by the high chemical reactivity of the materials, composition instability, vaporization, loss of mechanical strength, etc. These difficulties increase with the temperature (faster kinetics at high temperature) and with the prolonged time under extreme conditions. A summary of the more common techniques for melting temperature measurements is given in Appendix A.

In order to avoid or at least minimize these effects, possible ways are to limit the exposure time at high temperature, to limit the heated area of the specimen, to reduce the contact area between the materials under investigation and the containment.

Following these criteria, a new technique has been implemented in the recent years at ITU [1] with the specific goal of investigating nuclear materials at very high temperatures and particularly around their solid-liquid transition.

This device is composed by a Nd:YAG laser (1064 nm wavelength) for heating up the specimen in sub-second (ms) time duration and a radiation thermometer (pyrometry) is applied. Infact, it is the most suitable technique to record the surface temperature of the heated specimen because of the high temperatures and high heating/cooling rates involved, often exceeding 3000 K and 100000 K/s, respectively.

The specimen is mounted inside a graphite or tungsten holder with only three or four screws, in turn put in an autoclave with controlled atmosphere.

Laser heating has already been employed for the investigation of melting point of nuclear fuels (UO_2, PuO_2 / MOX) [2,3], actinide oxide (NpO_2) [4], uranium carbides (UC, UC_2) [5], zirconium carbides (Zr-C) [6].

In Fig. 2.1 it is shown an overview of the general set up.

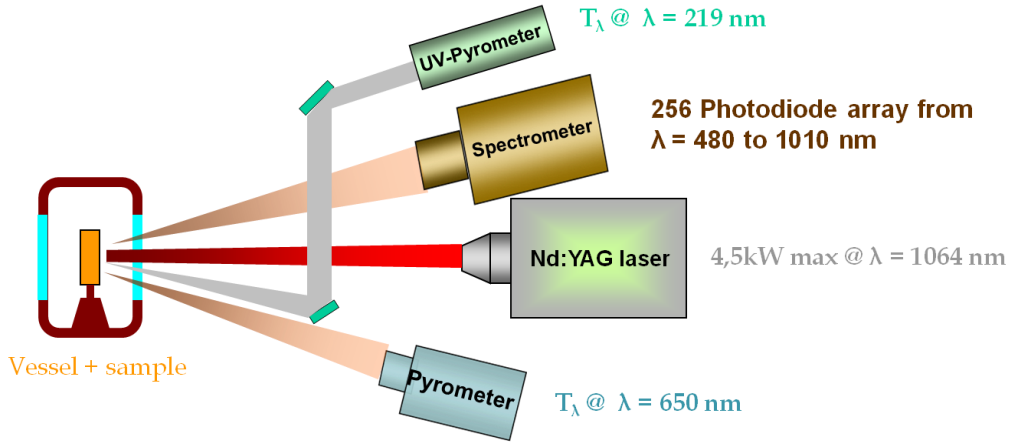

Fig. 2.1 Laser heating technique, general set-up.

2.1.1 Specimen holder

The specimen is supported with three or four screws, as mentioned before, or fixed in an alumina ring and tightened with the screws (Fig. 2.2a).

For high pressure measurements (up to 1500 bar), the holder is different, as it can be seen in Fig. 2.2b. The specimen is placed inside a cylindrical crucible of graphite, in turn mounted on a stainless steel support, the top of the crucible is closed with a sapphire window to avoid too much vaporization in the vessel and convection effects in the dense gas.

The holder for the metals used for the validation of the method is essentially different (see Chapter 3).

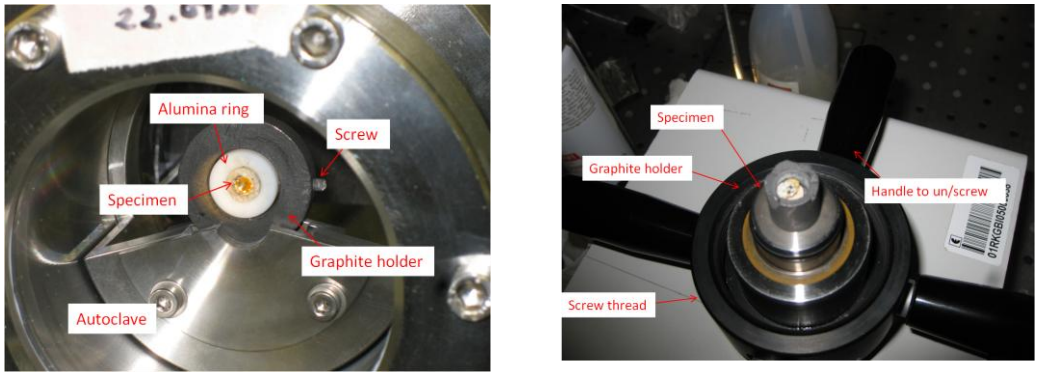

a) b)

Fig. 2.2. a) Low pressure holder and autoclave. b) High pressure holder.

In this research, only optics producing a 3 mm-diameter laser spot on the specimen were used, that implies the heating laser spot was always smaller than the specimen diameter. Therefore, when the central surface part was melted, the surrounding was still solid and considerably cooler. This solid part itself can be considered a kind of "self – crucible" made by the same material. Containment, by any material other than the specimen itself, is thus minimized or totally avoided.

2.1.2 Autoclaves – pressure devices

The "low" pressure device (up to 2,5 bar) is shown in Fig. 2.2a. The specimen and the holder are put inside a cylindrical vessel, which has two windows, one made of sapphire and the other of fused silica. The autoclave is connected with a vacuum / gas system. A few cycles of vacuum and refilling with Ar are made, in order to roughly purge the system and heat the specimen under a inert atmosphere. The vessel is then filled with 2 bar of Ar and/or air, to limit out-of-equilibrium violent evaporation during melting [1] and to perform experiments under reducing or oxidizing conditions.

For the high pressure device, Fig. 2.2.b shows part of the vessel that is then screwed on a cylindrical stainless steel container (Fig. 2.3a).

This cylindrical container can hold an internal pressure up to 4000 bar but in this research only a maximum of 1500 bar was needed. More specifically, the vessel contains a pressurized chamber of 1 cm^3 (Fig. 2.4), where the specimen is located,

connected with the high pressure system. On top of the chamber is fixed a 1-cm thick sapphire window and above it is mounted the optical system for the laser and pyrometer which consists of two mirrors. The first mirror is a dichroic one; it reflects infrared laser light but transmits visible light. The thermal light that is emitted by the specimen at the operating wavelength of the pyrometer passes through this first dichroic mirror and is reflected to the pyrometer (Fig. 2.3b) by the second mirror, a polished Al surface reflecting visible light. Both mirrors are flat and arranged at ca. 45° relative to the axis of the cylindrical high-pressure vessel.

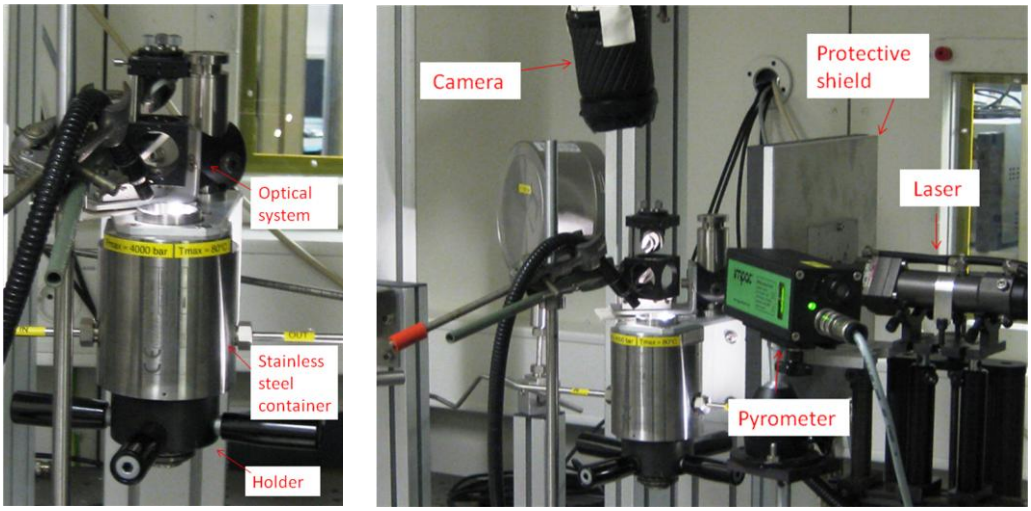

a) b)

Fig. 2.3. High pressure configuration: a) Stainless steel container and optical system. b) an overview of the configuration (laser, pyrometer and container).

The high-pressure cell could be filled either with pure inert gas or with a mixture of inert gas and oxygen (point 2 in Fig. 2.5) and it is connected as it can be seen in Fig. 2.4. High pressure is obtained with an electro-membrane compressor (point 3) reaching pressures up to 3000 bar. If a higher pressure is needed, a piston – pressure amplifier is enabled (point 4), filled with argon. The entire system is controlled electronically. Helium was mainly used as buffer gas, as it has the best optical characteristics among the inert gases at high pressure, especially in the presence of a strong heat source. In fact helium combines relatively high thermal conductivity and almost perfect optical transparency [7].

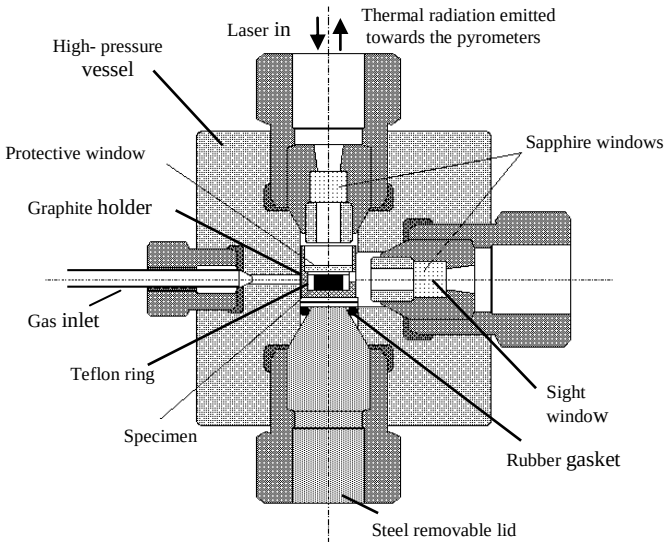

Fig. 2.4. High pressure cell [7].

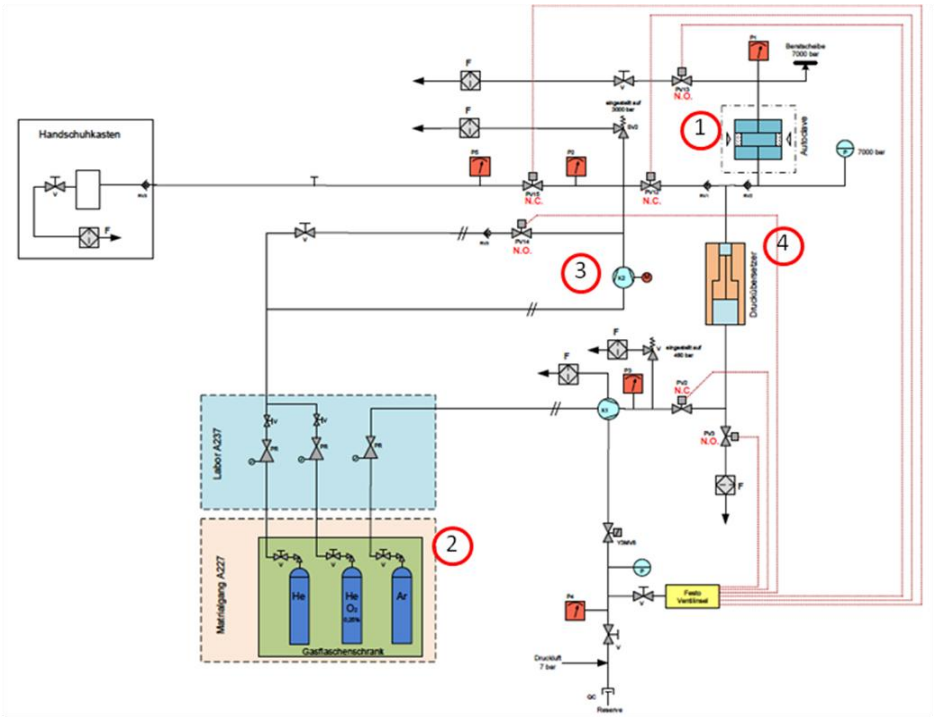

Fig. 2.5. High pressure system: 1) autoclave. 2) gas bottles. 3) compressor. 4) actuator.

2.2 Fast two – channel pyrometer

2.2.1 The pyrometer principle of operation

The main technical data are summarized in Table 2.1

Table 2.1. Technical data of the two – channel pyrometer.

Operational temperature range, K		1750-6000
Settling time to 1% of log outputs, μs		10
Number of brightness temperature channel		2
Distance to the target, mm		370-450
Working wavelengths, λ, μm	1st channel	0,650
	2nd channel	0,488
Bandwidth, Δλ, μm	1st channel	0,027
	2nd channel	0,007
Spot size at 400mm working distance, mm		0,5
Power consumption, W		15

A simplified functional block diagram is shown in Fig. 2.6. The objective lens (2) collects thermal radiation from the 0,5 mm diameter spot of the target (1) (at a nominal working distance of 400 mm) and focuses it on the mirror (4) with a pinhole which acts as the field stop of the system. After that, the light passes through the fibre optics splitting system and then, after passing the filter (5) is focused on Si photodiodes. The photodiodes are mounted in a metallic case, which is maintained at a fixed temperature thanks to a high precision miniature thermostat with a microprocessor controller. A folding mirror (8) is used to reflect the specimen's image, which is formed at the pinhole mirror (4), into a telescope (3) in order to align the pyrometer on specimen area of interest.

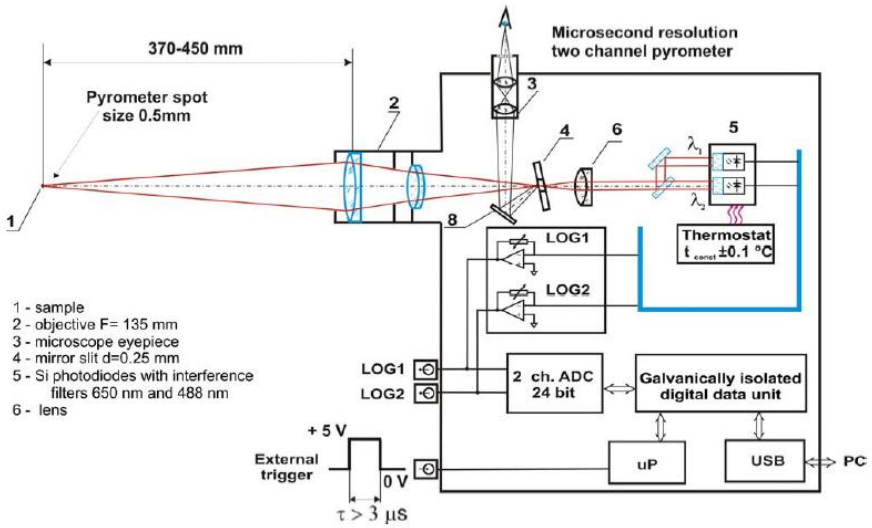

Fig. 2.6. Simplified functional block diagram of the pyrometer.

The currents signals from the photodiodes are converted in voltage signals thank to the logarithmic amplifiers (LOG1, LOG2). Then, a Nicolet Pro® 44C digital oscilloscope is fed with these voltage output signals. The output signal from the 650 nm – channel may be expressed, in the range of linear response of the pyrometer, as

$$V_{out}(T) = k_{\log} \log\left[\frac{i_{ref}}{i_p(T)}\right] \tag{2.1}$$

where $k_{\log}$ = 0,375 V is the scaling constant of the logarithmic amplifier and i_{ref} is an internal reference current of the amplifier integrated circuit.

The output is sent to a PC and recorded using LabView® software.

2.2.2 The pyrometer calibration

The pyrometer's 650 nm - channel was calibrated against two tungsten ribbon lamps. A Polaron 22/G argon filled lamp was used in the temperature range 1800 - 2500 K, whereas a Polaron 22/V lamp was used for the temperature range 1100 - 1800 K. A very accurate calibration was made for both the lamps to obtain a radiance temperature curve at 650 nm vs. input current by the PTB (Physikalisch-Technische Bundesanstalt) in Berlin in 2010.

The pyrometer and the lamps were set up on an optical table. The experimental setup is shown in Fig. 2.7a. The calibration was carried out according to OIML (International Organization of Legal Metrology) recommendation [8]. First of all the lamps were set vertically. Then the centre of the W-filament was aligned with the lens of the pyrometer every time the temperature was set to a new value (see Fig. 2.7b), because of the filament thermal expansion. A sighting pin inside the lamp indicates the centre of the filament (i.e., the hottest part of the ribbon) and the correct position for the calibration. Finally a check on the aplomb between the optical axis of the pyrometer and the ribbon was made.

The black-spot image of the pyrometer field stop is visible from the telescope on the specimen surface (see (3) and (4) in Fig.2.6). It should be as sharp as possible in order to ensure the focusing of the lens.

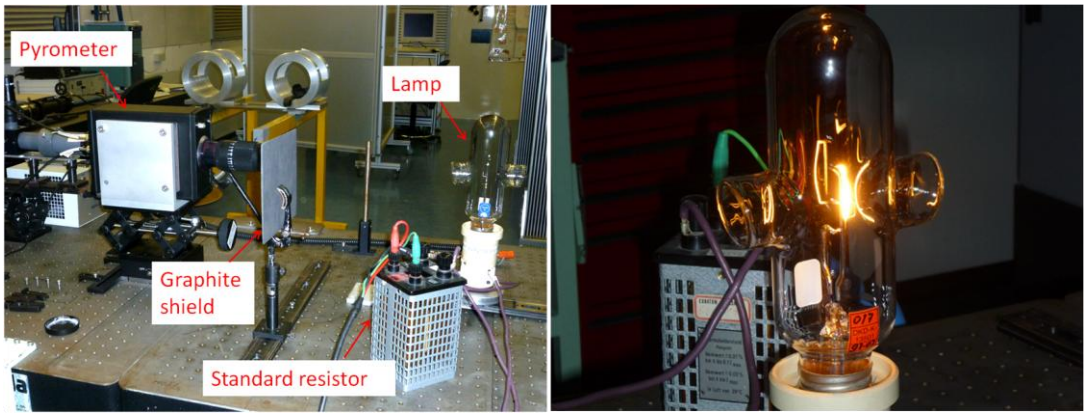

a) b)

Fig. 2.7. Calibration, a) Experimental set up. b) hot W stripped lamp.

In order to produce a stable input current in the lamps, an electric circuit was used. It was composed of:

- DC source
- Voltmeter
- Standard resistor R = 1 mΩ, in series with lamp

Through the measurement of the voltage drop across the standard resistor it was possible to measure the current flowing in the lamps. From this current it was

possible to obtain the lamps´ radiance temperature through the calibration curves from PTB [9].

When the alignment phase was concluded, the lamp was heated by the source. To ensure proper working of the lamps and measurement reproducibility, the lamps were heated slowly, especially during the first steps. At lower temperature the current was raised with a maximum rate of 5 A/min. After reaching the desired current value, some time was needed to stabilize it. In this way were minimized the uncertainties coming from fluctuation due to unstable current and no constant temperature reaching. Steps of current rising are summarised in Table 2.2.

Table 2.2 Current steps characteristics.

	Current / A	T_λ / K	Stabil. time / min
1	16,629	1800	45
2	19,774	2000	20
3	23,257	2200	20
4	25,113	2300	20
5	27,042	2400	20
6	29,040	2500	20

Two measurements were taken at every current step. One was an “off”-measurement, that is when the pyrometer cannot see the lamp's light due to a graphite shield interposed between the lamp and the pyrometer. The other was an “on”-measurement that is without the graphite shield. In this way it is possible to determine whether oscilloscope response (that is pyrometer response) is temperature-independent (due to the “off”-m.), and the relationship between lamp temperature and oscilloscope voltage output signals.

This procedure (i.e., slow raise in current, stabilizing time, re-alignment, on and off measurement) must be adopted after each current step for both the lamps.

A linear relationship can be derived, between the lamp’s radiance temperature and the pyrometer output signal, combining eq.(2.1) with Wien’s expression for blackbody spectral radiance:

$$V_{out}(T) = A + \frac{B}{T_\lambda} \tag{2.2}$$

This relationship can be taken to obtain coefficients *A* and *B* using a linear fit on the data (Fig. 2.8a).

Once constant *B* is known it is possible to obtain the mean effective wavelength (see Appendix B, section B.9.4.1) of the pyrometer using the following relation

$$B = (\log e) k_{\log} \frac{c_2}{\lambda} \tag{2.3}$$

And then

$$\lambda = 0{,}4343\, k_{\log} \frac{c_2}{B} \tag{2.4}$$

Where c_2 = 14388 μm K. The computed mean effective wavelength is 650 nm.

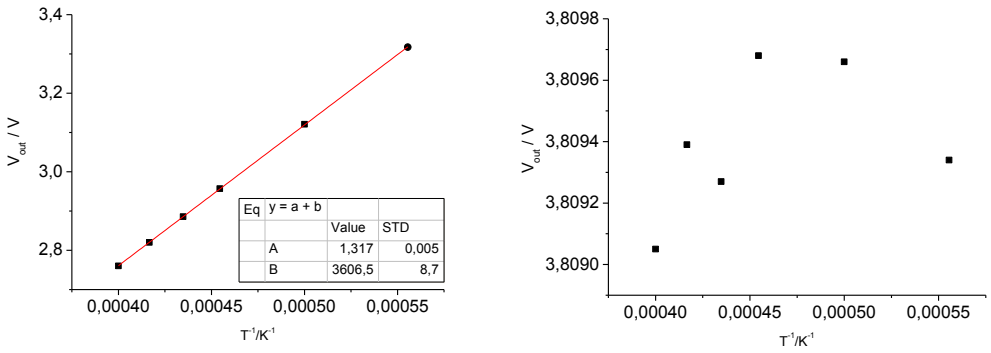

a) b)

Fig. 2.8. 650 nm – channel of the two channel pyrometer, a) Calibration ("on" – measurements). b) "off" – measurements.

It should be noted in Fig. 2.8b the low spread of the off-measurement data on the inverse of the temperature.

2.3 Multi - channel pyrometer

In order to convert radiance temperature at a given wavelength (i.e., the temperature obtained with a pyrometer calibrated with blackbody radiance) to true temperature, knowledge of the normal spectral emittance of the target at the same wavelength is needed. For this purpose in the present work a 256 – channel pyrometer [1] was employed.

2.3.1 Principle of functioning

This multi – channel pyrometer consists of an integrated array of 256 Si photodiodes recording the signal in the spectral range between 488 and 1011 nm. The photodiode array is directly mounted as a card in a PC; the data card memory can hold 256 full spectra. Therefore, after each measurement a data file with 256 spectra is transferred and saved on the PC. What it is recorded is a 256 × 256 array where the i-th row represents the i-th spectra acquired at time i times the integration time. The latter is the time needed to record a full 256 spectra and it is adjustable depending on the quality of the signal.

2.3.2 Calibration of the 649 nm - channel

Following the same procedure described for the 650 nm channel of the two – channel pyrometer, the 649 nm – channel of the spectrometer was calibrated, considering it as a "single – channel pyrometer", against the argon filled reference lamp. Setting a 4 ms integration time, a measurement was performed at each scheduled radiance temperature of the lamp. A *ln(Counts)* vs. T^{1} curve is obtained and used as the calibration of the photodiode (Fig. 2.9). As a matter of fact, since the counts from the detector are linearly dependent on the radiance, their natural logarithm has to be linearly dependent on the inverse of the radiance temperature of the lamp's ribbon, according to Wien's equation:

$$\ln\left(Counts\right) = A\left(\lambda\right) + \frac{B\left(\lambda\right)}{T_{\lambda}} \tag{2.5}$$

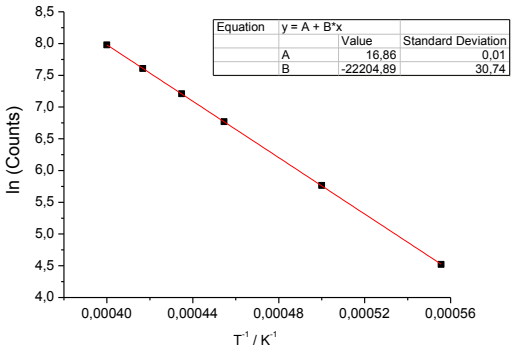

Fig. 2.9. Calibration of the 649 nm – channel of the spectrometer.

2.3.3 Calibration of the whole 256 – channel spectra

Black body

In order to calibrate the whole photodiode array and to obtain the transfer function $K(\lambda)$ of the spectrometer's opto–electronic system, a black body able to reach high temperatures (in this work, up to 2900 K) was used. In Fig. 2.10 the black body is shown.

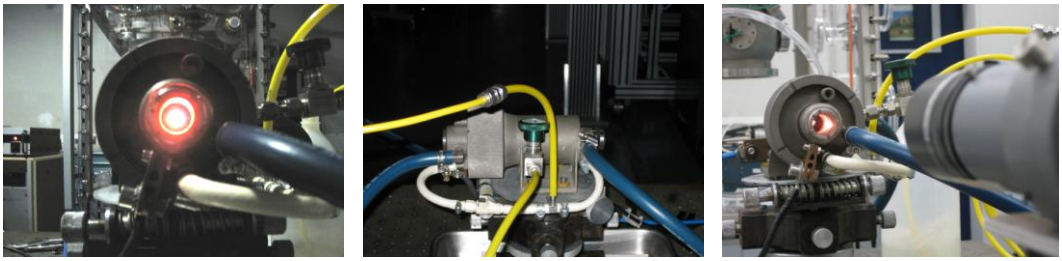

a) b) c)

Fig. 2.10. Black body: a) front view. b) side view. c) front view with the multi-channel pyrometer.

The black body is a graphite tube of 60 mm in length (L) with an internal diameter (D) of 2,85 mm. In the middle of the tube there is a graphite (Fig. 2.11a) circular wall 3,8 mm thick in order to obtain a cavity with a ratio $L/D \geq 5$ that is the minimum ratio with which a cavity can be considered a black body [10]. This tube is fixed to a graphite holder inside a metallic case (Fig. 2.11b). Both sides of this case are closed by fused silica windows. Due to the very high temperatures achievable a water cooling system is needed. In order to avoid excessive graphite sublimation and oxidation, which may cause relevant changes in the transmittance of the path between the cavity and the window and also to keep the carbon from coating the windows, an argon flow system is set inside the chamber.

a)

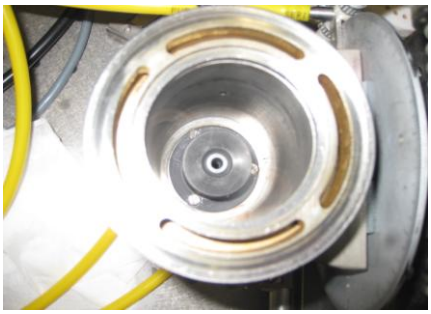

b)

Fig. 2.11. Black body equipment: a) graphite tube. b) graphite holder.

An DC source generating currents up to 115 A was used to heat the graphite tube, through copper electrical connections.

Window's transmittance

For the characterization of the fused silica window's transmittance both theoretical and experimental approaches were used.

Using Sellmeier dispersion equation [11], it is possible to obtain refractive index for the fused silica:

$$n^2 - 1 = \frac{B_1 \lambda^2}{\lambda^2 - C_1} + \frac{B_2 \lambda^2}{\lambda^2 - C_2} + \frac{B_3 \lambda^2}{\lambda^2 - C_3} \tag{2.6}$$

where n is the refractive index, λ is the wavelength in µm and B_1, B_2, B_3, C_1, C_2, C_3 are dispersion equation constants of the fused silica. Both data from [11] and Schott data sheet [12] were used for this calculation and they are summarized in Table 2.3 and in Fig. 2.12.

Table 2.3. Dispersion equation constants for fused silica.

Ref.	B_1	B_2	B_3	C_1	C_2	C_3
[11]	0,696166	0,4079426	0,897479	0,00467915	0,01351206	97,934003
[12]	0,670711	0,4333229	0,877379	0,00449192	0,01328130	95,889988

Since this equation is valid at 20 °C and 1 atm and during the heating of the graphite tube the window was in contact with hot argon, it was important to check

whether this would have a significant effect on its trasmittance. For these corrections, equations from Schott technical recommendation [13] were used:

$$\Delta n(\lambda,T)=\frac{n^2(\lambda,T_0)-1}{2\,n(\lambda,T_0)}\left(D_0\,\Delta T+2\,D_1\,\Delta T^2+3D_2\,\Delta T^3+\frac{E_0\,\Delta T+2\,E_1\,\Delta T^2}{\lambda^2-\lambda_{TK}^2}\right) \tag{2.7}$$

where D_0, D_1, D_2, E_0, E_1 and λ_{TK} are constants taken from [13] and summarized in Table 2.4, T_0 is the reference temperature (i.e., 20 °C). The corrected refractive index is obtained as:

$$n_{CORR}(\lambda,T)=n(\lambda,T)+\Delta n\ (\lambda,T) \tag{2.8}$$

As shown in Fig. 2.13 the correction was negligible for our purposes and was, therefore, omitted from the following calculations.

For normal incidence the Fresnel reflectance R, i.e., the portion of the incident light which is reflected by the first interface, may be expressed as [14]:

$$R=\left(\frac{n-1}{n+1}\right)^2 \tag{2.9}$$

$$t=(1-R)^2 \tag{2.10}$$

where again n is the reflective index of the fused silica and t is the single interface transmittance.

Considering now reflection at the second interface, as well as absorption in going through the window thickness, the overall reflectance ρ, and then the overall transmittance τ are of the form [14]

$$\rho=R\cdot\left[1+\frac{T^2\cdot(1-R)^2}{1-R^2T^2}\right] \tag{2.11}$$

$$\tau=T\cdot\left[\frac{(1-R)^2}{1-R^2T^2}\right] \tag{2.12}$$

where T is the internal transmittance, that is the transmittance within the fused silica window which is not affected by or inclusive of interface influences. In this case it can be assumed unitary T because the window is thin.

Plots of single interface and overall transmittances are in Fig. 2.14.

Table 2.4. Constants valid in the range -100 °C to + 140 °C.

Ref.	D_0	D_1	D_2	E_0	E_1	λ_{TK}
[12]	$2{,}06\ 10^{-5}$	$2{,}51\ 10^{-8}$	$-2{,}47\ 10^{-11}$	$3{,}12\ 10^{-7}$	$4{,}22\ 10^{-10}$	$1{,}60\ 10^{-1}$

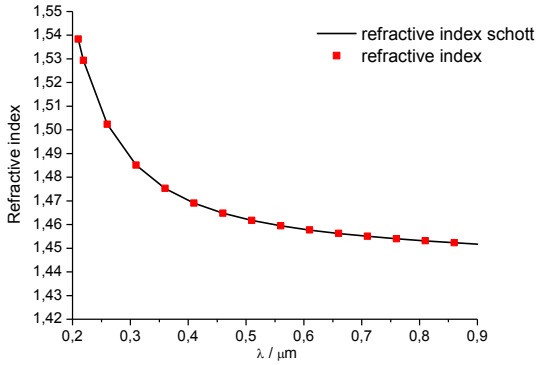

Fig. 2.12. Refractive index of fused silica.

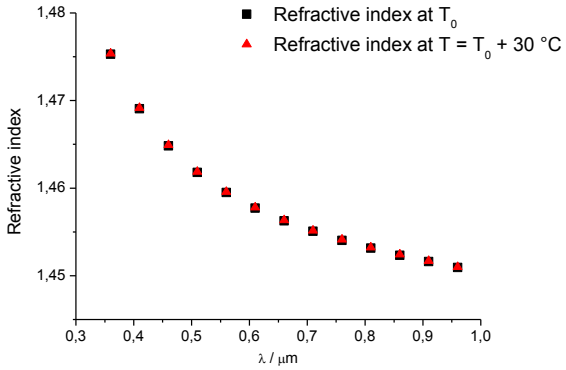

Fig. 2.13. Refractive index of fused silica at reference temperature and at T = T_0+30°C.

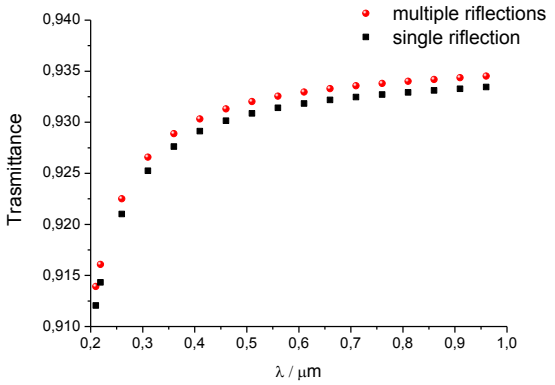

Fig. 2.14. Fused silica transmittance.

The experimental method, used as check of the theoretical results, was a direct measurement of the window's transmittance using a comparable method to one used for the calibration of the 649 nm – channel of the spectrometer. The window was interposed between the spectrometer and a reference lamp, a few centimetres from the lamp in order to reproduce at best the black body furnace conditions. Then three measurements both with and without window were performed at the highest lamp radiance temperature (i.e., the situation with the highest signal to noise ratio). For each column of the arrays an averaging operation was made, obtaining the average counts for each wavelength

$$Counts_{k,AV}(\lambda_j) = \frac{\sum_{i=1}^{256} Counts_i(\lambda_j)}{256} \quad j = 1,...,256 \quad k = 1,2,3 \qquad (2.13)$$

where λ_j is the j –th wavelength and $Counts_{k,AV}(\lambda_j)$ are the average counts in the k – th measurement of the j –th wavelength.

For each measurement and wavelength a ratio was made between the with-window and without-window counts, obtaining

$$\tau_k(\lambda_j) = \frac{Counts^{W}_{k,AV}(\lambda_j)}{Counts^{WW}_{k,AV}(\lambda_j)} \quad j = 1,...,256 \quad k = 1,2,3 \qquad (2.14)$$

where $\tau_k(\lambda_j)$ is the transmittance at the j -th wavelength recorded during the k –th measurement.

Finally, the three transmittance's series were averaged to obtain an average transmittance function of wavelength

$$\tau_{AV}(\lambda_j) = \frac{\sum_{i=1}^{3} \tau_k(\lambda_j)}{3} \quad j = 1,...,256 \tag{2.15}$$

Because of the low signal to noise ratio at very short and long wavelengths, only the range 500-900 nm was considered as reliable. In that range, a very good agreement exists between the theoretical transmittance and one obtained through the spectrometer. Using again the spectrometer, both the used window and a new window from the same manufacturer transmittance were measured and the results were in great accordance with the theoretical one.

Finally, a value of 0,933 for the trasmittance was computed.

Transfer Function K(λ)

Once the 649 nm – channel was calibrated and the transmittance of the blackbody window was determined, several measurements with the high temperature black body were performed in order to obtain the transfer function *K(λ)* for the entire spectral range as:

$$K(\lambda) = \frac{\tau(\lambda)}{Counts(\lambda, T_b)} \frac{1}{\lambda^5 \left[\exp\left(\frac{c_2}{\lambda T_b} \right) - 1 \right]} \tag{2.16}$$

In eq.(2.16) *τ(λ)* is the window transmittance at the wavelength λ, $Counts(\lambda, T_b)$ is the measured signal expressed in counts and T_b is the black body temperature obtained using the calibration eq.(2.5). The transfer function was calculated using different integration times in order to check for linearity, in fact the signal is expected to be proportional to the integration time.

Knowledge of the transfer function (Fig. 2.15) permits to obtain from the measured signal a quantity that is directly proportional to the thermally emitted spectral radiance:

$$E_{\mathrm{det}}(\lambda,T)=K(\lambda)\,Counts(\lambda,T) \tag{2.17}$$

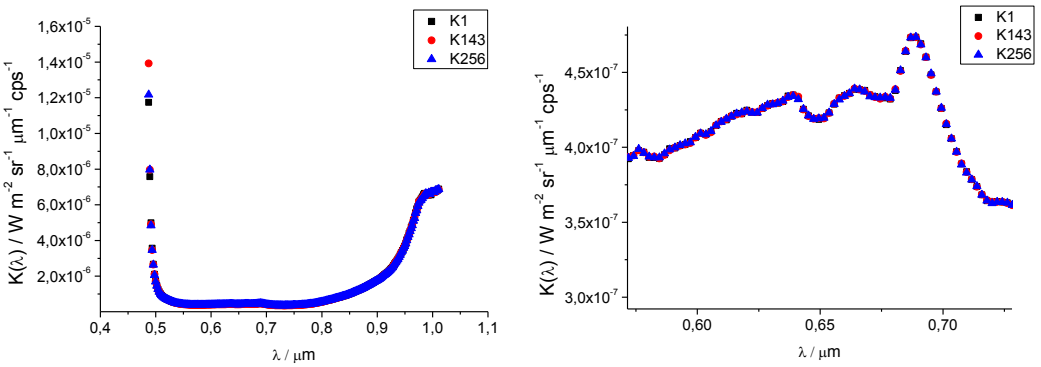

a) b)

Fig. 2.15. K-factor at 2900 K: a) transfer functions of different channels. b) magnification of figure a.

2.3.4 Emittance measurements by radiance spectral analysis

In order to convert the radiance temperature to true temperature, it was adopted two slightly different approaches to compute the normal spectral emittance from the measured radiance spectra [7].

The first one employs a non – linear fitting of the thermal emission spectra with

$$E_{\mathrm{det}}(\lambda,T)=\frac{L_{\lambda,rs}(\lambda,T)}{c_{1L}}=\frac{1}{\lambda^5}\cdot\frac{\varepsilon(\lambda,T)}{\exp\left(\frac{c_2}{\lambda T}\right)-1} \tag{2.18}$$

Where the emittance and the temperature are the free parameters.

It is reasonable to approximate the emittance by a polynomial of the form

$$\varepsilon(\lambda)\cong\sum_{i=0}^{n}a_i\,\lambda^i \tag{2.19}$$

n = 0 corresponds to a constant emittance (greybody assumption) that generally gives already acceptable results for oxide materials in the spectral range of interest (Fig. 2.16).

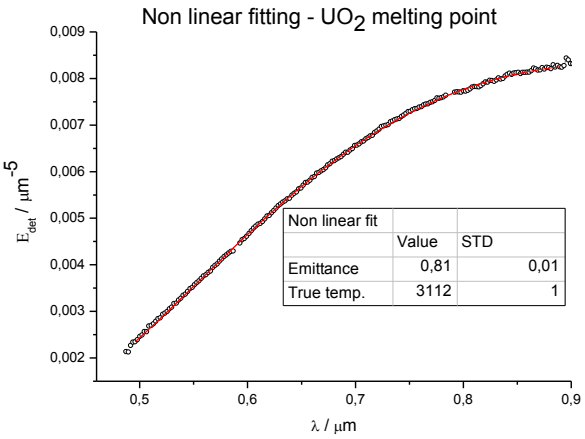

Fig. 2.16. Non linear fitting of radiance spectrum emitted by freezing UO_2.

The other method consists of converting the measured radiance temperature to true temperatures through the calibration of the spectrometer and rearranging eq.(B.28) of Appendix B

$$\frac{1}{T_\lambda} = \frac{1}{T} - \frac{\lambda}{c_2} \ln \varepsilon(\lambda, T) \qquad \text{(B.28)}$$

Then, assuming the greybody assumption, it is possible to plot the inverse of radiance temperature as function of the wavelength, resulting in a straight line that when extrapolated to zero wavelength intersects the inverse true temperature, as one can easily see from Fig. 2.17.

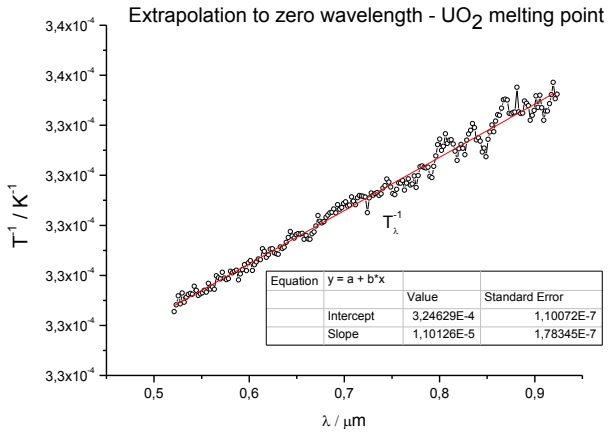

Fig. 2.17. "Extrapolation to zero wavelength" at the melting point of UO_2.

In conclusion, multi-wavelength pyrometers have the main advantage to be able to deduct both the temperature and the emittance from measurements of the spectral radiance at several wavelengths. On the other hand, all methods are based on the assumption of a mathematical function instead of the real physical variation of the normal spectral emittance and this involves a systematic error that can affect strongly (or not) the calculations. For this reason these methods can only be applied with acceptable accuracy if the variation of the normal spectral emittance with wavelength can be described by a known function with sufficient accuracy [15, 16, 17].

2.4 Ultra – Violet pyrometer

In addition to the two previous pyrometers, a UV – pyrometer with a mean effective wavelength (see Appendix B, section B.9.4.1) of 219 nm was calibrated in the present work.

The main advantage of this kind of radiation thermometer is its short operational wavelength, resulting in a correspondingly low influence of the emittance on the final temperature reading. This can be seen immediately recalling eq.(B.28) and rearranging the two equations hereafter

$$\Delta\left(\frac{1}{T}\right) = \frac{1}{T} - \frac{1}{T_\lambda} = \frac{n\lambda}{c_2} \ln \varepsilon(\lambda, T) \qquad (2.20)$$

$$\lim_{\lambda \to 0} \Delta\left(\frac{1}{T}\right) = \frac{n\lambda}{c_2} \ln \varepsilon(\lambda, T) = 0 \tag{2.21}$$

In Fig.2.18 is shown the linear dependence expressed in eq.(2.20)

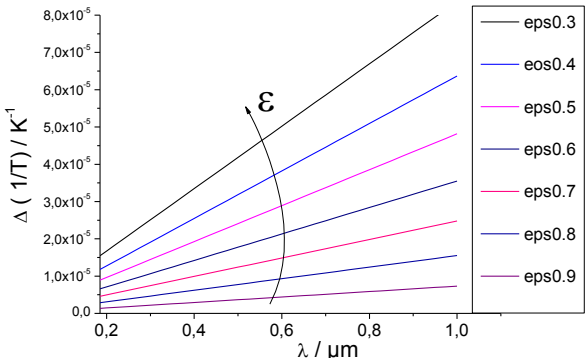

Fig. 2.18. Inverse temperature error as a function of wavelength [18].

Differentiating eq.(B.28) yields an expression which demonstrates how the uncertainty on the emittance can affect the measure of the temperature

$$\frac{dT}{T} = \frac{\lambda T}{c_2} \frac{d\varepsilon(\lambda)}{\varepsilon(\lambda)} \tag{2.22}$$

2.4.1 Set-up

The UV – pyrometer consists of two 2 inch-diameter, 90° off-axis parabolic mirrors that focus the radiance flux into the field stop in front of a photomultiplier tube; the latter is a Hamamatsu® R6834 PM with a Cs – Te 28mm-diameter photocathode with solar-blind response (from 160 nm to 320 nm), with 11-stage dynodes and a window made of synthetic silica [19].

An interference filter is placed behind the field stop and in the front of the PM. It has centre wavelength of 215 nm [20]. After the PM, the signal is amplified first by a transimpendance and then by a ± 10 V amplifier, then the signal in volt is acquired by a Nicolet Pro® 44C digital storage oscilloscope.

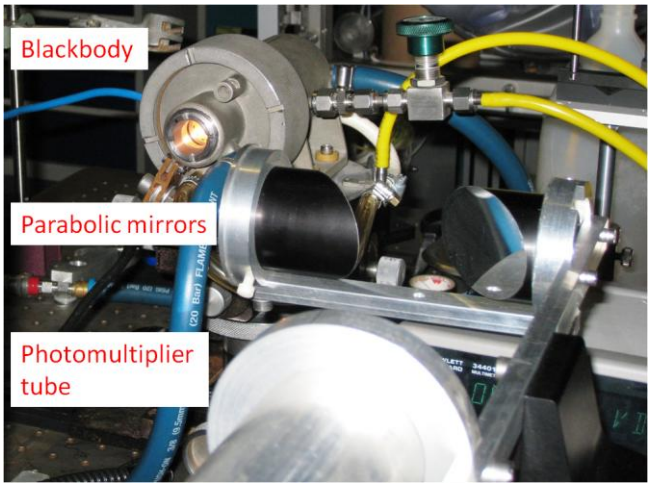

Fig. 2.19. UV- pyrometer in front of the blackbody for calibration.

2.4.2 Calibration

The UV- pyrometer was calibrated against a blackbody cavity using the following equation

$$K_{cal} = V_{out}(T_{cal,b})\left[\exp\left(\frac{c_2}{\lambda T_{cal,b}}\right) - 1\right] \tag{2.23}$$

Where V_{out} is the signal in voltage from oscilloscope, $T_{cal,b}$ is the temperature of the blackbody (measured with the two - channel pyrometer) and λ is the mean effective wavelength calculated as reported hereafter.

The K_{cal} factor obtained is $(2{,}0 \pm 0{,}3)\cdot 10^8$ V.

When the calibration is done, it is possible to measure the radiance temperature from eq.(2.24)

$$\frac{1}{T_\lambda} = \frac{1}{T_{cal,b}} - \frac{\lambda}{c_2}\ln\left(\frac{V_{out}(T_\lambda)}{V_{out}(T_{cal,b})}\right) \tag{2.24}$$

2.4.3 Determination of the mean effective wavelength

The mean effective wavelength of a pyrometer is described in Appendix B, section B.9.4.1. For calculating this quantity in a UV – pyrometer the spectral radiance responsivity must be computed taking into account various contributions, namely the UV filter transmission ($\tau(\lambda)$), the reflectance of the mirrors ($\rho_{mirror}(\lambda)$) and the

radiant flux responsivity of the photomultiplier ($R_\phi(\lambda)$). The latter is defined as the photoelectric current generated by the photocathode divided by the incident radiant flux at a given wavelength [21].

$$R_L(\lambda) = \tau(\lambda)\tau_{mirror}(\lambda)R_\phi(\lambda) \tag{2.25}$$

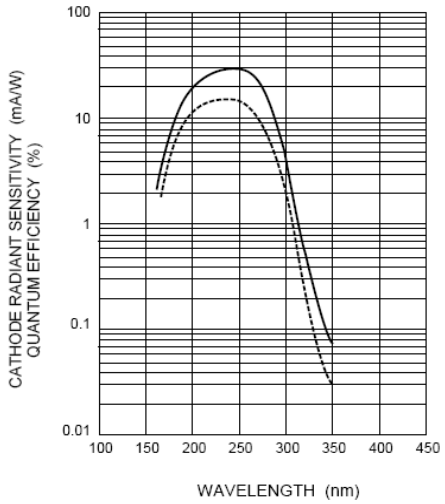

Fig. 2.20. Relative cathode radiant flux responsivity and quantum efficiency of Hamamatsu® R6834 tube[1] [19].

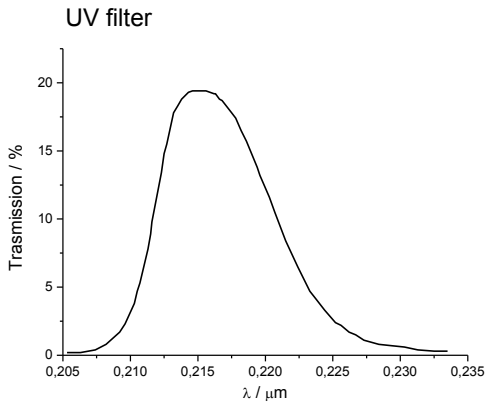

Fig. 2.21. Transmission of the UV filter centred at 215 nm wavelength.

[1] Quantum efficiency is the number of photoelectrons emitted from the photocathode divided by the number of incident photons. Photons at shorter wavelengths carry higher energy compared to those at longer wavelength and contribute to increase in the photoemission probability, so the maximum quantum efficiency occurs at a wavelength slightly shorter than the wavelength of peak radiant flux responsivity [21].

Assuming the reflectance of mirrors constant within the filter passband, the spectral radiance responsivity is reported in Fig. 2.31 (red line).

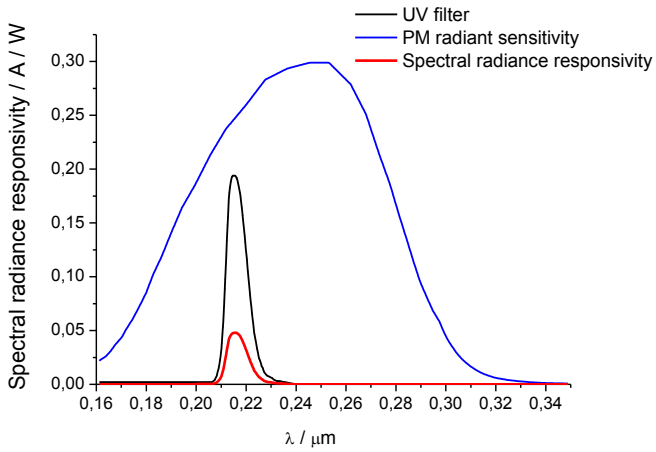

Fig. 2.22. Spectral radiance responsivity of the UV – pyrometer.

Finally, the analysis yielded a value of 219 nm for the mean effective wavelength in the temperature range between 2500 K and 3600 K.

2.5 Temperature measurement uncertainty

In order to estimate the uncertainty of temperature measurements, several contributions were taken into account.

Recalling the calibration eq. (2.2) and considering the trasmittance[2] τ of the optical system , the radiance temperature can be expressed as

$$T_\lambda = \frac{B}{V_{out}(T) + k_{\log} \log(\tau) - A} \tag{2.26}$$

[2] Trasmittance of the autoclave windows (both, front laser and rear) were well known and they were checked by experimental way. Concerning the total trasmittance of the high pressure system, it was well established.

and it comes out that the radiance temperature uncertainty depends on the uncertainties of the linear fitting (*A*,*B*), of the k_{log}, of the trasmittance τ and of V_{out} due to the oscilloscope uncertainty; each component can be obtained by forming the partial derivative of T_λ with respect to each component,

$$u_B(T_\lambda) = \frac{T_\lambda}{B} u(B) \tag{2.27a}$$

$$u_A(T_\lambda) = \frac{T_\lambda^2}{B} u(A) \tag{2.27b}$$

$$u_{k_{\log}}(T_\lambda) = \frac{T_\lambda^2 \log\tau}{B} u(k_{\log}) \tag{2.27c}$$

$$u_{\log\tau}(T_\lambda) = \frac{T_\lambda^2 k_{\log}}{B} u(\log\tau) \tag{2.27d}$$

$$u_{V_{out}}(T_\lambda) = \frac{T_\lambda^2}{B} u(V_{out}) \tag{2.27e}$$

And using the law of propagation of uncertainty, it is possible to obtain the combined standard uncertainty as

$$u_c(T_\lambda) = T_\lambda^2 \sqrt{(\frac{u(B)}{B}\frac{1}{T_\lambda})^2 + (\frac{u(A)}{B})^2 + (\frac{u(k_{\log})\log\tau}{B})^2 + (\frac{u(\log\tau)k_{\log}}{B})^2 + (\frac{u(V_{out})}{B})^2} \tag{2.28}$$

Table 2.5. Uncertainties for different radiance temperatures.

Source of uncertainty	Standard uncertainty in T_λ / K		
	at 2000 K	at 2400 K	at 3000 K
$u_B(T_\lambda)$	1,6	1,9	2,4
$u_A(T_\lambda)$	1,4	2,1	3,2
$u_{klog}(T_\lambda)$	0,4	0,6	0,9
$u_{log\tau}(T_\lambda)$	0,4	0,6	0,9
$u_{Vout}(T_\lambda)$	14,3	21	31

Fig. 2.23 shows the trend of the expanded uncertainty (with a coverage factor of 2 [22]) as function of radiance temperature.

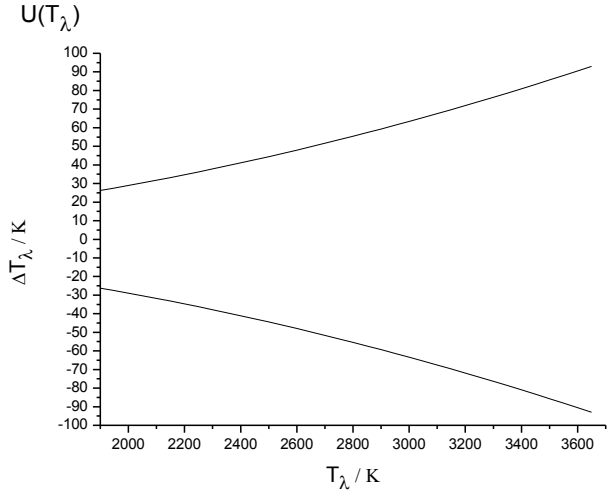

Fig. 2.23. Expanded uncertainty as function of T_λ.

Now, it is possible to compute the uncertainty on the true temperature recalling another time eq.(B.28) and rearranging

$$T = \left(\frac{1}{T_\lambda} + \frac{\lambda}{c_2}\ln\varepsilon\right)^{-1} \tag{2.29}$$

where λ is the mean effective wavelength from eq.(2.4). As before, it can be computed each contribution as

$$u_{T_\lambda}(T) = \frac{T^2}{T_\lambda^2}u_c(T_\lambda) \tag{2.30a}$$

$$u_\varepsilon(T) = \frac{\lambda T^2}{c_2\varepsilon}u(\varepsilon) \tag{2.30b}$$

where $u(\varepsilon)$ is the uncertainty of the normal spectral emittance calculated by the methods discussed previously. The temperature dependence of ε is ignored, also the component due to the wavelength uncertainty is negligible.

Finally, the combined standard uncertainty for the true temperature is

$$u_c(T) = T^2 \sqrt{\left(\frac{u_c(T_\lambda)}{T_\lambda^2}\right)^2 + \left(\frac{u(\varepsilon)\lambda}{c_2 \varepsilon}\right)^2} \tag{2.31}$$

Hereafter, it will be mentioned several contribution of uncertainties that are negligible compared with the previous ones

- pyrometer calibration stability: it was checked the new calibration against previous calibrations (2010, 2009) and it resulted in a very good agreement between each other;
- use of Wien's law instead Planck's law: the difference in temperature, at this mean effective wavelength, is approximately 0,13 K at 2800 K;
- mean effective wavelength: it is not constant with *T* and it should be the mean effective wavelength between radiance temperature and real temperature (see eq.(B.40)) and not the one calculated from the calibration. This source of uncertainty is described deeply in Ref. [23].

2.6 Specimen preparation and characterisation

2.6.1 Introduction

In order to give a full description of the high temperature behaviour of the investigated materials, a pre- and post-melting characterisation of them is needed. Several methods have been used for this purpose, in particular Scanning Electron Microscopy (SEM), X Ray Diffraction (XRD) and Raman spectroscopy have been exploited to investigate the crystal structure and composition of the specimens, and to monitor the segregation. Thermogravimetry (TG) has been utilised to check the stoichiometry of the specimens. This chapter will give a theoretical background of the methods and a brief description of each technique and utilised instruments.

2.6.2 SEM – Scanning Electron Microscopy

The SEM (Fig. 2.24) is an instrument that produces a high-magnification image by using electrons instead of light to form an image. This technique exploits a electron beam, coming from a heated W–filament (electron gun), and accelerated against the

specimen in a strong potential (from kV to tens of kV). Under these conditions the electrons have a shorter De Broglie wavelength (~10^{-12} m) than that of visible light resulting in a higher resolving power of a diffraction – limited – image – system. The De Broglie wavelength can be written as

$$\lambda_e = \frac{h}{m_e v_e} \tag{2.32}$$

where m_e and v_e are respectively the mass and the velocity of an electron and h is the Planck constant. From the formula, it is clear how the higher is the velocity, the shorter is the wavelength.

Since the limit of the resolution is due to diffraction phenomena, which occurs when the dimension of the observed object is comparable with the associated wavelength of the probe, the lower is the latter, the higher can be the magnification and the smaller the observable objects.

Electrons are scattered by the specimen both elastically and inelastically. Elastic scattering with the specimen atoms leads to the detection of more energetic electrons (Back – Scattered Electrons, BSE), whereas secondary electrons (SE) are directly emitted by the specimen following the inelastic interaction with the beam.

Since electrons strongly interact with matter, SEM is used only to study surface features of the specimen.

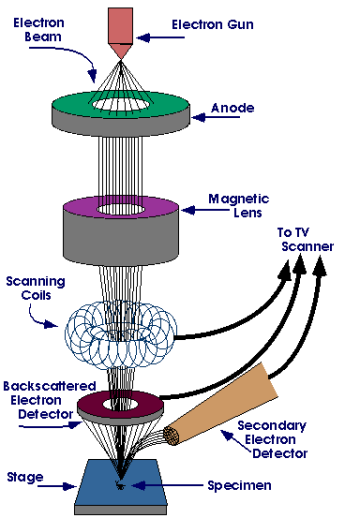

Fig. 2.24. Schematic SEM.

Since SE have low energy, measurements are performed under high vacuum, in order to enable them to reach the detector. Moreover only conductive materials can

be analysed. Insulator can only be analysed if they are coated with a thin layer of gold or graphite.

Detection techniques are related to the energies of the electrons of interest. As far as SE are concerned, they are deviated in the direction of a photomultiplier going through a grid biased at 400 V, in order to accelerate them. BSE are identified using a ring shaped coaxial detector, which is a semiconductor or a photomultiplier, in order to maximise the geometrical efficiency of the detection. Since BSE have high kinetic energy, they are not deviated by the biased grid.

BSE images provide qualitative information on the distribution of the elements present on the surface. As a matter of fact, if an electron is back-scattered by a heavy element, it keeps the most of its initial energy, so that the resulting image is brighter than that obtained when scattering occurs against a relatively light element. Thus with a BSE image it is possible to distinguish zone richer (or poorer) of heavy elements.

Characteristic X–rays emitted by the atoms present on the surface can be used for a semi-quantitative chemical analysis (EDS). However, due to the fact that this method is affected by many factors, such as window absorption, peak overlapping and surface roughness, it can be used only with qualitative aims for light elements. The analysis can be considered as semi-quantitative for heavier elements, starting from sodium.

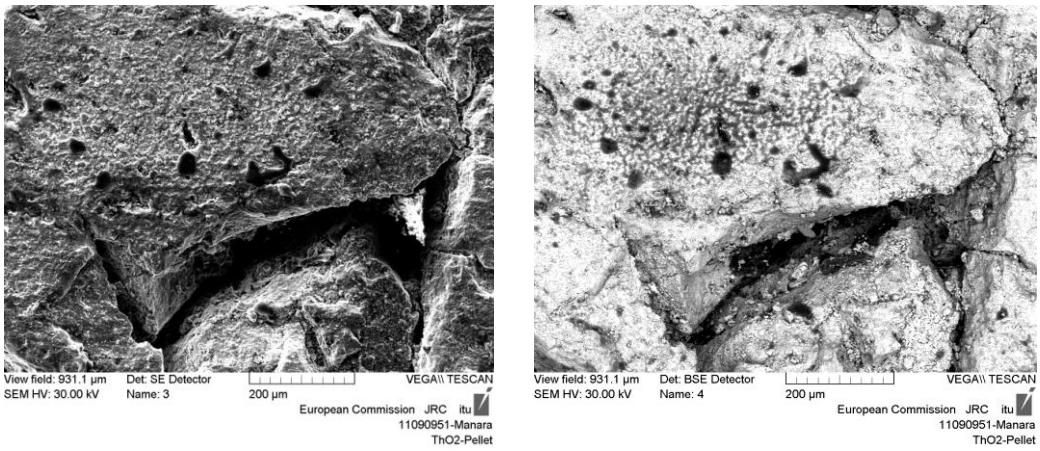

a) b)

Fig. 2.25. a) SE image. b) BSE image. The images were obtained with the same voltage and the same resolution on unmolten thoria.

2.6.3 X – Ray Diffraction (XRD)

When a X–ray beam interacts with matter, the most important observed effect is the 3D spherical elastic scattering of the incident beam. An electron can be considered as an electromagnetic field which oscillates with its own frequency. The electrons surrounding the nucleus of an atom which are on the path of an X-ray beam start to oscillate with the same frequency of the incoming radiation. Thus they become secondary sources of X–rays with the same energy as the incident. In almost all directions the scattered X–rays are out of phase, leading to destructive interference. In some particular directions, however, the scattered beams are in–phase. In–phase scattering is called diffraction. The diffraction angles characteristic of a material depend only on the size and the shape of the unit cell which composes the crystal lattice.

Diffraction can be seen as a reflection of the incident beam from lattice planes within the crystal structure, as discovered by Sir W.L. Bragg in 1912. In Fig. 2.26 is sketched a situation in which an X – ray beam hits parallel crystal planes separated by an inter planar distance *d*.

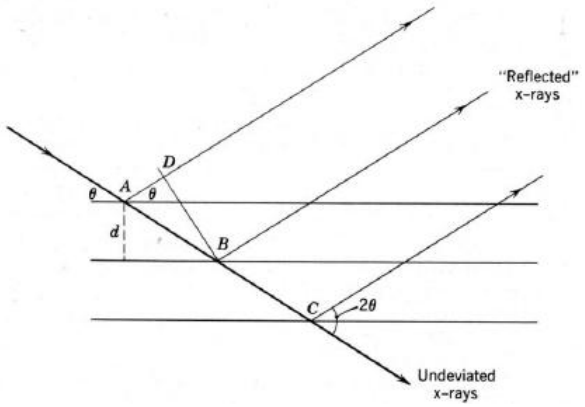

Fig. 2.26. The condition for reflection.

The reflected rays interfere constructively to form a diffracted beam, only if their phases differ for a whole number of wavelength, that is, if

$$AB - AD = n\lambda \tag{2.33}$$

where

$$AB = \frac{d}{\sin\theta} \tag{2.34}$$

and

$$AD = AB\cos 2\theta = \frac{d}{\sin\theta}\cos 2\theta \tag{2.35}$$

$$n\lambda = \frac{d}{\sin\theta} - \frac{d}{\sin\theta}\cos 2\theta = \frac{d}{\sin\theta}(2\sin^2\theta) \tag{2.36}$$

therefore

$$n\lambda = 2d\sin\theta \tag{2.37}$$

This is the Bragg condition for diffraction.

X-ray diffraction (XRD) was performed in this work using a Bruker® D8 Advance diffractometer (Cu-Kα_1 radiation) with a 2θ range of 10°-120° using 0,009° steps with 2 s of count time per step at operating conditions of 40 kV- 40 mA. The XRD instrument was equipped with a Lynxeye® 3° linear position sensitive detector.

2.6.4 Raman spectroscopy

Elementary Raman scattering (see [24]) involves two photons, one impinging on the specimen surface with frequency ω, one emitted from the specimen after the interaction. For incident light with wavelengths in the visible to infrared range, the interaction consists of annihilation or excitation of vibrational states in the material. If a vibration is excited or annihilated during the interaction with matter, the specimen will respectively either absorb or release energy and, correspondingly the photon emitted will have lower or higher energy than the impinging one. However, most of the incident photons are scattered elastically, producing the very intense Rayleigh line. If part of the energy held by the incident photon is absorbed by the material, the less energetic emitted photons undergo the so called Stokes scattering. If the ejected photon has more energy of the incident one, then a phonon has been annihilated, leading to the so called anti–Stokes scattering. Since the inelastic scattering does not depend on the type of incident photons used, Stokes and anti–Stokes peaks in Raman spectra are symmetric relative to the Rayleigh line. The de-

excitation of a vibration mode (anti-Stokes) requires the vibrational state to be initially populated by phonons. The population of vibrational states follows Boltzmann distribution and thus the higher the temperature, the more populated the higher levels are. Therefore in standard conditions (300 K), Stokes scattering is more probable as it does not require a phonon on an excited state. Spontaneous Raman scattering is typically very weak, and as a result the main difficulty of Raman spectroscopy is separating the weak inelastically scattered light from the intense Rayleigh scattered light.

A Raman spectrometer is a device to measure the intensity of the scattered radiation as a function of its frequency. A light source, usually a laser, is used to illuminate the specimen. In spectroscopy the energy of the outcoming photons is normally expressed in terms of wavenumber $k = \omega / 2\pi c$ (in cm^{-1}).

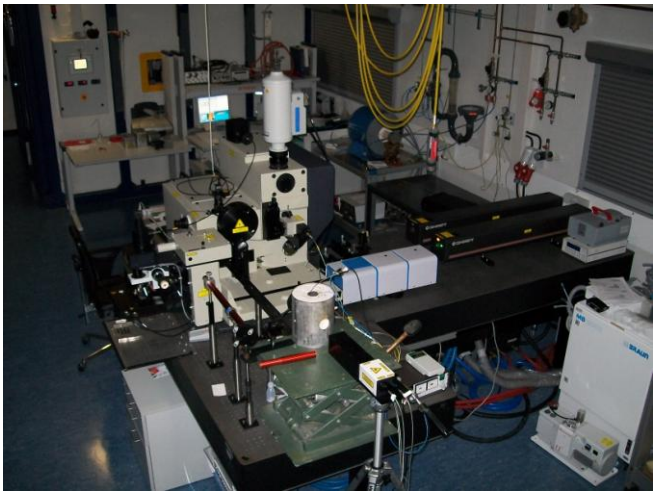

Fig. 2.27. Jobin –Yvon ® T64000 spectrometer.

Raman spectra were measured at ITU with a Jobin –Yvon ® T64000 spectrometer (Fig. 2.27) used in the single spectrograph configuration. The excitation source is an Ar^+ Coherent® cw laser radiating at 514,5 nm, with a nominal power of 100 mW at the exit of the cavity. The power impinging on the specimen surface is lower by a factor 10 approximately. Spectra are measured in a confocal microscope with a 50x magnification and long focal distance. This feature allows obtaining a good signal / noise ratio independently of the surface shape, with a spatial resolution of 2 μm x

2μm on the specimen surface. The spectrograph angle is calibrated with the T_{2g} excitation of a silicon single crystal, set at 520,5 cm^{-1} [25].

2.6.5 Thermogravimetry

A thermogravimetric (TG) analysis consists in heating the specimen under pre-set atmosphere conditions and simultaneously measuring its mass. The measurements were performed by using a NETZSCH Simultaneous Thermal Analysis Apparatus STA 409.

A small amount of material, is powdered and put into the thermobalance alumina crucible. The crucible is seated in an oven, where a certain gas flow and a raising ramp of temperature are set, and it is connected to a high-sensitivity analytical balance that allows in situ weighing of the powder during the oxidation process.

From the weight difference between initial and final powder one can calculate the initial composition, assuming that all the weight change is only due to the oxidation process.

Since all the investigated oxides have a stable maximum oxidation state (i.e., CaO, CeO_2 and ThO_2), during the experiments only an oxygen uptake could occur. By the use of the thermogravimetry analysis the amount of the possible oxygen uptake was measured.

The oxidation process, in the example of ThO_2, can be expressed as

$$ThO_{2-x} + \frac{x}{2} O_2 \rightarrow ThO_2 \tag{2.38}$$

The moles of oxygen in the final composition (i.e., after the heat treatment) can be determined through formula

$$n_{fin}(O) = 2 \cdot \frac{m_{fin}}{M(ThO_2)} \tag{2.39}$$

where m_{fin} is the final weight of the powder and $M(ThO_2)$ stands for "molar mass".

Based on the assumption that the moles of thorium do not vary during the treatment, it can be written

$$n(Th) = n_{in}(Th) = n_{fin}(Th) = \frac{n_{fin}(O)}{2} \tag{2.40}$$

and

$$n(Th) = n(ThO_{2-x}) = \frac{m_{in}}{M(Th) + (2-x)M(O)} \tag{2.41}$$

The comparison of the eq.(2.40) and eq.(2.41) leads to a relation for x

$$x = 2 - \frac{1}{M(O)} \cdot \left(\frac{m_{in}}{n(Th)} - M(Th) \right) \tag{2.42}$$

3.4 References

[1] D. Manara, M. Sheindlin, W. Heinz and C. Ronchi, Rev. Sci. Instrum., 79 (2008), 113.

[2] D. Manara, C. Ronchi, M. Sheindlin, M. Lewis and M. Brykin, J. Nucl. Mater., 342 (2005), 148.

[3] F. De Bruycker, K. Boboridis, D. Manara, P. Poml, M. Rini and R. J. M. Konings, J. Nucl. Mater., 419 [1-3] (2011), 186.

[4] R. Böhler, M. J. Welland, F. De Bruycker, K. Boboridis, A. Janssen, R. Eloirdi, R.J.M. Konings and D. Manara, "Revisiting the melting temperature of NpO_2 and the challenges associated with high temperature actinide compound measurements", submitted to Nature Materials.

[5] C.A. Utton, F. De Bruycker, K. Boboridis, R. Jardin, H. Noel, C. Guéneau and D. Manara, J. Nucl. Mater., 385 [2] (2009), 443.

[6] H. F. Jackson, D. D. Jayaseelan, D. Manara, C. P. Casoni and W. E. Lee, J. Am. Cer. Soc., 94 [10] (2011), 3561.

[7] D. Manara, "Melting transition measurements in uranium dioxide", PhD Thesis, Technical Note JRC-ITU-TN-2004/05 (2004).

[8] OIML R 48, Tungsten ribbon lamps for the calibration of radiation thermometers, Edition 2004 (E).

[9] PTB calibration sheet, 2010.

[10] D.P. De Witt and G.D. Nutter, "Theory and practice of radiation thermometry" (Wiley, 1988).

[11] I. H. Malitson, Journal of the Optical Society of America, 55 [10] (1965).

[12] Schott, technical info TIE-29 (01/2007).

[13] Schott, technical info TIE-19 (07/2008).

[14] D. P. De Witt and G. D. Nutter, "Theory and Practice of Radiation Thermometry", pag. 117.

[15] P. B. Coates, Metrologia, 17 (1981), 103.

[16] G. Neuer, L. Fiessler, M. Groll and E. Schreiber, Temperature: Its Measurement and Control in Science and Industry, 6, J. F. Schooley, ed., (AIP, New York, 1992), 787.

[17] P.B. Coates, High Temp. – High Pressures, 20 (1988), 433.

[18] F. De Bruycker, "High Temperature Phase Transitions in Nuclear Fuels of the Fourth Generation", PhD Thesis, Technical Note JRC-ITU-TN-2011/4 (2011).

[19] Hamamatsu® R6834 tube datasheet.

[20] L.O.T. – Oriel GmbH, Darmstadt datasheet.

[21] Hamamatsu photomultiplier tubes Basics and applications, 3rd edition.

[22] JCGM 100:2008, GUM 1995, "Evaluation of measurement data – Guide to the expression of uncertainty in measurement".

[23] K. Boboridis, "Application of single – wavelength radiation thermometry and high – speed laser polarimetry to thermophysical property measurements on pulse – heated metals", (2001) NIST, Institut für Experimentalphysik der Technischen Universität Graz, Austria.

[24] C. Kittel, "Introduction to Solid State Physics", J. Wiley and Sons, New York 1996 (7th Edition), Chapter 4.

[25] J. H. Parker, Jr., D. W. Feldman, and M. Ashkin, Phys. Rev., 155 (1967), 712.

Chapter 3

Validation of the method

As with every experimental technique, for the laser heating is essential to be validated with theoretical modelling, measuring reference materials and improving knowledge on all the possible sources of uncertainties that come out from experiments and to reduce them.

In this research, it was carried out a measurement campaign on five refractory metals whose radiance temperatures of melting are well established and recommended as secondary reference points on ITS-90.

Furthermore, it was provided a set of data for corroborating a Phase Field simulation, developed by Dr. M. J. Welland (RMC Kingston, Canada, and ITU Karlsruhe) using COMSOL Multiphysics, and finally the spatial beam profile was determined with a laser profile-meter.

3.1 Measuring campaign

3.1.1 ITS-90 secondary reference points

Other than the promulgation of the International Temperature Scale of 1990 (ITS-90) with its fixed points, exist also a list of temperatures associated with a number of secondary reference points (SRPs) [1] that was assessed after ITS-90 was introduced.

These SRPs have to meet some criteria such as

- The SRP must be highly reproducible
- There should be more than one experimental measurement of the value of temperature

- An estimate of the uncertainty of the assigned temperature should be reported
- The purity of the material corresponding to the assigned temperature should be stated
- References to the original experimental work should be given

And depending whether a SRP satisfies all or not the criteria above it is classified as first quality SRP or second quality SRP.

Concerning the radiance temperatures of melting (T_λ) of metals (Table 3.1), they are considered second quality SRPs. Values for several wavelengths are listed in [1] and *"These should be useful for calibration checks of high – temperature radiation thermometer measurements."* cit. Ref. [1].

It is important to note that all the radiance temperature values are determined with the specimens in vacuum or inert – gas environment at atmospheric pressure. Pressure corrections are negligible, if compared with measurement uncertainties.

The possibility to introduce the radiance temperature of melting of metals as reference values was studied for twenty years and strongly suggested by two renowned National Metrology Institute, NIST (National Institute of Standards and Technology) and IMGC (Istituto di Metrologia "G. Colonnetti") [2, 3], now called INRIM (Instituto Nazionale di Ricerca Metrologica).

Table 3.1. Secondary reference points on ITS-90 for the five refractory metals involved in this work, T_λ at λ = 650 nm.

Metal	T_λ / K SRP [i]
V	1988 ± 7
Nb	2422 ± 5
Mo	2530 ± 5
Ta	2847 ± 6
W	3207 ± 7

[i] Literature references are in Chapter 1.

3.1.2 Layout experiment / peculiarities

In contrast with the general set-up of the laser heating technique, described in Chapter 2, these experiments were performed with some changes.

First of all, the two-channel pyrometer and the spectrometer were placed on the opposite side of the incident laser beam, in Fig. 3.1 the laser is out of the image on the right side (from reader view), to prevent the pyrometers from seeing the bright laser light (due to the light reflectance of metals) which would have affected the ascending flank of the thermograms (Fig. 3.2).

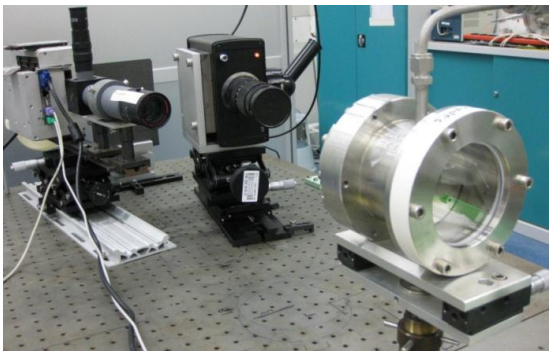

Fig. 3.1. Detail of the set – up used.

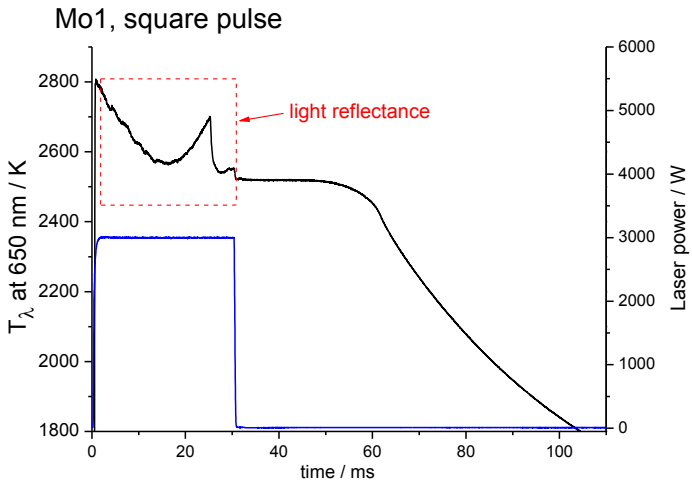

Fig 3.2. Effects of the light reflectance on a molybdenum specimen.

Experiments were performed only with the "low" pressure device and the vessel was filled with 2 bar of Ar + H_2 (hydrogen, a few % in volume to avoid the possible formation of an oxide coat on the surface).

The radiance temperature was measured with the two - channel pyrometer at 650 nm effective wavelength (see Appendix B). The spectrometer was used only for checking the good agreement of the measurement at the same wavelength of the pyrometer.

A specific specimen holder made of a tungsten alloy, it was designed (in Fig. 3.3a with inside a specimen of niobium and in Fig 3.3b a cross section)**.** As it may be seen from the "exploded" drawing (Fig. 3.3c), it is composed of several parts, three screws, a thin "upper" plate cover and a "bottom" plate cover that close the specimen in between; however the "quasi – containerless" is conserved in fact there is a gap of approximately 0,05 mm between the specimen (of 0,1 mm thickness) and the upper cover and in any case, it was used only the 3 mm laser optics.

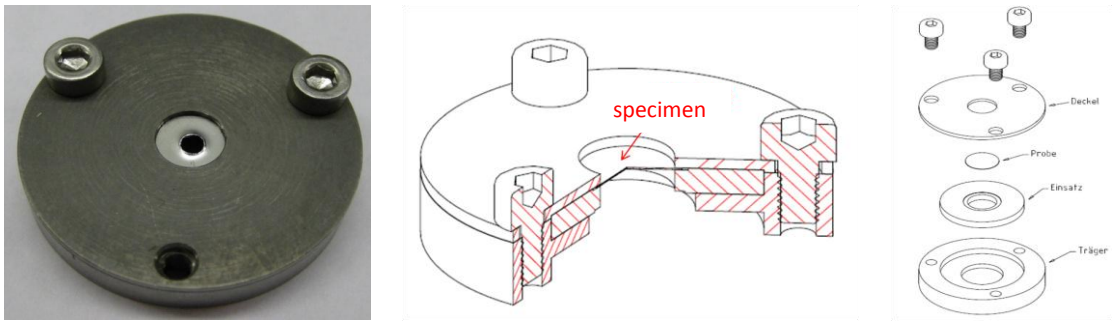

a) b) c)

Fig. 3.3. a) photo of the holder with a laser melted niobium specimen. b) cross section of the specimen holder. c) "exploded" drawing.

3.1.3 Metallic specimen

Specimens from two different suppliers were used and different thicknesses of different purities were selected. The latter was certified by "Certificate of Analysis" issued by the suppliers, where the amount of the different impurities is reported. All the specimens were disk of 8 mm diameter.

Vanadium

Table 3.2. Vanadium – specimen characteristics.

Thickness / mm	Purity (mol%)	Supplier
0,075	99,8	Alfa Aesar
0,127	99,8	Alfa Aesar

Niobium

To notice that for the higher purity specimens the amount of tantalum is explicitly given account because, the two materials are very similar and so is very hard to chemically/physically separate each other.

Table 3.3. Niobium – specimen characteristics.

Thickness / mm	Purity (mol%)	Supplier
0,05	99,995	Alfa Aesar
0,1	99,9	Goodfellow
0,125	99,9	Goodfellow
0,127	99,8	Alfa Aesar
0,127	99,97	Alfa Aesar

Molybdenum

Table 3.4. Molybdenum – specimen characteristics.

Thickness / mm	Purity (mol%)	Supplier
0,1	99,95	Alfa Aesar
0,125	99,9	Goodfellow
0,127	99,9	Goodfellow

Tantalum

Table 3.5. Tantalum – specimen characteristics.

Thickness / mm	Purity (mol%)	Supplier
0,025	99,997	Alfa Aesar
0,127	99,99	Alfa Aesar

Tungsten

Table 3.6. Tungsten – specimen characteristics.

Thickness / mm	Purity (mol%)	Supplier
0,05	99,95	Alfa Aesar
0,1	99,95+	Alfa Aesar

3.1.4 Experiments

Power profiles and thermograms

The experiments were carried out with several different laser programs (power vs. time). In most cases, square laser pulses were used, but they varied between short high-power and long with lower power, roughly keeping the pulse energy constant to reach a certain temperature for a given material, to investigate if there were some effects that can affect the thermogram by changing the heating rate. In some cases, "composite" pulses were used with a pre – heating stage to heat the specimen up below the melting point and then add a short high power pulse to "goes into the liquid quickly".
Examples of laser programs are shown in Table 3.7.

Table 3.7. Typical laser programs used for melting the metallic specimens.

Power / W	Time / ms	Pulse
4500	0-10	square
500	0-100	square
500 4500	0-100 100-108	"Composite" pulse

Fig. 3.4 shows an example of a thermogram (radiance temperature vs. time) acquired with a niobium specimen irradiated with a 700 W square laser pulse of 150 ms duration. It is possible to recognize some important features. Starting with the "heating" ramp then it is visible a long melting plateau at the constant radiance temperature of melting. When all the needed heat of fusion is provided the curve enters in the liquid region and the temperature starts again to increase. When the laser is switched off (in the figure after 150 ms) the temperature immediately drop off at a certain cooling rate, proportional to the slope of the curve. Then, before releasing the

heat of fusion, depending on the cooling rate, conditions of surface and stochastic mechanisms (see Appendix A), it is common to observe an undercooling stage.

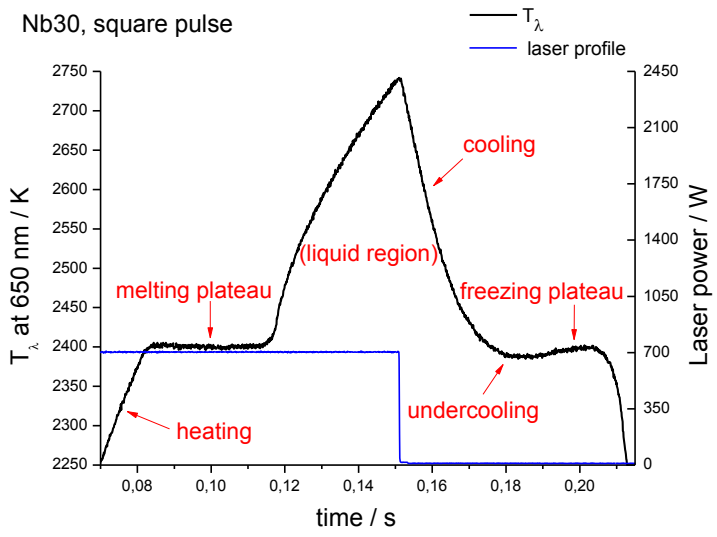

Fig. 3.4. Niobium specimen – thermogram overview.

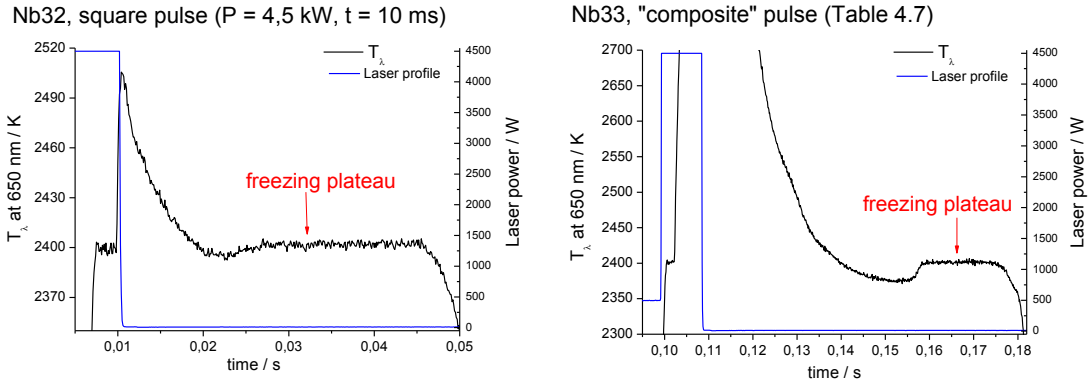

a) b)

Fig. 3.5. Niobium specimen – differences in freezing plateau, a) short pulse, high power. b) pre – heating + shorter pulse.

Differences are visible comparing Fig 3.4 with Fig. 3.5a and Fig. 3.5b, such as in the heating / cooling rate, certainly due to the different laser programs used, but especially on the shape of the freezing plateau. Even though the heating rate of Nb30 and Nb32

were very different the deposited laser power energy was similar and so were the molten area observed on the specimens after the experiments.

Repeatability

Concerning this aspect, it was observed for all metals, that after the first laser shot on the "as received" specimen the surface always looked shinier and smoother. Repeating another time the same experiment, with the same laser program, resulted in a depression of the maximum temperature of about 50 – 80 K; this difference was due to a change in emittance of the surface and therefore the heating is lower due to lower absorbed laser power (from Kirchhoff's law), as it can be seen in Fig. 3.6.

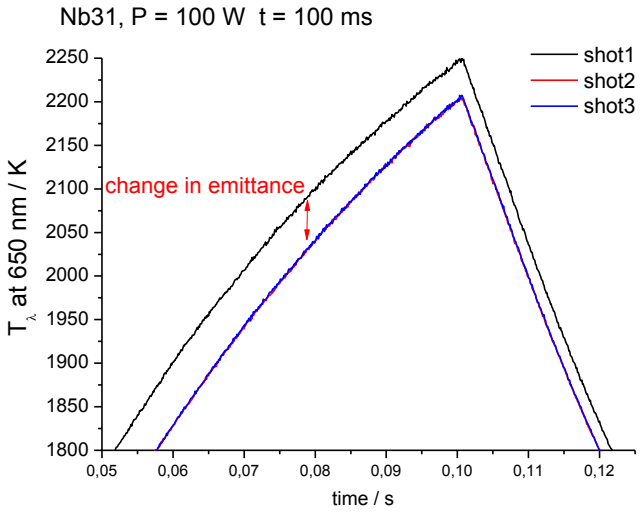

Fig. 3.6. Niobium specimen – repeatability, change in emittance. The laser pulse power and duration was indentical in the three experiments on the same specimen.

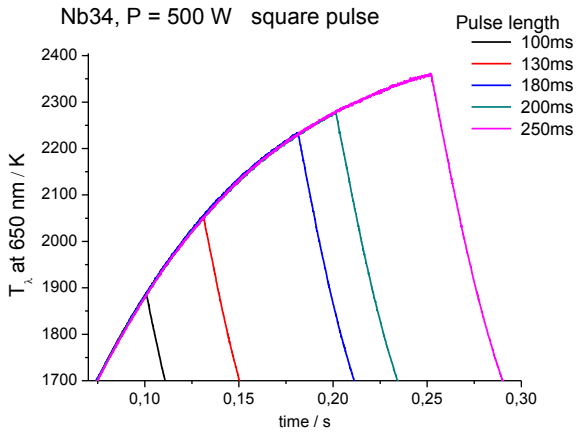

Fig. 3.7. Niobium specimen – repeatability, heating curve.

For this reason, at least two or three conditioning "shots" were performed before melting a specimen in order to improve the reproducibility of the thermograms in the solid state and make numerical modelling even possible (it will be discussed in section 3.2). In Fig. 3.7, it is evident how good the agreement of the "heating stage" was between seven different shots with the same power but different duration (square laser pulse). Then, Fig. 3.8 shows that the agreement of the melting plateaus was again very good.

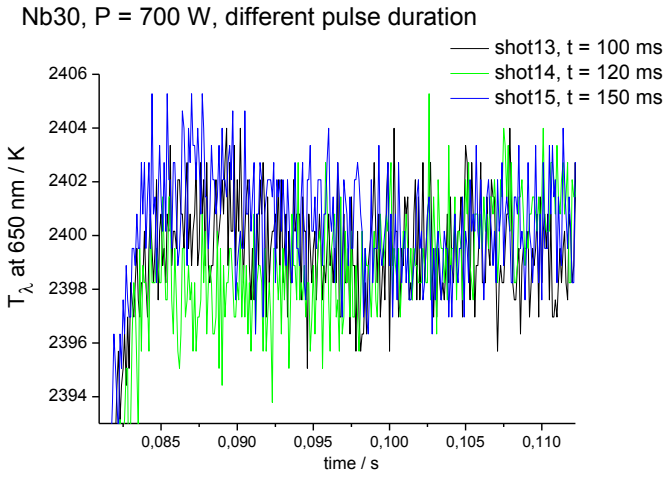

Fig. 3.8. Niobium specimen – repeatability, detail of melting plateau.

Particular features

Change in normal spectral emittance

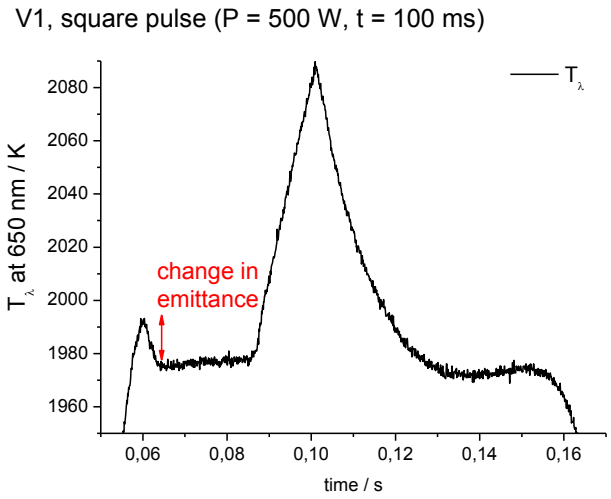

Fig. 3.9. Vanadium specimen – change in emittance.

A change in normal spectral emittance during melting was found several times, as shown in Fig. 3.9. In that particular case, an as – received specimen was melted already with the first shot. The melting plateau was preceded by a radiance temperature "spike" of 20 K.

As it is reported in Ref [4] this change in emittance can be linked with the degree of roughness of the surface and according to the author it is not related to a change in intrinsic properties of the specimen but a change of surface conditions.

In Refs [2], [5] and [6] it is reported that deliberately changing the roughness of the surface and the operational conditions (heating rate, experiment duration, etc) do not change the radiance temperature at the melting plateau (within ±1 K); this is the reason why Cezairliyan et al. in [2, 3] suggest the use of the radiance temperature of metals at the melting as SRPs. This feature can be seen in Fig. 3.10.

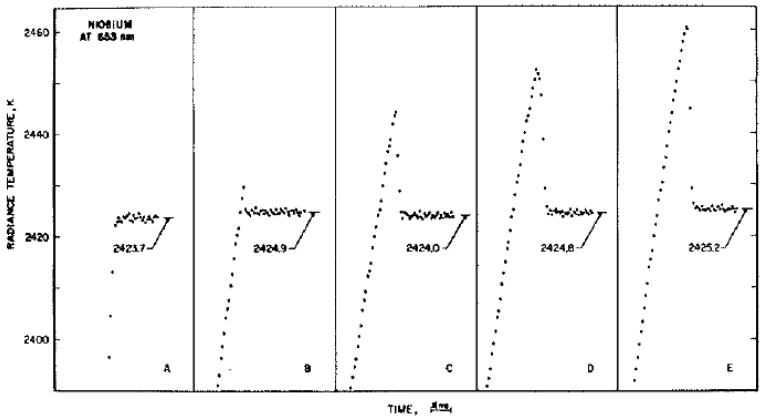

Fig. 3.10. Variation of radiance temperature (at λ = 653nm) of niobium for five typical experiments representing specimens with different surface roughness [2].

As it can be seen in Fig. 3.11 and in [7], this peak of radiance temperature is observed only in the first melting (Fig. 3.11a) of a specimen and this involves permanent changes in the surface texture. The second melting and the following ones show the behaviour of Fig. 3.11b.

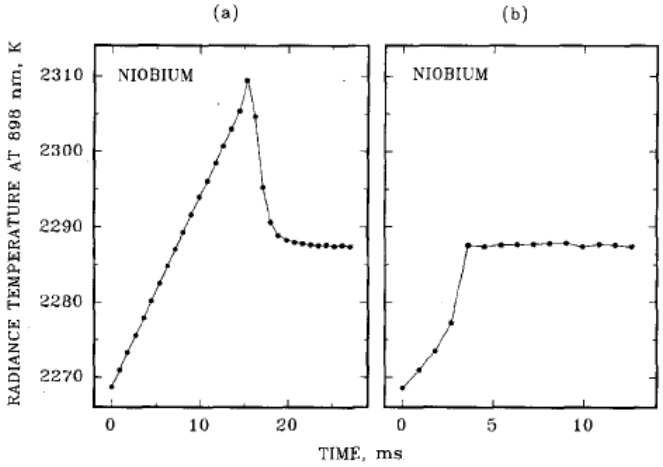

Fig. 3.11. Typical change in melting behaviour between a) the first melting and b) the second melting for a niobium specimen (at λ = 898 nm) [7].

Difference between melting and freezing radiance temperature

A mismatch between the melting temperature plateau and the freezing temperature plateau was observed systematically, as can be seen in Fig. 3.12 and Fig. 3.13. For the

metals investigated here the difference ranged from 1 K to 5 K expect for tungsten, for which it was around 10 K on average.

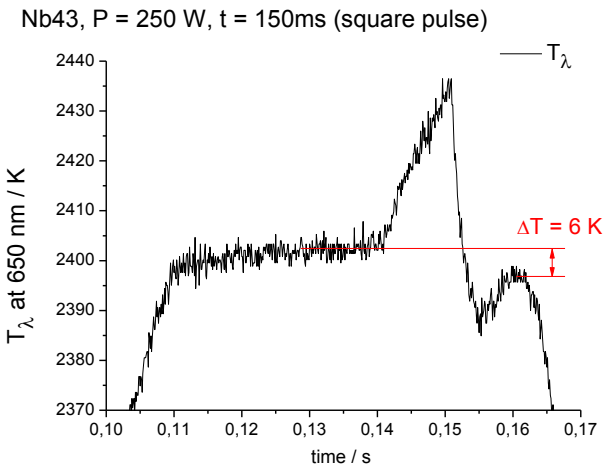

Fig. 3.12. Niobium specimen – difference in temperature between melting and freezing plateau.

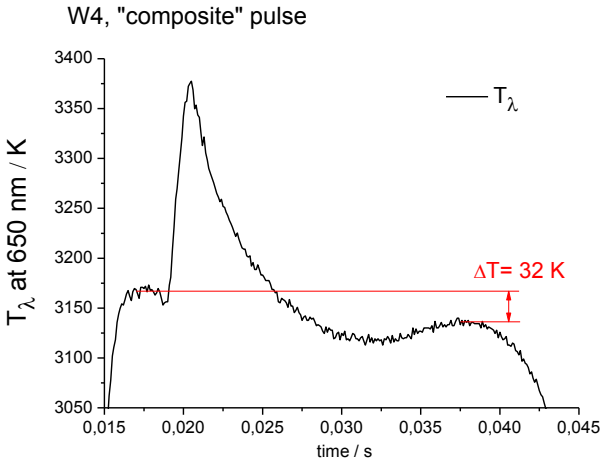

Fig. 3.13. Tungsten specimen – difference in temperature between melting and freezing plateau.

This effect can be due to the size of source effect (it will be discuss in section 3.1.6), as it is shown in Ref [8] where there is described an improvement of the melting and freezing curve after the correction.

Melting / freezing plateau not horizontal

It was noticed several times that the plateau during melting or freezing was not flat / horizontal. For the freezing plateau, this effect was found only in tungsten specimens, on the melting plateau it was found diffused on the other metals specimens instead. In Fig. 3.14 there is an example of a tantalum specimen and in Fig. 3.15 of a tungsten specimen.

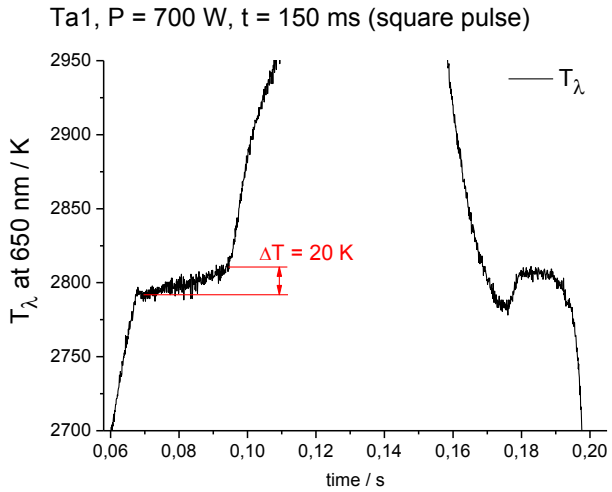

Fig. 3.14. Tantalum specimen – melting plateau not horizontal.

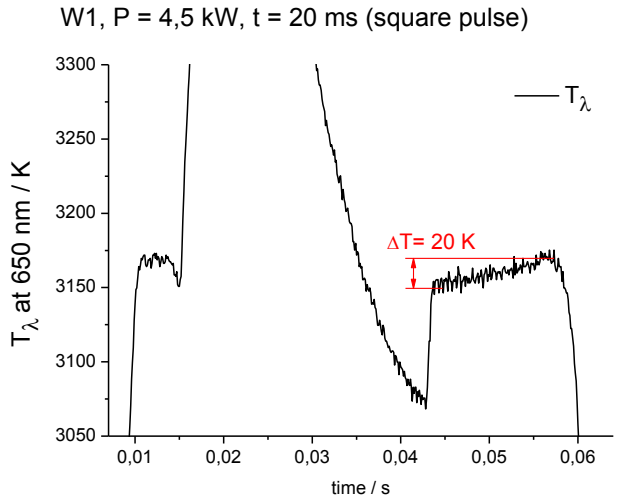

Fig. 3.15. Tungsten specimen – freezing plateau not horizontal.

In the melting plateau, this effect, in a first view, could result from non-isothermal melting, that means non equilibrium conditions on the surface, as it is shown in Ref [9].

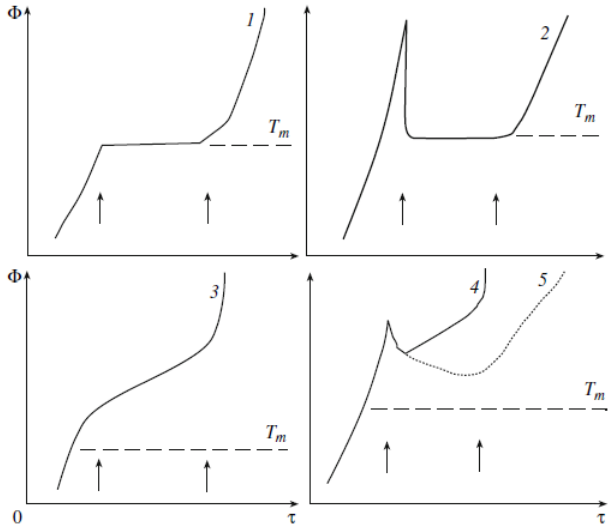

Fig. 3.16. Different melting behaviour: (1,2) equilibrium melting; (3,4) non equilibrium melting [9].

In Fig. 3.16 the difference is described between equilibrium and non-equilibrium melting. However, as it can be deduced from [9], this strange behaviour is observed only with very high heating rates (10^6 – 10^9 K/s) and furthermore it can be seen from the same figure that this effect can lead to an overheating (up to 30%) of the metal melting with respect to equilibrium melting temperature T_m.

However, in fast experiments at high temperature, it is quite impossible to obtain flat plateau of melting / freezing using a pyrometer that integrates the temperature on a finite area. Concerning the melting plateau, it is conceivable that some points in the pyrometer spot area are at the melting temperature and others are below and above this temperature and integrating can be resulted in a non horizontal plateau. On the other hand, for the freezing plateau, it can be that after the undercooling there are still few undercooled points in between of points at the freezing points or above, and so results in a non horizontal plateau. In this non horizontal plateau only the end of the plateau

could be the "real" radiance temperature of freezing but in this work the edge temperature was much below the reference one.

Furthermore, in Ref [7] it is written that after ten to fifteen melting plateaus on the same specimen, the surface quality becomes poorer and the melting plateau loses its flat shape. However, in this research it was never performed more than 10 melting experiments for each specimens and also a different methodology for heating up the materials was applied.

3.1.5 Results

Hereafter are shown the results of the radiance temperature of melting. For each metal the radiance temperature of melting and freezing measured are reported and compared with the reference.

The results for the radiance temperature are referred to the 650 nm mean effective wavelength (see Appendix B) of the two-channel pyrometer.

All the uncertainty bars, where not otherwise specified, are the expanded uncertainty calculated as described in Chapter 2.5.

Vanadium

A total of 35 experiments were performed, on 8 specimens numbered from V1 to V8. Twenty nine of them shown melting / freezing plateau and they were considered for the statistics reported below.

In Fig. 3.17, are shown the mean radiance temperatures of melting and freezing measured in this work.

The results are (1976 ± 28) K for the mean melting and (1975 ± 28) K for the mean freezing radiance temperature.

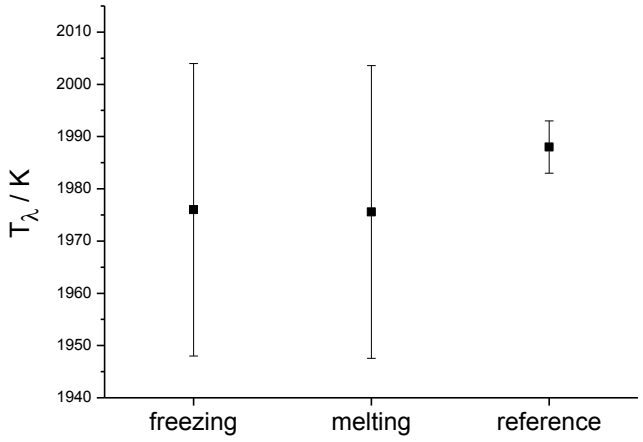

Fig. 3.17. Vanadium results – radiance temperature of melting / freezing.

Niobium

A total of 111 experiments were performed, on 18 specimens numbered from Nb29 to Nb44. Fifty one of them shown melting / freezing plateau and they were considered for the statistics reported below.

In Fig. 3.18 is shown the reproducibility of the measurements on the melting plateau during all the measurement campaign.

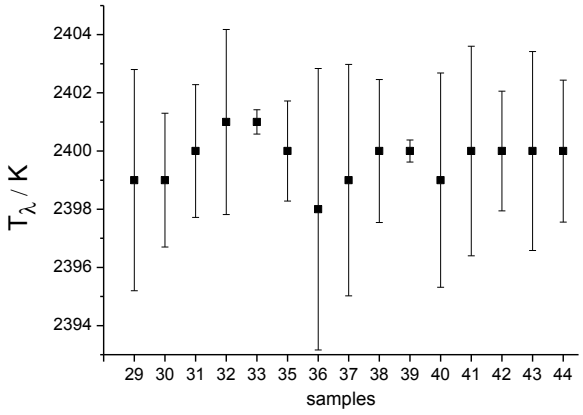

Fig. 3.18. Niobium statistics on melting plateau, overview of each specimens. The error bars indicate the standard deviation of the measurements on each specimen.

In Fig. 3.19, are shown the mean radiance temperatures of melting and freezing measured in this work.

The results are (2400 ± 41) K for the mean melting and (2398 ± 41) K for the mean freezing radiance temperature.

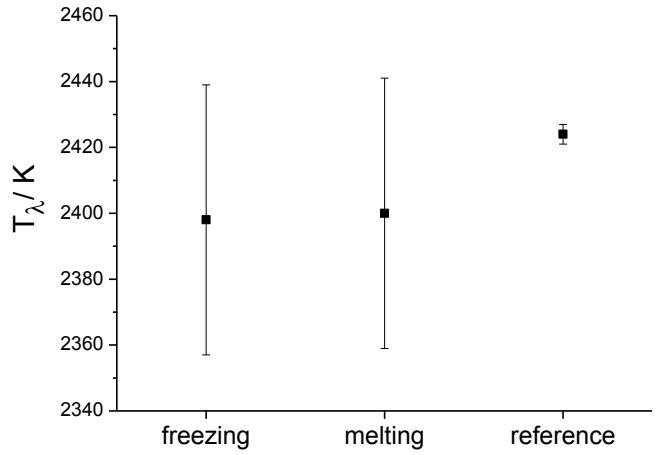

Fig. 3.19. Niobium results – radiance temperature of melting / freezing.

Molybdenum

A total of 30 experiments were performed, on 5 specimens numbered from Mo34 to Mo38. Twelve of them shown melting / freezing plateau and they were considered for the statistics reported below.

In Fig. 3.20, are shown the mean radiance temperatures of melting and freezing measured in this work.

The results are (2509 ± 45) K for the mean melting and (2504 ± 45) K for the mean freezing radiance temperature.

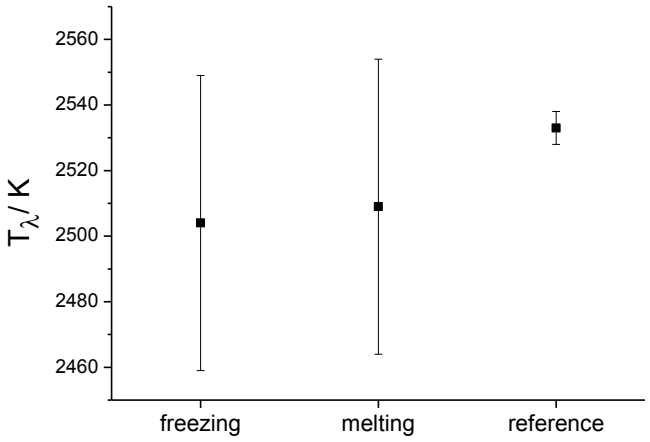

Fig. 3.20. Molybdenum results – radiance temperature of melting / freezing.

Tantalum

A total of 55 experiments were performed, on 5 specimens numbered from Ta1 to Ta5. Fifteen of them shown melting / freezing plateau and they were considered for the statistics reported below.

In Fig. 3.21, are shown the mean radiance temperatures of melting and freezing measured in this work.

The results are (2823 ± 53) K for the mean melting and (2825 ± 53) K for the mean freezing radiance temperature.

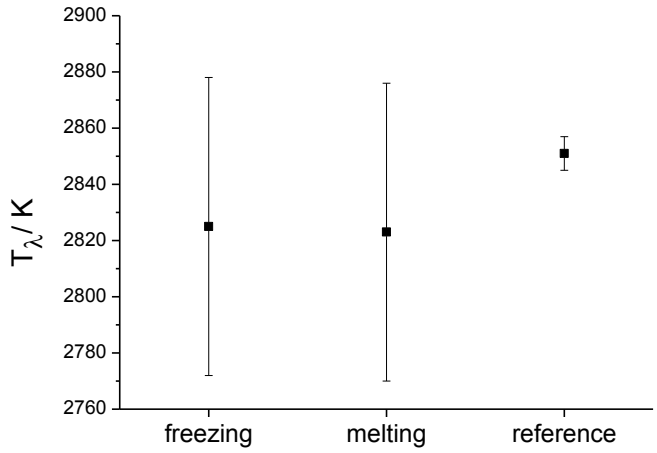

Fig. 3.21. Tantalum results – radiance temperature of melting / freezing.

Tungsten

A total of 36 experiments were performed, on 6 specimens numbered from W1 to W6. Thirteen of them shown melting / freezing plateau and they were considered for the statistics reported below.

In Fig. 3.22, are shown the mean radiance temperatures of melting and freezing measured in this work.

The results are (3169 ± 71) K for the mean melting and (3156 ± 71) K for the mean freezing radiance temperature.

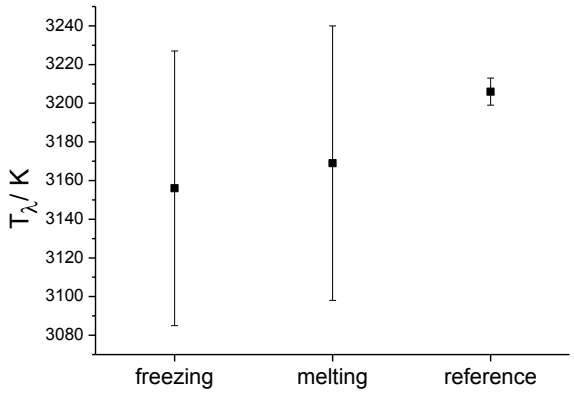

Fig. 3.22. Tungsten results – radiance temperature of melting / freezing.

Summary of the results

Table 3.8 shows an overview of the results for the radiance temperature of melting and freezing for all five refractory metals involved in this work.

It can be seen immediately that there is a mismatch between the measured radiance temperatures and the reference values.

Table 3.8. Summary of the results – radiance temperature of melting / freezing.

Metal	Specimens	Shots[i]	T_λ / K [ii] (m) (f)	T_λ / K SRP [iii]
V	8	35(29)	1976 ± 28 1975 ± 28	1988 ± 7
Nb	18	111(51)	2400 ± 41 2398 ± 41	2422 ± 5
Mo	5	30(12)	2509 ± 45 2504 ± 45	2530 ± 5
Ta	5	55(15)	2823 ± 53 2825 ± 53	2847 ± 6
W	6	36(13)	3169 ± 71 3156 ± 71	3207 ± 7

[i] The values in the brackets are the number of shots considered in the statistics.

[ii] Two standard deviation of uncertainty were used. (m) stand for the radiance temperature of the melting plateau and (f) for the radiance temperature of the freezing plateau.

[iii] Literature references in Chapter 1.

It is possible to analyze these discrepancies computing also the relative percentage deviation between the measured radiance temperatures and the references, as it is shown in Fig. 3.23.
As can be seen, this difference is around 0,6 % for vanadium, 1 % for niobium, molybdenum and tantalum and around 1,1 % – 1,2 % for tungsten.

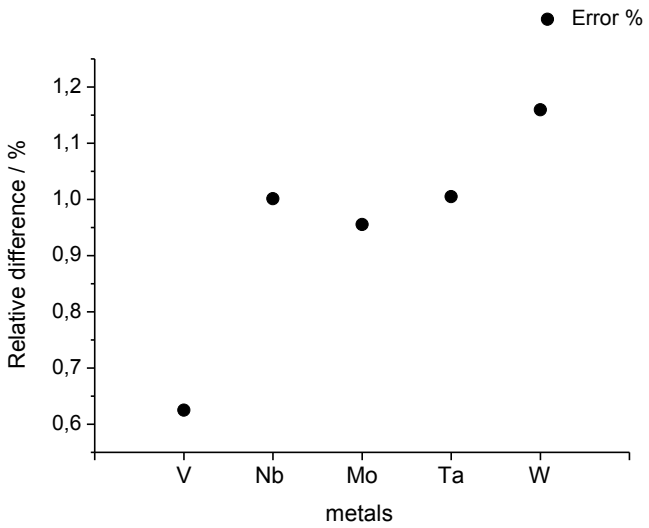

Fig. 3.23. Relative difference of current measurement results from the references values.

3.1.6 Discussion

As it can be deducted from the previous section, the results seem to indicate an error in the measurements performed. This depression of the radiance temperature can be due to several reasons, such as specimen impurities, a "pyrometry effect" linked with the behaviour of the materials (the so called size-of-source effect, discussed hereafter), deviations from the theoretical experimental parameters (the spatial laser profile, the spot size or the laser power) or a calibration / instrument error.
This error was already observed in 2010 on molybdenum and tungsten [10, 11] and a first "correcting study" was carried out by experimental and modelling way in ITU: this effort was on the characterisation and the correction of the size of source effect.
Hereafter the size-of-source effect will be described and discussed, then concerning the deviations from the theoretical experimental parameters in sections 3.2 and 3.3 will be

reported the efforts on the simulation of niobium and the measurements of the spatial laser profile. A fully discussion on the depression of the melting point due to impurities is reported elsewhere [12,13]. Concerning the possibility to have a calibration / instrument error is still on studying.

The size of source effect (SSE)

The temperature reading of a radiation pyrometer depends to some degree on the size of the source it is aiming at, so sources of equal temperature but different size may give rise to different apparent temperatures. This effect is due to diffracted light, inter – reflections between optical elements or surfaces of the same optical element, scattering of light at imperfections or dust, and optical aberrations. The result is that part of the radiance from the nominal target is lost and, conversely, part of the radiation originating from the surroundings is measured by the pyrometer. This effect is cancelled if the measurement conditions are identical to the calibration conditions or if the radiance temperatures of the target and surroundings are equal.

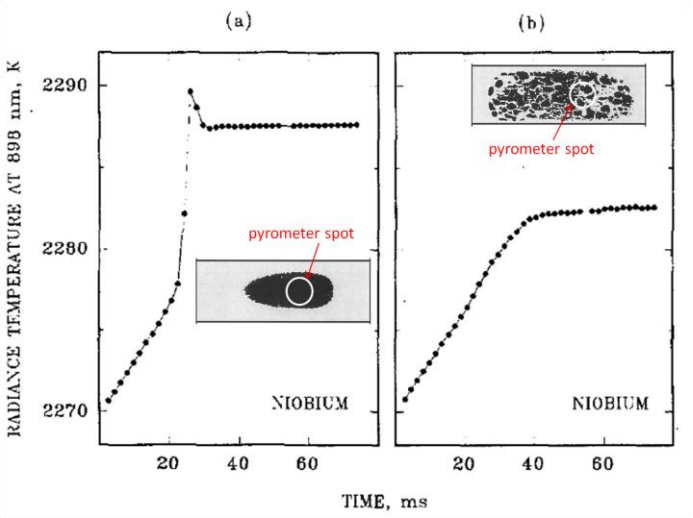

Fig. 3.24. SSE, depression of radiance temperature of melting due to non uniform sources, niobium specimens [7]. In the box it is shown the different molten area that the pyrometer spot sees.

The SSE can appear in two different situations: when there is a uniform source but it is smaller than the effective measurement spot or there is a source large enough but the uniform area is too small and surrounded by colder regions. An example of this latter situation is shown in the Fig. 3.24. In laser heating experiments large temperature gradients are generated. The area of uniform temperature is limited around the centre of the laser spot but its strongly depends on the nature of the material (oxides or metals) and on the thermophysical properties.

There are several techniques for measuring the SSE: the direct method, the scanning method and the indirect one, that are described elsewhere [14,15]. In 2010 at ITU a "modified" indirect method was implemented in – situ. It was taken molybdenum and tungsten thin specimens and a hole of different size was drilled through their centre. The specimens were heated above the melting point with the laser spot centred on and around the hole. The pyrometer was focused on the hole and the measurements were taken on the freezing plateau. As a reference, the signal at the freezing point was also measured on specimens without hole.

The difference was a measure of the contribution to the signal of radiation emitted from the central specimen area of the size of the hole and it can be directly linked with the SSE and so, at the end, with the possible impact on the measured temperature. Hereafter it is shown the possible impact in temperature ΔT as function of the "effective" measurement spot size of the pyrometer, in other words the area from which virtually 100% of the detected radiance originates [10, 11].

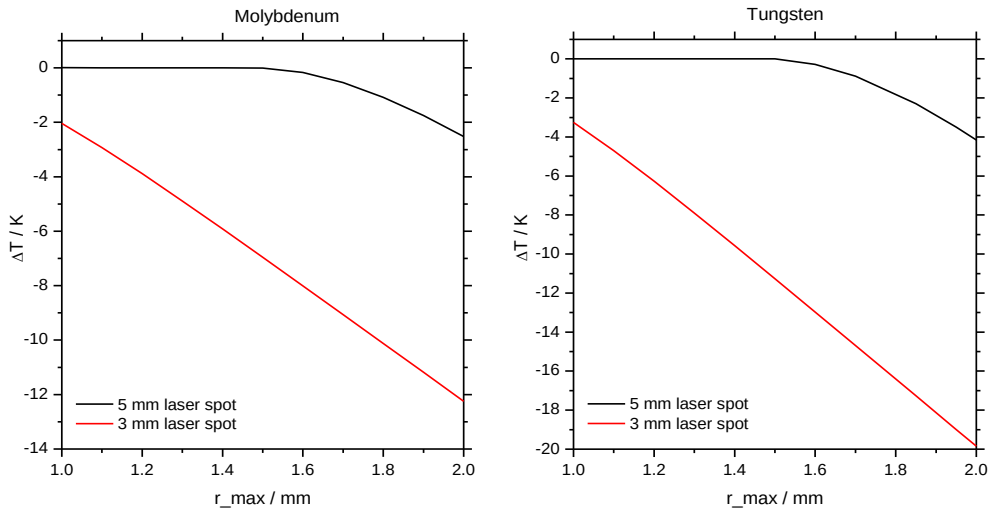

Fig. 3.25 Computed temperature measurement error due to the measured SSE at the freezing point of molybdenum (right graph) and tungsten (left graph) for two different laser spot sizes [10, 11].

The SSE effect can affect also the "shape" of the thermogram itself, for instance it was observed rounded edge in freezing plateau in contrast with a sudden transition between the emittance of the liquid and that of the solid material [10].

3.2 Modelling on niobium

Concerning the validation of the laser heating technique, another aspect is the numerical simulation of the experiment conducted by Dr. M. J. Welland (RMC Kingston, Canada, and ITU Karlsruhe), by means of the software COMSOL Multiphysics. The description of the theoretical model and the previous results attained by Dr. M. J. Welland are described elsewhere [16].

Following the previous work on oxides, a simulation on niobium was implemented and for this purpose a set of data was provided to validate the simulation.

This set of data included shots on niobium specimens with different thicknesses, using laser pulses of varying power and duration.

The theoretical model is a function of various thermophysical properties of the materials, for instance specific heat capacity, thermal conductivity, density, thermal expansion.

For this reason, before adding another degree of freedom (the change of phase) to model the melting behaviour, it is needed to "adjust" these parameters simulating an "easier" case with a heating and cooling the solid. To achieve this goal, several heating curves of niobium specimens were provided, such as Nb34 shown in Fig. 3.7 or Nb41 shown in Fig. 3.26.

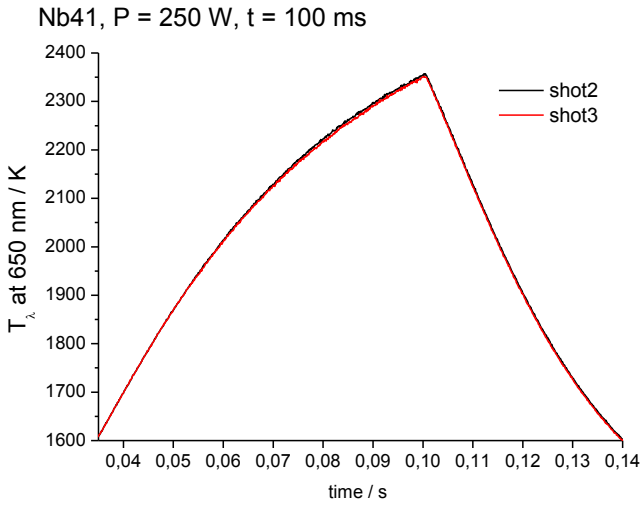

Fig. 3.26. Thermogram provided for simulations (1).

To reduce the degrees of freedom of the model and to check the quality of the thermophysical properties data (from the literature), it was supplied data on a steady state condition on Nb45, as is shown in Fig. 3.27 in the final part of the thermogram. In this particular condition, the heat capacity and the density of the material do not affect the simulation, whereas is mainly the heat losses that determine the steady – state temperature.

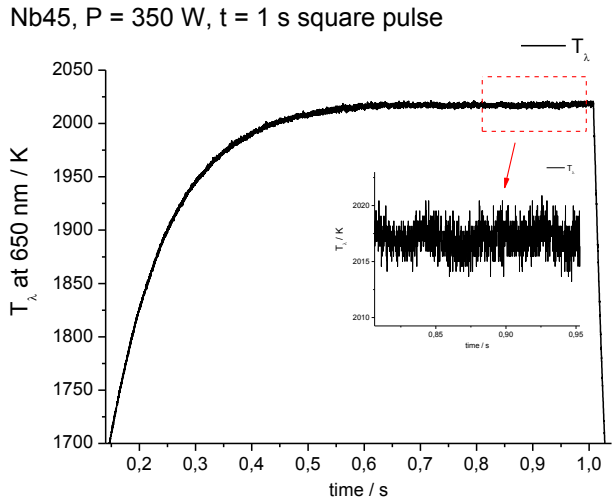

Fig. 3.27. Thermogram provided for simulations (2).

Finally, a set of "complete" thermogram was provided, with different power and time trying to simulate also the different behaviour of the freezing or melting plateau.

In Fig. 3.28 it is shown Nb30 and it can be notice how good is the repeatability (not only on the melting plateau, as discussed previously) on all the shape of the thermogram.

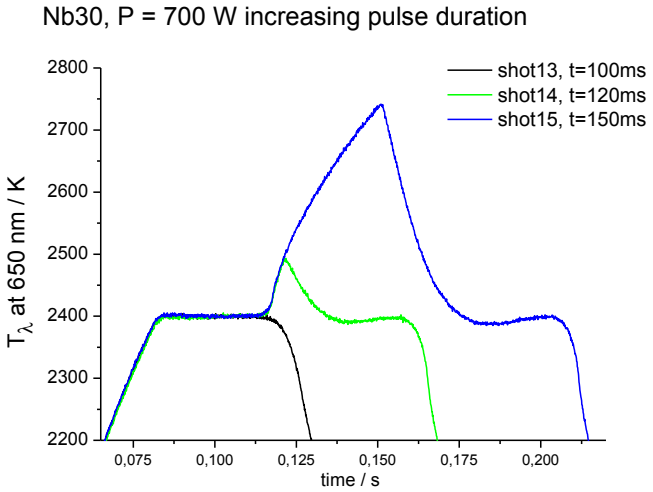

Fig. 3.28. Thermogram provided for simulations (3).

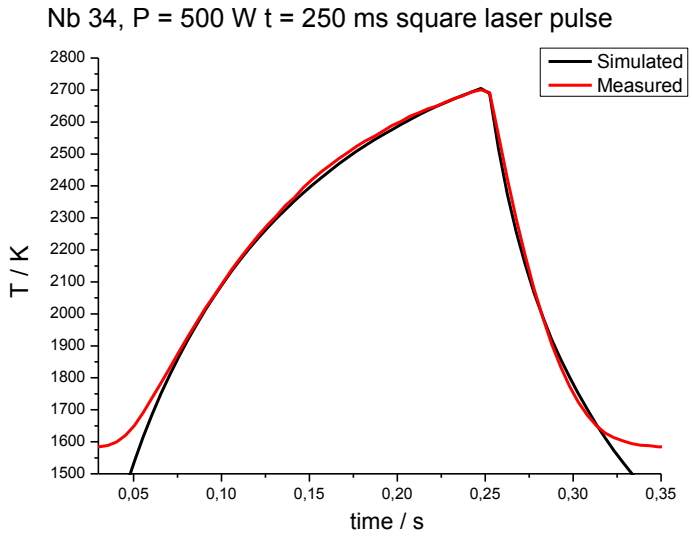

Fig. 3.29. Preliminary simulation results – niobium heating stage.

Concerning the results, in Fig. 3.29 it is possible to observe a preliminary simulated curve of Nb34 (black line) compare with the measured one (red line) and it can be stated that the agreement is very good. However, this curve was calculated by taking a normal spectral emittance constant and equal to 0,3 for the 650 nm wavelength of the pyrometer (between room temperature and melting point), imposing a laser power equal to 90 % of the nominal value used in the experiment and increasing the thickness of the specimen by 25 %.

Regarding the modelling of the melting / freezing curve, the work is still ongoing.

Therefore, there are several parameters to be investigated: first of all the "real" power setting during experiments and for this reason a calibration in energy and power of the laser was performed, but the data analysis is still ongoing.

3.3 Spatial laser beam profile

It was performed the measurement of the spatial laser beam profile with a USBeamPro Laser beam profiler [17]. The profiler records a 2D intensity map, integrating over time. This map may then be used to conduct a statistical analysis on the beam spot, or to produce either a pinhole or slit profile. The pinhole profile produces a plot of power vs. position for the horizontal and vertical axes of the beam. The coordinates of the centroid are determinable by the statistical analysis, as are the radii which encircle 50 %, 13.5 % ($\exp^{-2}$) and 5 % of the total beam power.

The position of best laser focus was determined by manually adjusting the distance of the profiler camera form the laser optics while seeking to minimize the calculated 5 % width. Distances were then measured moving the beam profiler away from the laser. Using the horizontal and vertical pinhole profiles and the centroid information, two half – profiles in the horizontal directions and two in the vertical directions were obtained for each position. These were averaged and fit using two straight line segments.

The radial profile, in Fig. 3.30 and Fig. 3.31, plots have in abscissa the fractional radius, r_f, defined as the ratio of the radius, r, with the nominal laser optic beam spot radius, R_{optic} (three possible laser optic can be used : 1.5 mm, 2.5 mm or 4 mm).

$$r_f = \frac{r}{R_{optic}} \tag{3.1}$$

The ordinate is the fractional power density multiplied by factor of R_{optic}^2. The plots are normalized so that the integrated power density is always equal to the total power, regardless of the chosen optic.

The choice of abscissa and ordinate as being independent of the optic, implies linear scaling of the profiles with different optics[1].

[1] The radial profile retains its shape between optics, only changing their magnitudes. This is an assumption and assumes the optics only vary by magnification and should be verified experimentally.

It was measured four different positions, the best focus and 4 cm, 5 cm , 6 cm distances far from the best focus. In Fig. 3.30 it is shown the result for the best focus and in Fig. 3.31 for the 5 cm distance.

As it can be noted, in both figures, the profiles are noisy and also not radially symmetric, observable from the 2D intensity maps. Even at best focus, the radial extent is larger than expected according to the optic.

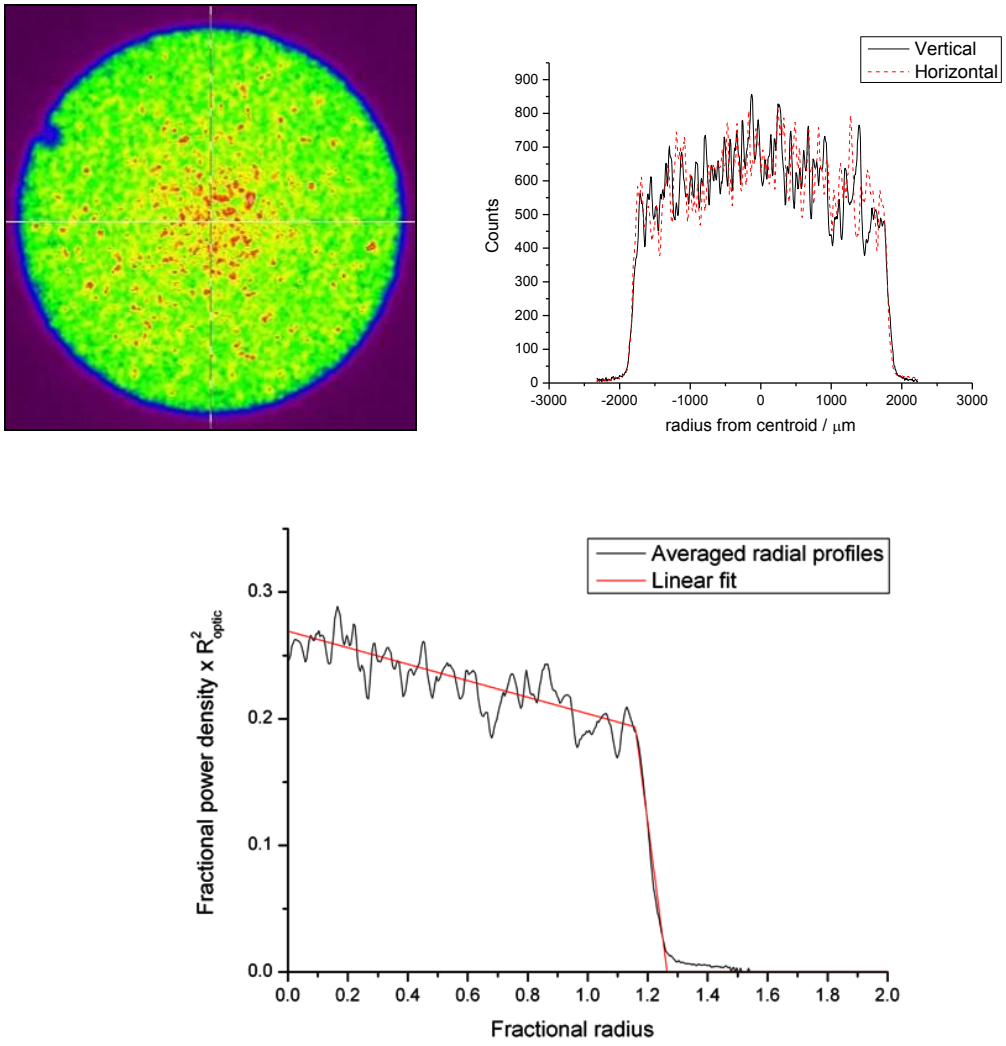

Fig. 3.30. Best focus: 2-D intensity map (top left), profiles (top right), (bottom) average radial profiles (assuming radial symmetry) and linear fits.

By changing the distance from the best focus the beam resulted defocused (Fig. 3.31), the profile was 'smeared' out, resulting in a larger radial extent, but the maximum power density in the centre of the beam increases with defocusing and the reason for this, is unclear as smearing would typically reduce this value.

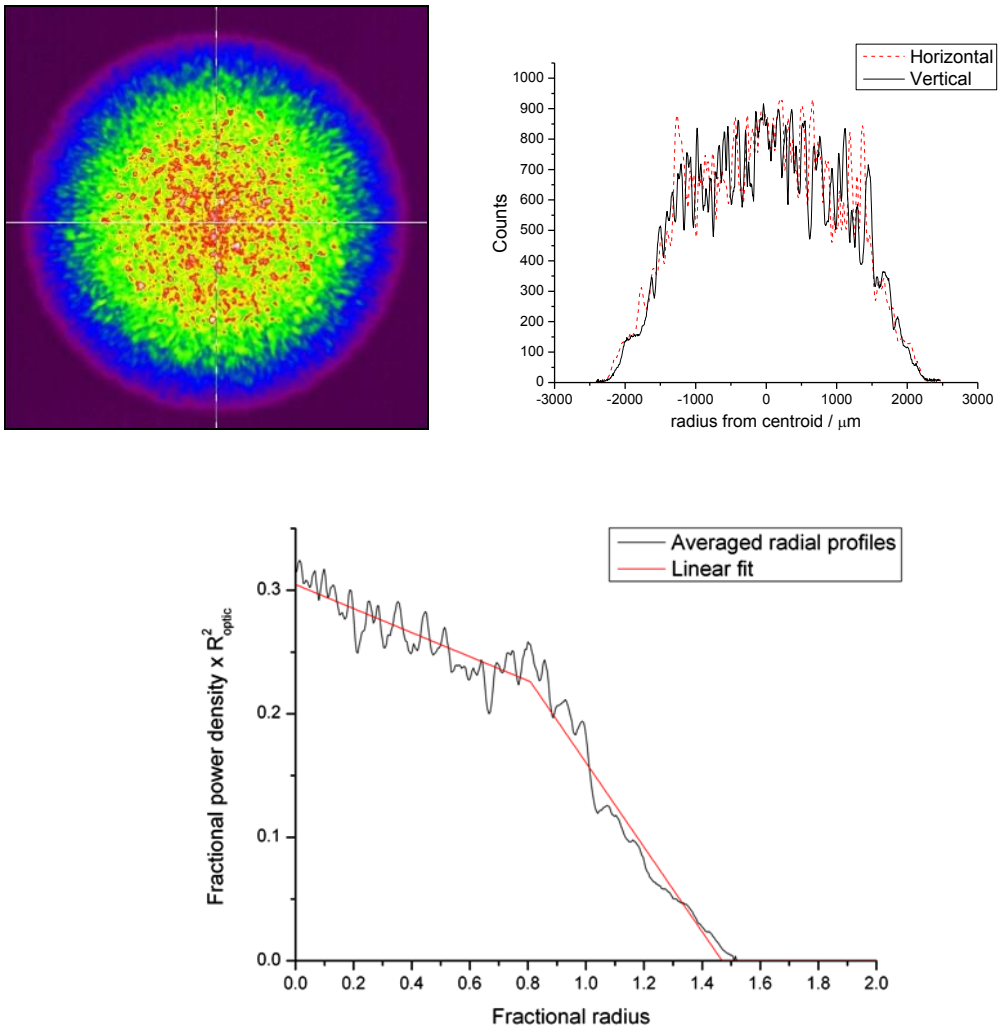

Fig. 3.31. Best focus at -5cm: 2-D intensity map (top left), profiles (top right), (bottom) average radial profiles (assuming radial symmetry) and linear fits.

Finally, another important information obtained by this work is described hereafter. In a typical experiment, the position of the specimen is setting up respect to the laser focus of the pilot laser (that is a visible red light). This corresponds to the 5 cm case shown in the Fig. 3.31 and it is clear that the spatial laser profile is very different from the hypothetical one thought (fractional power density constant and nominal radius equal to R_{optic}). In Fig. 3.32, it can be seen the power density and the spatial profile, corresponding to a 1000 W beam at 5 cm for the 3 mm, 5 mm and 8 mm laser optics.

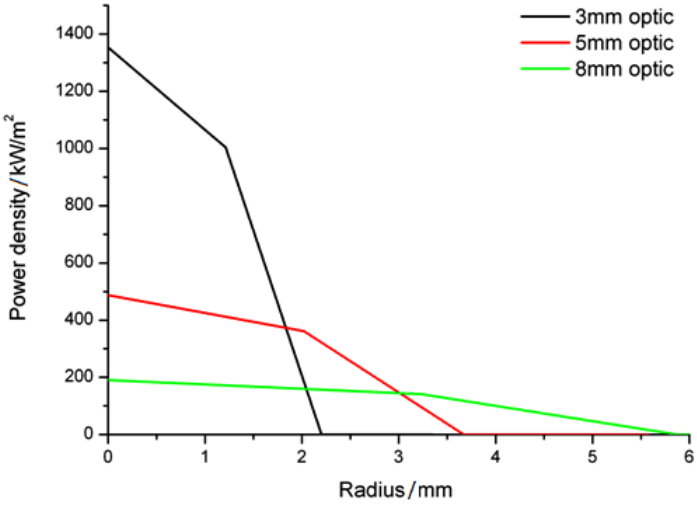

Fig. 3.32. Spatial laser profile and power density corresponding to a 1000 W at the 5 cm distance best focus.

3.4 References

[1] R. E. Bedford, G. Bonnier, H. Maas and F. Pavese, Metrologia, 33 (1996), 133.

[2] A. Cezairliyan, A. P. Miiller, F. Righini and A. Rosso, in Temperature: Its Measurement and Control in Science and Industry, 5 [1], J. F. Schooley, ed., (AIP, New York, 1982), 377.

[3] A. Cezairliyan, A. P. Miiller, F. Righini and A. Rosso, in Temperature: Its Measurement and Control in Science and Industry, 6 [1], J. F. Schooley, ed., (AIP, New York, 1992), 377.

[4] A. Cezairliyan, Surface Science, 40 (1973), 429.

[5] K. Boboridis, A. Seifter, A. W. Obst and D. Basak, Int. J. Thermophys., 28 [2] (2007), 683.

[6] K. Boboridis, A. Seifter, A. W. Obst and D. Basak, Int. J. Thermophys., 25 [2] (2004), 1187.

[7] F.Righini, G. C. Bussolino, A. Rosso and J. Spisiak, Int. J. Thermophys., 14 [3] (1993), 485.

[8] Y. S. Yoo, B.-H. Kim, C. W. Park and S.-N. Park, Metrologia, 47 (2010), 561.

[9] V.Ya. Chekhovskoi and V.D. Tarasov, Russian Metallurgy (Metally), 2009 [4] (2009), 297.

[10] F. De Bruycker, "High Temperature Phase Transitions in Nuclear Fuels of the Fourth Generation", PhD Thesis, Technical Note JRC-ITU-TN-2011/4 (2011).

[11] K. Boboridis, F. De Bruycker, D. Manara, R. Bohler, F. Chretien and M. Malki, "Impact of the size-of-source effect in laser pulse-heating experiments", presented at the 10th International Workshop on Subsecond Thermophysics, 21–24 September 2010, Graz, Austria.

[12] J. V. Widiatmo, AIST Bulletin of Metrology, 3[2] (2004), 317.

[13] W. P. White, J. Phys. Chem., 24 [5] (1920), 393.

[14] P. Saunders and H. Edgar, Metrologia, 46 (2006), 62.

[15] X. Hao, Z. Yuan, X. Lu and W. Zhao, Int. J. Thermophys., 32 (2011), 1655.

[16] M. J. Welland, W. T. Thompson, B. J. Lewis and D. Manara, J. Nucl. Mater., 385 (2009), 358.

[17] USBeamPro Model 2323 Laser Beam Profiler by Photon Inc., data sheet.

Chapter 4

Experimental results

This chapter presents the main results of the current study on the melting behaviour plus the pre- and post-melting characterisation of the refractory oxides introduced in Chapter 1. This experimental investigation was particularly difficult due to the extreme conditions produced during the experiments (in terms of temperature, vapour pressure, chemical reactivity, etc.). In addition, UO_2, ThO_2 and the mixed $(U,Th)O_2$ oxides had the additional problem related to the radioactivity of their components. For these reasons, the experimental data reported in this chapter are often affected by large uncertainty bands. On the other hand, they add precious information to databases on the behaviour of these materials under extreme conditions. Such databases are still today quite poor and approximate, if existing at all.

4.1 Calcium oxide

4.1.1 Preparation

The preparation started with commercial CaO powder. Since the powder was probably partly transformed to $CaCO_3$ due to contact with the atmospheric CO_2, it was necessary to perform a heat treatment before pressing the powders, to get rid of the CO_2. This was done at 1800 K, in an Ar atmosphere. Then the pellets were pressed, and sintered again at 1800 K in Ar for 8 hours.

4.1.2 Laser heating results

Fig. 4.1 shows the results of a melting point measurement on calcium oxide. The black line is the thermogram T = T(t)[1] recorded by the 650 nm channel of the two-channel pyrometer, whereas the red line is the power vs. time profile of the laser beam impinging on the specimen.

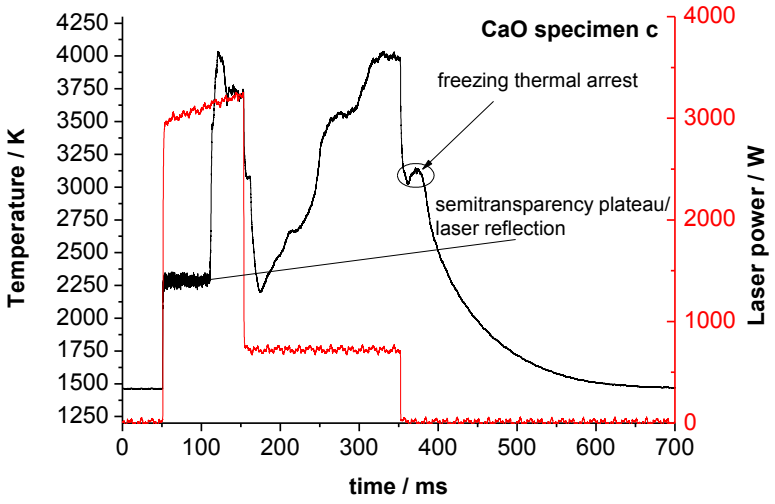

Fig. 4.1. Melting point measurement on calcium oxide in oxidising atmosphere (2 bar Air).

After the end of the laser pulse, the specimen surface cooled naturally, and a freezing thermal arrest was visible. At the beginning of the thermogram, one can observe the plateau due to semitransparent feature of calcium oxide and to the reflection of a fraction of the heating laser beam, as already discussed in Chapter 1.
The laser pulse shape plotted in red in Fig. 4.1 was conceived to overcome the semitransparency limit for this material, without leading to specimen destruction. For this reason, a ramp-like increasingly higher power (> 3 kW) was delivered to the specimen surface in the first part of the pulse, in order to compensate for the losses due to the specimen's non-opacity up to the optical transition temperature. In the second part of the pulse, when the specimen had finally become opaque, a much lower laser power was sufficient to heat the specimen well beyond its melting point. This behaviour was probably favoured also by the formation of transversal fractures

[1] All the thermograms of calcium oxide are referred to radiance temperature. Only the assessed melting / freezing temperatures are corrected for emittance.

in the specimen surface, resulting in a lower apparent thermal conductivity and therefore in a lower power needed to heat the specimen beyond its melting point. In fact, the unpredictable and uncontrollable formation of cracks on the surface is likely to play a major role in the entire heating process. In this case, the experiment was only partly successful, as the two-step laser pulse resulted in two successive thermal cycles in the specimens. On the other hand, the maximum temperature reached (in both cases around 4000 K) was moderate enough for the specimen to remain integer throughout the experiment. It was therefore possible to clearly identify the freezing thermal arrests on the cooling flanks of the thermogram. Because of the probably crack formation and the possible interaction between the laser beam fraction reflected into the pyrometer detector and the thermal radiation emitted by the specimen, features on the heating flanks of the thermogram were generally ignored for the present analysis.

Several experiments were repeated on different CaO specimens under different atmospheric conditions and with different laser pulse shapes. The vessel was filled with either compressed air or argon in order to operate under an oxidising or reducing atmosphere respectively.

When the specimen was heated under an oxidising atmosphere, the detected melting temperatures resulted comparable with those measured by Yamada et al. [1]. In this conditions, a stable composition close to stoichiometric CaO was most probably maintained throughout the heating cycle, and a congruent melting transition was observed.

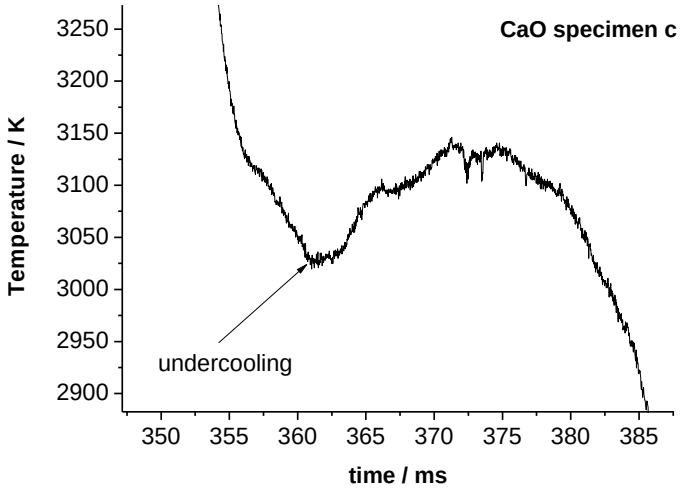

Fig. 4.2. Magnification of Fig. 4.1. Freezing thermal arrest after undercooling.

Since however only the second cooling stage took place while the laser was switched off, exclusively the corresponding freezing arrest has been included in the statistics, whereas the first plateau, although it was consistent with the other shot results, has not been used.

Fig. 4.2 shows a magnification of this second freezing thermal arrest.

Undercooling can be seen. This phenomenon has to be ascribed to the high cooling rate, which hinders the crystal nucleation in the liquid calcium oxide (cf. Appendix A). Since the solidification starts at the bottom of the molten pool formed on the specimen surface, where the liquid is in contact with a solid catalysing surface, only when the upper liquid is in contact with the growing solid edge the temperature starts to raise until freezing temperature is reached. In the meanwhile, the liquid mass in the vicinity of the external specimen surface gets under-cooled below its equilibrium freezing point.

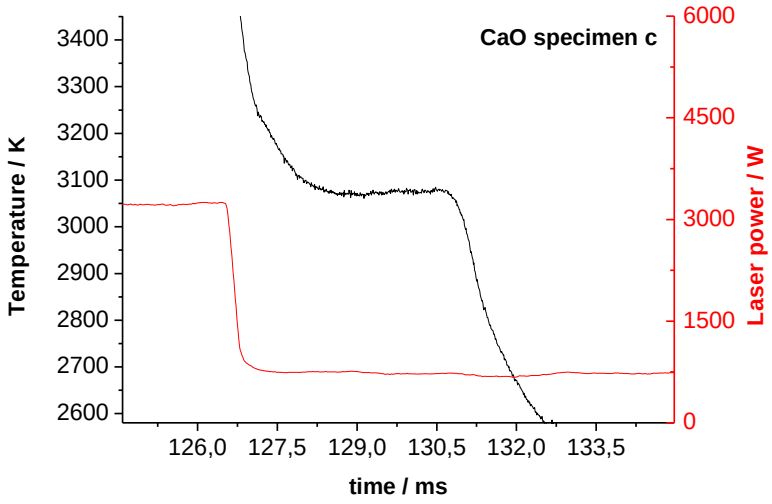

Fig. 4.3. Magnification of Fig. 4.1. First freezing thermal arrest.

It is interesting to note the different behaviour during the two thermal arrests. In Fig. 4.3, a magnification of the first one is shown. In this case, the laser was still on during the freezing plateau. This reduced the cooling rate enough to avoid undercooling phenomena. This condition resulted in a flatter thermal arrest.

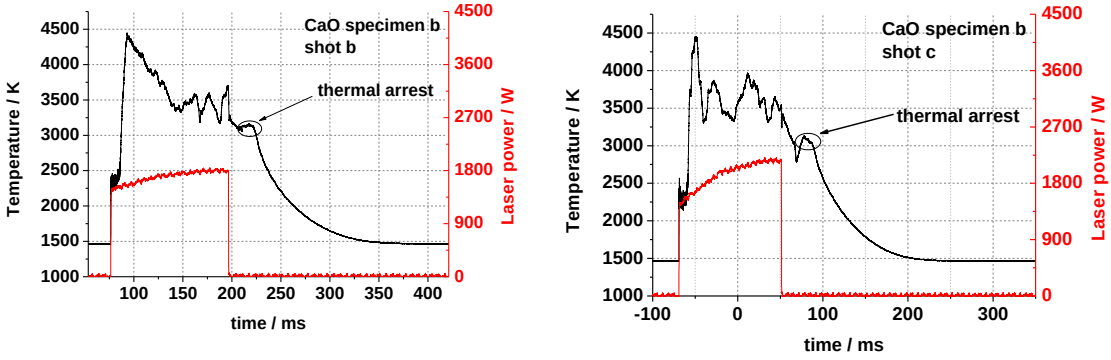

a) b)

Fig. 4.4. a) b). Different shots on specimen b in oxidising atmosphere (2 bar air).

Same atmospheric conditions but different laser shapes were produced on specimen b, as it can be seen in Fig. 4.4. Once more, solidification temperatures close to those reported by Yamada were obtained. Due to the different shape of the laser power compared to the shot on specimen c, no double heating/cooling stages were visible this time. The fact that with the laser power still increasing the detected temperature

seems to drop can be ascribed to the formation of a gas phase. This would imply further thermal losses and also screen both the heating laser beam and the thermal radiance emitted by the specimen. This latter effect, in particular, would largely disturb the pyrometer reading, which can explain the irregular shape of thermograms in Fig. 4.4a and Fig. 4.4b. Phenomena of this kind are often visible when a too high maximum temperature is reached during the experiment (exceeding 4300 K in both the examples of Fig. 4.4).

Lower melting / freezing temperatures were observed when experiments were carried out in a reducing atmosphere, as it can be seen in Fig. 4.5. Moreover, under these conditions the molten material became black (Fig. 4.6).

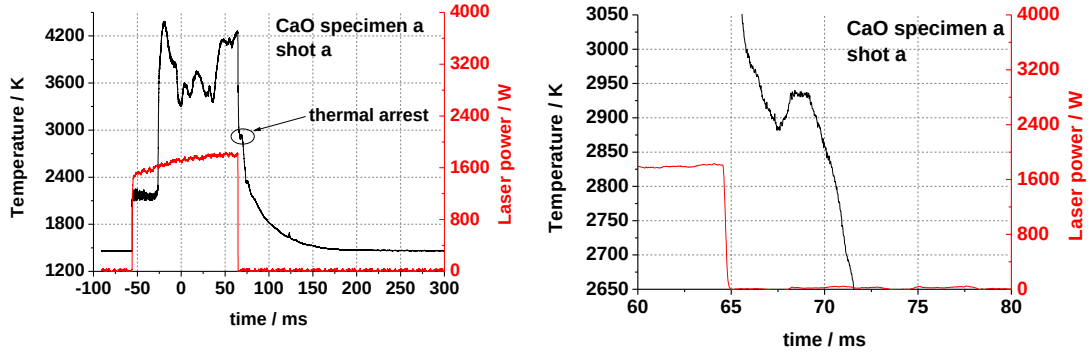

a) b)

Fig. 4.5. Shot in reducing atmosphere (2 bar Ar). a) Thermogram of the shot. b) Magnification of the freezing thermal arrest.

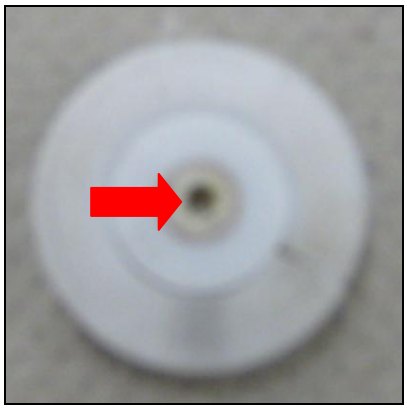

Fig. 4.6. Black molten area obtained after an experiment carried out under Ar.

This observation is most probably due to oxygen losses from the specimen at high temperature. The Ca-O phase diagram in Fig. 1.7 (Chapter 1) reports in fact a metastable liquidus line, which extends from the congruent melting point of CaO until the eutectic point at 1107 K. According to such a description, it could be possible that during the heating / cooling cycle, some oxygen left from the specimen following such metastable liquidus line. This would result in a lower apparent solidification temperature, and could also explain the change in colour observed in specimens melted under reducing conditions. If this interpretation was correct, the phase diagram recommended by Lindberg and Chartrand [2] and reproduced in Fig. 1.17 should be considered as representative of the Ca-O system under reducing conditions only. This would also be consistent with the CaO congruent melting temperature reported in that diagram, 2845 K. This value is not far from the average of the solidification points obtained in this work for CaO melted under argon (Fig. 4.7).

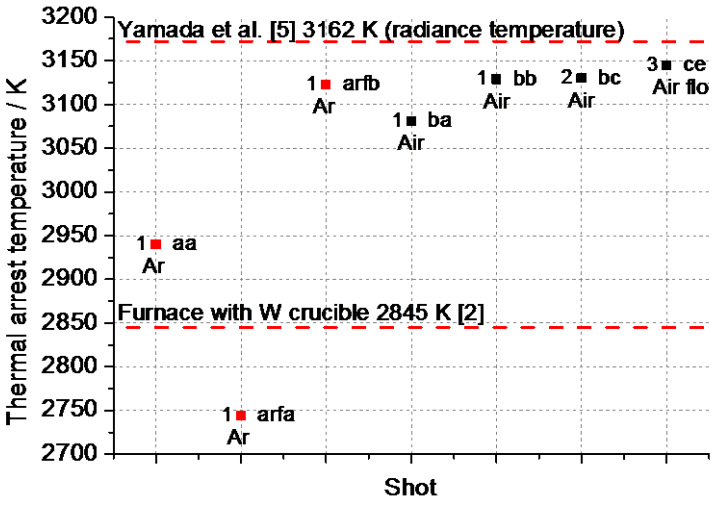

Fig. 4.7. Experimental results obtained in this work compared with literature data.

Fig. 4.7 shows an overview of the current experimental results. The average melting temperatures reported in literature are also displayed as horizontal dotted lines. It is clear how in the experiments carried out under oxidising conditions, the obtained melting/freezing temperatures are comparable with Yamada's [1] solidification

point. In Fig. 4.7 the numerical labels next to experimental points indicate the different laser pulse shape employed in the different tests. No systematic influence of the laser pulse shape can be seen in these results.

Considering only the experiments performed under oxidising conditions (i.e., under air), and a normal spectral emittance of 0,95 ± 0,03, the present value for the true melting temperature of stoichiometric CaO is (3126 ± 79) K. The large uncertainty band (two standard deviations) is due to the experimental difficulties already discussed.

Solidification points measured under reducing atmosphere (argon) were more dispersed, most probably because the system tended to lose oxygen in a complex way (cf. the metastable liquidus in Fig. 1.7), not well reproducible from experiment to experiment.

Some tests were also performed on CaO using the high pressure system described in Chapter 2. The goal of these tests was to check whether oxygen losses could be minimised by limiting the vaporisation kinetics thanks to the presence of a buffer gas at very high pressure. In this case, helium was used instead of argon as inert buffer gas. In fact, when the specimen-containing vessel is filled with heavy gases (such as argon) at high pressure, large convection effects occur during the laser heating, which hamper the temperature measurement and consequently a sound interpretation of the thermograms. In Fig. 4.8, a typical thermogram is shown. Remarkable here is the very long duration of the initial semitransparency plateau. This is probably due to the effect of the high pressure on the heat balance at the surface of the specimen. In the presence of a highly compressed gas, the heat losses from the surface to the buffer gas itself increase, and more and more energy is needed to heat up the specimen.

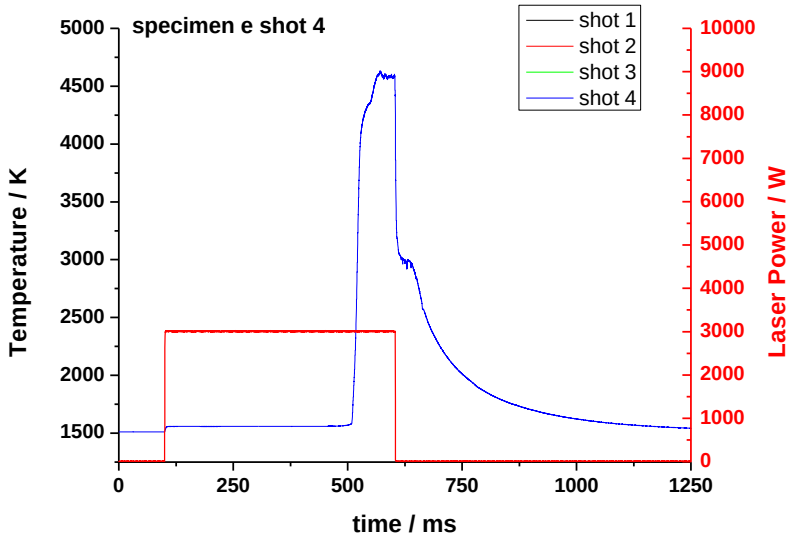

Fig. 4.8. High pressure thermogram.

The high pressure results (red circles) are shown in Fig. 4.9 together with the average true melting temperatures found in literature (blue dashed lines). The current results are scattered on a 300 K temperature range between the two values found in literature for the CaO solidification point under oxidising and reducing conditions. Apparently, the kinetic effect of the buffer gas could not be kept under full control in the present tests, so that no systematic trend could be reproduced by setting different pressures and different combinations of buffer gases (helium, helium + oxygen).

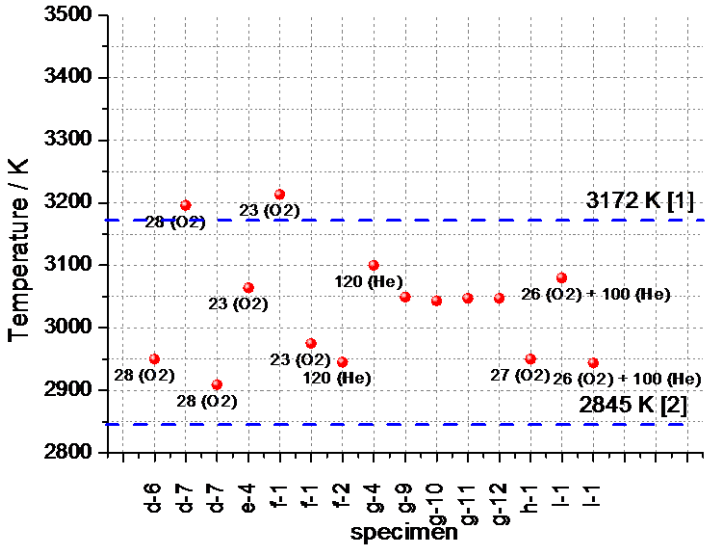

Fig. 4.9. High pressure results.

4.1.3 Normal Spectral Emittance

In this research, the normal spectral emittance (NSE) was obtained from the analysis of spectral radiance data measured with the multi-wavelength spectro-pyrometer described in Chapter 2. Because of the limited time resolution of the spectro-pyrometer (1 ms at best), temperature and emittance calculation are strongly affected by the high cooling/heating rates. The NSE analysis requires therefore a temperature as stable as possible and a high signal/noise ratio. Both "planckian fit" and “extrapolation to zero wavelength” approaches were used to exploit the multi-channel spectro-pyrometer data for calcium oxide. Results obtained with the former method are reported in Fig. 4.10.

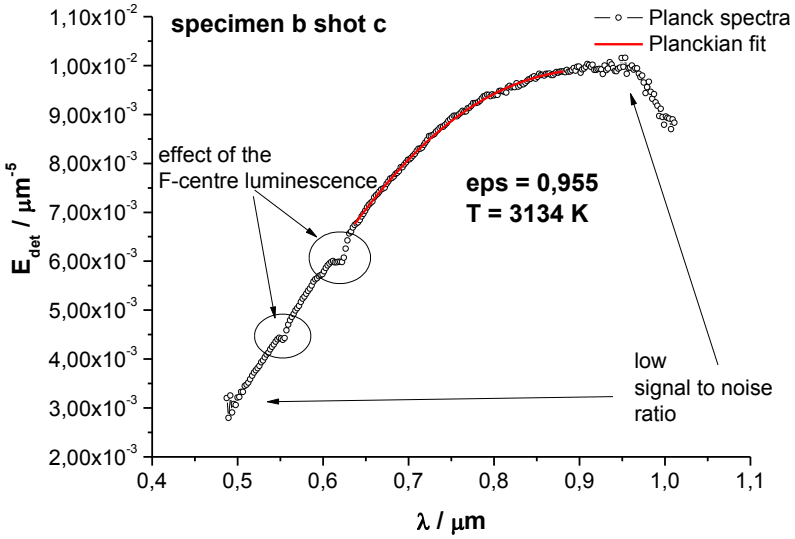

Fig. 4.10. Planckian fit of a radiance spectrum measured on solidifying CaO.

For the planckian fit only a small wavelength range was used, because of the low signal/noise ratio at the edges of the detected band and for the presence of peaks due to the F-centre luminescence of CaO [3]. Using the latter method, a comparable result, shown in Fig. 4.11, was obtained. The effect of the luminescence is even more visible with the "extrapolation to zero" method. The mean value for the NSE of calcium oxide near the freezing transition was 0,95 ± 0,03, in a good approximation independent of the wavelength.

Within this grey-body assumption, the radiance temperature obtained with the two-channel pyrometer can be corrected with the NSE in order to obtain the true freezing transition temperature.

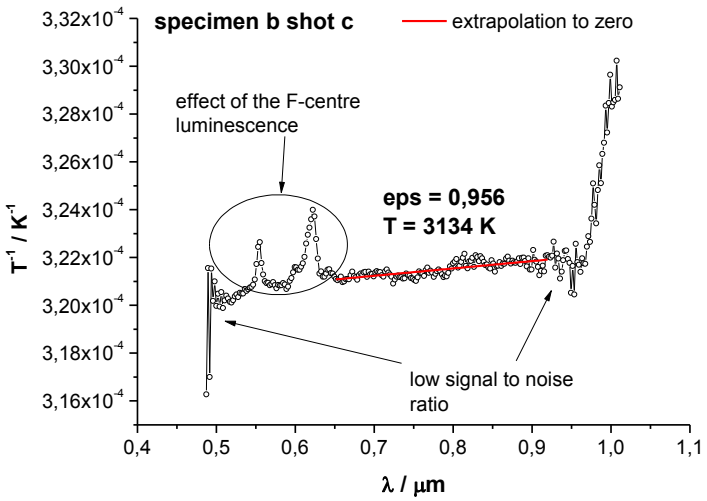

Fig. 4.11. Extrapolation to zero wavelength method.

Comparing the real temperature from the "extrapolation to zero" method (i.e., 3134 K as shown in Fig. 4.11) and the real temperature obtained by correcting the radiance temperature from the two-channel pyrometer, a slight mismatch arises, which corresponds to the accuracy limits of the two approaches and the uncertainty introduced by obtaining the NSE from a broad wavelength range. In fact (see Fig. 4.7), the radiance freezing temperature found during shot c on the specimen b was 3130 K. Correcting this value with the NSE yields a real freezing temperature of 3151 K. The appreciable discrepancy between the two values has then to be ascribed to the uncertainties related to the NSE determination procedure. The use of multiple-wavelength data to correct a single-wavelength radiance temperature introduces uncertainties related to the assumption of the validity of grey-body behaviour, the spectral background noise and goodness of the data fit.

4.1.4 Raman analysis

In order to identify possible changes in the crystalline structure of calcium oxide during the laser heating and the effects related to the different atmospheric conditions used during the experiments, a Raman analysis of the specimens has been provided. Firstly, a review of the data found in literature is shown in Table 4.1. A modest number of Raman studies on calcium oxide have been found in literature.

Table 4.1. Raman modes of CaO considered in this work.

Raman shift /cm^{-1}	Assignment	Reference	Comments
~ 533	TA+TO combination	[3]	Observed between 521 and 528 cm^{-1}
~ 655	TO overtones	[3]	Reference peak
~ 780	LO+TO combination	[3]	
~ 830	2LO(X)	[3]	
~ 945	2LO(L)	[3]	

A second-order Raman spectra was obtained by Rieder et al. [4]. Rieder performed measurements of the irreducible component of several alkaline-earth oxides with fcc structure. The authors used single crystals of CaO with very high purity (99,99 %) and polished mechanically. The measurements were performed under vacuum to avoid the contamination from the atmospheric air. The peak observed at 533 cm^{-1} was assigned to the combination of the optical and acoustic transversal bands. In the present work, a similar band was observed, but at lower wavenumber. The current Raman spectra of CaO powder and a sintered pellet are reported in Fig. 4.12. On the other hand, the fingerprint of the CaO Raman spectra is the peak at 655 cm^{-1}, which is identifiable in all the current specimens.

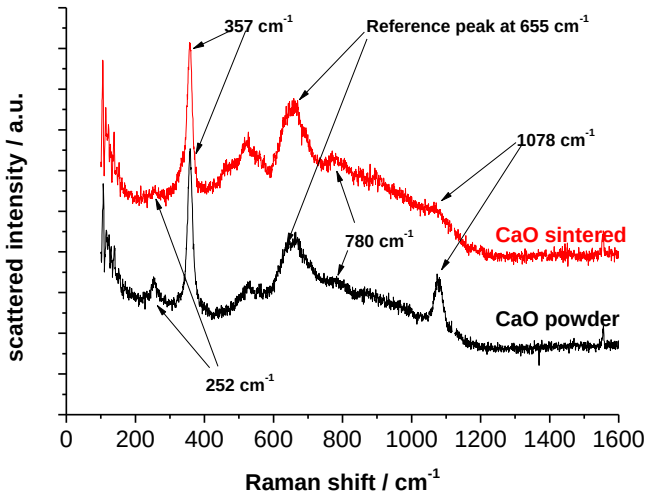

Fig. 4.12. Raman spectra of powdered and sintered CaO.

The weak peak at 780 cm^{-1} is probably related to the combination of optical transversal and longitudinal bands. In the high wavenumber region of the spectra,

the scattering with the longitudinal optical bands is predominant. The bands at 830 cm^{-1} and 945 cm^{-1} due to the optical bands in the L and X points in the Brillouin zone, respectively, are not present in the present results.

Several peaks, which are not ascribable to literature data, are visible in all the obtained spectra. The reference peak at 655 cm^{-1} is well visible. The strong peak at 357 cm^{-1} is attributed to traces of $Ca(OH)_2$. Fig. 4.13 displays a comparison of the Raman spectra of CaO and the spectrum of $Ca(OH)_2$ (blue line), all measured in this research. Calcium hydroxide forms when calcium oxide, in contact with water (or simply with the atmospheric humidity), undergoes the chemical reaction $CaO(s) + H_2O(l) \rightarrow Ca(OH)_2(s)$. Some other peaks can be related to the presence of calcium hydroxide. The low wave-number zone presents a weak peak at ~252 cm^{-1} whilst in the high energetic region a mode well visible at ~1078 cm^{-1}.

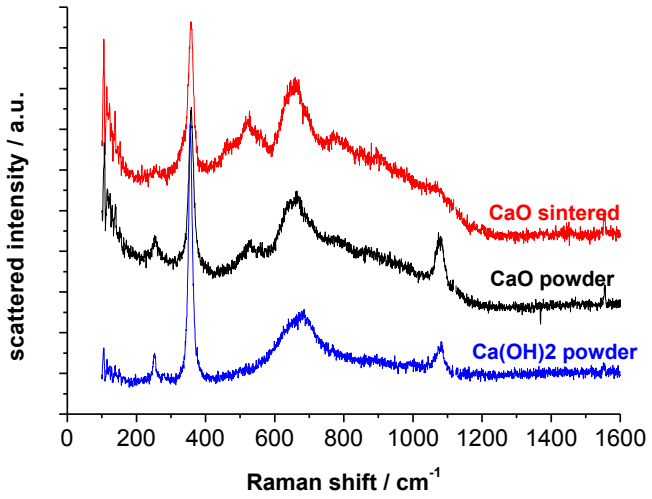

Fig. 4.13. Raman spectra of $Ca(OH)_2$ compared with CaO.

In the sintered CaO spectra (red line), these peaks are weaker than in the powdered CaO (black line), probably because the strongest influence of the fluorescence which partially overlap the bands. Comparing it with the Raman spectra of calcium oxide, a good correspondence of the 252 and 1078 cm^{-1} peaks can be noticed, confirming that the previous assumption on the effect of calcium hydroxide is reasonable. Another narrow peak was observed at about 3620 cm^{-1} (not shown in Fig. 4.13) as a further confirmation of the presence of hydroxide impurities on the

specimen surface. This last peak is recommended as a fingerprint of the most intense stretching vibrational mode (νOH) of the hydroxide group [5]. These hydroxide impurities had no effect on the current melting experiments, as $Ca(OH)_2$ is well known to decompose in CaO and water at around 700 K [6].

Pre and post-melting Raman measurement were performed, in order to detect possible changes in the spectra. In Fig. 4.14 a comparison between melted and a "fresh" specimen is shown.

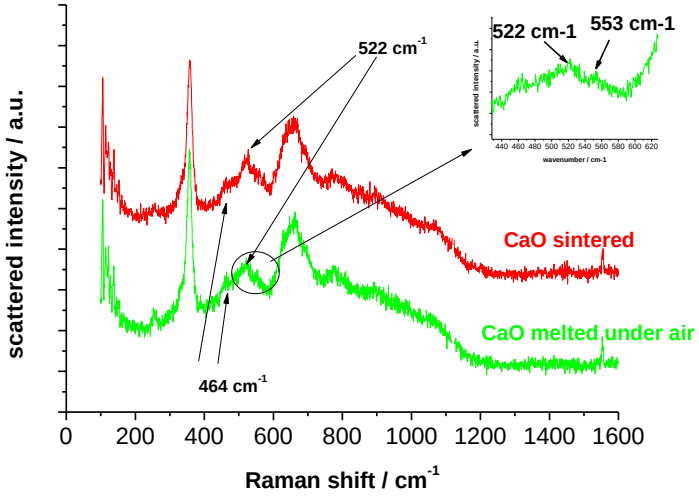

Fig. 4.14. Pre and post- melting Raman spectra of CaO.

The after-melting spectrum does not show visible changes with respect to the "fresh" pellet. The weak peak at 553 cm^{-1} is more visible after melting but it is still overlapped by the broader and more intense peak at 522 cm^{-1}.

4.1.5 XRD analysis

XRD analysis on the molten / refrozen material was only possible by scratching the laser heated surface away from the bulk. This constituted a delicate operation, and it was hardly possible to separate the melted material from the unmolten one. Therefore, XRD measurements were performed on a specimen inevitably containing a mixture of the two, although the melted /refrozen part was largely in excess.

The resulting diffractogram (Fig. 4.15) clearly shows the presence of an additional unknown phase together with the majority of CaO, as visible in. This phase probably corresponds to the black material observed in CaO molten and refrozen under reducing condition. It could alternatively be attributed to the formation of new $Ca(OH)_2$ on the specimen surface in partial contact with air during its transfer to the XRD facility. However, further research is needed for a full characterization of this phase.

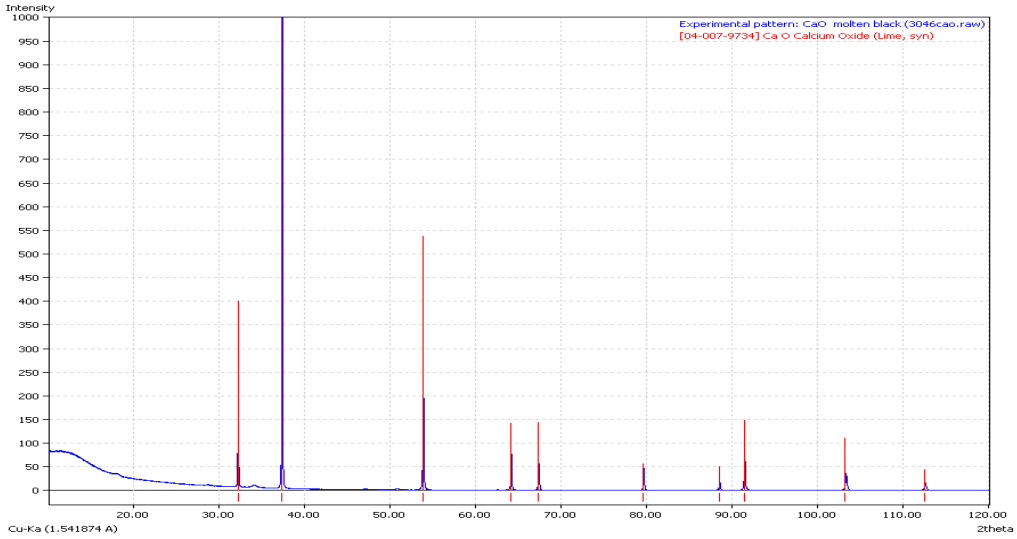

Fig. 4.15. XRD analysis on the black molten area of CaO.

4.1.6 Conclusions

Several experiments on the melting temperature of calcium oxide were carried out at different pressures and under different atmospheric conditions. The assessed value under oxidising atmosphere is (3126 ± 79) K. The average solidification temperature under a reducing atmosphere was 2963 K, but further experiments should be performed, in order to better understand the after-melting colour change. The high pressure device gave results consistent with the literature, but from the remarkable dispersion of the results can be deduced that reproducible surface conditions are hardly reachable during these experiments. Finally, no appreciable changes in the specimen structure or composition could be observed with the pre- and post-melting specimen characterisation carried out in this research. Further investigation is needed especially to better define the origin of the second phase

detected through XRD analysis on the black molten area obtained with reducing conditions.

4.2 Cerium dioxide

4.2.1 Preparation

Commercial CeO_2 powders were pressed into pellets and sintered under air for 6 h at 1800 K.

4.2.2 Laser heating results

A typical thermogram measured on CeO_2 in this work is shown in Fig. 4.16a. A clear semitransparency effect is well visible in the first part of the experiment, resulting in a 12ms-plateau and delaying the rise in temperature.

During the laser pulse, the temperature rose until a maximum value of 3200 K. When the laser was switched off, the temperature rapidly decreased producing a clear freezing thermal arrest.

The vessel was filled with argon or air in order to reproduce reducing or oxidising conditions respectively. During the experiments also different laser pulse shapes were used, so as to detect possible systematic effects on the temperature results.

The experiment reported in Fig. 4.16a was performed using compressed air at 2 bar as buffer gas. The freezing melting temperature in this experiment is comparable with the results found in literature [7] with an atmosphere of air, as it is clearer from the magnification in Fig. 4.16b.

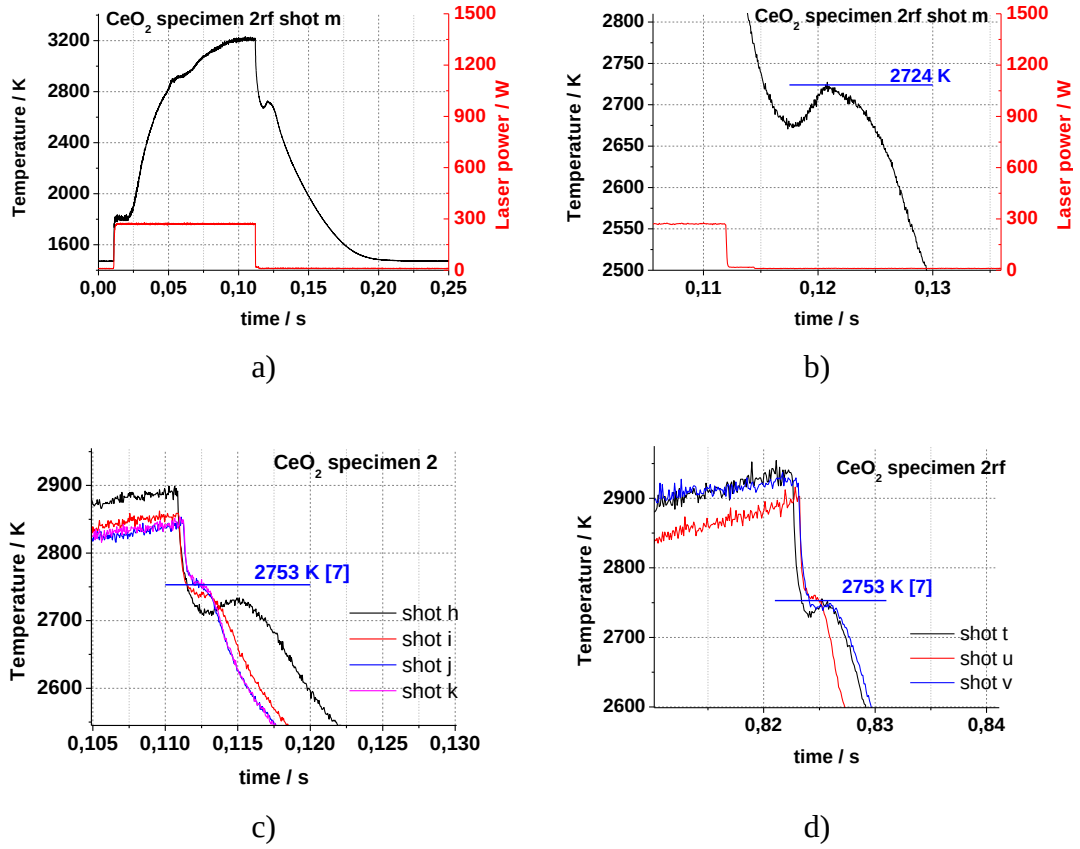

Fig. 4.16. Melting temperature experiments under oxidising conditions. a) Thermogram obtained during an experiments on specimen 2rf. b) Magnification of the freezing thermal arrest seen in a). c) Sequence of experiments carried out under air on specimen 2. d) Sequence of experiments performed under air on specimen 2rf.

In Fig. 4.16b, undercooling can also be seen. The resulting molten area on the specimen was black, as in all the shots where the melting temperature was overcome. This behaviour can be ascribed to oxygen losses possibly leading to some changes in the crystalline structure of the specimen. Some other experiments were carried out under oxidising atmosphere (Fig. 4.16c), leading to results in accordance with Foex's [7]. In Fig. 4.16c, four consecutive shots on specimen 2 are shown, all performed under air. The same sequence of shots with the same atmosphere inside the vessel was performed on the rear face of specimen 2, as sketched in Fig. 4.16d. All these results are rather close to the literature data. From Fig. 4.16c and Fig. 4.16d can also be noted the presence of undercooling only in the first and higher-maximum-temperature shot in both the sequences, that is during shot j and shot t, respectively.

When argon instead of air was used as buffer gas, lower freezing temperatures were systematically observed (Fig. 4.17). The solidification arrests visible in Fig. 4.17, for example, occur at a temperature reasonably comparable to the result reported in Mordovin's work [8].

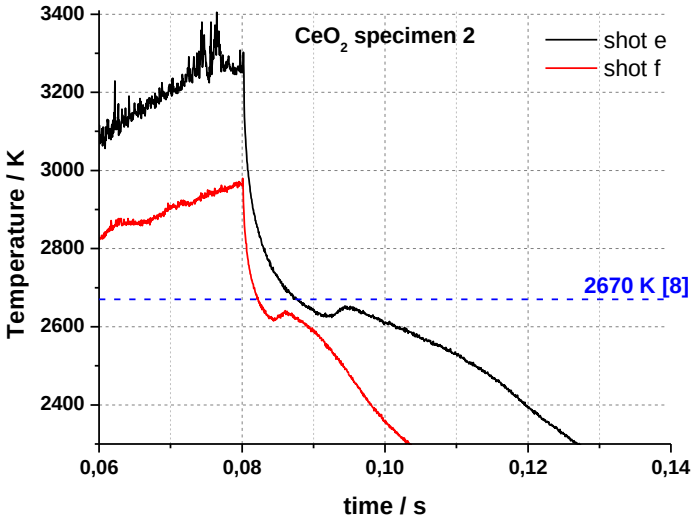

Fig. 4.17. Freezing thermal arrest during experiments carried out under Ar-atmosphere.

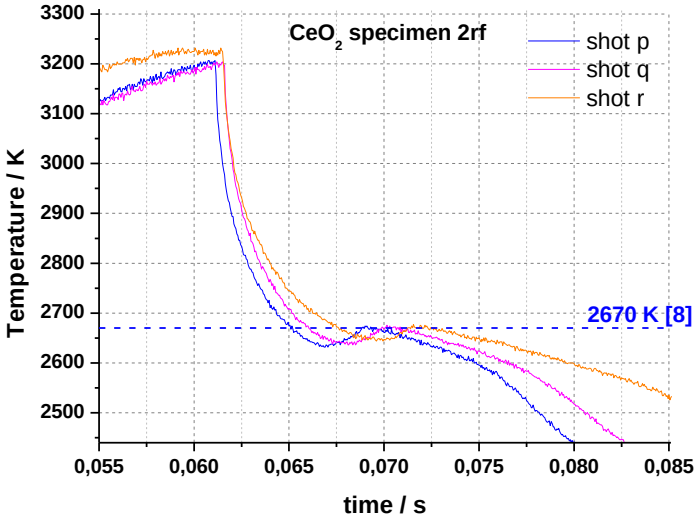

Fig. 4.18. Experimental results obtained under Ar-atmosphere.

It is also interesting to remark that undercooling was present in each shot performed under reducing atmosphere, regardless of the maximum temperature or the position

in the sequence. The sequence of shots showed in Fig. 4.18 was obtained using a fixed laser pulse. While the freezing thermal arrests are fairly reproducible, the cooling regions after the freezing show different behaviours. Going from shot p to shot r, the cooling rate decreases and gradually a further inflection visible after the freezing arrest in the earlier shots tends to disappear. This is probably due to changes in the specimen surface morphology after consecutive shots. This second and less clear inflection in the cooling stage is only visible when the melting experiments were carried out under reducing atmosphere, as it can be seen in Fig. 4.19, where two representative thermograms performed under air and Ar atmosphere, respectively, are compared.

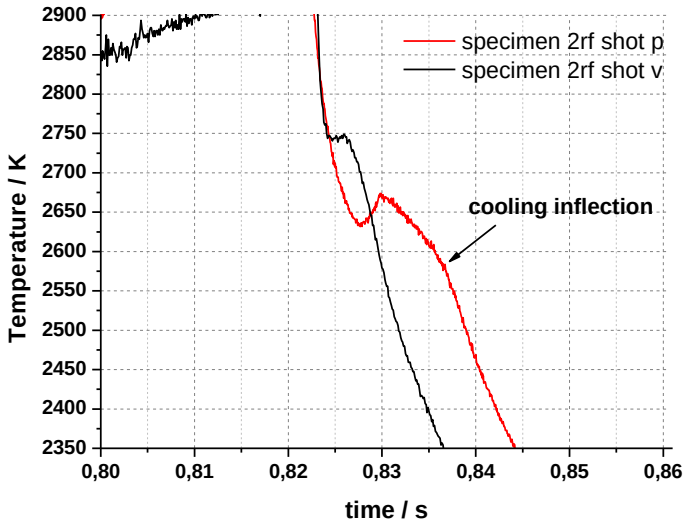

Fig. 4.19. Comparison of the cooling stages of thermograms obtained under air and Ar.

The thermogram obtained under reducing conditions (red line) shows a change in the slope at about 2570 K. This phenomenon, which cannot be detected in the black thermogram (recorded under air), can be explained with a non-congruent melting process occurring in the experiments carried out under reducing atmosphere. Since cerium dioxide has a marked tendency to reduction, the use of argon as buffer gas may have promoted the departure of oxygen from the specimen. During the experiments, a shifting of the pre-melting-composition to the hypostoichiometric region may have occurred, leading to a double inflection in the thermogram (see

also the Ce-O phase diagram in Figure 1.10 in Chapter 1). When air was used instead of argon, this second inflection was not detectable anymore, conducing to think that a melting/freezing process much closer to congruent occurred.

All the melting / freezing temperature results obtained in this work are summarised in Fig. 4.20, where they are also compared with the literature values.

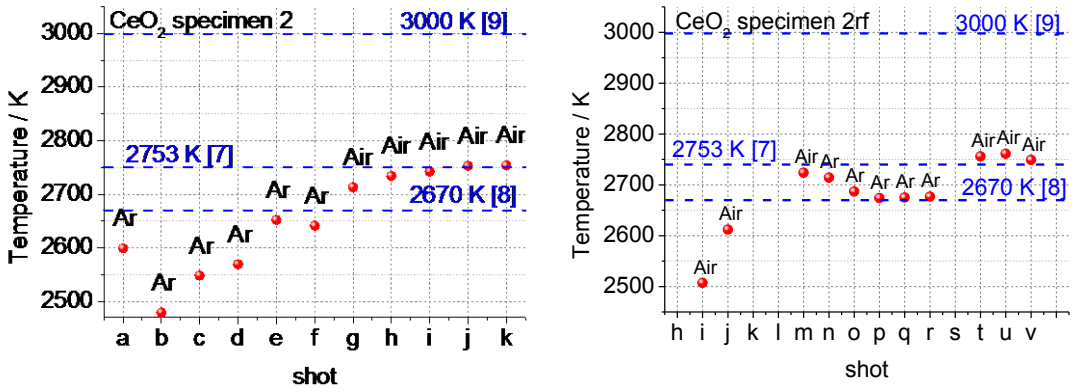

a) b)

Fig. 4.20. a) Experimental result on specimen 2. b) Experimental result on specimen 2rf

A rather consistent trend for the current CeO_2 data can be observed. When a sequence of shots performed under reducing conditions were set, the temperature tended gradually to reach the value found in Mordovin's work under reducing conditions [8]. When oxidising instead of reducing conditions were used, the transition temperature tended to the value reported in Foex's work [7].

In sequence of shots performed on specimen 2rf shown in Fig. 4.20b, the same trends were reproduced even when alternating the reducing / oxidising atmospheres in successive sets of three to five shots. It can be appreciated that in some cases two – three shots were needed to stabilise the observed solidification temperature. This confirms even further the systematic effect of the vessel atmosphere, with which the specimen reacts over successive shots until equilibrium conditions are fully reached. Using a value of 0,90 for the emittance of ceria, the melting temperatures suggested in this work are (2675 ± 47) K and (2743 ± 33) K for the experiments carried out under Ar and air, respectively.

4.2.3 High pressure melting characterisation

In order to try to reach the highest melting temperature reported in literature for cerium dioxide (close to 3000 K under a high, but not specified, oxygen pressure [9]), the high-pressure device was also used. A typical thermogram recorded during a high-pressure laser heating experiment is reported in Fig. 4.21.

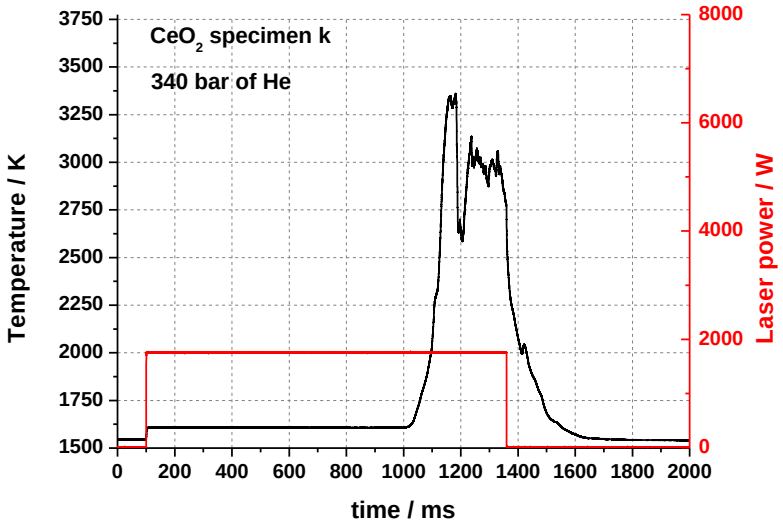

Fig. 4.21. Experimental result led with the high pressure device.

It is immediately noticeable the length of the plateau at the beginning of the thermogram. While during "normal" pressure experiments the typical length of the initial plateau was less than 20 ms, in this case the duration is about 900 ms, almost 40 times longer. This strong effect of the high pressure inside the vessel can be explained by a large increase of the convective heat exchange between the specimen and the surrounding gas, making more difficult the rise in temperature of the specimen surface. However, if the pressure displays a clear effect on the length of the initial plateau, a systematic connection between them has not been found yet. In fact, the surface behaviour under these extreme temperature and pressure conditions was hardly controllable. For the same reason, the melting/freezing temperatures measured under high pressure do not show a specific and well defined trend as the low pressure results do. In Fig. 4.22, a summary of the experimental results under high pressure are shown.

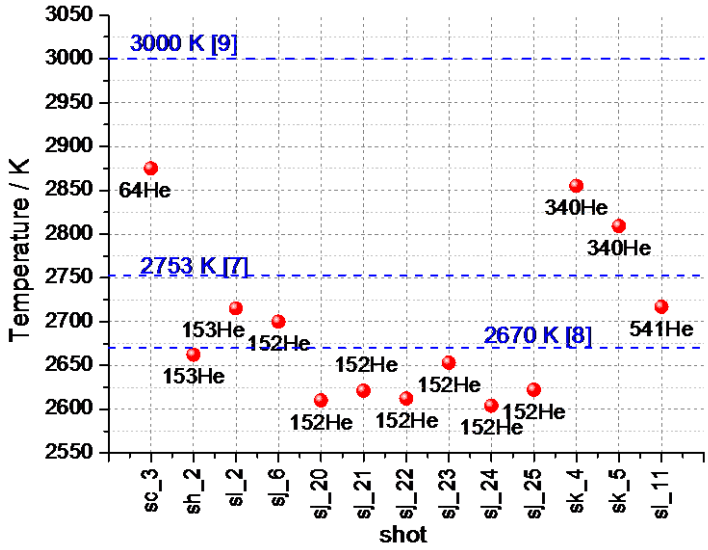

Fig. 4.22. High pressure results on cerium dioxide. The melting temperature results are labelled with the pressure used during the experiments and the buffer gas.

Even if in some experiments higher melting temperature results were obtained, a reproducible trend cannot be detected. The majority of the high pressure results on CeO_2 have comparable or even lower values with respect to the low pressure ones. For these reasons, a statistical analysis of the results obtained with the high pressure device is not feasible with the present results.

4.2.4 Raman analysis

Cerium dioxide, as thorium dioxide, crystallises in the fluorite-structure lattice (space group O_h^5).

A second-order Raman scattering analysis of CeO_2 was reported in Weber, Hass and McBride's work [10].

The frequencies (wavenumbers) reported in their work are 272, 465 and 595 cm^{-1}, which correspond to the double degenerative TO mode, the triply degenerate Raman-active mode, and the non-degenerate LO mode, respectively. In the present work, these features can be detected at rather different Raman shifts. As reported in Table 4.2, the first peak was observed at 287 cm^{-1}, whilst the reference peak at 462 cm^{-1} is in good agreement with the literature. Some further confirmation of the

latter value can be found in Kourouklis, Jayaraman and Espinosa's work [11] and in Keramidas and White's study [12].

The third frequency band was observed at 585 cm^{-1}, just between the values reported in [11] and [12]. Since a consistent number of other peaks were seen during the present work, only the most intense are reported. Between 1000 and 1250 cm^{-1}, a remarkable number of very intense and narrow peaks can be seen. Since from literature no data are available for the 1200-1700 cm^{-1}, only a list of the peaks observed in that region is reported in Table 4.2, their assignment being beyond the goal of this thesis.

Table 4.2. Summary of the data found in literature for CeO_2. "/" symbol stands for non reported or not reported but detected in the present work.

Raman shift / cm^{-1}	Assignment	Reference	Comments
~ 198	/	/	The peak at 254 cm^{-1} correspond to feature at 264 cm^{-1} in [10]. These three peaks form a typical fluorite-structure feature.
~ 235	/	/	
~ 254	$2TA(L) - L_3^{'} \times L_3^{'}$	[10]	
~ 287	*TO(X)*	[10] [12]	
~ 417	/	/	Typical fluorite-structure feature. The last is the reference peak. 465 cm^{-1} in literature
~ 434	/	/	
~ 462	Raman active mode.	[10] [11]	
~ 476	$TO_R(X)$	[10]	
~ 582	/	[11]	
~ 653	/	[11]	The peak found in literature is at 660 cm^{-1}.
~ 675	$2LO_R(X) - X_3^{'} \times X_3^{'}$		
~ 779	/	/	
~ 873		[11]	
~ 945	$2TO_R(X) - X_5^{'} \times X_5^{'}$	[10]	
~ 1102	/	/	
~ 1133	/	/	
~ 1166	*2LO*	[10] [11]	In [10] it is reported at 1180 cm^{-1} whilst in [11] at 1160 cm^{-1}.
~ 1196	/	/	All these peaks are not reported in literature. All the research found in literature reports peaks with a maximum Raman shift of 1180 cm^{-1}.
~ 1310	/	/	
~ 1428	/	/	
~ 1467	/	/	
~ 1541	/	/	
~ 1553	/	/	
~ 1605	/	/	
~ 1615	/	/	
~ 1649	/	/	
~ 1690	/	/	

The Raman spectrum of melted CeO_2 was also measured in order to detect possible changes in the crystalline structure. The comparison between "fresh" and molten ceria spectra is shown in Fig. 4.23.

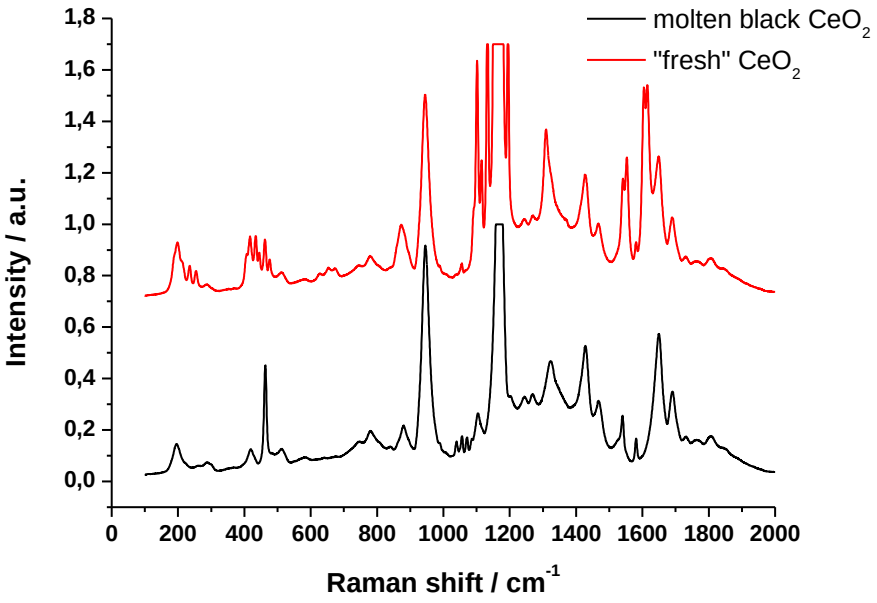

Fig. 4.23. Raman spectra of "fresh" and molten CeO_2.

In the spectrum of the melted specimen, some differences can be detected in the low-wavenumbers region, typical of the peculiar fluorite-structure sequences. While the width of the sequences is unchanged, the number of peaks decreases and the relative intensity of the reference peak increases. The value of the T_{2g} peak slightly shifts at higher wavenumber, that is 464 cm^{-1}, whereas its intensity increases. In the vicinity of 1200 cm^{-1}, the two intense peaks which surround the narrow peak at 1166 cm^{-1} disappear in the melted material spectrum. The same happens in the high-wavenumber region, where the peaks at 1541, 1605 and 1615 cm^{-1} are not visible in the spectrum of melted/refrozen ceria. All these differences between the two spectra shown in Fig. 4.23 confirm that, after the specimen was melted, some changes in the crystalline structure took place. Since the general structure of the spectrum does not change, it can also be assumed that only a little shift toward the hypostoichiometric region of the phase diagram occurred. This confirms that in the vicinity of stoichiometric ceria a number of commensurate superstructures of the fluorite-type lattice exists [13], produced by the increase of the oxygen deficiencies in the specimen.

4.2.5 Conclusions

In the present work, several melting temperature experiments on ceria were performed. The current results are rather in agreement with the literature. Similarly as for CaO, reducing and oxidising atmospheres were set for the melting experiments in order to detect possible changes in the behaviour of CeO_2. It was actually observed that the results do strongly depend on the atmospheric conditions. Accordingly, two distinct values are assessed in this work for the solidification temperature of cerium dioxide. Using a reducing atmosphere, a value of (2675 ± 47) K is recommended, whilst in presence of oxidising conditions a value of (2743 ± 33) K is suggested. The high pressure results confirm the complexity of the system when high-temperature and high-pressure experiments are performed. Therefore, the expected behaviour of ceria at high pressure has not been completely reproduced, probably because even higher oxygen pressures would be needed, forbidden in the current set-up for safety reasons. Through the use of Raman analysis, the formation of a black zone on the surface of the specimen after the experiments can be ascribed to loss of oxygen and formation of superstructures of the fluorite-type lattice of ceria. XRD analyses on the current ceria specimens could not be performed in the present study. They are nonetheless planned for the follow-up of this work, and they will help a deeper understanding of the material behaviour presented in this section.

4.3 Uranium dioxide

A first test for the validity of the current experimental method for the investigation of U and Th mixed oxides consisted in measuring the well established melting temperature of pure UO_2.

For this purpose, different specimens of UO_2 were used. Some specimens were industrial, nuclear plant grade uranium dioxide pellets fabricated by Advanced Materials Inc.®. Other specimens were prepared by sol-gel precipitation, powder pressing, sintering under a Ar/H_2 atmosphere and successive oxidising annealing under CO / CO_2 to reach the exact stoichiometry. In both cases, laser heating

experiments were carried out under pressurised argon at 2,5 bar providing thermograms with a clear and pronounced thermal arrest upon freezing (Fig. 4.24).

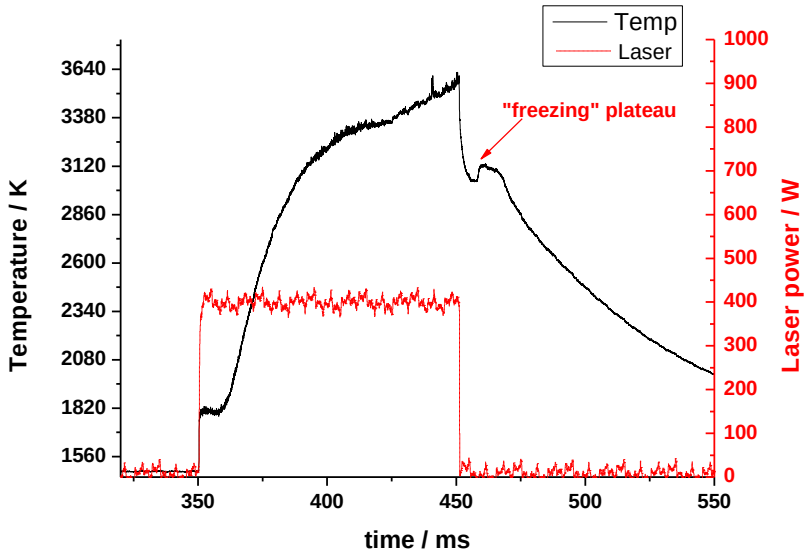

Fig. 4.24. Melting experiment carried out on UO_2.

The corresponding congruent melting/freezing temperature, obtained with the literature emittance [15] of 0,83 is (3115 ± 30) K. This value agrees reasonably well with the most recent literature recommendations [15]. Since this test was successful, the present research was continued with the investigation of the melting temperature of (U,Th) mixed dioxides, starting with pure ThO_2.

4.4 Thorium dioxide

4.4.1 Preparation

Different specimens of ThO_2 were used. They were prepared by sol-gel precipitation, powder pressing, sintering under a Ar/H_2 atmosphere and, sometimes, a successive oxidising annealing under air at 1500 K to ensure the exact stoichiometry.

4.4.2 Laser heating results

In Fig. 4.25, a typical result of a melting experiment on ThO_2 (black line) is shown together with the laser pulse used to melt the specimen (red line).

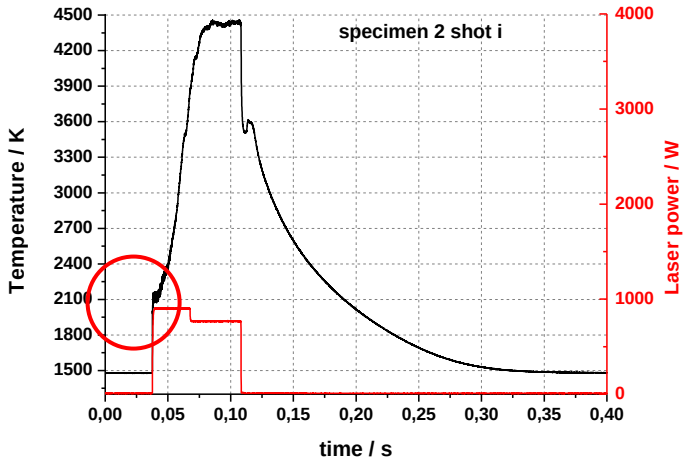

Fig. 4.25. Melting point measurement on thorium dioxide.

At the beginning of the thermogram, is visible the semitransparency effect on the temperature profile already observed for CaO and CeO_2. Due to the presence of this particular behaviour, a first higher laser step was used in order to rapidly overcome the “semitransparent plateau”. This optical effect was less spectacular in ThO_2 than in the other "white oxides" investigated in this work. At the end of this step, a lower but longer laser power step was set in order to stabilise the temperature. When the laser was switched off, the temperature drop and a thermal arrest can be detected between 0,11 s and 0,12 s.

The radiance temperatures were corrected with a NSE of 0,870 ± 0,002 in order to obtain the true melting temperature of ThO_2. This NSE was obtained with the same methods described in section 2.3.4. An example of a NSE results obtained through a non-linear “Planckian” fit is shown in Fig. 4.26.

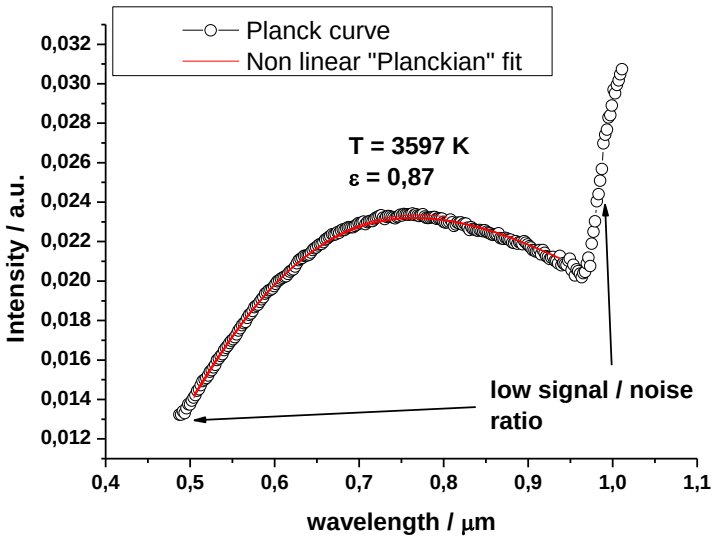

Fig. 4.26. Non-linear "Planckian" fit measured on solidifying ThO_2.

A considerable number of experiments were performed in this work in order to better understand the high temperature behaviour of thoria in the vicinity of the stoichiometric composition. As with the other oxides investigated here, both reducing and oxidising atmospheric conditions were set, in order to check for possible shifts in the specimen composition after melting. In addition, different laser pulses were used in order to detect possible links between the melting temperature values and the maximum temperature obtained.

Two types of specimen were used:

- pressed pellets successively sintered under reducing atmosphere (type 1);
- a type 1 pellet successively annealed under air at 1500 K. This further heat treatment changed the specimen colour from white to orange (type 2).

The most recent study on thoria melting found in literature was made by Ronchi and Hiernaut using four laser beams in a tetrahedral symmetry as heat sources [14]. They investigated nominally-stoichiometric thoria and hypostoichiometric thoria obtaining results as shown in Fig. 4.27a. Whilst with the stoichiometric specimens they obtained single and fairly flat thermal arrests (named in Fig. 4.27a as "MELTING"), during the experiments on the hypostoichiometric specimens more inflections were detected. They argued the peak after undercooling was the liquidus

temperature (labelled “LIQUIDUS”), while the following change in the slope of the thermogram was considered as the solidus temperature (“SOLIDUS”).

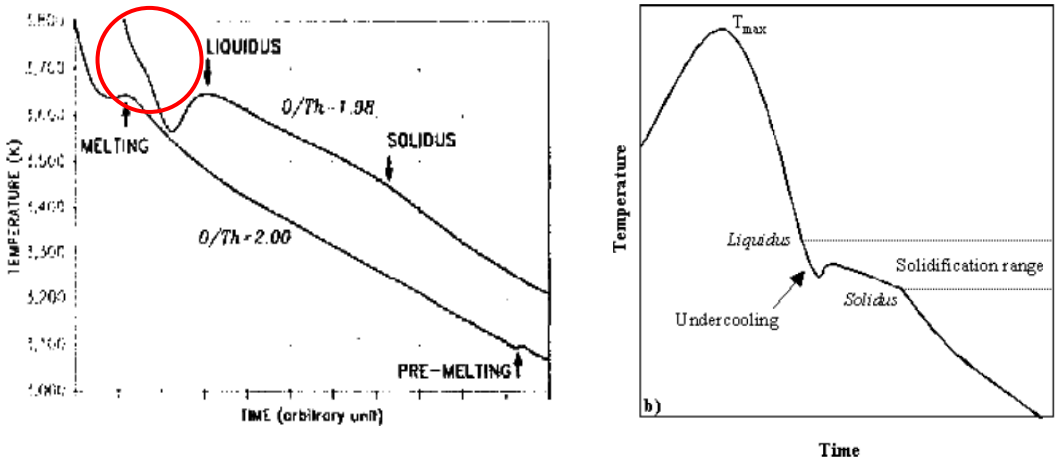

a) b)

Fig. 4.27. a) Experimental results obtained by Ronchi and Hiernaut [14]. b) An example fictive thermogram showing undercooling upon freezing of a non-congruent melting [15].

Fig. 4.26b shows a fictive thermogram where non-congruent solidification takes place. Comparing the hypostoichiometric result obtained by Ronchi and Hiernaut and the schematic representation, one can notice some similarities. A slightly inflection, highlighted with the red circle in Fig. 4.27a, is visible in Ronchi's thermogram at about 3700 K. This first change in the slope of the cooling curve, also visible in Fig. 4.27b, may be ascribed to the a non-congruently melting compound. It was however overlooked by Ronchi and Hiernaut, whose results might therefore need a slight revision. A similar behaviour was also observed in the present work, as it can be seen in Fig. 4.28.

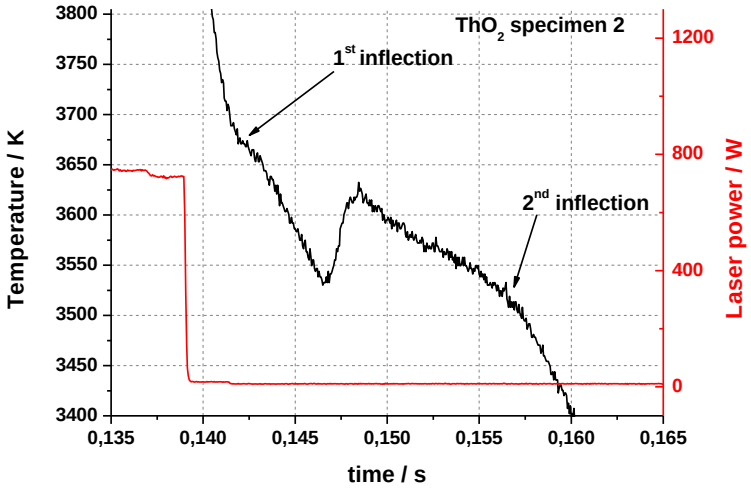

Fig. 4.28. Freezing thermal arrest recorded on a type 2 ThO_2 specimen.

The first inflection in Fig. 4.28 can be compared with Fig. 4.27a. Similar undercooling and thermal arrests were also detected. A second inflection, which is also visible in Ronchi's results and in the scheme in Fig. 4.27b, finally appears. The first inflection is rather reproducible, even though it is hardly detectable in most of the current experiments. The thermal arrest, much more pronounced, can be ascribed to the solidification of most molten material. The third feature seems to represent a further solidification event. This complex behaviour could have been caused by oxygen losses from the initial nominally-stoichiometric thoria, leading to the formation of a little amount of hypostoichiometric thoria and consequent segregation. The detected inflection, through this interpretation, may be a solidus transition of ThO_{2-x}.

The cooling stages of the experiments carried out on specimen 1 show similar features, regardless of the atmosphere used to fill the vessel. After a problematic heating stage, where probably formation of gas phase caused an unstable temperature signal in the pyrometer, two subsequent thermal arrests are visible in the cooling stage of the thermograms. This unusual double-thermal arrest shown in Fig. 4.29 may be correlated with the series of inflection already discussed above.

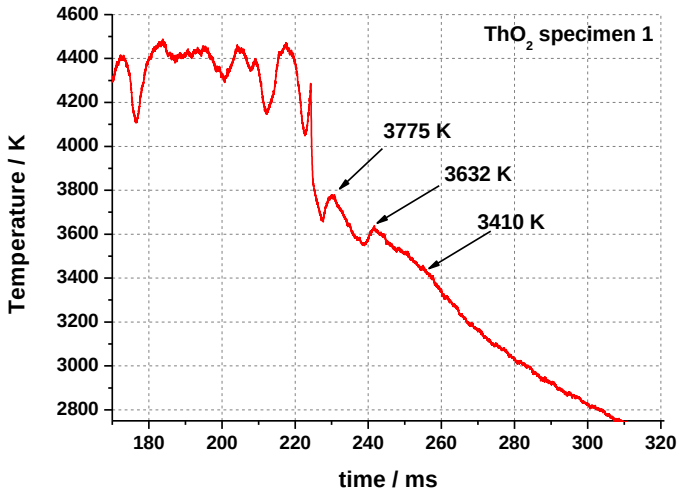

Fig. 4.29. Cooling stage of an experimental result led under compressed air on specimen 1.

The thermogram measured in the experiment 2b (Fig. 4.30), shows a rather different behaviour compared to those discussed so far.

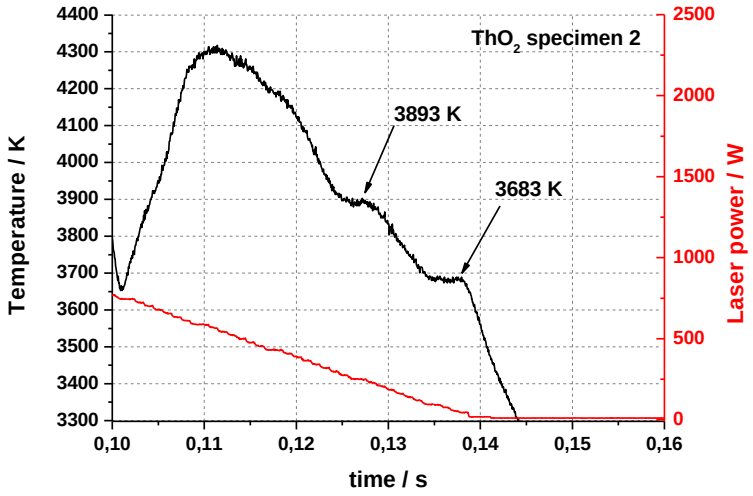

Fig. 4.30. Experimental thermogram recorded on thoria specimen 2.

Two noticeable thermal arrests can be seen in this thermogram. Since the laser still supplied energy during the cooling stage, these inflections are rather clear and flat. After the inflection at about 3900 K, a second lower temperature inflection took place. The latter has a value, within the uncertainties of the method, comparable with the thermal arrest visible in the majority of the experiments. The first arrest,

which was also detected in few other experiments, may be related to a gas/liquid transition (boiling point). Although this interpretation needs to be confirmed, a liquid/solid transition at this temperature is rather unlikely.

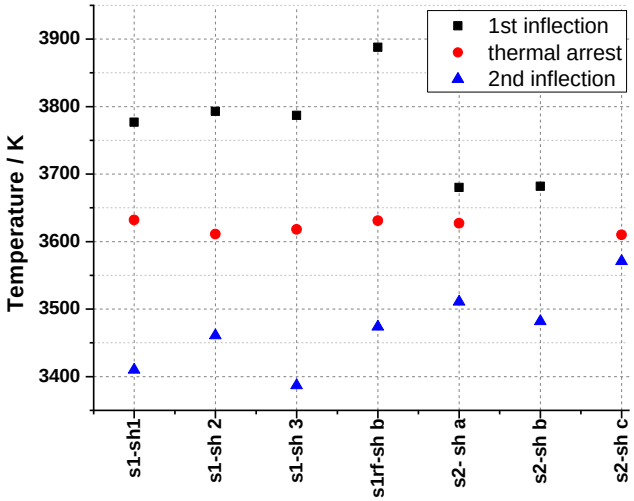

Fig. 4.31. Summary of the results under oxidising atmosphere.

Fig. 4.31 summaries the features observed in the current cooling curves of ThO_2 in all the experiments carried out under oxidising conditions. Whilst the temperature of the thermal arrest is rather reproducible, the temperatures at which the two other inflections occur are quite scattered and do not seem to follow any clear trend.

The values obtained from all the thermograms recorded during the experiments under reducing atmosphere are summarised in Fig. 4.32. During these subsequent shots, again, the thermal arrests occur at rather reproducible temperature. The drop of the last three experimental points is reasonably due to spoiling of the specimen surface. Even if the temperatures corresponding to the two other inflections summarised in Fig. 4.32 do not follow any clear trend, they appear to be dispersed around values comparable to those obtained under oxidising conditions (Fig. 4.31).

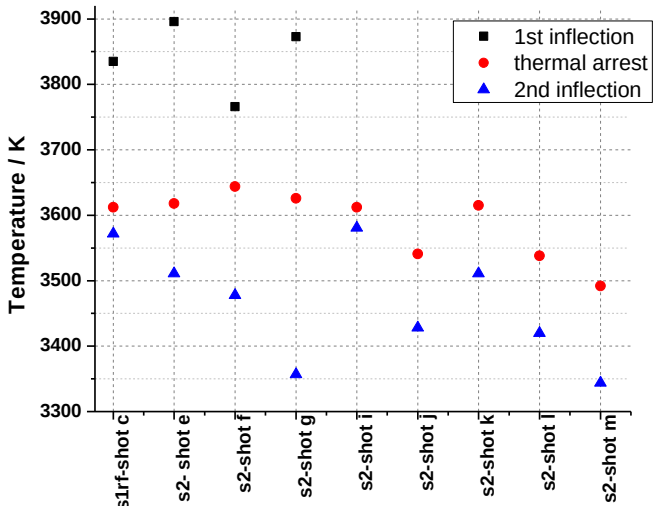

Fig. 4.32. Summary of the experiments carried out under reducing atmosphere.

Although thoria has the lowest oxygen potential among all the actinide oxides at a given temperature, as shown in Fig. 4.33 from [16], during the melting experiments oxygen losses could occur due to the extremely high temperature.

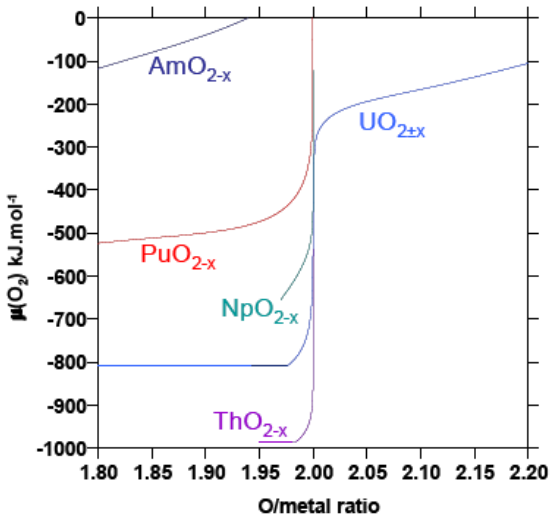

Fig. 4.33. Oxygen potential of different actinide oxides [16].

It seems therefore reasonable to suppose that under oxidising atmosphere, despite the extreme experimental conditions, thoria is more likely to preserve its stoichiometric state. Therefore, a statistical analysis of the data obtained under air

seems to be the most reliable. A value of (3622 ± 65) K (two standard deviations) is recommended for the temperature of the thermal arrest under air (melting point of ThO_2). This inflection certainly corresponds to the melting / freezing temperature reported in the literature. Even if a clear origin for the other two inflection has not been found yet, values of (3808 ± 155) K and (3468 ± 77) K are assessed. In a first approximation, they can be attributed to thoria boiling, and to the full solidification (solidus) of a segregated hypostoichiometric ThO_{2-x}. The exact attribution of these two latter inflections needs to be confirmed by further investigation, and this research task appears considerably challenging at the present stage.

As with the other investigated materials, also for ThO_2 some experiments were carried out under higher pressure. The melting temperature results are summarised in Fig. 4.34.

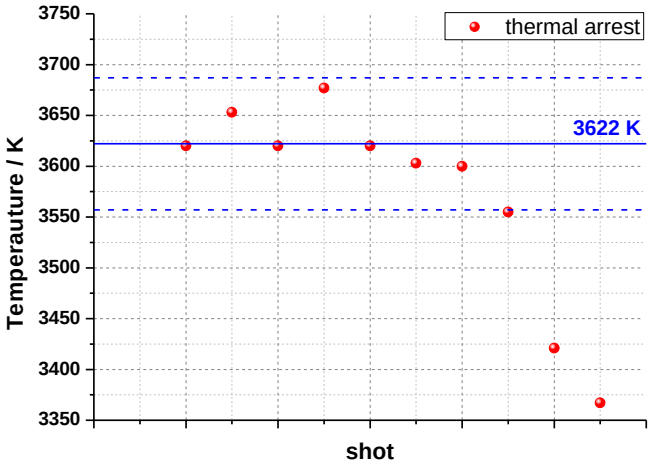

Fig. 4.34. High pressure solidification points measured in thoria in this work.

The values of the thermal arrests do not seem to be affected by the high pressure, and most of them are comparable with the "close-to-atmospheric" pressure ones presented above. The last two shots in Fig. 4.34 are certainly affected by spoiling of the specimen, and can therefore be left out of the analysis.

It is also interesting to consider the change in colour observed during the current experiments, depending on the type of atmosphere used. When the melting point

was reached under a reducing atmosphere (Fig. 4.35a), the molten area became dark blue/black, while if oxidising conditions were set inside the vessel, the molten area turned to a bright glassy orange colour (Fig. 4.35b). Even with a lower temperature (~1500 K) annealing process carried out under air, a white specimen turns to bright orange (Fig. 4.35c). Whilst the dark colour of thoria heated under reducing conditions can be related to oxygen losses [14], the phenomenon observed in air may rather be ascribed to the formation of colour-centres at high temperature and/or to the presence of impurities, such as Ca^{2+} [17], which would migrate to the surface leading to a permanent colour change. TG analysis was performed in order to compare the pre- and post-meting composition of the investigated thoria. The black molten part resulted strongly hypostoichiometric, confirming the existence of a link between oxygen losses and change in colour of the specimen. Although TG analysis is affected by several error sources (unstable oxidising flux, instability of the thermobalance, etc.), an indicative composition of $ThO_{1.5}$ can be given for the black molten thoria.

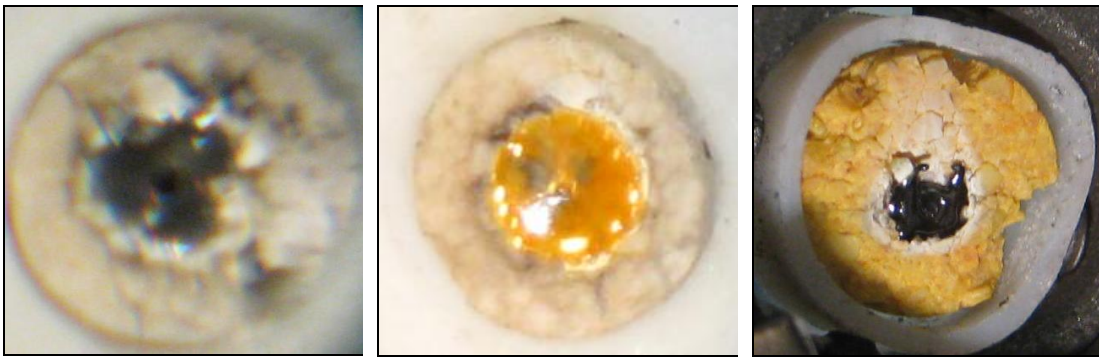

a) b) c)

Fig. 4.35. Pictures of thoria molten surfaces after different shots under different atmospheric conditions. a) Specimen 1 melted under Ar atmosphere. b) Specimen 1 melted under compressed air. c) Specimen 2 melted under Ar atmosphere. The white rings around the molten areas are the plume of vaporised and then condensed thoria.

Fig. 4.35a and Fig. 4.35b show the molten area of specimen 1 obtained under Ar-atmosphere and compressed air respectively. Both the molten zones appear different from the fresh specimen. Whilst the unmolten specimen looks white and rather brittle, the molten areas, black or orange, look glossy and more homogeneous. Fig. 4.35c represents the molten area of specimen 2 after an experiment carried out in

reducing atmosphere. The black molten zone looks once more glossy and more uniform than the surrounding unmolten specimen, which seems to be brittle and easily breakable. Around all the molten areas shown in Fig. 4.35 is also visible a white "ring". The presence of this feature can be related to the maximum temperature often beyond 4200 K. It is presumable that a certain amount of liquid thoria vaporised or became even gas at that temperature and then rapidly condensed on the surface of the specimens. This would be in agreement with the above interpretation of a boiling point for the highest temperature inflection observed in the ThO_2 thermograms. This hypothesis could not be confirmed by further analysis (e.g., by detecting a weight difference in the heated material). However, one should not forget that the vaporized mass in such a short dwelling time (a few tens ms at most) at high temperature must have been extremely tiny, especially in the presence of a pressurised buffer gas in contact with the specimen surface. The only detectable sign of this supposed solid/vapour/solid transition is the clear formation of this white phase. The white condensed plume clearly visible in Fig. 4.35c represents a further confirmation of the initial formation of vapour over the surface of the specimen. Pre- and post-melting XRD analyses were performed on ThO_2. Comparing the fresh thoria with a small amount of the black molten zones (black and orange), only a modest shift in the peaks can be detected, as notable in Fig. 4.36.

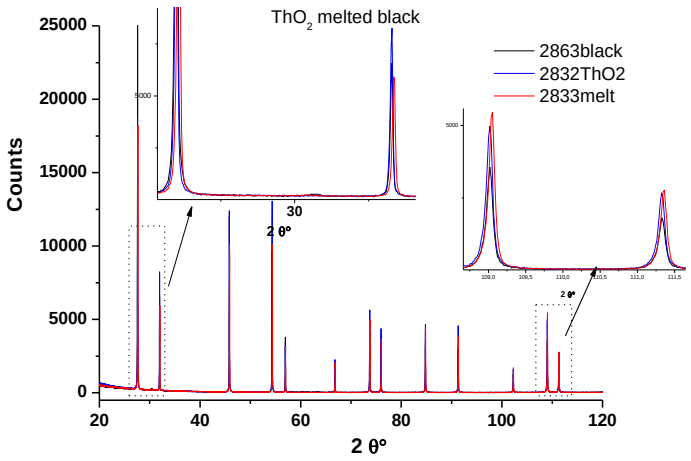

Fig. 4.36. XRD results on fresh (blue pattern) and molten thoria (red pattern for the material molten under reducing conditions and black pattern for ThO_2 molten under compressed air).

In the three XRD patterns only one phase, with a Fm-3m space-group, was detected, confirming that the fluorite-type structure is conserved throughout the melting / freezing. The shift in the peaks reveals a very slight decrease in the lattice parameter from the fresh to the molten thoria: 5,59722 Å for fresh thoria to 5,59715 Å for the molten zone. The difference between orange and black molten zone is even smaller, and it is difficult to distinguish it within the resolution limit of the current XRD analysis. Unfortunately, no systematic correlation between the lattice parameter and the O / Th ratio in thoria exists in the scientific literature. This is essentially due to the fact that thorium is well known to be stable in its +4 oxidation state. Therefore, unlike uranium dioxide, thorium dioxide is not likely to exist as hypo-soichiometric compound, at least at moderate temperature. The same is however not true at very high temperature (> 1700 K), as it can be seen in the Th–O phase diagram reported in Fig. 1.13 and Fig. 1.14 of Chapter 1. In such temperature domain, however, a direct analysis of the lattice parameter is extremely hard. For this reason, if the current XRD results ensure that the fluorite-like lattice symmetry has been maintained throughout the laser heating cycles, they are not conclusive about the final composition of the investigated materials.

4.4.3 Raman analysis

The thorium dioxide fluorite structure belongs to the O_h^5 space group. In order to detect some possible after-melting-changes in the symmetry properties of thorium dioxide, Raman analysis was performed. The characteristic peaks found in literature are summarised in Table 4.3. Because of the large number of peaks (see Fig. 4.37), only the most intense ones are reported here.

Table 4.3. Raman modes found in the present work for ThO_2. The symbol "/" states that no literature data exist for the marked modes, although they have been observed in all the current spectra.

Raman shift / cm^{-1}	Assignment	Reference	Comments
~ 165	/	/	Did not find in literature , but intense peak.
~ 467	T_{2g}	[18],[12]	Reference peak.
~ 935	$2\Gamma^{+}_{2\,5}$	[18]	±1 cm^{-1}.
~ 1029	$2M_5'$	[18]	
~ 1099	/	/	Shoulder did not find in literature.
~ 1125	/	/	Intense peak did not find in literature.
~ 1135	$2M^{-}_{2\,5}$	[18]	Intense peak.
~ 1260	/	/	Intense peak.
~ 1306	/	/	
~ 1356	/	/	
~ 1475	/	/	
~ 1531	/	/	Broad peak. In several spectra cover a peak at 1549 cm^{-1}.
~ 1584	/	/	

Keramidas and White [12] studied the first-order Raman scattering of ThO_2. Ishigame and Kojima [18] performed a second-order Raman investigation of ThO_2. The first-order Raman spectrum of ThO_2 exhibits a single strong band at (467 ± 1) cm^{-1} corresponding to the T_{2g} Raman active mode, considered as the reference peak for this compound. Raman spectra of specimen 1 of ThO_2 before and after the laser heating treatment are shown in Fig. 4.40. They were recorded using an Ar^+ excitation source at 514 nm. The first Raman spectrum reported in Fig. 4.37 (red curve) refers to the "fresh" white-greyish specimen (no annealing treatment and no laser heating). The second spectrum (blue) was recorded on the same specimen after melting it in argon. The molten part had therefore turned to dark grey/black.

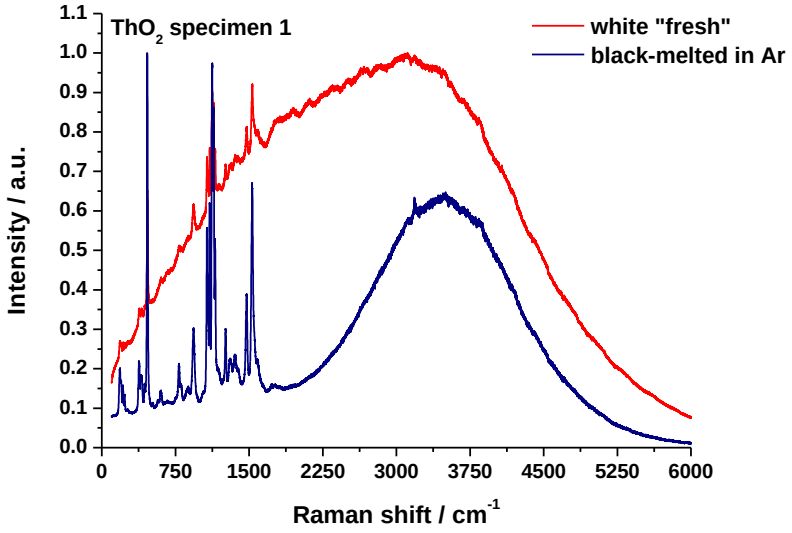

Fig. 4.37. Raman spectra of ThO_2 specimen 1 before- (red line) and after- (red line) melting.

The peculiarities of the spectra in Fig. 4.37 are the high concentration of peaks in the low-wavenumber region and the presence, in both cases, of a fluorescence peak centred between 3000 and 3750 cm^{-1}. While in the "fresh" specimen the fluorescence covers the wavenumber range from 0 to more than 6000 cm^{-1}, in the spectra of the melted specimen it shifts to higher wavenumbers and becomes much narrower. In Fig. 4.38, a magnification of the low-wavenumber region is shown.

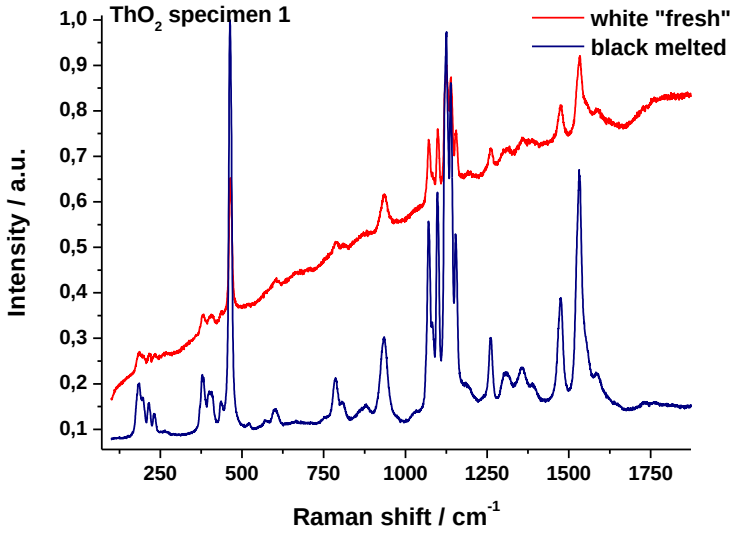

Fig. 4.38. Magnification of the low-wavenumber region of Fig. 4.37.

Pre and post-melting spectra do not show appreciable differences except for the shift to higher wavenumbers and the narrowing of the fluorescence peak, obviously related to the colour change.

The Raman spectra of pre- and post-melting specimen 2 is shown in Fig. 4.39. This specimen, before it underwent the melting experiments, was heat treated in an air-furnace at 1500 K in order to anneal it and make it less fragile. After that, the specimen became pale orange.

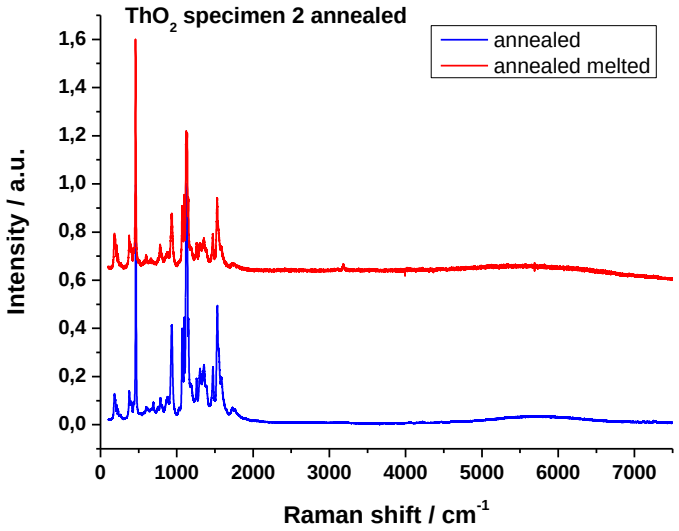

Fig. 4.39. Raman spectra of melted and non-melted thoria specimen 2.

The fluorescence detectable in Fig. 4.37 is not visible in Fig. 4.39 anymore. This phenomenon can be ascribed to the colour change after the annealing treatment. Such observations are in line with some recent literature [19], and will be deepened in future research on the same subject. The useful result for the current investigation is that even in these spectra, the characteristic peaks occupy the low-wavenumber region, and no appreciable differences can be detected before and after the annealing and melting treatments.

4.4.4 SEM-EDS

The micro-structure of molten and re-solidified thoria was studied by SEM. Although after the melting experiments the specimens were generally broken, it was

possible to perform an analysis on both molten and non-molten surfaces. EDS analysis was also performed in order to check the presence of impurities. Fig. 4.40 shows the molten zone of a thoria melted specimen.

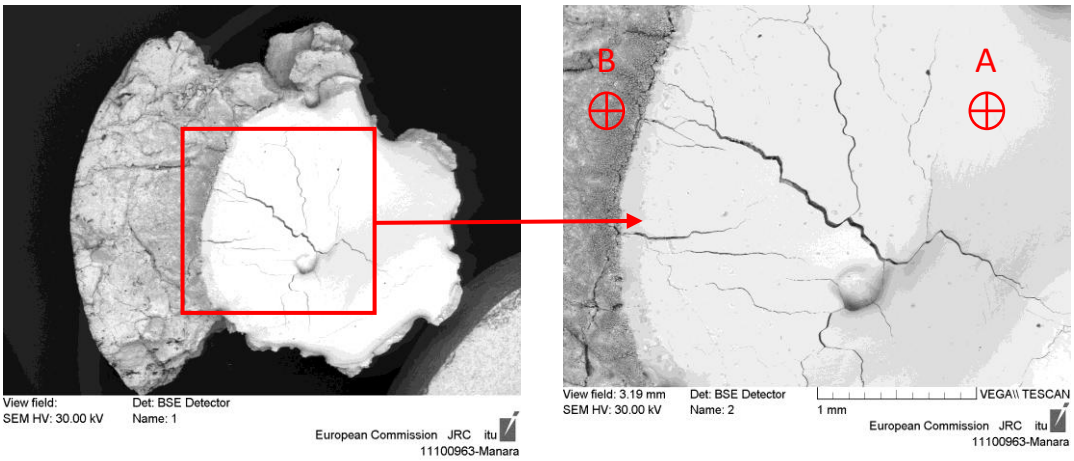

a) b)

Fig. 4.40. SEM images of a thoria melted specimen. a) Overview. b) Magnification of the molten zone.

Some differences between the microscopic structure of the unmolten and molten thoria are easily visible. The molten and lighter zone seems more homogeneous and characterized by several cracks, probably due to the high temperature gradients during the heating/cooling processes. EDS analyses on the points A and B marked in Fig. 4.40b were thus performed to check for possible segregation of impurities (oxygen and lighter elements cannot be quantitatively analysed by means of the current SEM-EDS facility). Whilst in the point A only thorium and oxygen were found, in the second investigated point named B, also traces of calcium impurities were detected. This confirms the possible relation between the annealing process in air and the final orange coloration of the specimen [17] [19].

4.4.5 Conclusions

Despite the extreme conditions achieved and the difficulties in the analysis of the obtained data, a melting temperature value of (3622 ± 65) K for stoichiometric thoria can be assessed from the current investigation, in good agreement with the most recent literature data [14]. Only the thermal arrests observed in oxidising

conditions were taken into account, because of the uncertainties in the after-melting-compositions during the experiments carried out under Ar. Additional inflections often detected in the thermograms at higher temperature may be ascribed to a gas/liquid equilibrium, whereas lower temperature features can be attributed to complex solidification and oxygen segregation in hypo-stoichiometric ThO_{2-x}. Further investigation is anyway needed in order to better define these phenomena. The post-melting characterizations confirm, within its uncertainty limits, the link between oxygen losses and blackness of the molten area of the specimens. The orange coloration of specimens heated under air, instead, can be attributed to the migration towards the hot surface of calcium impurities.

4.5 Mixed oxides $(U,Th)O_2$ (TOX)

4.5.1 Preparation

A series of six compositions of mixed $(U, Th)O_2$ specimens containing from 5 to 95 mol% ThO_2 were prepared. They were identified, for the sake of simplicity, with the acronym TOX followed by a number indicating the nominal ThO_2 content (in mol%): TOX 5, TOX 20, TOX 40, TOX 60, TOX 80 and TOX 95. The starting material was powder obtained by gel-supported solidification (SOL-GEL). The specimens were then pressed into cylindrical pellets, which successively underwent a heat treatment in a dry $Ar+H_2$ atmosphere and successively an oxidizing annealing treatment under CO / CO_2 to reach the exact stoichiometry. The goodness of the nominal specimen composition was tested by XRD analysis, which gave values for the lattice parameters vs. mol% ThO_2 in agreement with Vegard's law, as shown in Fig. 4.41.

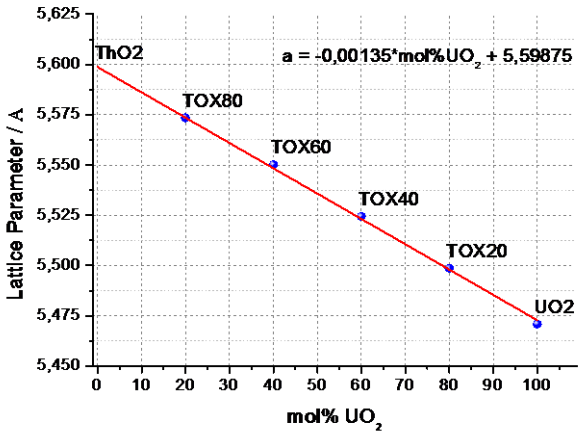

Fig. 4.41. Vegard's law for some of the mixed (U,Th) oxides analysed in this work.

4.5.2 Laser heating results

Six different compositions of (U,Th) mixed oxides have been studied in this work. Compared with the pure oxides compounds previously described, much more difficulties arose in the analysis of the intermediate compositions of this binary system. The control of the uranium, thorium and oxygen distribution is more difficult, especially during the current very rapid heating and cooling processes. In addition, phenomena like segregation and non-congruent evaporation had to be limited as much as possible.

The high pressure device was therefore used for the first set of experiments on TOX (from 20 mol% to 80 mol% ThO_2) in order to limit the departure of oxygen from the specimen. The drawback of this approach was the possible onset of convective motion in the high pressure buffer gas in contact with the hot specimen surface, hindering the pyrometric temperature detection, as shown in Fig. 4.42.

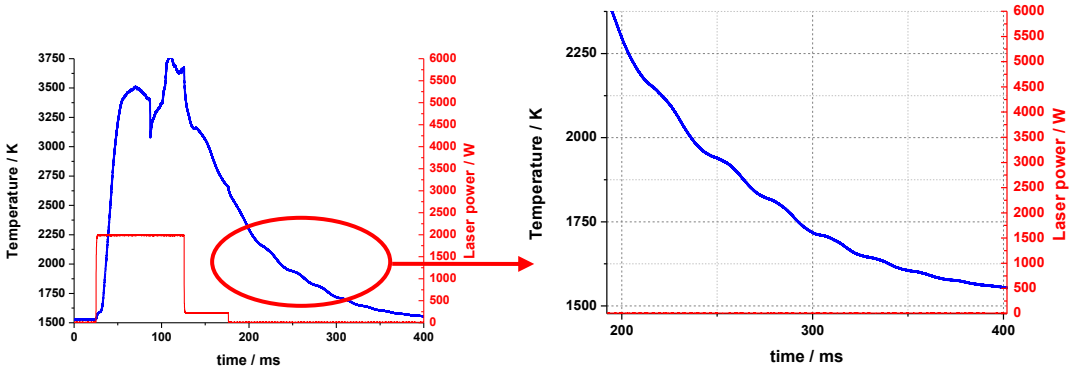

a) b)

Fig. 4.42. High-pressure gas convective motion effect on a thermogram recorded on specimen TOX 20. a) Complete thermogram. b) Magnification of the cooling stage, after the laser was switched off.

After the laser pulse ended, convective waves are well visible and continued until the temperature limit of detection of the pyrometer.

Thermograms recorded for the different TOX investigated under high-pressure buffer gas are shown in Figs. 4.43-46.

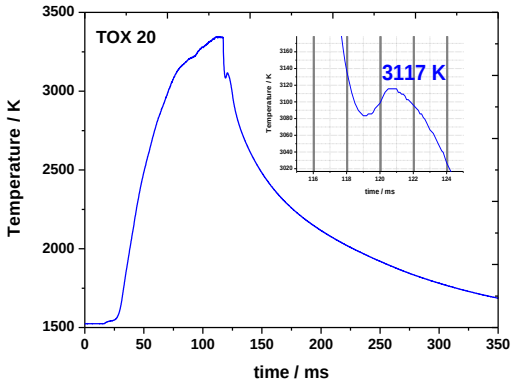

Fig. 4.43. Thermogram recorded with the fast pyrometer on TOX 20_3.

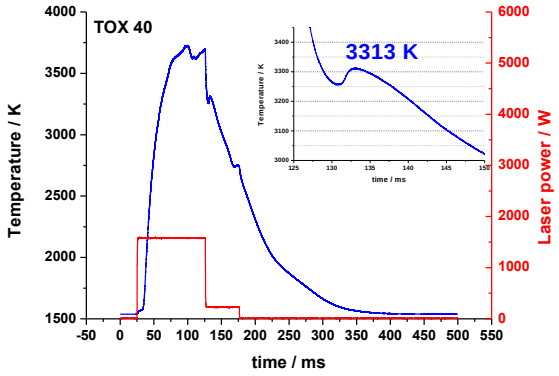

Fig. 4.44. Thermogram recorded with the fast pyrometer on TOX 40_2.

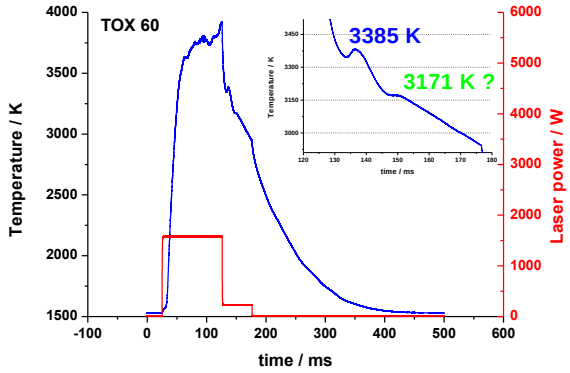

Fig. 4.45. Thermogram recorded with the fast pyrometer on TOX 60_1rf.

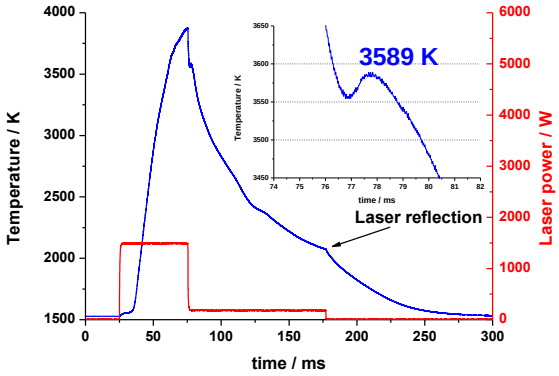

Fig. 4.46. Thermogram recorded with the fast pyrometer on TOX 80_2.

The thermal arrests on the cooling stages seemed to indicate a congruent melting process. Since for the investigated compositions congruent solidification was

unlikely that a uncongruent solidification occurs, it can argued that the liquidus and solidus temperatures were mostly too close together to be detected during the extremely rapid cooling process produced through the present method. However, in some cases, two inflections can be seen on the thermogram. In order to better see the second inflections, further experiments were performed, with slower cooling rates. This was realised in the present work by using a two-step laser pulse, where the first high-power stage was followed by a second longer step at lower power, in order to condition the cooling rate. Unfortunately, this approach was no sufficient to avoid undercooling in some cases, and in any case to detect two distinct inflections in the thermograms. The high pressure inside the vessel probably increased the cooling rates, limiting the effect of the laser pulse shape. All the recorded thermal arrests were considered as solidus transition, considering that, frequently, this type of transition is better visible with the current method because it implies the release of a larger amount of latent heat from the solidifying melt. At the end of the laser pulse, most thermograms show a marked change in the slope, corresponding to the end of the second step of the laser pulse.

In order to obtain the true melting temperature of the investigated compounds, all the radiance temperatures were corrected with a NSE to obtain the real temperature. Since only a study on the emittance of the pure end members of the system (UO_2 and ThO_2) were available, for the mixed oxide compositions only interpolated values could be assigned. A linear interpolation between the two NSE of UO_2 and ThO_2 was calculated, giving to the generic intermediate composition a weighted value related to the amount of the two pure components.

Table 4.4. NSEs of the mixed oxides compositions.

Composition	NSE
TOX 5	0,832
TOX 20	0,838
TOX 40	0,846
TOX 60	0,854
TOX 80	0,862
TOX 95	0,868

A value of 0,83 was used for pure UO_2 [15], while the value obtained during the present work was adopted for pure ThO_2, that is 0,870 ± 0,002. The values for the NSE assigned to the mixed oxides compositions are shown in Table 4.4. This assumption seems reasonable especially considering the close emittance values of the two end members. Nonetheless, further confirmation should be provided by experimental studies on these compounds.

The solidification temperatures obtained on the investigated compositions are summarised in Table 4.5 with their respective uncertainty bands (two standard deviations). These bands are rather large, essentially due to the low number of tests performed and to the difficult experimental conditions.

Table 4.5. Melting temperature of the investigated mixed(U,Th) oxides compositions (TOX).

Composition	Melting temperature / K	Uncertainties / K
UO_2	3106	75
TOX 20	3158	69
TOX 40	3336	39
TOX 60	3348	61
TOX 80	3573	55
ThO_2	3616	73

Whilst the results obtained on TOX 20 and TOX 40 are fairly in agreement with those of Lambertson, Mueller and Gunzel's [20] work, the value obtained for the melting temperature of TOX 80 is higher compared to the predicted value found in the same work. This is a consequence of the too low melting temperature chosen for thoria in that early investigation, and to a correspondingly non-satisfactory experimental dataset in the high-thoria percentage region of the phase diagram. On the other hand, the present result on TOX 60 is sensibly lower than the extrapolated value found in [20]. This last measurement should be repeated under different conditions.

The second set of experiments was performed on 5, 20 and 95 mol% ThO_2, using the lower pressure device (3 bar). A summary of the second set of results is shown in Table 4.6.

Table 4.6. Second set of TOX melting experiments results.

Composition	Melting temperature / K	Uncertainties / K
UO_2	3115	30
TOX 5	3020	67
TOX 20	3149	19
TOX 95	3587	34
ThO_2	3622	65

The results on TOX 20 specimens confirm those of the high pressure experiments. In fact, the currently measured liquidus and solidus temperatures (distinct inflections) were remarkably closer to the results of Lambertson et al. The solidus temperature for this composition is reported in Table 4.6. Another clear and reproducible inflection was detected in this case at about (3254 ± 77) K (two standard deviations), to be attributed to the liquidus point. A thermogram recorded for TOX 20 is shown in Fig. 4.47.

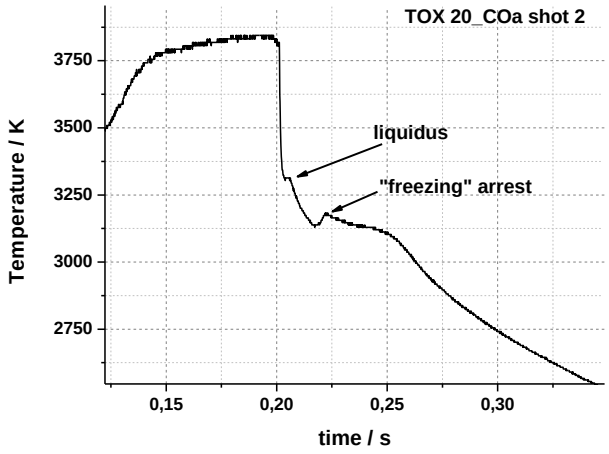

Fig. 4.47. Thermogram recorded on specimen TOX 20_COa.

The melting temperatures detected in the experiment on TOX 95 are close to that of pure ThO_2, and confirm the previously described results for the high-percentage of thoria region of the phase diagram. Compared with Lambertson et al.'s results, this region is once more characterised by a remarkably higher liquid/solid transition temperatures, as already discussed above.

Finally, the experiments performed on the mixed oxide composition with 5 mol% ThO_2 confirm, at least qualitatively, the results reported by Latta, Duderstadt and

Fryxell [21]. Even if at a temperature some tens K lower than reported in [21], the solidification point measured here confirms the existence of a minimum melting point around this composition. The experimental results obtained in this work on the melting / solidification transition in (U,Th) mixed dioxides are plotted in Fig. 4.48.

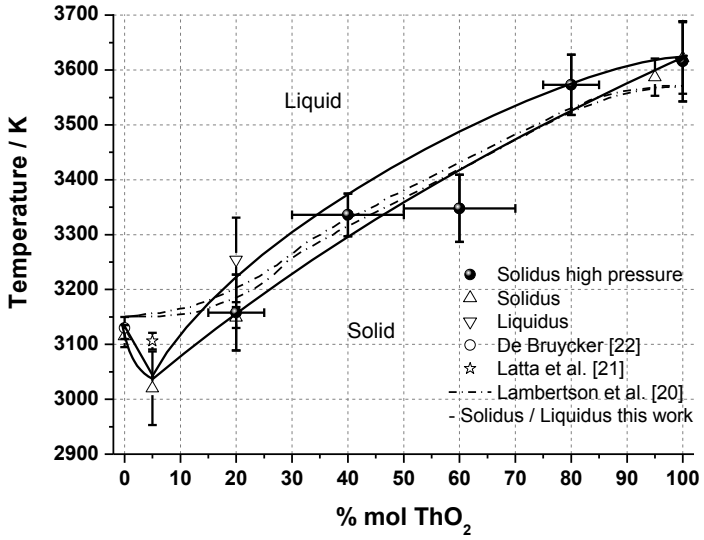

Fig. 4.48. Solidus and liquidus temperatures measured in this work on mixed (U,Th) oxides (TOX). Dotted line: Lambertson et al.'s solidus and liquidus. Solid lines: current assessment. These lines are only a guide for the eye.

Fig. 4.48 shows the current results together with the solidus and liquidus lines extrapolated in Lambertson et al.'s work and some other literature data. The phase diagram predicted by Lambertson et al. is in fair agreement with the present results, with the exceptions of the minimum melting temperature at around 5 mol% ThO_2 (already observed by Latta et al. [21]) and the region with high ThO_2 content ($\geq$ 80 mol%). In this last composition range, the experimental transition temperatures of Lambertson et al. were underestimated, as already noticed by Ronchi and Hiernaut [14] for pure thoria.

XRD analysis shows that traces of a second phase appear in TOX 40 after laser melting. This composition was chosen as the most representative for this kind of test, because it corresponds to a point in the phase diagram where the solidus and liquidus lines are far apart (see Fig. 4.48). The obtained diffractograms are shown in

Fig. 4.49. The two phases detected have both a Fm-3m space group, and respectively a lattice parameter of 5,5241 Å (attributable to the 40 mol% ThO_2 composition) and 5,54891 Å. The lattice parameter of the second phase can be attributed, through Vegard's law reported in Fig. 4.41, to a composition closer to 50 mol% ThO_2. According to the current shape of the solidus and liquidus curves, such an effect can be easily related to some segregation during the melting / freezing process. This is more likely to happen at compositions where solidus and liquidus are further apart, for example between 20 mol% ThO_2 and 80 mol% ThO_2. Although no similar segregation effects could be observed for any other compositions, nor by other investigation techniques such as Raman spectroscopy or SEM - EDS analysis, as shown in the following sub-sections, horizontal error bands have been added to the current experimental points to conservatively take them into account. These horizontal uncertainty bands are estimated to be larger at intermediate compositions and smaller in the vicinity of the end members (UO_2 and ThO_2), where segregation phenomena are less likely to occur because the solidus and liquidus lines are much closer to each other.

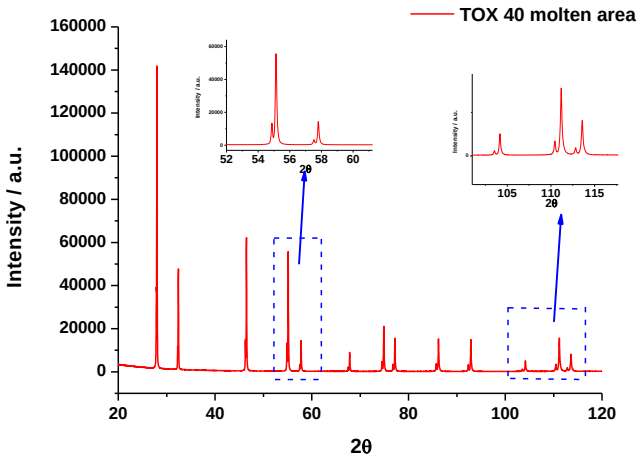

Fig. 4.49. XRD analysis on molten TOX 40 specimen.

4.5.3 Raman analysis

A pre- and post-melting Raman analysis was performed on the investigated compositions of mixed $(U,Th)O_2$ oxides. The main purposes were the detection of

possible segregation effects on the spectra and a check about the possible appearance of new bond types after the laser heating cycles.

The reference peak of stoichiometric urania is at 445 cm^{-1} [15]. It is related to the T_{2g} triply degenerate Raman active vibration, typical feature of the fluorite-like structures. On the other hand, as shown in the section 4.4.3, thoria presents a reference peak of the same origin at 467 cm^{-1}. A typical Raman spectrum of unmolten TOX 40 together with pure urania and thoria is reported in Fig. 4.50.

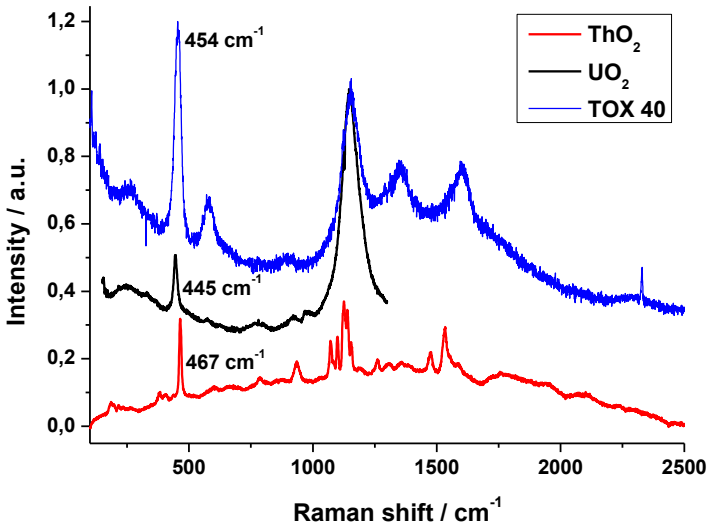

Fig. 4.50. Raman spectra of unmolten TOX 40 together with the spectra of pure urania and thoria. The light source was an Ar^+ laser at 514 nm.

The narrow peak present in the Raman spectrum of TOX 40 at 454 cm^{-1}, is the convolution of the previously mentioned peaks of urania and thoria. The second narrow peak, well visible in the spectrum of TOX 40, at about 1150 cm^{-1}, overlaps a similar peak in the spectrum of pure urania, and a vibration band of pure thoria.

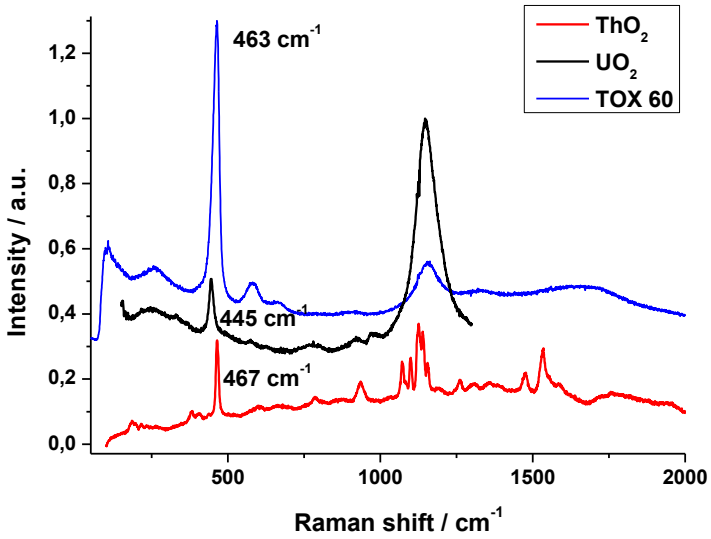

Fig. 4.51. Raman spectrum of TOX 60.

It is clear how, increasing the amount of thoria in the matrix of the TOX specimens, the reference peak shifts correspondingly. A magnification of Fig. 4.51 in the region of interest is shown in Fig. 4.52.

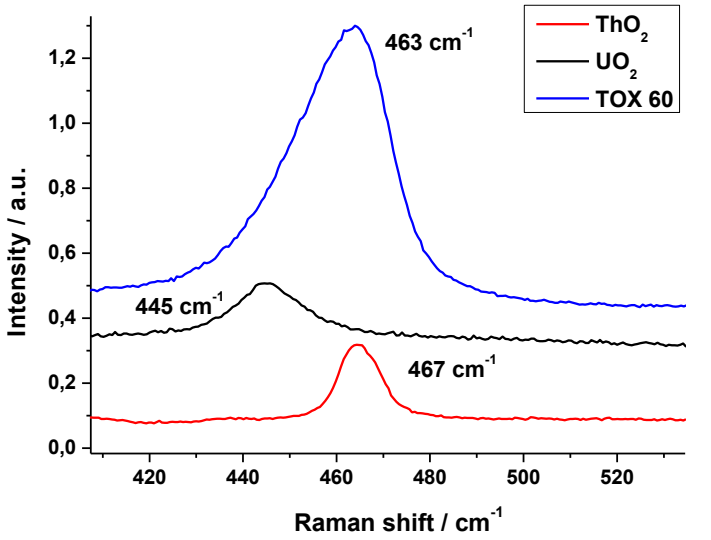

Fig. 4.52. Magnification of Fig.4.51 in the region of the reference peaks.

Fig. 4.52 gives a further confirmation of the convolution of urania and thoria spectra to form the spectra of the mixed compositions. The higher is the amount of

thoria, the closer is the characteristic peak in the TOX spectra to the reference peak of thoria. The same effect is also visible in the spectrum of unmolten TOX 80, where the reference peak is at 464 cm^{-1}. A plot of the dependence of the position of the reference peak with the ThO_2 content is shown in Fig. 4.53.

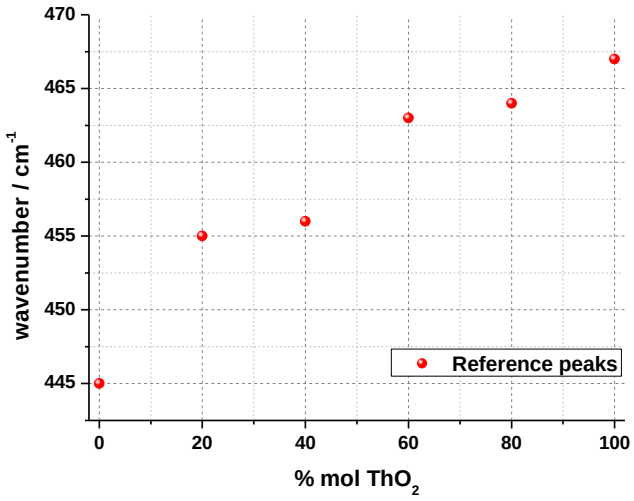

Fig. 4.53. Dependence of the reference peak with ThO_2 content.

A well visible trend can be seen, although a precise quantification of it is made difficult by the spectral uncertainty (± 1 cm^{-1}) and the specimen composition uncertainty.

It is also remarkable the effect of the thoria content on the peak at about 1150 cm^{-1}. Whilst in the low-percentage compositions this peak is rather visible, in the spectrum of TOX 60 it became less evident and in the TOX 80 disappeared. Therefore, the presence of such a feature in the mixed oxides is to be attributed to an uranium-oxygen vibration rather than modes involving thorium atoms.

The post-melting analysis did not show any detectable changes in most of the spectra, as visible in the example of Fig. 4.54. Although only the reference peaks at 454 and 1150 cm^{-1} were practically used for the current analysis, both the pre- and post-melting spectra present other bands of uncertain origin.

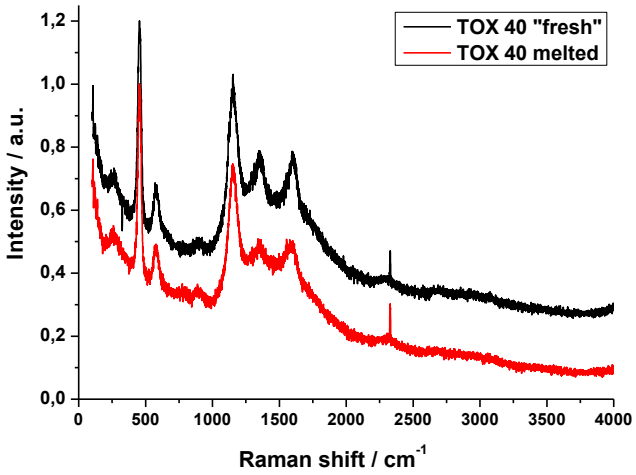

Fig. 4.54. Comparison between the spectra of unmolten and molten TOX 40 specimen.

4.5.4 SEM-EDS

In order to check the surface homogeneity of the specimens after the melting experiments, SEM-EDS analyses were performed on all the investigated mixed oxides compositions. Even if most of the melted specimens broke after the experiments, it was possible to compare molten and unmolten regions and see the changes in the structure and the relative U / Th composition. As an example, Fig. 4.55 shows an SEM image of the edge between molten and unmolten region of TOX 20.

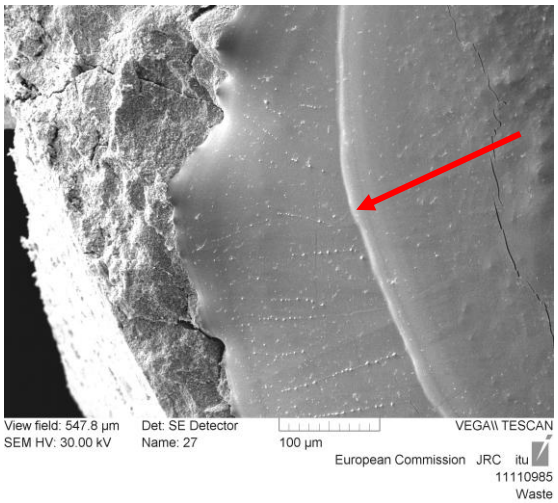

Fig. 4.55. SEM image of a melted TOX 20.

It is immediately noticeable the change in the microstructure of the molten region of the specimen. Whilst the unmolten zone appears rough, the molten area looks more homogeneous. The lighter line indicated with the red arrow seems to correspond to the "solidification front" started from the outer part of the molten zone and rapidly drifted toward the centre of the specimen during the cooling of the specimen. This radial movement of the solid edge is also confirmed by the numerous quenched bubbles along radial directions. These little spots are slightly richer in uranium, meaning that probably the coefficient of diffusion of thoria is higher than the one of urania. In all the analysed compositions, there are no more evident traces of segregation, and the ratios U / Th in the molten areas remain very close to the unmolten matter one, at least within the experimental uncertainty. It is therefore reasonable to assume, in a first approximation, that if the melting/solidification temperature measurements have been influenced by a slight segregation of the U / Th relative composition, these changes are in the worst case limited to horizontal uncertainty bands plotted in Fig. 4.48.

4.5.5 Conclusions

The current results on mixed $(U,Th)O_2$ oxides confirm and refine previous literature data. The results on the intermediate compounds seem to follow a well reproducible trend, regardless the pressure used during the experiments. The melting behaviour of this system seems to be slightly irregular only in the low-thoria region, where a minimum melting point has been observed in the vicinity of 5 mol% ThO_2, as already observed in earlier research. Further experiments should be planned in order to better understand the roots of this phenomenon and reduce the uncertainties related to the current melting temperatures. Traces of segregation were found through XRD analysis in the 40 mol% ThO_2 composition after melting and re-solidification. Therefore, further post-melting analyses should be planned in order to refine also the uncertainty bars related to the compositions at which the liquid/solid transitions were detected.

On the other hand, even with the current uncertainty bands, the present results follow a meaningful trend in line with other recent literature data. In this work, it

has thus been possible qualitatively reassess the solidus and liquidus lines of this pseudo-binary system for the first time since the 1960's.

4.6 References

[1] T. Yamada, M. Yoshimura, and S. Somiya, J. Am. Ceram. Soc., 69 [10] (1986), C-243.

[2] D. Lindberg and P. Chartrand, J. Chem. Thermodynamics, 41 (2009), 1111.

[3] B. Henderson, S. E. Stokovski and T. C. Ensign, Phys. Review, 183 [3] (1969), 826.

[4] K. H. Rieder, B. A. Weinstein, M. Cardona and H. Bilz, Phys. Rew. B, 8 [10] (1973), 4780.

[5] Y. Hase, J. Braz. Chem. Soc., 17 [4] (2006), 741.

[6] P. E. Halsted and A. E. Moore, J. Chem. Soc., 769 (1957), 3873.

[7] M. Foex, Rev. Hautes Temp. Refract., 3 (1966), 309.

[8] O. A. Mordovin, N. I. Timofeeva and L. N. Drozdova, Inorg. Mater. (URSS), 3 (1967), 159.

[9] L. Brewer, Chem. Rev., 52 (1953), 1.

[10] W. H. Weber, K. C. Hass and J. R. McBride, Phys. Rev. B, 48 [1] (1993), 178.

[11] G. A. Kourouklis, A. Jayaraman and G. P. Espinosa, Phys. Rev. B, 37 (1988), 4250.

[12] V. G. Keramidas and W. B. White, J. Chem. Phys., 59 (1973), 1561.

[13] M. Zinkevich, D. Djurovic and F. Aldinger, Sol. Stat. Ion., 177 (2006), 989.

[14] C. Ronchi and J. P. Hiernaut, J. Alloy Compd., 240 (1996), 179.

[15] D. Manara, "Melting transition measurements in uranium dioxide", PhD Thesis, Technical Note JRC-ITU-TN-2004/05 (2004).

[16] C. Guéneau, A. Chartier, L. Van Brutzel, Chapter 9: the Actinide Oxides, Comprehensive Nuclear Materials, Edited by R. Konings, Elsevier, 2012.

[17] C. Linares, J. Phys. Chem. Solids 28, (1967), 1285.

[18] M. Ishigame and M. Kojima, J. Phys. Soc. Japan, 41[1] (1976), 202.

[19] T. R. Griffiths and J. Dixon, Inorg. Chim. Acta, 300-302 (2000), 305.

[20] W. A. Lambertson, M. H. Mueller and F. H. Gunzel, Jr., J. Am. Ceram. Soc., 36 (1953), 397.

[21] R. E. Latta, E. C. Duderstadt and R. E. Fryxell, J. Nucl. Mater., 35 (1970), 347.

[22] F. De Bruycker, " High Temperature Phase Transitions in Nuclear Fuels of the Fourth Generation", PhD Thesis, Technical Note JRC-ITU-TN-2011/4 (2011).

Conclusions

The main goal of this eight month traineeship with the Institute for Transuranium Elements of Karlsruhe, Germany, has been the study of the high temperature behaviour of some high-melting oxides of interest for the production of nuclear energy for civil purposes. More in particular, the investigated uranium-thorium mixed oxides can be employed as a “sustainable” nuclear fuel in countries rich in thorium ores. The non-nuclear oxides have been studied essentially in order to better understand the semitransparency effect and to simulate the behaviour of more dangerous and radio-chemical toxic compounds. A lot of difficulties related to the extreme experimental conditions have been faced. The main of these difficulties has been the high chemical reactivity of the investigated compounds at very high temperature. These compounds, in this conditions, easily underwent fast oxidation / reduction processes and volatilisation. Furthermore, the high oxygen potential at high temperature of the compounds tended to oxidise their environment, leading to a reduction of the initial stoichiometric specimens. Additional problems have been the interaction of the specimens with the container and the temperature detection itself. As a matter of fact, in this context, the only possible method of temperature detection is optical pyrometry, for which the normal spectral emittance of the investigated compounds must be determined.

A number of new experimental data have been produced in this work by using an innovative method recently developed at ITU. It is based on laser heating coupled with a fast two-channel optical pyrometer for the detection of the radiance transition temperature and a spectro-pyrometer used for the normal spectral emittance.
At the same time, the current experimental method has been accurately validated through the measurements of the melting radiance temperature of five refractory metals recommended as secondary references points for the ITS-90. These tests have also served to identify some important error sources of this approach.

The next sections summarise the main outcomes and the still open questions of the present work.

Validation of the method

The radiance temperatures of melting (T_λ) of vanadium, niobium, molybdenum, tantalum and tungsten recommended as secondary reference points of the International Temperature Scale 1990 (ITS-90) are reported in Table 1, and compared with the current measurements.

Table 1. Summary of the results of the five refractory metals. There are also the number of specimens involved in the experiments and the total number of shots performed.

Metals	Specimens	Shots[i]	T_λ / K[ii] (m) (f)	T_λ / K SRP[iii]
V	8	35(29)	1976 ± 28 1975 ± 28	1988 ± 7
Nb	18	111(51)	2400 ± 41 2398 ± 41	2422 ± 5
Mo	5	30(12)	2509 ± 45 2504 ± 45	2530 ± 5
Ta	5	55(15)	2823 ± 53 2825 ± 53	2847 ± 6
W	6	36(13)	3169 ± 71 3156 ± 71	3207 ± 7

[i] [i]The values in the brackets are the number of shots considered in the statistics.
[ii] Two standard deviation of uncertainty were used. (m) stands for the radiance temperature of the melting plateau and (f) for the radiance temperature of the freezing plateau.
[iii] Literature references in Chapter 1.

As it can be seen, the results were not in perfect agreement with the references. The observed depression of the radiance temperature can be due to “pyrometry effects” linked with the behaviour of the specimens more than an insufficient purity of the specimens themselves. These sort of tests have permitted to identify some important error sources of the present approach, like for example the fact that an irregular distribution of the laser power profile on its spot on the specimen surface, and a high thermal conductivity of the specimen itself can result in a slightly wrong temperature reading by the pyrometer (e.g., size of source effect).

Some additional experiments were carried out on niobium specimens in order to validate a Phase Field simulation of the current laser heating tests developed by Dr. M. J. Welland using COMSOL Multiphysics. In this part of the work, experimental and calculated heating curves without phase transitions, melting / freezing thermograms and steady state conditions were compared successfully, ensuring that most of the phenomena occurring during the experiments are reasonably understood. This kind of simulation has in fact the goal of helping the comprehension of phenomena which would not be directly accessible to measurements under the current experimental conditions.

Finally, the spatial profile of the heating laser beam was directly measured on the specimen surface. A large discrepancy (around 5 cm) was found between the laser focal distance of the high-power infrared laser and the focal distance of the visible low-power pilot laser employed for alignment. This was an important finding insofar it resulted in many practical cases in an effective high power laser profile considerably different from the one expected (flat power profile on the specimen surface). The measured real laser profile could partly explain some deviation of the current test results from the melting points of standard metals. It is at the same time a fundamental input parameter for the Phase Field modelling of the current experiments. This last part of the work is still ongoing at ITU.

Refractory oxides properties

The current investigation on the melting behaviour of refractory oxides yielded new data for three types of compounds: CaO, CeO_2 and the mixed oxides UO_2 - ThO_2. The melting point of CaO, which has been for three decades a controversial data, has been reassessed in the present work. The obtained value is in reasonable agreement with the previous works carried out with containerless techniques. The assessed value of the present work for the melting /freezing point of CaO under oxidizing conditions (compressed air) is (3126 ± 79) K (two standard deviations). The experiments performed under reducing conditions (i.e., under Ar) returned a value comparable with the previous investigations led with more traditional

techniques of furnace heating: 2963 K, sensibly lower respect to the assessed one. Interestingly, in the latter case, the molten area resulted black. This phenomenon can be ascribed to a change in the crystalline structure of the molten area, or to metastable oxygen losses. Therefore, it seems reasonable to consider only the experiments under oxidising conditions as representative for the melting/freezing point of stoichiometric CaO. A similar behaviour was observed in the experiments performed on CeO_2. When the specimens were melted under a reducing atmosphere, the molten area became black. This was ascribed to oxygen losses and, consequently, to a modification in the crystalline structure of the specimens. During the experiments on this compound, the atmosphere effect on the detected melting temperature was evident. The current melting/solidification temperature of CeO_2 under oxidising conditions is (2743 ± 33) K, whereas under reducing conditions is (2675 ± 47) K (two standard deviations). The first temperature is lower than the highest reported in the literature (around 3000 K), which indicates that the oxygen potential produced in the current experiments was probably still to low to maintain the O/Ce = 2 stoichiometry during melting. Higher oxygen pressures could however not be produced with the set-up used in this work for safety reasons. The CeO_2 solidification temperature obtained under reducing conditions agrees well with earlier investigations, instead. Both the studies on CaO and CeO_2 were useful not only from a fundamental research viewpoint, but also for the optimization of the experimental parameters in order to study semi-transparent oxides with high oxygen potential at the melting point. These parameters could then be employed for the study of ThO_2 and the mixed UO_2-ThO_2 oxides (TOX). For ThO_2 the results obtained in this work under oxidising and reducing conditions are comparable. This indicates that the thorium dioxide vapour pressure is low enough for its effects to be compensated by the quickness of the experiments, despite the extremely high melting point. The solidification thermal arrest was detected at a rather reproducible temperature of (3622 ± 65) K (two standard deviations), in accordance with literature data. In addition, however, two other features were observed. An higher-temperature inflection, tentatively attributed to a gas / liquid transition, at (3808 ± 155) K and a lower-temperature inflection probably related to a non-congruent

solidification of non-stoichiometric ThO_2 at (3468 ± 77) K are reported. These inflections had already been reported in some literature, but they had probably been overlooked by previous researchers. The rather large uncertainty bars (two standard deviations) are related due to the difficulties in the detection of the latter features and in the control of the experimental conditions. In this case the important message issued from this work is that even the melting behaviour of an extensively studied compound like ThO_2 still presents open questions, mostly related to the complex oxygen chemistry at very high temperature.

For comparison, also the melting point of pure UO_2 was measured at (3115 ± 30) K. This value is in fair agreement with the well assessed literature data (3130 ± 20) K, confirming the good accuracy of the current experimental method for the measurement of this kind of compounds. The slight discrepancy can probably be attributed to some of the aforementioned error sources extensively deepened in the validation study carried out on reference metals. Finally, six intermediate composition of the pseudo-binary system UO_2-ThO_2 (TOX) were analysed with the same experimental approach. The main issue of these last experiments was the control of oxygen, uranium and thorium distribution before and after the melting process, in order to avoid segregation. This phenomenon was limited by the optimisation of the experimental parameters, particularly the short duration of the heating / cooling cycles and the atmospheric conditions aimed at minimizing the non-congruent vaporization. In addition, the uncertainties related to the values of the normal spectral emittance, used to correct the data from the fast pyrometer, highly affected the final results of the intermediate compositions. Despite the large uncertainties affecting the results, they follow a fairly well defined trend throughout the TOX compositions. Whilst between the 20 and 40 mol% ThO_2 the current results well suit the older data, in the region of high content of ThO_2 they follow a similar trend but shifted at higher temperature. This behaviour is logic, when one considers that the old solidus and liquidus lines were assessed in the 1950's and the ThO_2 - rich part of the phase diagram had never been revisited since then, with the exception of pure thorium dioxide. Clearly, these early curves could not take into account the higher melting point of ThO_2, which was soundly assessed only in the

1980's and 1990's. As far as the low-content of ThO_2 results are concerned, they confirm the pronounced change in the slope of the solidus / liquidus line with a minimum value at about 5 mol% ThO_2. Further experiments are needed in order to refine the current data, especially in the vicinity of the 50 mol% ThO_2 and in the low – content of ThO_2 region. In addition, a deeper analysis of the normal spectral emittance should be planned so as to reduce the experimental uncertainties band. A summary of the experimental results obtained in this work on refractory oxides is reported in Table 2.

Table 2. Summary of the experimental campaign on refractory oxides. The sub – column labelled "hp", resume the experiments performed with the high – pressure system.

Materials	Specimens	Experiments [i]		Assessed melting temperature / K		Comments
			hp		hp	
CaO	10	28(10)	42(/)	3126 ± 79	/	
CeO_2	13	41(16)	67(/)	2675 ± 47	/	Under Ar
				2743 ± 33	/	Under Air
UO_2	3	5(4)	3(3)	3115 ± 30	3106 ± 75	
TOX 5	1	9(6)	/	3020 ± 67	/	
TOX 20	4	4(4)	15(4)	3149 ± 19	3158 ± 69	
TOX 40	2	/	10(3)	/	3336 ± 39	
TOX 60	1	/	7(7)	/	3348 ± 61	
TOX 80	2	/	5(3)	/	3573 ± 55	
TOX 95	2	6(4)	/	3587 ± 34	/	
ThO_2	6	35(20)	12(8)	3622 ± 65	3616 ± 73	

[i]The values in the brackets are the number of experiments considered in the statistics.

Future work

The current laser heating / fast pyrometry approach for the study of the melting behaviour of refractory ceramics has led in the last few years to results in agreement with previous literature data only in a limited number of cases. The new experimental data were far from the earlier ones whenever highly reactive compounds (particularly compounds with an elevated oxygen pressure) were investigated. This showed the better suitability of a fast and containerless heating for materials chemically active at high temperature.

In the present thesis, a thorough research of the error sources related to the experimental method (e.g., SSE, laser spot size, etc.) and their following limitation or correction has been extensively initiated. This research work has yielded important results, and should be continued. In particular, the calibration in energy and in power of the excitation laser should be completed, and the technique for the emittance determination improved or changed.

This experimental approach has then been extended in this work to semitransparent oxides, and to nuclear materials like UO_2, ThO_2 and their mixed oxides. Since these latter compounds are characterized by a relatively low oxygen potential, as expected, the current results obtained on them are in fair agreement with the literature ones, which could however be refined thanks to the present data. This confirms the validity of the current approach, and encourages the use of the current method to complete the investigation of the melting behaviour of more actinide oxides, and more generally, to investigate high-melting temperature and / or high-oxygen potential materials.

Appendix A

Experimental methods for phase transition temperature measurements

A.1 Introduction

The study of a physico - chemical system under extreme conditions can lead to a much clearer insight into its thermodynamic and thermophysical properties. In particular, the investigation of the high temperature and high pressure regions of the phase diagram has seemed in the last decades particularly promising, especially as more and more sophisticated experimental devices have been studied and developed. In this work a well known method [1] described in detail in Chapter 2 has been used to investigate the melting temperature of some high-melting materials, of interest for nuclear industry, and their behavior under these conditions. Thanks to this technique some experimental issues have been dealt with:

- Measurements were performed under pressurized gas has been performed in order to minimize incongruent sample evaporation;
- Containerless conditions have been produced in order to avoid contamination of the samples.

This appendix, after a short review on the fundamental concept behind the method, contains a brief introduction to the experimental techniques for the detection of the HT phase transition.

A.2 Backgrounds – the phase rule

A phase is a homogeneous, physical distinct and mechanically separable portion in a heterogeneous system. Willard Gibbs (1839 - 1903), Professor of Physics in Yale University, exhibited how, in a perfectly general manner, without any hypothetical assumption as to the molecular condition of the participating substances, all equilibrium cases could be grouped into classes [2]. Using the laws of thermodynamics and considering only three independent variables - temperature, pressure and concentration of the components (neither gravity nor other forces) - he enunciated the theorem known as Phase Rule, by which he defined the condition of equilibrium as a relationship between phases and components of a system. The peculiarity of a component is that its concentration can undergo independent variations in the different phases. For example in the system liquid water – ice, there are two phases (liquid and solid) and only one component, which is water. Oxygen and hydrogen, the chemical elements which form water, are not components, because they are present in the system in a given amount and definite proportion to form water, therefore their concentration cannot be varied independently.

According to Gibbs' phase rule the degree of freedom (or variance) of a system, i.e., the number of independent variables necessary to fully define the state of the system, is given by

$$F = C + 2 - P \tag{A.1}$$

being C the number of components and P the number of phases inside the system. If one of the intensive variables is fixed (e.g., the pressure), eq. (A.1) becomes

$$F = C + 1 - P. \tag{A.2}$$

Generally, systems possessing the same variance will exhibit a similar behavior during phase transitions, no matter how dissimilar the systems may appear. According to the Phase Rule, therefore, it may possible to classify different systems as invariant ($F = 0$), univariant ($F = 1$), bivariant ($F = 2$) and multivariant ($F > 2$).

A.3 Methods for the melting temperature investigation

Both an accurate temperature determination and a thorough characterisation of the sample at the moment of the phase transition are fundamental issues in the experimental determination of a phase diagram.

When the transition is detected with "static" methods, the sample is kept under certain temperature and pressure conditions, then the number of components and phases are determined. This can be done by measurements at temperature (e.g., high temperature X-ray diffraction) or by cooling the system so rapidly as to maintain the phase produced during the transition even at room temperature (quenching).

When the sample temperature is changed and scanned in order to detect the transition, the method is called “dynamic”. Thermal arrest is the most used method of this kind.

A.3.1 Thermal analysis

During the transition two phases coexist, thus $P = 2$. If a single-component system is considered, then $C = 1$. Considering a constant pressure situation, from the Phase Rule, an invariant system is obtained, that is $F = 0$. This means that the temperature must be constant during all the melting/freezing process. Fig. A.1a represents a typical solidification arrest of congruent melting materials.

More complicated is the situation in which more than one component is present inside the system. If $C = 2$ then $F = 1$, thus the temperature does not remain constant during the phase transition. In this situation liquid and solid phases coexist in general with different compositions, and the phase transition occurs in a temperature range instead of at a single temperature (Fig. A.1b). During a heating process, the temperature at which the first drop of liquid is formed is called solidus, whereas the temperature at which all the sample is liquid is called liquidus. On a cooling stage the temperature at which the first solid nucleus appears is the liquidus, whilst the solidus is the temperature of complete solidification of the specimen.

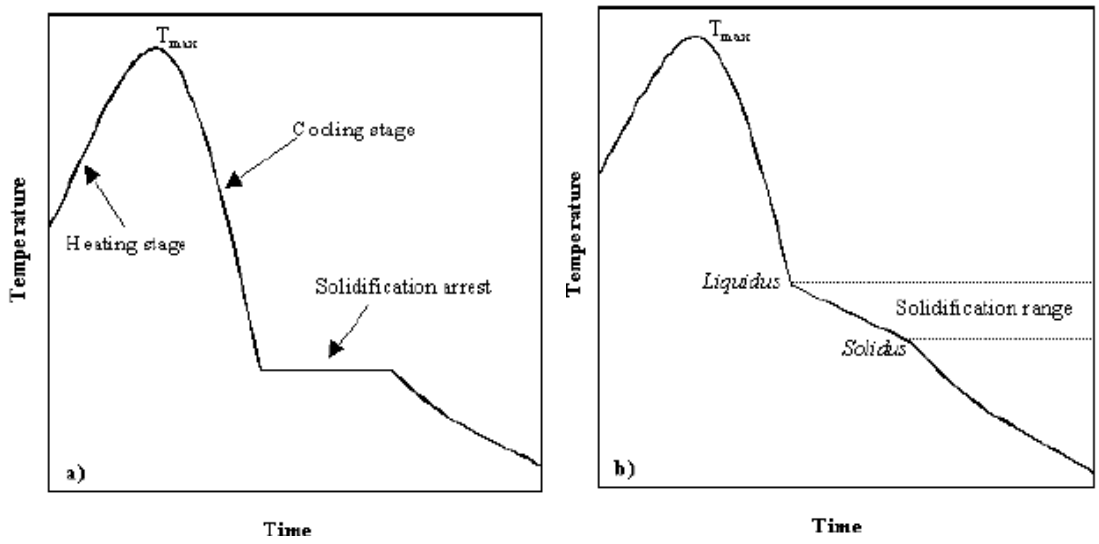

Fig. A.1. a) Freezing transition of congruent melting materials. b) Freezing transition of non – congruently melting sample [1].

During solidification, two distinct phenomena occur: "nucleation", that is when a small piece of solid is formed inside the liquid, and growth which occurs when atoms from the liquid "stick" to the solid part until no liquid remains. No similar process occurs on melting when whole crystalline structure collapse into the liquid phase at once at the melting temperature. With the approach employed in this work, it is much more difficult to identify melting than solidification. For this reason, most of the current analysis refers to the solidification transition.

In an ideal system at the Thermodynamic (TD) equilibrium, the formation of the first solid should start when the temperature of the liquid cools below the freezing temperature due to the low free energy of the crystalline structure of the solid. However, even below the equilibrium melting temperature a small particle of solid is not necessarily stable because of the free energy associated to the solid – liquid interface. Therefore the change in free energy between the liquid and the solid phase has to take into account the contribution due to the interface as well as the contribution of the volumetric free energy of the phases as [3]

$$\Delta G = -\frac{4}{3}\pi r^3 \Delta G_V + 4\pi r^2 \Delta G_{INT} \qquad \text{(A.3)}$$

where ΔG_V is the volumetric free energy variation between liquid and solid, and ΔG_{INT} the interfacial free energy variation. ΔG_V can be written as

$$\Delta G_V = \Delta H - T\Delta S \tag{A.4}$$

where ΔH is the enthalpy variation, T the temperature and ΔS the entropy variation. When during solidification the system reaches the equilibrium

$$\Delta G_V = \Delta H_f - T_e \Delta S_{sl} = 0 \tag{A.5}$$

being ΔH_f the latent heat of fusion (i.e., the enthalpy of fusion), T_e is the equilibrium temperature and ΔS_{sl} is the variation of the entropy of the system when from liquid it becomes solid. From eq. (A.5):

$$\Delta S_{sl} = \frac{\Delta H_f}{T_e} \tag{A.5a}$$

Substituting eq. (A.5a) in eq. (A.4) in the case of the transition from liquid to solid phase:

$$\begin{aligned} \Delta G_V(T) &= \Delta H_f - T\Delta S_{sl} = \Delta H_f - T\frac{\Delta H_f}{T_e} = \\ &= \Delta H_f \frac{\Delta T}{T_e} \end{aligned} \tag{A.6}$$

being ΔT the difference between the equilibrium temperature and the temperature T, which is called undercooling.

Replacing the derived eq. (A.6) in eq. (A.3), ΔG is derived as a function of the solid grain radius r:

$$\Delta G(r) = -\frac{4}{3}\pi r^3 \frac{\Delta H_f \Delta T}{T_e} + 4\pi r^2 \Delta G_{INT}\,. \tag{A.7}$$

ΔG is plotted in Fig. A.2.

During the cooling, assuming that the solid crystallite has a spherical shape, when its radius is smaller than a critical radius r^* it tends to remain liquid in order to minimize the free energy. In fact a further growth of the solid nucleus would cause an increase in free energy. The specimen in this situation continues to cool down until a temperature T, lower than the equilibrium solidification temperature T_e, is reached for which the solid radius is larger than the critical radius.

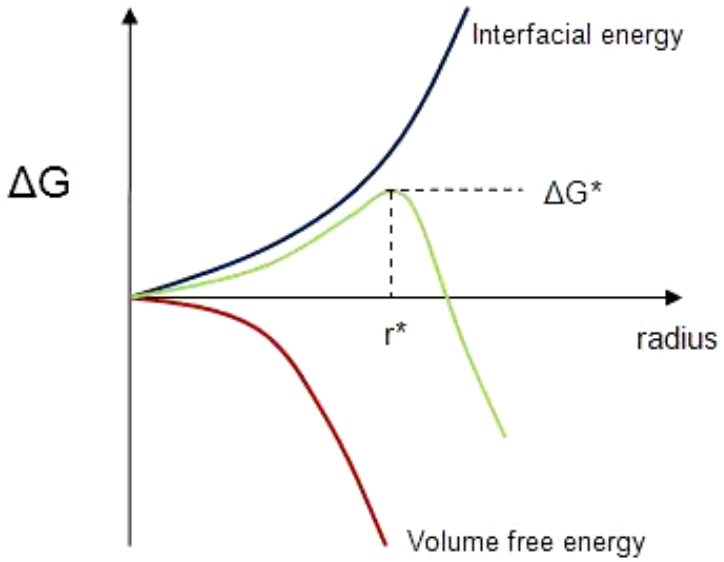

Fig. A.2. Change of the free energy due to the formation of a spherical crystal.

The critical radius at a temperature $T = T_e - \Delta T$ is the value of the radius at which $\Delta G(r)$ is maximum. r^* is therefore the radius at which vanishes the derivative of $\Delta G(r)$ with respect to r [3]

$$r^* = \frac{2 \cdot \Delta G_{INT} \cdot T_e}{\Delta H_f \cdot \Delta T} \tag{A.8}$$

However, except for some particular experimental conditions, "homogeneous" nucleation that is promoted only by free energy fluctuation into the liquid when the concentration of the impurities is very low hardly happens [4]. In fact most materials solidify with much smaller undercooling than predicted for homogeneous nucleation ($\approx 0{,}2T_e$) based on fluctuations only. Impurities present inside the liquid

or the wall of the liquid container can catalyse the nucleation by making the radius of the solid embryo greater than the critical radius with very little liquid-solid surface. In the current approach, the catalysing surface is the unmolten material that surrounds the liquid pool of molten material. In this way the molten material cannot be contaminated with other elements, leading to more accurate freezing temperature measurements.

Undercooling is an important source of error if the determination of the equilibrium freezing temperature of the system is sought. The cooling rate is one of the most important parameters to be controlled during the experiments, in order to minimise the extent of the undercooling. Increasing/decreasing of the cooling rate can change radically the behavior of the system. Since for some applications, nucleation must be avoided, rapid cooling rate is imposed to the system. Thus there may be not enough time for the nuclei to form and grow (quenching of the high temperature phases). From another point of view, depending on the interfacial energy and the speed of diffusion, high cooling rate may increase the amount of undercooling which the system undergoes. Another consequence of rapid cooling can be the production inside the system of non – equilibrium structures (e.g., glasses).

An example given in [4] is the copper–nickel alloy, which has an isomorphous binary phase diagram. In this kind of system, only one solid phase forms, hence the two component exhibit complete solid solubility. During slow cooling, nuclei can diffuse and form equilibrium structures. Since the diffusion is low in solid, it may happen, during a fast cooling, that nuclei from the first formed solid do not reach the new solid nuclei formed by the solidifying liquid. This process producing a non–uniform composition in the material is called segregation. In this event the resulting solid phase often exhibits a so called cored structure.

A.3.2 Thermal arrest methods

In this category of experimental methods the temperature of the phase transition is detected by looking at the change in the cooling/heating rate of the sample due to the release/absorption respectively of the latent heat of transition.

In traditional thermal arrest techniques applied to materials melting below 2700 K approximately, electrical furnaces are generally used as heat sources. If the sample is metallic, inductive heating furnaces can be employed, with the advantage that the electromagnetic field induced in the specimen acts as a stirrer of the liquid. Stirring is a key concept for the homogeneity of the process and it must be provided in some other way if an inductive furnace cannot be used. Temperature can be measured by means of traditional thermocouples, or with optical pyrometers, which are the only possibility above 2500 K. When thermocouples are employed contamination of the specimen represents a considerable problem. Otherwise when an optical pyrometer is used, the holder and the specimen must be shaped in such a way that blackbody conditions are achieved (optical emittance as close as possible to unity), or alternatively, the sample optical emittance must be known. On the other hand, containerless conditions are desirable in order to avoid contamination of the sample. Sample levitation is a possible method of holding a specimen under containerless conditions. Several types of levitation systems can be implemented based on hydrodynamic, acoustic and electromagnetic techniques.

Nelson et al. [5], for example, coupled a levitation technique with solar image heating to obtain high temperature measurements in containerless conditions, (Fig. A.3).

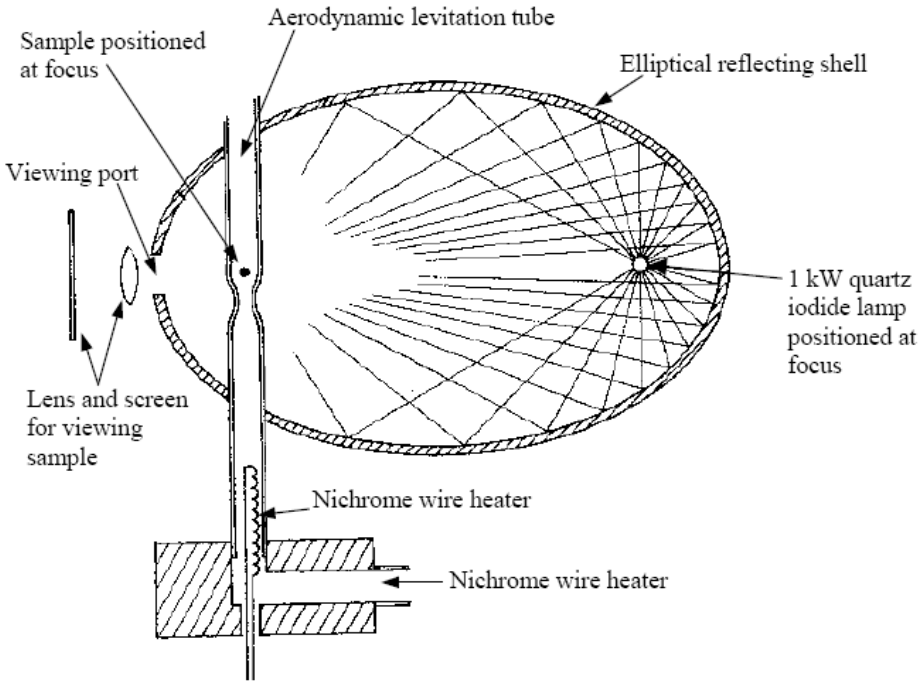

Fig. A.3. Schematic of a solar image heating coupled with levitation technique [5].

The specimen is placed at one of the foci of the ellipsoidal reflecting shell, the inner wall of which has a reflectance close to unity. A 1 kW quartz iodide lamp is positioned at the other focus of the ellipsoid. In this way, all the light emitted by the lamp is concentrated on the sample, which can be heated up to temperatures above its melting point. The advantages of this method are the absence of electrical heating, which permits to use it even with insulators and the possibility of carrying the experiments under high pressure. Furthermore, since no time limit exists for the duration of the experiment, static equilibrium conditions can be reached even at high temperature. The fact that the sample is heated by white light, which can mix up with the radiation from the hot specimen, inhibits pyrometric measurements and it is a drawback of the method.

Foex [6] used a solar furnace containerless technique to measure melting points of several refractory oxides. The solar apparatus (Fig. A.4) consists of a parabolic, fixed mirror with silvered glass backing. This mirror, receives solar radiation from a movable mirror (heliostat). The sample is placed inside a centrifuge furnace consisting of a metallic cylinder that turn around its axis and it is refrigerated by

flowing water. The thermal analysis is made during the cooling stage by means of a pyrometer placed in front of the cavity.

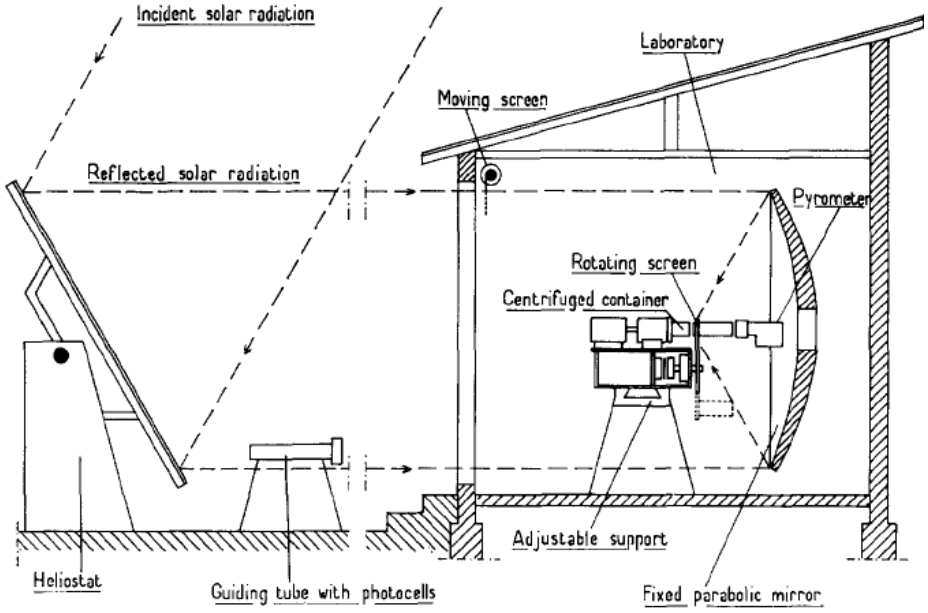

Fig. A.4. Solar furnace used in Foex's experiments [6].

During the experiments, it was possible to obtain conditions approximating those of a blackbody. This remote heating technique has remarkable features in common with the method used during the present work. Firstly, it is a containerless method, because the molten matter is surrounded by the same unmolten material, avoiding chemical contamination. Secondly, with this technique, Foex managed to measure very high temperature liquid/solid transition in very common refractory oxides. Finally, Foex obtained results on calcium oxide which are rather in agreement with the present work.

Noguchi et al. [7] used a similar heliostat to measure the system ZrO_2-CaO, but they detected radiance temperature at 650 nm instead of true temperature by analysis of the cooling curves. They calculated the spectral emittance from reflectance data at 650 nm.

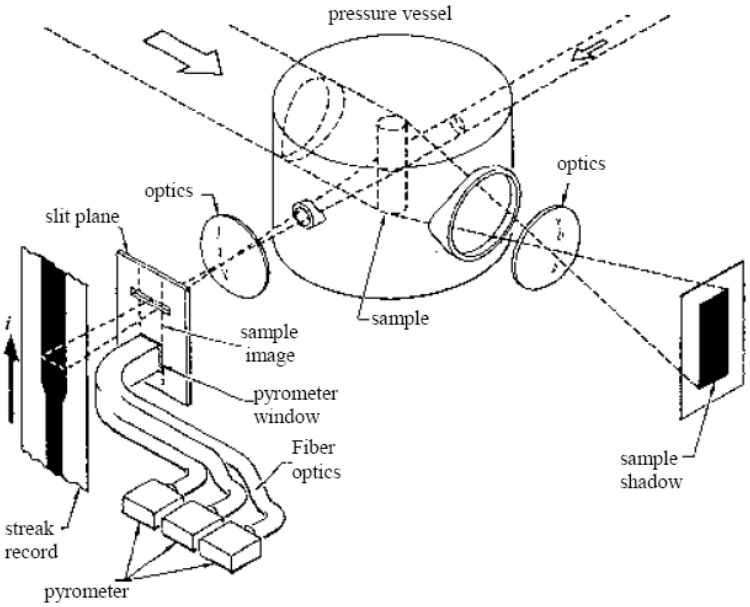

Fig. A.5. Schematic representation of exploding wire used reported in [8].

Dynamic methods can constitute a better approach with respect to problems due to long duration of experiments carried out with static methods (i.e., chemical reaction, evaporation, contamination from the container, etc.). One of the most frequently used is the so called "exploding wire", well described in Cezairiliyan's [8] review. The apparatus, shown in Fig. A.5, consist of an electrical power-pulsing circuit and high-speed measuring circuits, able to detect the electrical current through and voltage across the sample. The temperature is measured by a high-speed pyrometer. Both high-temperature and high-pressure conditions can be achieved with this method. On the other hand, the fact that ceramic and non-uniform conductor materials cannot be investigated is an important restriction.

If the detection of the solidus transition is investigated, the heating stage is preferably used. In fact, undercooling and fast liquid diffusion phenomena can alter the measurement during the cooling stage. A rather old, but effective technique is the Pirani and Alterthum [9] method, in which the first drop of liquid is directly observed on the sample. The sample is a rectangular or cylindrical bar, in which flows an electrical current. A hole is made in the centre of the bar in the normal direction respect to the axis (Fig. A.6), and a pyrometer is focused on it.

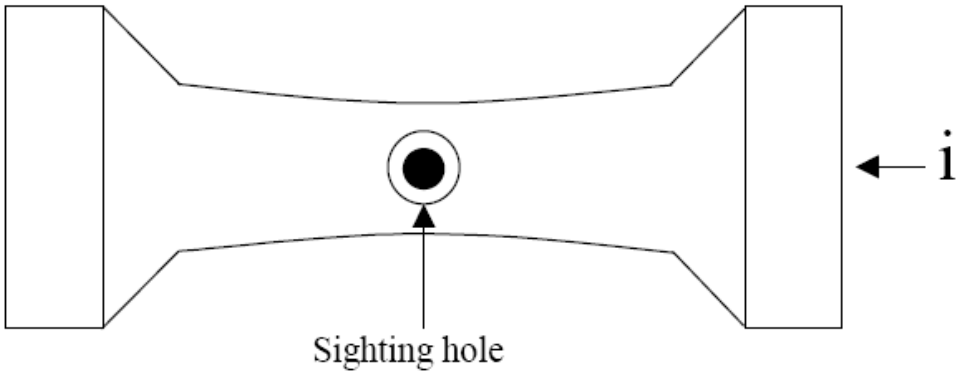

Fig.A.6. Pirani and Alterthum method [9].

Since near the hole the cross section is least, and the current density maximum, it will appear brighter than the sample when current is flowing. Moreover, the hole can be considered, with good approximation, as a blackbody. When the melting temperature is reached and the first liquid is formed, the emittance drops and a black spot can be seen. From the registered thermogram, the last temperature at which liquid has not appeared yet, should be taken as the solidus. Since the heating source is electric current, this method can be applied only with conductive materials. Latta and Fryxell [10] built a special device to detect phase transition with classical thermal arrest methods, and with the aim of reach conditions as close to equilibrium as possible and reduce the effect of the poor stability of hypo- and hyper-stoichiometric uranium dioxide. The furnace and the crucible used in Latta and Fryxell experiment are shown respectively in Fig. A.7a and Fig. A7b. The furnace was designed in order to have homogeneous temperature. Latta and Fryxell detected a relevant W-contamination of the encapsulated samples. The poor chemical stability of the compounds under investigation carried to the formation of a ternary oxide U_xWO_3, detected by XRD analysis, which is of the same form as the detected in Foex's work.

Kato et al. [11] published a study on the mixed (U, Pu)O_2 oxides, using a traditional thermal arrest technique. They used crucibles of different materials (tungsten and rhenium) and shapes, in order to demonstrate that in the Pu-rich samples, the contamination affect the solidus/liquidus results. Kato et al. used five different capsules (Fig. A.8).

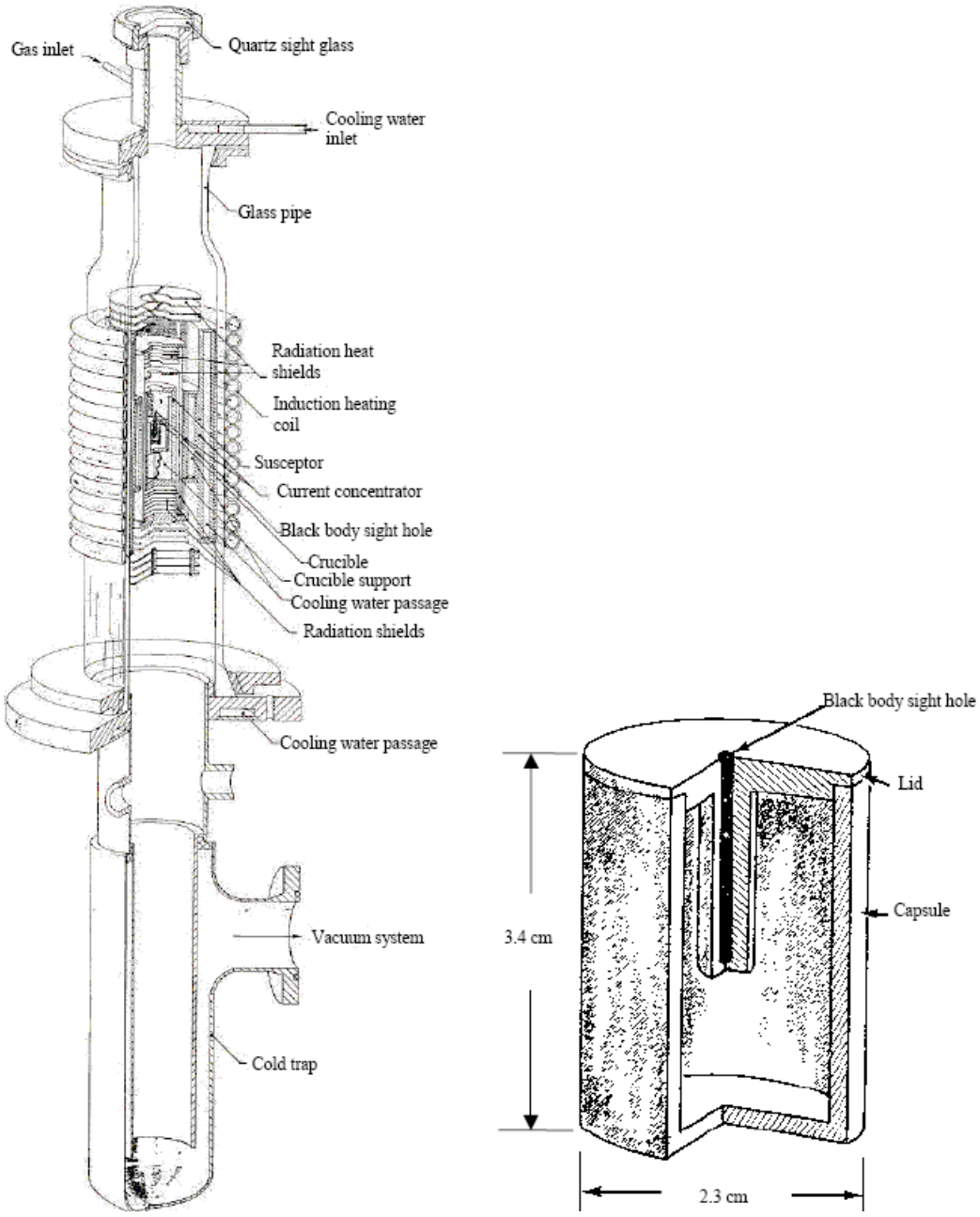

Fig. A.7. a) Furnace used in Latta and Fryxell experiments [10]. b) W- capsule sample container used by same authors [10].

The samples were heated above their melting temperature, and both heating and cooling curves were observed. Temperatures were measured with optical pyrometer focused on the bottom of the W-capsules where blackbody conditions were achieved with good approximation.

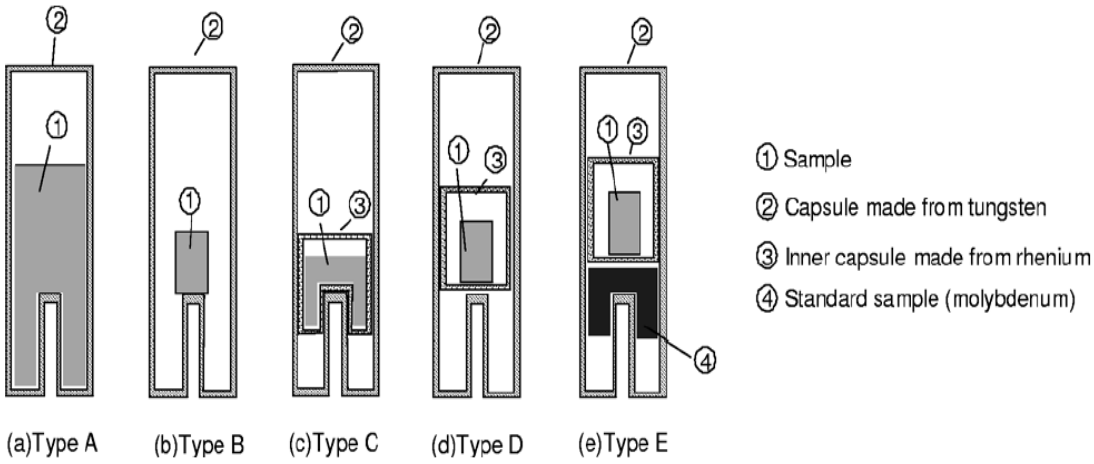

Fig. A.8. Capsules used in Kato's work [11].

Kato et al. were not able to measure directly the melting temperature of pure PuO_2, because they detected two distinct inflection instead of one, as expected with congruent melting materials. They attributed this results to the high chemical reactivity of liquid PuO_2 in presence of rhenium and strongly with tungsten. This could have carried to the oxidation of Re and to the reduction of the samples. The remote heating method used during the present work, was previously adopted by De Bruycker [12] to study the pseudo binary UO_2-PuO_2 system. Thanks to the containerless conditions and the short duration of the experiments, he was able to limit the effects of the liquid PuO_2 reactivity.

Accurate measurements of calcium oxide melting temperature was obtained by T. Yamada et al. [13], using another remote heating technique. The apparatus is shown in Fig. A.9.

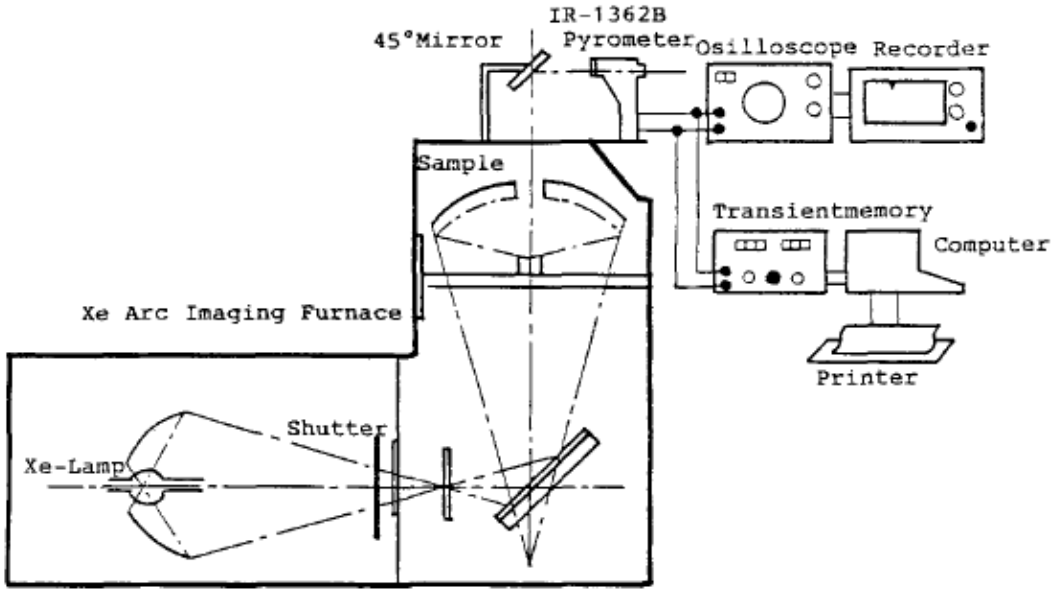

Fig. A.9. Arc imaging furnace with digital pyrometer [13].

The Pyrometer with Arc Image Furnace (PAIF-I) system consisted of the arc imaging furnace, a micro–computer with transient memory and a pyrometer which detects the radiance temperature of the sample at different wavelength. Since Yamada's method is a containerless technique, contamination is avoided. Previous results obtained with traditional furnace heating technique, underestimated the calcium oxide melting temperature by 300 K, due to contamination of the sample.

A.4 Conclusions

The investigation of physico–chemical properties of refractory materials is subjected to difficulties, which were encountered in previous studies, and which must be dealt:

- Container which avoids sample contamination is needed. Otherwise containerless technique should be used.
- Incongruent evaporation or sample decomposition due to very high temperature conditions should be faced using suitable methods.
- The heating source should be compatible with the sample and with the temperature measurements.

A.5 References

[1] D. Manara, "Melting transition measurements in uranium dioxide", PhD Thesis, Technical Note JRC-ITU-TN-2004/05 (2004).

[2] A. Findlay, A. N. Campbell and N. O. Smith, "The Phase Rule", 9th edition, Dover Publication Inc., 1961.

[3] D. R. Askeland, "The Science and Engineering of Materials", 3rd S.I. Edition, Chapman & Hall, 1996.

[4] R. W. Cahn and P. Haasen, "Physical Metallurgy", 3rd revised and enlarged edition, Elsevier Science Publisher BV, 1983. H. Biloni, Cap. 9, "Solidification", 478.

[5] L. S. Nelson, N. L. Richardson, K. Keil and S.R. Skaggs, High Temp. Sci., **5** (1973), 138.

[6] M. Foex, Sol. Energy, 9 [1] (1965), 61.

[7] T. Noguchi, M. Mizuno and W. M. Conn, Sol. Energy, 11 [3 – 4] (1967), 145.

[8] A. Cezairiliyan, High Temp. – High Press., 11 (1979), 9.

[9] M. Pirani and H. Alterthum, Z. Electrochem., 29 (1923), 5.

[10] R. E. Latta and R. E. Fryxell, J. Nucl. Mater., 35 (1970), 195.

[11] M. Kato, K. Morimoto, H. Sugata, K. Konashi, M. Kashimura and T. Abe, J. Nucl. Mater., 373 (2008), 237.

[12] F. De Bruycker, " High Temperature Phase Transitions in Nuclear Fuels of the Fourth Generation", PhD Thesis, Technical Note JRC-ITU-TN-2011/4 (2011).

[13] T. Yamada, M. Yoshimura, and S. Somiya, J. Am. Ceram. Soc., 69 [10] (1986), C–243.

Appendix B

Background on pyrometry

Optical pyrometry is practically the only temperature measurement technique available for the high temperatures, above 2500 K. Through this technique is in principle possible to measure the temperature of a specimen through the detection of radiant flux thermally emitted by it.
The main properties and definitions of thermal radiation processes are described in this section.

B.1 Spectral Radiance

Taking into account a surface element of area dA_1 and the emitted radiant power Φ from that surface element, spectral radiance is defined as the radiant power emitted at the wavelength λ in the (θ,ϕ) direction, per unit area of the emitting surface normal to this direction, per unit solid angle $d\omega$ around this direction and per unit wavelength $d\lambda$ around λ [1].

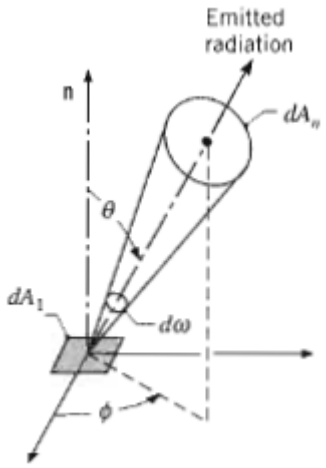

Fig. B.1. Emission of radiation from a differential area dA_1 [1].

$$L_\lambda(\lambda,\theta,\phi) = \frac{d^3\Phi}{dA_1 \cos\theta \, d\omega \, d\lambda} \tag{B.1}$$

In eq.(B.1) the area dA_n is the component of dA_1 perpendicular to the direction of the radiation so it is equal to $dA_1 \cos\theta$.

B.2 Self – exitance

The spectral self – exitance M_λ of a surface element dA_1 at a wavelength λ is defined as the radiant power per unit area associated with emission into the hemispheric space above dA_1 within an infinitesimal wavelength interval $d\lambda$ around λ [1].

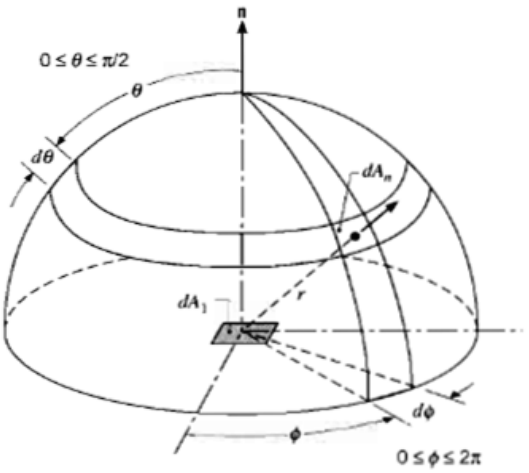

Fig. B.2. Emission from a differential element of area into a hemisphere [1].

If the directional distribution of spectral radiance is known, spectral self - exitance may be calculated by integration of eq.(B.1) as:

$$M_\lambda(\lambda) = \frac{d^2\Phi}{dA_1 \, d\lambda} = \int_{\phi=0}^{2\pi} \int_{\theta=0}^{\pi/2} L_\lambda(\lambda,\theta,\phi) \cos\theta \, \sin\theta \, d\theta \, d\phi \tag{B.2}$$

with

$$d\omega = \sin\theta \, d\theta \, d\phi \tag{B.3}$$

The so-called total self-exitance, M, may be computed by integration over all wavelengths.

If a surface emits radiation independently of the direction, (isotropically diffuse emitter) the spectral self - exitance becomes a function of the wavelength only and it follows from eq.(B.2)

$$M_\lambda = \pi L_\lambda \tag{B.4}$$

$$M = \pi L \tag{B.5}$$

where L is the total radiance. Note that self – exitance refers to emitted radiation only, instead of exitance that refers to radiation leaving a surface due to emission and reflection.

B.3 Irradiance

When the radiation is incident on a surface the foregoing concepts may be adapted to define radiometric quantities for incident radiant. In equation B.2, B.4 and B.5, M_λ is replaced by the spectral irradiance E_λ and M by the total irradiance E.

B.4 Blackbody

To evaluate all the quantities described above for a real surface it is first necessary to introduce the concept of blackbody.

A blackbody is a surface that absorbs all incident radiation regardless of wavelength and direction. Furthermore, it is an isotropically diffuse emitter. Finally, for a prescribed temperature and wavelength no surface can emit more than it.

The concept of a blackbody serves as an ideal standard to which real surfaces are referred. There is no real surface that has these properties. However, a very good approximation is realised by the aperture of a cavity with internal isothermal walls (Fig. B.3).

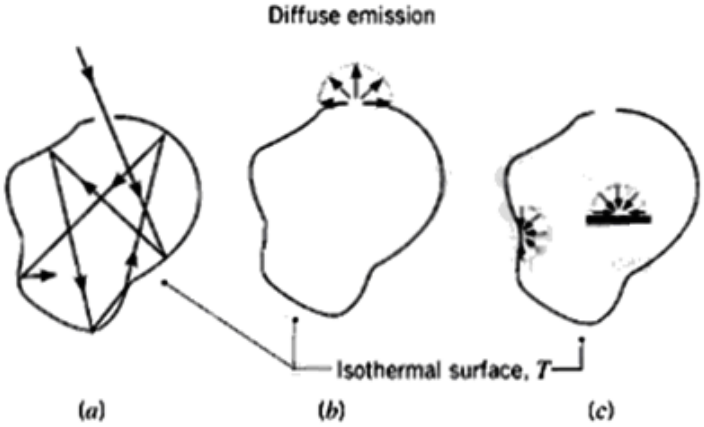

Fig. B.3. Characteristics of an isothermal blackbody cavity. (a) Complete absorption. (b) Diffuse emission from an aperture. (c) Diffuse irradiation of interior surfaces [2].

B.5 The Planck distribution

Planck's radiation law establishes a link between the spectral radiance $L_{\lambda,b}$ at "local" wavelength λ emitted by a blackbody and its temperature T:

$$L_{\lambda,b}(\lambda,T) = \frac{c_{1L}}{n^2\lambda^5}\left[\exp\left(\frac{c_2}{n\lambda T}\right)-1\right]^{-1} \tag{B.6}$$

where $c_{1L} = 2\,h\,c_0^2$ is the first radiation constant for spectral radiance and $c_2 = h\,c0\,k_B^{-1}$ is the second radiation constant. c_0 is the speed of light in vacuum, h is Planck's constant of action, k_B is the Boltzmann constant and n is the index of refraction of the non-attenuating medium in which the blackbody spectral radiance propagates.

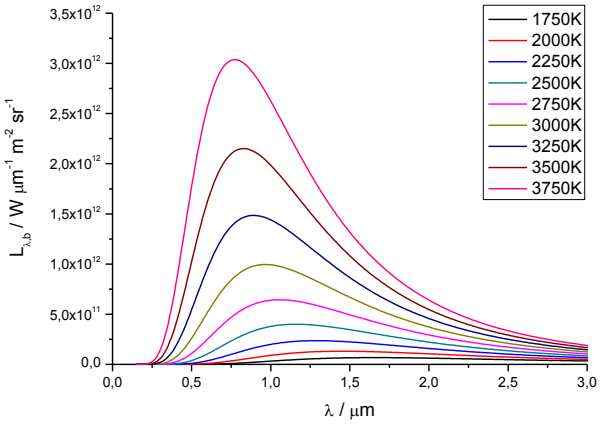

Fig. B.4. Planck's distribution for several temperatures.

In Fig. B.4 it can be seen that

- The spectral radiance is a continuous function of the wavelength;
- At any wavelength the magnitude of the emitted radiation increases with increasing the temperature;
- The spectral region in which most of the radiation is concentrated depends on temperature.

In the limit of the so-called $n\,\lambda\,T << c_2$ Wien´s approximation it is possible to approximate eq.(B.6) as

$$L_{\lambda,b}(\lambda,T)=\frac{c_{1L}}{n^2\lambda^5}\left[\exp\left(\frac{c_2}{n\lambda T}\right)-1\right]^{-1}\approx\frac{c_{1L}}{n^2\lambda^5}\left[\exp\left(\frac{c_2}{n\lambda T}\right)\right]^{-1} \qquad \text{(B.7)}$$

This expression is accurate for short wavelengths and for low temperatures and is better than 1% if $n\,\lambda\,T \leq 3100$ µm K, as can be calculated from eq. (B.7) and eq. (B.6).

Within the measurement uncertainty reported in the present work, n can be approximated by unity, because the pyrometers (detecting radiance) were always located in air at ambient pressure and temperature.

B.6 Wien's displacement law

It can be noticed from Fig. B.4 that the maximum spectral radiance depends on temperature; more precisely it shifts to shorter wavelengths with increasing temperature.
Eq. (B.8) describes this behaviour; it was obtained by differentiating eq.(B.6) with respect to the wavelength and setting the result equal to zero.

$$n\,\lambda_{\max}\,T = 2897{,}8\,\mu\mathrm{m\,K} \tag{B.8}$$

B.7 Stefan – Boltzmann Law

Knowing the spectral radiance of a blackbody from Planck's law and recalling that a blackbody is an isotropically diffuse emitter (the spectral self-exitance is π times the spectral radiance), it is possible to calculate the total exitance as

$$M_b(T) = \int_0^\infty M_{\lambda,b}\,d\lambda = \int_0^\infty \pi L_{\lambda,b}\,d\lambda = \int_0^\infty \frac{\pi c_{1L}}{n^2\lambda^5}\left[\exp\left(\frac{c_2}{n\lambda T}\right)-1\right]^{-1} d\lambda \tag{B.9}$$

Evaluating the integral results in a total exitance that is propotional to the fourth power of the absolute temperature.

$$M_b(T) = \sigma T^4 \tag{B.10}$$

The proportional constant is called the Stefan-Boltzmann constant and it has the value of $5.670\cdot10^{-8}$ W m^{-2} K^{-4}.

B.8 Real surfaces

B.8.1 Emittance[1]

After introducing the concept of a blackbody, it is possible to study the behaviour of real surfaces compared to this standard reference.

A real surface cannot emit more than a blackbody so the ratio of radiation emitted by the real surface to the radiation emitted by the ideal one is defined as emittance.

As indicated in Fig. B.5, radiance may differ considerably from Planck shape for non-ideal radiator. Emittance, in general, is a function of the temperature, direction and wavelength

$$\varepsilon(\lambda,\theta,\phi,T)=\frac{L_{\lambda}(\lambda,\theta,\phi,T)}{L_{\lambda,b}(\lambda,T)} \tag{B.11}$$

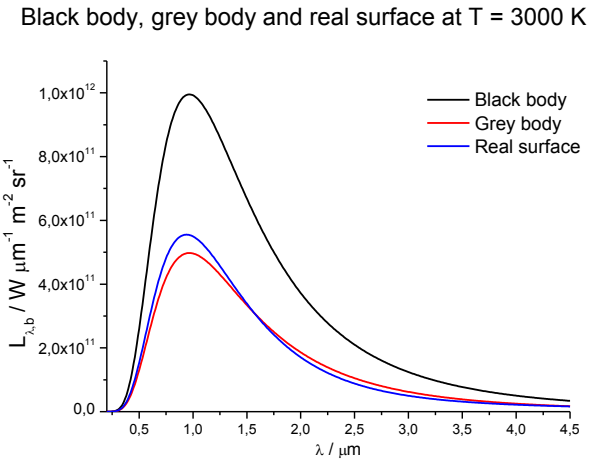

Fig. B.5. Comparison between black body, grey body and a real surface.

The expression above refers to the spectral – directional emittance.

The spectral – hemispherical emittance can be obtained from eq.(B.9) by integration on the direction (θ,ϕ), the result is a ratio of spectral self – exitances

[1] In the literature "emissivity" and "emittance" are often used interchangeably. In some case, the ending "ivity" is reserved for the properties of an optically smooth, uncontaminated surface while the ending "ance" is used to signify that the emissive properties of the surface have been altered by roughness and/or contamination (e.g., an oxide layer). Still others authors, generally use "emissivity" for opaque materials while reserving the ending "ance" for semi-trasparent materials for which the "emittance" varies with thickness. In the present work, emittance will generall be used, even in the case of samples that have melted and re-solidified, whose surface is then quite smooth and clean.

$$\varepsilon_{2\pi}(\lambda,T)=\frac{M_{\lambda}(\lambda,T)}{M_{\lambda,b}(\lambda,T)} \tag{B.12}$$

In the same way, the total – hemispherical emittance is given by integration of the eq. (B.12) over all wavelengths

$$\varepsilon_{t,2\pi}(T)=\frac{M(T)}{M_b(T)}=\frac{\int_0^{\infty}M_{\lambda}(\lambda,T)\,d\lambda}{\int_0^{\infty}M_{\lambda,b}(\lambda,T)\,d\lambda}=\frac{\int_0^{\infty}\varepsilon(\lambda,2\pi,T)\,M_{\lambda,b}(\lambda,T)\,d\lambda}{\int_0^{\infty}M_{\lambda,b}(\lambda,T)\,d\lambda} \tag{B.13}$$

In the case the radiator is a gray body (Fig. B.5), the original shape of Planck´s curve is preserved but with lower emission: the spectral – directional emittance is independent of wavelength.

B.8.2 Other properties (Absorptance, Transmittance, Reflectance)

In section B.1 the concept of radiance (spectral, total radiance) was introduced. Here the processes resulting from interaction of this radiation with a solid (or liquid) medium will be considered.

If the interaction is with a semitransparent medium (Fig. B.6) the radiation incident may be reflected, absorbed and transmitted. Evaluation of these components is difficult because the processes depend on the beam geometry, the incident wavelength, surfaces conditions, the composition and thickness of the medium. These processes are influenced by volumetric effects occurring within the medium.

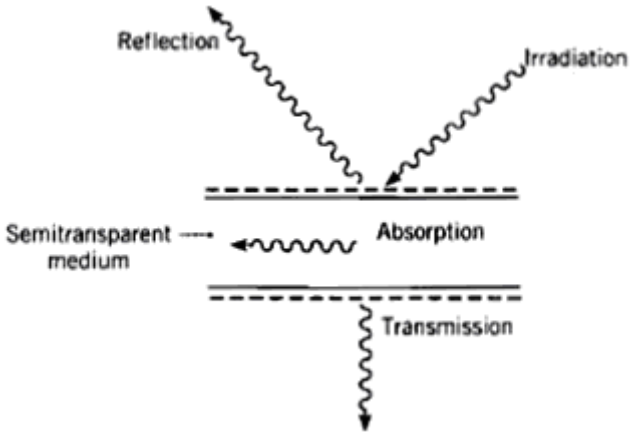

Fig. B.6. Absorption, reflection and transmission processes associated with a semitransparent medium [2].

When the radiation is incident on an opaque medium where the absorption process occurs at only a few wavelengths from the surface, the transmission process can be neglected and the other two processes may be considered as surface phenomena.

B.8.2.1 Absorptance

The absorptance is the ratio between the fraction of the incidence radiation on a surface that is absorbed (*a*) and the incident radiation itself (*i*); like the emittance also the absorptance depends on direction and wavelength and a spectral – directional absorptance may be defined as

$$\alpha(\lambda,\theta,\phi,T) = \frac{L_{\lambda,a}(\lambda,\theta,\phi,T)}{L_{\lambda,i}(\lambda,\theta,\phi)} \tag{B.14}$$

In general, the fraction of radiation absorbed is a function also of the temperature.
If the directional distribution is known, eq. (B.14) can be integrated to obtain a ratio between spectral irradiances

$$\alpha_{2\pi}(\lambda,T) = \frac{E_{\lambda,a}(\lambda,T)}{E_{\lambda}(\lambda)} \tag{B.15}$$

Similarly, the total – hemispherical absorptance is defined as

$$\alpha_{t,2\pi}(T) = \frac{E_a(T)}{E} = \frac{\int_0^\infty E_{\lambda,a}(\lambda,T)\,d\lambda}{\int_0^\infty E_\lambda(\lambda)\,d\lambda} = \frac{\int_0^\infty \alpha(\lambda,2\pi,T)\,E_\lambda(\lambda)\,d\lambda}{\int_0^\infty E_\lambda(\lambda)\,d\lambda} \tag{B.16}$$

B.8.2.2 Reflectance

The reflectance is the fraction of the incident radiation that is reflected by a surface. This property is inherently bidirectional, that is it depends on the direction of the incident and the reflected radiation.

One of the possible definitions is the spectral directional-hemispherical reflectance that considers an integrated average over the hemisphere above the surface associated with the reflected radiation

$$\rho_{2\pi}(\lambda,\theta,\phi,T) = \frac{M_{\lambda,r}(\lambda,T)}{E_\lambda(\lambda,\theta,\phi)} \tag{B.17}$$

where $M_{\lambda,\mathrm{r}}$ is the spectral exitance due to reflection (not emission) and E_λ is the spectral irradiance in the incident direction.

A surface is called isotropically diffuse if, regardless of the direction of incident radiation, the radiance of the reflected radiation is independent on the reflection angle. On the other hand, specular reflection is said to occur all the reflected flux is concentrated along a single direction that lies in the plane of incidence and is symmetric to the direction of incidence with respect to the surface normal (i.e., angle-of-reflection = angle-of-incidence). In this latter case, the surface is called specular.

B.8.2.3 Transmittance

In a semitransparent medium, the transmittance through it, as the reflectance, is a bidirectional property and depends on the modality of interreflections at internal surfaces and on the thickness of the material and its optical properties.

A spectral directional-hemispherical transmittance is defined as

$$\tau_{2\pi}(\lambda,\theta,\phi,T) = \frac{M_{\lambda,t}(\lambda,T)}{E_{\lambda}(\lambda,\theta,\phi)} \tag{B.18}$$

Where $M_{\lambda,t}$ is the spectral exitance at the back surface.

B.8.3 Radiation balance

From energy balance considerations it follows that the sum of the reflected, absorbed and transmitted radiant fluxes must equal the incident radiant flux.

$$\Phi_{\lambda,i} = \Phi_{\lambda,r} + \Phi_{\lambda,a} + \Phi_{\lambda,t} \tag{B.19}$$

Now, recalling the definitions above, eq.(B.19) may be rewritten as

$$1 = \rho_{2\pi}(\lambda,\theta,\phi) + \alpha(\lambda,\theta,\phi) + \tau_{2\pi}(\lambda,\theta,\phi) \tag{B.20}$$

B.8.4 Kirchhoff's law

Kirchhoff's law in its general form states that the spectral – directional emittance is equal to the spectral – directional absorptance for a surface

$$\varepsilon(\lambda,\theta',\phi',T) = \alpha(\lambda,\theta,\phi,T) \tag{B.21}$$

This expression is applicable without restrictions because the two properties are inherent of the surface, the only requirements are that the directions (θ', ϕ' of emission and θ, ϕ of absorption) and wavelength be the same and that the surface be at thermal equilibrium with the environment.

If the incident radiation is isotropically diffuse or absorptance and emittance are both independent of angle (diffuse - spectral surface) eq.(B.21) becomes

$$\varepsilon_{2\pi}(\lambda,T) = \alpha_{2\pi}(\lambda,T) \tag{B.22}$$

On the other hand, if the same incident radiation has a spectral distribution proportional to that of a blackbody at that temperature *T*, or both absorptance and emittance are independent of wavelength (directional-gray surface), then Kirchhoff's law holds for the directional-total properties

$$\varepsilon_t(\vartheta,\varphi,T) = \alpha_t(\vartheta,\varphi,T) \tag{B.23}$$

Combining eq.(B.22) and eq.(B.23) and the conditions of their validity the expression of Kirchhoff's law for the hemispherical-total properties follows as

$$\varepsilon_{t,2\pi}(T) = \alpha_{t,2\pi}(T) \tag{B.24}$$

B.9 Radiation thermometry

Tthis section describes how to apply the foregoing concepts in relation with the radiation thermometers, for measuring the temperature and how the instrument responds to the incident radiation.

First of all two important concepts will be introduced: the definition of the temperature scale and the spectral radiance temperature.

B.9.1 The International temperature scale of 1990 (ITS-90)

The International temperature scale of 1990 (ITS-90) [4,5] defines the temperature *T* above the freezing point of silver (1234,93 K) as

$$\frac{L_{\lambda,b}(\lambda_0,T)}{L_{\lambda,b}(\lambda_0,T_0)} = \frac{\exp\left(\frac{c_2}{\lambda_0 T_0}\right)-1}{\exp\left(\frac{c_2}{\lambda_0 T}\right)-1} \tag{B.25}$$

where T_0 is a reference temperature (the freezing point of Ag, Au or Cu).

The right side of equation is the ratio between the blackbody spectral radiance at an unknown temperature *T* and the blackbody spectral radiance at the temperature of freezing point calculated at a specific wavelength (in vacuum) λ_0.

Eq. (B.25) requires that the radiation thermometer be effectively monochromatic but in real cases it is not and for that reason in the next sections a more operational version of the above definition will be introduced.

B.9.2 Spectral radiance temperature

Considering a real surface (*rs*) and a blackbody (*b*) at the same temperature, they have different spectral radiance because the former has an emittance less than one and they are related by

$$L_{\lambda,rs}(\lambda,\vartheta,\phi,T)=\varepsilon(\lambda,\vartheta,\phi,T)L_{\lambda,b}(\lambda,T) \tag{B.26}$$

Therefore, the concept of spectral radiance temperature T_λ is introduced. It is the temperature of a blackbody emitting the same spectral radiance at a given wavelength as the real surface

$$L_{\lambda,rs}(\lambda,T_\lambda)=\frac{c_{1L}}{n^2\lambda^5}\left[\exp\left(\frac{c_2}{n\lambda T_\lambda}\right)-1\right]^{-1} \tag{B.27}$$

Now, taking into account the spectral region where Wien's approximation is valid, comparing the latter definition with eq.(B.26) and Planck's equation it is easy to obtain an expression that links the real temperature and the spectral radiance temperature

$$\frac{1}{T}=\frac{1}{T_\lambda}+\frac{n\,\lambda}{c_2}\ln\varepsilon(\lambda,\vartheta,\phi,T) \tag{B.28}$$

The above relation is most used in pyrometry. The radiance temperature is always lower than the true temperature since the emittance is less than one.

B.9.3 Spectral response function of radiation thermometer

Recalling the previous definition of the spectral radiance, the radiant infinitesimal flux that enters in the radiation thermometer is

$$d^3\Phi(\lambda,A,\theta,\phi)=L_\lambda(\lambda,\theta,\phi)\,dA\cos\theta\,d\omega\,d\lambda \tag{B.29}$$

The radiation flux passes through several optical elements (filters and lens), with a total trasmittance τ and is then collected by a detector (photodiodes) is

$$d\Phi'(\lambda, A, \theta, \phi) = \tau(\lambda, A, \theta, \phi) L_{\lambda}(\lambda, \theta, \phi)\, dA \cos\theta\, d\omega\, d\lambda \qquad \text{(B.30)}$$

Thanks to the detector the light is converted in an electronic signal S and it may be possible to define the instrumental flux responsivity as the ratio of change in output signal to change in incident flux on the detector

$$R_{\Phi}(\lambda, A, \theta, \phi) = \frac{dS(\lambda, A, \theta, \phi)}{d\Phi'(\lambda, A, \theta, \phi)} \qquad \text{(B.31)}$$

Combining eq.(B.30) and eq.(B.31), an expression for the signal will be obtained

$$dS(\lambda, A, \theta, \phi) = b\,\tau(\lambda, A, \theta, \phi)\, L_{\lambda}(\lambda, \theta, \phi)\, R_{\Phi}(\lambda, A, \theta, \phi)\, dA \cos\theta\, d\omega\, d\lambda \qquad \text{(B.32)}$$

Where b is a constant determined by the electronics that process the detector output signal. If the irradiated area and solid angle became sufficiently small, the dependence on A and (θ,ϕ) of trasmittance, spectral radiance and responsivity will be negligible and only the dependence on the wavelength will remain

$$R_{L}(\lambda) = \tau(\lambda)\, R_{\Phi}(\lambda) \iint_{A\omega} dA \cos\theta\, d\omega \qquad \text{(B.33)}$$

$$S = \int_{\Delta\lambda} L_{\lambda}(\lambda)\, R_{L}(\lambda) d\lambda \qquad \text{(B.34)}$$

where $\Delta\lambda$ is the effective wavelength band width.

Eq.(B.33) defines the spectral radiance responsivity and eq.(B.34) the total output signal of the radiation pyrometer on $\Delta\lambda$.

B.9.4 Measure of blackbody temperature

In eq.(B.31), if the wavelength bandwidth approaches zero one has the ideal case of a monochromatic pyrometer and, if it is calibrated with a blackbody, it is possible to use directly the definition of the ITS-90 (section B.9.1).

On the contrary, in real cases radiation thermometers are not monochromatic so the definition of the temperature scale becomes a ratio *r* as

$$r = \frac{\int_{\Delta\lambda} L_{\lambda,b}(\lambda,T_0) R_L(\lambda) d\lambda}{\int_{\Delta\lambda} L_{\lambda,b}(\lambda,T) R_L(\lambda) d\lambda} \tag{B.35}$$

Solving an integral equation numerically presents no problem to a digital computer, but there are situations where it is desirable to have some simpler algorithm available.

For that reasons the concepts of limiting effective wavelength and mean effective wavelength were introduced.

B.9.4.1 The mean effective wavelength and the limiting effective wavelength

Eq.(B.35) may be written as

$$\int_{\Delta\lambda} r\, L_{\lambda,b}(\lambda,T) R_L(\lambda)\, d\lambda = \int_{\Delta\lambda} L_{\lambda,b}(\lambda,T_0) R_L(\lambda)\, d\lambda \tag{B.35bis}$$

It can be noticed that for eq. (B.35bis) to hold, the two integrands must intersect at least once. The intersection wavelength is called the mean effective wavelength $\lambda_{T_0\text{-}T}$ [6].

By means of this definition the integrals in eq.(B.36) are reduced to the ratio of spectral radiances calculated at a specific wavelength

$$r = \frac{\int_{\Delta\lambda} L_{\lambda,b}(\lambda,T_0) R_L(\lambda)\, d\lambda}{\int_{\Delta\lambda} L_{\lambda,b}(\lambda,T) R_L(\lambda)\, d\lambda} = \frac{L_{\lambda,b}(\lambda_{T_0-T},T_0)}{L_{\lambda,b}(\lambda_{T_0-T},T)} = \frac{\exp(\frac{c_2}{n\lambda_{T_0-T}T})-1}{\exp(\frac{c_2}{n\lambda_{T_0-T}T_0})-1} \tag{B.36}$$

This is the working version of the defining equation of the ITS-90 (eq. (B.25)).

Now, to compute the mean effective wavelength, the limiting effective wavelength (λ_T) should be introduced. It is defined as the limit of the mean effective wavelength as $T \rightarrow T_0$.

Starting with the ratio of eq. (B.36) and taking into account the Wien approximation an expression for λ_T is obtained.

$$\frac{1}{\lambda_T} = \frac{\int_{\Delta\lambda} \frac{1}{\lambda} L_{\lambda,b}(\lambda,T) R_L(\lambda)\, d\lambda}{\int_{\Delta\lambda} L_{\lambda,b}(\lambda,T) R_L(\lambda)\, d\lambda} \tag{B.37}$$

And , eq. (B.36) can be rearranged as

$$\frac{1}{\lambda_{T_0-T}} = \frac{1}{\frac{1}{T} - \frac{1}{T_0}} \int_{1/T_0}^{1/T} \frac{1}{\lambda_T} d\left(\frac{1}{T}\right) \tag{B.38}$$

In addition, it is shown from experience that the inverse limiting effective wavelength is approximately linear with the inverse temperature, so finally the mean effective wavelength can be computed as

$$\frac{1}{\lambda_{T_0-T}} \cong \frac{1}{2}\left(\frac{1}{\lambda_{T_0}} + \frac{1}{\lambda_T}\right) \tag{B.39}$$

where λ_{T0} is defined from eq.(B.37) with T equal to T_0. It is also clear the meaning of "mean".

In addition it can be noticed that eq.(B.39) can be evaluated if the temperature is known, but the temperature cannot be known without calculating the mean effective wavelength. So it is an iterative problem that is solved by successive approximations, beginning with the use of the centre wavelength of the passband of the radiation thermometer as a first approximation of the mean wavelength, with that it is possible to calculate a first approximation temperature from eq.(B.36) and consequently a better approximation of the mean effective wavelength.

B.9.5 Measurement of non blackbody temperature

Considering a non-blackbody surface of spectral radiance given by eq.(B.26), if it can be assumed that the emittance is independent of direction within the angle of acceptance of the pyrometer and of the radiated area and recalling the concept of spectral radiance temperature, one can write an expression as eq. (B.35bis) but for the emittance

$$\int_{\Delta\lambda} \varepsilon(\lambda) L_{\lambda,b}(\lambda,T) R_L(\lambda)\, d\lambda = \int_{\Delta\lambda} L_{\lambda,b}(\lambda,T_\lambda) R_L(\lambda)\, d\lambda \tag{B.40}$$

If the emittance can be assumed to be constant throughout the passband (local graybody assumption), then it is possible to choose an appropriate mean effective wavelength, between the real temperature and the spectral radiance one, and to infer an equation very close to eq.(B.36)

$$\varepsilon_g = \frac{\int_{\Delta\lambda} L_{\lambda,b}(\lambda,T_\lambda) R_L(\lambda)\, d\lambda}{\int_{\Delta\lambda} L_{\lambda,b}(\lambda,T) R_L(\lambda)\, d\lambda} = \frac{L_{\lambda,b}\left(\lambda_{T_\lambda - T},T_\lambda\right)}{L_{\lambda,b}\left(\lambda_{T_\lambda - T},T\right)} = \frac{\exp\left(\frac{c_2}{n\,\lambda_{T_\lambda - T}\,T}\right)-1}{\exp\left(\frac{c_2}{n\,\lambda_{T_\lambda - T}\,T_\lambda}\right)-1} \tag{B.41}$$

B.10 References

[1] D. P. De Witt and G. D. Nutter, Theory and practice of radiation thermometry (Wiley, 1988), Chapters 1, 2, 4.

[2] F. P. Incropera, D. P. DeWitt, T. L. Bergman, A. S. Lavine , Fundamental of Heat and Mass Transfer, (Wiley, 6^{th} edition), Chapter 12.

[3] K. Boboridis, "Application of single-wavelength radiation thermometry and high-speed laser polarimetry to thermophysical property measurements on pulse-heated metals", (2001) NIST, Institut für Experimentalphysik der Technischen Universität Graz, Austria.

[4] H. Preston – Thomas, Metrologia 27 (1990), 3.

[5] "Supplementary information for ITS-90", BIPM-1990, Chapter 6.

[6] H. J. Kostkowski and R. D. Lee, in Temperature: Its Measurement and Control in Science and Industry, 3 [1] (Reinhold Publishing Co., 1962), 449.